HAL
open science

Dispositifs de puissance en diamant à base de contact Schottky : réglage des propriétés interfaciales pour démontrer les performances ultimes du diamant

Jesus Canas Fernandez

To cite this version:

Jesus Canas Fernandez. Dispositifs de puissance en diamant à base de contact Schottky : réglage des propriétés interfaciales pour démontrer les performances ultimes du diamant. Micro et nanotechnologies/Microélectronique. Université Grenoble Alpes [2020-..]; Universidad de Cádiz, 2022. Français. NNT : 2022GRALT004 . tel-03660573

HAL Id: tel-03660573

https://theses.hal.science/tel-03660573v1

Submitted on 6 May 2022

HAL is a multi-disciplinary open access archive for the deposit and dissemination of scientific research documents, whether they are published or not. The documents may come from teaching and research institutions in France or abroad, or from public or private research centers.

L'archive ouverte pluridisciplinaire **HAL**, est destinée au dépôt et à la diffusion de documents scientifiques de niveau recherche, publiés ou non, émanant des établissements d'enseignement et de recherche français ou étrangers, des laboratoires publics ou privés.

THÈSE

Pour obtenir le grade de

DOCTEUR DE L'UNIVERSITE GRENOBLE ALPES & DE L'UNIVERSIDAD DE CÁDIZ

Spécialité: **NANO ELECTRONIQUE ET NANOTECHNOLOGIES**

Arrêté ministériel : le 6 janvier 2005 – 25 mai 2016

Présentée par

Jesús Cañas Fernández

Thèse dirigée par **Etienne GHEERAERT, Université Grenoble Alpes**
Codirigée par **Marina GUTIÉRREZ PEINADO, Universidad de Cádiz**
Et co-encadrée par **David EON, Université Grenoble Alpes** et **Julien PERNOT, Université Grenoble Alpes**

préparée au sein des **laboratoires Institut NÉEL, CNRS**
dans **l'École Doctorale Electronique, Electrotechnique, Automatique, Traitement du Signal (EEATS) et Institut IMEIMAT dans l'Escuela de Doctorado de la Universidad de Cádiz (EDUCA)**

Schottky contact based diamond power devices: tuning the interfacial properties to demonstrate diamond unleashed performance

Dispositifs de puissance en diamant à contact Schottky: réglage des propriétés interfaciales pour démontrer les performances ultimes du diamant

Thèse soutenue publiquement le **28 janvier 2022**,
devant le jury composé de :

Monsieur Denis DAUVERGNE
Directeur de recherche, CNRS-LPSC (France), Président
Monsieur Robert NEMANICH
Professeur, Arizona State University (USA), Rapporteur
Monsieur Philippe GODIGNON
Directeur de recherche, CSIC-CNM (Espagne), Rapporteur
Madame Mariko SUZUKI
Chargée de recherche, Universidad de Cádiz (Espagne), Membre
Madame Eva MONROY
Directrice de recherche, CEA-IRIG-PHELIQS (France), Membre
Monsieur Etienne GHEERAERT
Professeur, Université Grenoble Alpes (France), Directeur de thèse
Madame Marina GUTIÉRREZ PEINADO
Maîtresse de conférences, Universidad de Cádiz (Espagne), Directrice de thèse
Monsieur David EON
Maître de conférences, Université Grenoble Alpes (France), Co-encadrant
Monsieur Julien PERNOT
Professeur, Université Grenoble Alpes (France), Co-encadrant

UNIVERSITÉ GRENOBLE ALPES &
UNIVERSIDAD DE CÁDIZ

DOCTORAL THESIS

Schottky contact based diamond power devices: tuning the interfacial properties to demonstrate diamond unleashed performance

Author:
Jesús CAÑAS FERNÁNDEZ

Supervisors:
Pr. Etienne GHEERAERT
Dr. Marina GUTIÉRREZ

A thesis submitted in fulfillment of the requirements for the degree of Doctor of Philosophy

in the

Wide band gap semiconductors group (Institut NÉEL - CNRS) &
Material science and engineering group (Science Faculty - UCA)

January 28th, 2022

Acknowledgements

This work wouldn't have been possible without the contribution, help and support of many people which I would like to address in their respective languages:

Quiero agradecerle a mi madre el haberme inculcado el interés y la fascinación por la ciencia. No puedo imaginarme haber llegado hasta aquí sin ti. A mi padre, le agradeco su paciencia al aguantar tantas comidas familiares hablando de ciencia. Bromas aparte, tampoco hubiera llegado hasta aquí sin tu ayuda. A mis abuelos, con los que me gustaría haber pasado más tiempo y la distancia nos robó tantos ratos juntos.

También quiero darle las gracias a mis amigos, los que a pesar de vernos de tanto en tanto, saben que todo sigue siempre igual. Y a mis amigos emigrados, con los que he compartido alegrías y sufrimientos desde que llegue a Grenoble. También debo darle las gracias a Daniel Araujo por introducirme al bonito mundo del diamante y guiarme en mi investigación, mas que como un jefe, como un amigo. Igualmente, tengo que agradecer a mi directora de tesis, Marina Gutiérrez. Gracias también a Bea y Gonzalo por tantas horas juntos. Gracias a Daniel Fernández y Fernando LLoret por vuestra gran ayuda con la microscopía. Debo agraceder también a Dietmar Leinen por su excelente y detallado trabajo en XPS. Por último, me gustaria agraceder al resto de mis compañeros de grupo en Cádiz y a los técnicos que han hecho posibles tantos resultados experimentales.

Je tiens à remercier mon directeur, Etienne Gheeraert, pour l'opportunité qu'il m'a donnée de venir dans un laboratoire prestigieux comme l'institut NEEL et de travailler sur un projet extraordinaire comme le GreenDiamond. J'aimerais également remercier David Eon pour son soutien et ses discussions intéressantes et pour m'avoir donné l'opportunité de travailler sur le projet HVDC. Je dois également remercier Julien, Juliette, Cédric, Khaled, Jessica, Martin, Sylvain et le reste de l'équipe SC2G pour tout ce que j'ai appris à vos côtés. Mon travail n'aurait pas été possible sans votre aide. Je dois également remercier Bruno, Gwenelle et Thierry de Nanofab pour les nombreuses lithographies réalisées ensemble ainsi que Fabrice, Laurent, Richard et Eric pour leur aide.

Finalmente, non potrei mai ringraziare abbastanza Martina per la sua pazienza dopo tanti fine settimana di lavoro. Anche i giorni peggiori sono stati resi più piacevoli con te.

Contents

Introduction **1**

1 Diamond Power Electronics: Material Properties and State of Art **5**
1.1 Power electronics nowadays . . . 6
1.2 UWBG semiconductors properties for power electronics . . . 8
1.3 Diamond synthesis, wafers, dopants and surfaces . . . 10
1.3.1 High-pressure high-temperature synthesis . . . 10
1.3.2 Wafers . . . 11
1.3.3 Epitaxy & dopants . . . 12
1.3.4 Surfaces . . . 14
1.4 Diamond devices state of the art . . . 16
1.4.1 Schottky diodes . . . 16
1.4.2 Transistors . . . 17
1.5 Summary & conclusion . . . 19

2 Schottky Contact-Based Diamond Devices: Physical Models and Technology **21**
2.1 Metal-Semiconductor junctions . . . 22
2.2 Diamond Schottky contacts modelization . . . 24
2.2.1 Forward state . . . 24
2.2.1.1 Thermionic emission . . . 24
2.2.1.2 Diamond resistivity physical models . . . 25
2.2.2 Reverse state . . . 27
2.2.2.1 Depletion region . . . 28
2.2.2.2 Schottky barrier height . . . 29
2.2.2.3 Leakage current model . . . 31
2.2.2.4 Avalanche breakdown . . . 34
2.3 Ohmic contacts in diamond . . . 36
2.4 P-type diamond Schottky diodes . . . 37
2.4.1 Non-Punch Through Performance . . . 37
2.4.2 Technological constraints and their limitations to performance . . . 38
2.5 P-type diamond reverse blocking MESFET . . . 42
2.5.1 Concept and functioning . . . 42
2.5.1.1 On-state . . . 42
2.5.1.2 Off-state . . . 46

2.5.2 Normally-off character . . . 46
2.5.3 Non-Punch Though Performance . . . 46
2.6 Conclusion . . . 48

3 Diamond-metal interface: The search for an ideal Schottky metal 51
3.1 LD1 sample fabrication . . . 52
3.1.1 p-type drift layer epitaxy . . . 52
3.1.2 Ohmic contact fabrication . . . 53
3.1.3 Schottky contact fabrication . . . 53
3.2 Lateral diodes characteristics . . . 54
3.3 TEM study of the interface . . . 56
3.4 XPS studies of the interface . . . 61
3.5 Kelvin probe studies . . . 67
3.6 DFT simulation of the interface . . . 72
3.6.1 (100) O-terminated diamond . . . 73
3.6.2 (100) molybdenum - (100) O-terminated diamond interface . . . 75
3.7 Conclusion . . . 79

4 Vertical Schottky diodes: interface solutions and HV implementation 81
4.1 VD1 & VD2 samples fabrication process . . . 82
4.1.1 Encapsulated p+ layer epitaxy . . . 82
4.1.2 p-type drift layer epitaxy . . . 83
4.1.3 Ohmic contact fabrication . . . 84
4.1.4 Schottky contact fabrication . . . 84
4.2 Sample VD1 . . . 84
4.2.1 I-V characteristics . . . 85
4.2.2 C-V characteristics . . . 87
4.2.3 Thermal stability . . . 88
4.2.4 I-V characteristics at high temperature . . . 89
4.2.5 High field off-state I-V characteristics . . . 90
4.2.6 Sample VD1 conclusion . . . 92
4.3 Sample VD2 . . . 92
4.3.1 I-V characteristics . . . 93
4.3.2 C-V characteristics . . . 93
4.3.3 I-V characteristics at high temperature . . . 95
4.3.4 High field off-state I-V characteristics . . . 96
4.3.5 EBIC & cathodoluminiscence characterization . . . 98
4.3.6 Sample VD2 conclusion . . . 100
4.4 Summary and Conclusions . . . 102
4.5 Road-map . . . 103

5 1 kV Normally-off Lateral Reverse-Blocking MESFET **105**
5.1 Design . . . 106
5.2 RB sample fabrication process . . . 107
5.2.1 Drift layer epitaxy . . . 108
5.2.2 Metallic mask fabrication and p+ selective growth . . . 108
5.2.3 Contacts fabrication and surface oxygenation . . . 110
5.3 Sample characterization . . . 110
5.3.1 p+ layer and contact resistivity . . . 110
5.3.2 Transfer characteristics at RT . . . 112
5.3.3 Gate characteristics . . . 114
5.3.4 Transfer characteristics vs temperature . . . 116
5.3.5 Higher temperature effects . . . 119
5.3.6 Failure analysis . . . 120
5.4 Conclusion and future steps . . . 121

Conclusions and Perspectives **123**

Bibliography **127**

A Experimental techniques and simulation tools **145**
A.1 Transmission electron microscopy . . . 145
A.1.1 Technique description . . . 145
A.1.2 TEM in this work . . . 146
A.2 X-rays photoelectron spectroscopy . . . 147
A.2.1 Technique description . . . 147
A.2.2 XPS in this work . . . 147
A.3 Kelvin probe force microscopy . . . 148
A.3.1 Technique description . . . 148
A.3.2 Kelvin probe in this work . . . 149
A.4 Electric measurements . . . 149
A.4.1 Electrical measurements in this work . . . 149
A.5 EBIC & Cathodoluminiscence . . . 150
A.5.1 Techniques descriptions . . . 150
A.5.2 Role in this work . . . 151
A.6 Density functional theory . . . 152
A.6.1 Theoretical description . . . 152
A.6.2 Role in this work . . . 154

B Samples summary **155**

C Thesis summaries **157**
C.1 English Summary . . . 157
C.2 Resumé Français . . . 162

C.3 Resumen Español 167

D Publications and Conferences **175**

D.1 Publications 175

D.2 Conferences 175

D.2.1 Oral presentations 175

D.2.2 Poster presentations 176

E Abstracts **179**

List of Figures

1.1 On vs off state characteristics of a p-type Schottky diode. On the left, the off-state is characterized by the breakdown voltage V_{BD} and parasitic leakage current. The vertical diode shows the space charge region produced by the depletion under the Schottky. On the right, the on-state is schematized being characterized by the on-state resistance R_{ON}. The diode scheme shows the flow of holes (i.e. the sense of the current) from ohmic to Schottky. 7
1.2 UWBG materials properties comparison. Diamond takes advantage over competitors especially because of its thermal conductivity, mobility, saturation velocity and low dielectric constant. 10
1.3 Scheme showing the main growth directions appearing in high temperature high pressure (HPHT) diamond synthesis. Courtesy to Dr. Alba. 11
1.4 Diamond wafer size, dislocation density and cost comparison for the different production methods and their expected future projection [44]. 12
1.5 Schematic process for diamond MPCVD epitaxy. 13
1.6 Schematic illustration of the transfer doping process. a) On the left, the scheme and the energy bands of the H-terminated diamond in the (100) direction. On the right, a molecule before adsorption with its associated molecular orbitals. b) The molecule is adsorbed causing the electrons from diamond VB to be transferred to the LUMO orbitals leaving behind a 2D hole gas. 15
1.7 Oxygen-terminated diamond possible surface groups. 16
1.8 Scheme for the different Schottky architectures. On the left, encapsulated type diode. The CVD p+ growth extend over the edge allowing its contact through the back face. On the center, the vertical structure. This structure tends to display a resistive on-state due to the thick and low conductive p+ HPHT substrate. On the right, the pseudo-vertical architecture. While this structure is very efficient in terms of performance, the early stage of diamond technology makes it very limited in drift layer thickness. 17
1.9 Scheme of the different fabricated lateral unipolar transistors. 19

2.1 Band structure of a metal/p-type semiconductor junction: a) before contact for a metal and a p-type semiconductor. b) After intimate contact at thermal equilibrium. 22

2.2 Free hole density and mobility versus temperature. The discontinuous lines represent the mobility and free hole density for $N_A = 10^{16}\ cm^{-3}$ while the continuous for $N_A = 10^{15}\ cm^{-3}$. 26
2.3 Diamond resistivity versus temperature for $N_A = 3 \cdot 10^{16} cm^{-3}$ for different compensation ratios. 28
2.4 Schottky barrier potential energy plot based on eq. 2.31 for a 1.6 eV Schottky barrier height, $N_A = 3 \cdot 10^{16} cm^{-3}$ with and without image force lowering and with and without electric field. The classical turning point are represented for an arbitrary energy ε. 30
2.5 Reverse leakage current density and its mechanisms represented for a $N_A = 10^{15} cm^{-3}$ and a temperature of a) 300K and b) 500K for a different set of ϕ_b values. 32
2.6 Reverse leakage current density represented for a set of doping levels versus a) field and b) voltage at 300K and c) versus field at 550K for a ϕ_b of 1.5 eV. . . 33
2.7 Reverse leakage current density for a $N_A = 10^{15} cm^{-3}$ and ϕ_b of 1.5 eV for temperature of 300K, 400K and 500K. 35
2.8 Avalanche breakdown field and voltage versus doping level for boron doped diamond based on ref. [50] for a non punch through design. 36
2.9 Specific on-state resistivity vs breakdown voltage for a non-punch through diamond Schottky diode at RT and 550K. For comparison, the trade-off is also represented for Si at RT, based on [133], and calculated for SiC at RT and 500K based on [134] for mobility and [130] for the doping dependence of the critical electric field. Some of the best experimental results from diamond Schottky diodes are also represented for comparison from [83, 135, 136, 79, 137]. 37
2.10 E_{max} vs V_{BD} comparison between a NPT design and a 5 μm PT design with $N_A = 10^{15} cm^{-3}$. 39
2.11 Scheme of the possible configurations of the RBMESFET. On the top, the on-state configuration with the current flowing from source to drain. On the bottom, the three off-state configurations: i) Close channel, ii) Schottky diode and iii) Reverse blocking configurations. 41
2.12 RBMESFET scheme used for the modelization of the on-current. 43
2.13 Transfer characteristics of a RBMESFET with $\phi_b = 1.6V$, $n = 1.4$, $N_A = 3 \cdot 10^{16}$ cm^{-3}, $t_{eff} = 500nm$, $W_c = 650\mu m$ and $L_c = 68\mu m$ for V_{GS} =0 to 15V every 5V step. 45
2.14 Transfer characteristics of a RBMESFET with $\phi_b = 1.6V$, $n = 1.4$, $N_A = 3.5 \cdot 10^{16}\ cm^{-3}$, $N_A/N_D = 0.2$, $t_{eff} = 180nm$, $W_c = 650\mu m$ and $L_c = 68\mu m$ for $V_{GS} = -1.2V$ for temperatures between 300K and 425K with a 25K step. . . . 45
2.15 On vs off state trade-off for a NPT RBMESFET with $\phi_b = 1.6V, n = 1.4$, no compensation, $Wc = 650\mu m$ and $Lc = 68\mu m$ with normally-off character at RT and 500 K and normally-on character with $V_{TH}^{ON} = 15V$ at RT. 47

3.1 Schematic fabrication process for the lateral diamond Schottky diode sample LD1. The first step is the epitaxy of the drift layer. Once the epitaxy is finished, the ohmic contacts are fabricated following the usual lithography plus lift-off process, followed by a thermal treatment at 750 K to reduce the contact resistance. The top surface is then treated by means of an ozone plasma in order to acquire an oxygen-terminated surface. A laser lithography process is again used to define the Schottky electrodes, followed by the deposition of the molybdenum and zirconium Schottky metal stacks. 52
3.2 Optical microscope image of the LD1 sample after the full fabrication process. 53
3.3 I-V measurements for a molybdenum contact and a zirconium contact with 100 micron radius and 5 microns spacing before and after the O_3 surface passivation treatment. 55
3.4 Mott-Schottky plot for C-V measurements performed on a molybdenum contact and a zirconium contact with 100 micron radius and 5 micron spacing. The $N_A - N_D$ value deduced from both curves is $1.6 \cdot 10^{16}\ cm^{-3}$. However, the V_{BI} for the molybdenum contact is 3.0 eV while for the zirconium contact is 3.4 eV. The depletion region reaches the substrate SCR at 3.8 V for zirconium and at 4.2 V for molybdenum. The deduced channel thickness is 900 nm, 400 nm being always depleted due to the p-n junction between drift layer and substrate. 55
3.5 a) High resolution transmission electron microscopy image of the diamond-molybdenum interface. The micrograph presented shows diamond on the left and molybdenum on the right with their associated fast Fourier transform for their phase identification. b) Zoomed-in high resolution transmission electron microscopy image of the diamond-molybdenum interface. 57
3.6 a) TEM, STEM-HAADF and EDX-calculated compositional images from the same region in the lamella with diamond on the left followed by the Mo/Pt/Au metal stack and the FIB deposited platinum during the lamella preparation on the right. b) Atomic fraction profile across the stack calculated based on a Brown-Powell ionization cross section model to each EDX spectrum from the previous EDX image. 58
3.7 a) High resolution transmission electron microscopy image of the zirconium-diamond interface. The micrograph presented shows zirconium on the left and diamond on the right, with their associated fast Fourier transform performed on the blue regions. b) Zoomed-in high resolution transmission electron microscopy image of the zirconium-diamond interface. 59
3.8 a) TEM, STEM-HAADF and EDX-calculated compositional images from the same region in the lamella with diamond on the left followed by the Zr/Pt/Au metal stack. b) Atomic fraction profile across the stack calculated based on a Brown-Powell ionization cross section model to each EDX spectrum extracted from the previous EDX image. 60

3.9 Chemical profile of the Au/Pt/Mo contact on diamond extracted from spectra alternately recorded each 30 seconds while sputtering etching using 0.5 kV Ar+ ions at 33° incidence angle with respect to the sample surface with Zalar compucentric rotation is performed. 62
3.10 Representative regions of the spectra (C(1s), Mo(3d) and VB) recorded at different sputtering times between 51 and 92 min. The molybdenum layer (51 min), its interface with diamond (66 and 70 min) and pure diamond (80 and 92 min) are distinguished. Only the position of the peaks are representative while the height of the peaks are chosen in order to ameliorate the reader comprehension of the spectra. 63
3.11 Chemical profile of the Au/Pt/Zr contact on diamond extracted from spectra alternately recorded each 30 seconds while sputtering etching using 0.5 kV Ar+ ions at 33° incidence angle with respect to the sample surface with Zalar compucentric rotation is performed. 65
3.12 Representative regions of the spectra (C(1s), Zr(3d) and VB) recorded at different sputtering times between 50 and 88 min. The zirconium layer (50 and 52 min), its interface with diamond (58 min) and pure diamond (88 min) are distinguished. Only the position of the peaks are representative while the height of the peaks are chosen in order to ameliorate the reader comprehension of the spectra. 66
3.13 Band scheme of three different profiles in a Schottky contact. 1) The vertical band scheme of a diamond-metal junction. 2) The vertical band scheme of diamond and its oxygen-terminated surface. 3) The lateral band scheme along diamond-metal interface up to its oxygen-terminated surface. In this band scheme, the diamond bands are bent from their position at the interface of the Schottky contact to the position at the oxygen-terminated surface. As this band bending happens laterally over the interface-surface, the work function of diamond depends on the lateral distance, enabling to observe the lateral depletion region of the contact by KPFM. 68
3.14 a) Atomic force microscopy image of a molybdenum Schottky contact with diamond in the left and the Mo/Pt/Au contact stack in the right. b) The KPFM (red) and AFM (blue) profiles along the diamond surface and the Mo/Pt/Au contacts in the region specified in the figure a). 69
3.15 a) Atomic force microscopy image of a zirconium Schottky contact with diamond in the left and the Zr/Pt/Au contact stack in the right. b) The KPFM (red) and AFM (blue) profiles along the diamond surface and the Zr/Pt/Au contacts in the region specified in the figure a). 71
3.16 (100) O-terminated diamond relaxed slab based on ketone 1x1 reconstruction. The highlighted distances between the atoms are in 3D (not projected) and are displayed in angstrom. 73

3.17 a) 2D (x-y plane) averaged potential energy distribution along the (100) O-terminated diamond slab. b) Density of states in the vicinity of the band-gap region calculated for the (100) O-terminated diamond slab. 74
3.18 Relaxed slab of (100) molybdenum interface with (100) O-terminated diamond. The full slab is composed of 346 atoms. 76
3.19 Electron localization function calculated for the interface of (100) molybdenum and (100) oxygen-terminated diamond projected along the x-direction on the y-z plane of the unit cell in the left and along the y-direction on the x-z plane of the unit cell in the right. The red colors in the graph show high probability electron regions, while the blue colors show low probability regions. 77
3.20 2D (x-y plane) averaged potential energy distribution calculated on relaxed slab of the interface of (100) molybdenum and (100) oxygen-terminated diamond. 78

4.1 Schematic fabrication process for an encapsulated diamond Schottky diode. The first step is the epitaxy of the encapsulated p+ layer. After the p+ layer, the epitaxy of the p-type drift layer follows. Once the epitaxy of both layers is finished, the ohmic metals are evaporated on the back face followed by a thermal treatment to reduce the contact resistance. The top surface is then treated by means of an ozone plasma in order to acquire an oxygen-terminated surface. A photolitography is then used to define the Schottky electrodes, followed by the deposition of the Schottky metal stack. 82
4.2 Optical image of the back face of samples a) VD1 and b) VD2. The p+ encapsulation can be observed on the corners of both samples. 83
4.3 Optical image of the top face of samples a) VD1 and b) VD2 after the full fabrication process. The sample VD1 is composed of molybdenum and zirconium electrodes, its drift layer its thin ($\sim 430nm$) and has a doping level of $N_A = 3 \cdot 10^{16} cm^{-3}$. The sample VD2 is only composed of molybdenum electrodes. Its drift layer is a thick non-intentionally doped layer with expected residual concentration of boron of $N_A \sim 2 \cdot 10^{15}\ cm^{-3}$. A notable concentration of hillocks and round defects are present on the top surface. These are attributed to the prolonged epitaxy process both for the p+ and non-intentionally doped layers. 85
4.4 I-V characteristics for a) 50 microns molybdenum contact and b) 50 microns zirconium contact before and after an ozone passivation treatment carried out after the sample VD1 fabrication. 86
4.5 I-V characteristics for a set of different 50 microns contact for a) molybdenum and b) zirconium after an ozone passivation treatment carried out after the sample VD1 fabrication. 87
4.6 Mott-Schottky plot for a) a 50 microns molybdenum contact and b) a 50 microns zirconium contact. Both curves are measured after the ozone passivation treatment carried out after the sample fabrication. 88

4.7 I-V characteristics at RT for a) a 50 microns molybdenum and b) a 50 microns zirconium contact before and after a 400 K and 500 K thermal treatments. . . 89
4.8 I-V versus temperature characteristics for a 50 microns molybdenum contact after ozone passivation and thermal treatments carried out after the sample fabrication. 90
4.9 I-V characteristics for a set of different 50 microns contact for a) molybdenum and b) zirconium after an ozone passivation and annealing treatment carried out after the sample fabrication for molybdenum and before the annealing for zirconium. 92
4.10 I-V characteristics for seven 50 microns radius molybdenum contacts from different regions in the sample VD2 showing a reproducible behaviour with a turning-on voltage of 1.22V. 94
4.11 Mott-Schottky plot showing the measured data and a fit performed based on eq. 2.24 and the $N_A - N_D$ depth profile for a 100 micron radius molybdenum Schottky contact. 95
4.12 I-V versus temperature characteristics for a 50 microns radius molybdenum contact. The curves were fitted according to eq. 2.10 in order to extract the ϕ_b and ideality factor values displayed. 96
4.13 Reverse I-V characteristics up to 1.1 kV at RT for a set of five circular 50 microns radius and two 100 microns radius molybdenum Schottky contacts. Two 50 micron contacts display no detectable leakage current up to 1.1 kV. The rest of the 50 micron contacts show a rapidly increasing leakage current at 1kV, 0.68kV and 0.64 kV irreversibly degrading the contact blocking capabilities after the high voltage stress. Also, the reverse I-V characteristics up to 1.1 kV at 500 K are represented for one the best performing circular 50 microns radius molybdenum Schottky contact (C7 cs2) sustaining 0.7 kV. 97
4.14 a) The 5k exciton CL spectrum measured on the sample VD2 at 10 kV is represented. The spectrum remained unchanged independently of the position in the sample and whether if defects were present or not. The active boron concentration extracted from the ratio between the FE^{TO} and BE^{TO} peaks is $3 \cdot 10^{15}\ cm^{-3}$ according to ref. [164]. b) The 5K CL visible range spectrum (from 250 nm to 620 nm) measured on three regions of the sample VD2 at 10 kV is represented. The spectra is normalized respect to the FE^{TO} peak as it height and morphology is similar in all regions. Three spectra are represented: i) in yellow, the spectrum for a defect free sample region, ii) in red, the spectrum obtained from a round defect and iii) the spectrum obtained from a hillock. 99

4.15 a) and c) present the scanning electon microscopy (SEM) micrograph of two 100 micron side square Schottky contact. In a), the imperfections due to fabrication are highlighted with black arrows with special emphasis in a zoomed-in region showing the typical morphology of these fabrication related defects. In c) a squared hillock is observed inside the contact. b) and d) present the EBIC images obtained at 30 kV and 200 V and 150 V in reverse bias superimposed to the previous SEM micrographs a) and c) respectively. In b) the SCR region and hotspots are identified at the near edge region of the contact. In d) the hillock show a strong EBIC signal especially on the aristas. 101
4.16 Sustained electric field versus Schottky electrode area for this work molybdenum contacts compared with numerous bibliographic references [167, 168, 150, 149, 169, 170, 171, 172] 103

5.1 RBMESFET designed layout using circular architecture, common source electrodes and $L_{GS} = 8\mu m$, $L_G = 30\mu m$ and $L_{GD} = 30\mu m$ with minimum pad size of 100x120 microns. The light blue represents the p-type drift layer while the darker blue represents the p+ selectively grown layer under the yellow ohmic electrode. The black electrodes account for the Schottky drain and gate. Several circular TLM structures and Schottky contacts are also present in the layout for testing purposes. 107
5.2 RBMESFET fabrication process scheme. 108
5.3 a) Phase shift interferometry of the sample RB after the drift layer epitaxy. The rugosity of the surface remained similar to the substrate before the epitaxy. b) CL 5K exciton spectra showing FE^{TO} and BE^{TO} peaks. The ratio between the two peaks is associated with a doping level of $N_A = 3.5 \cdot 10^{16}\ cm^{-3}$ [164]. . . . 109
5.4 a) Optical image of a p+ feature of the sample RB . b) Phase level interferometry image of the same feature. 109
5.5 Optical image of the fabricated sample RB: Device picture showing the ohmic source over the p+ diamond layer and the molybdenum Schottky drain, gate and test structure on the left. On the right, a full picture of the sample. 110
5.6 Transmission Line Method (TLM) on a test sample to determine the p+ and contact resistivities. 111
5.7 Room temperature transfer characteristics for the normally-off RBMESFET at different gate voltages. The transistor is off at V_{GS}=0 and reaches $\sim 1.5\ \mu$ A/mm at V_{DS}=-25 V and V_{GS}=-0.8 V. No leakage current is observed in reverse. 112
5.8 High voltage transfer characteristics for the a) closed channel configuration and b) reverse blocking configuration of the RBMESFET both sustaining 1 kV. 113
5.9 I-V characteristics (in red) and Mott-Schottky plot (in blue) for the molybdenum Schottky gate. Lateral and vertical depletion capacitance under the gate are fitted with dashed line. $N_A - N_D$ extracted from the slope of the C^{-2} plot is $10^{16}\ cm^{-3}$ for the vertical depletion region and $4 \cdot 10^{16}\ cm^{-3}$ for the lateral. From the intercept with the x axis a V_{BI}= 1.72V is extracted. 115

5.10 I_{GS} versus V_{GS} represented at RT, 350 K and 400K. The ideality factor decreases from 1.67 at RT to 1.28 at 400K while the barrier increases from 1.02 eV to 1.2 eV. 116
5.11 a) Transfer characteristics for the normally-off RBMESFET at V_{GS}=-0.8V versus temperature. No leakage current is observed in reverse BIAS. The current at 425K is increased by a factor $\sim$ 40 compared to RT reaching $70\mu A/mm$ at -25V. b) Transconductance vs V_{GS} plot for the normally-off RBMESFET at $V_{DS} = 10V$ versus temperature. 117
5.12 HV transfer characteristics for the RBMESFET at 425K for the close channel configuration with $V_{GS} = 5V$ in the red curve and for the on-state and Schottky diode configuration in the blue curve with $V_{GS} = -0.8V$. 118
5.13 Transfer characteristics for the RBMESFET at 500K for negative to positive V_{DS} sweep in (a) and viceversa in (b). The high temperature operation ionize the substrate dopants causing the values of V_{GS} and V_{DS} to affect the SCR of the back p-n junction preventing the normal transistor operation. 119
5.14 Micrograph of the sample RB showing the working transistors in the sample and the p+ features that create leaky drains and gate-drain shortcuts. 121

A.1 a) Transmission electron microscopy scheme showing the condenser lens, the beam being transmitted parallel through the specimen and the image formation thanks to the objective lens and aperture in a CCD camera. b) Scanning transmission electron microscopy scheme showing the condenser aperture and polepiece focusing the electron beam on a spot on the specimen. The different images are formed through bright field and annular dark field detectors. Complementary, energy dispersive x-rays and electron energy loss spectroscopy can also be collected to enlarge the chemical and structural composition of the sample. 146
A.2 a) Scheme representing the Ar+ sputtering through the metal contact layer while applying a Zalar compucentric rotation. b) Scheme of the x-rays focused in the well formed by the Ar+ sputtering and the XPS spectrometer collecting the photoemitted electrons to study the depth profile of the contact. 147
A.3 a) Scheme representing the system KPFM tip-sample at thermal equilibrium. b) Scheme of the system KPFM tip-sample when a potential equal to the contact potential difference is applied. 148
A.4 Home-made vacuum probe station at the Institut NEEL where the electrical measurements were performed using: a) Keithley SMU 2636A, b) SMU 2410 and c) ModuLab XM MTS Solartron. 150
A.5 Scheme of the bands of a Schottky contact on p-type diamond where electon hole pairs (EHP) are generated by an e-beam. Two phenomena are sketched, the diffusion plus drift of the electrons from the EHP that lead to electron beam induced current (EBIC) and the radiative recombination of the EHP which is used in catodoluminiscence (CL) spectroscopy. 151

A.6 An image of the used set-up to perform electron beam induced current (EBIC) and cathodoluminiscence (CL) spectroscopy. 152
A.7 Illustrative picture on how modern pseudo-potentials are obtained inverting the free-atom Schrödinger equation for a given reference electronic configuration and forcing the pseudo-wavefunctions to coincide with the true valence wavefunctions beyond a certain distance. 154

B.1 Description of the diverse epitaxy conditions and Schottky electrodes used in this thesis samples. 155

C.1 Sustained electric field versus Schottky electrode area for this work molybdenum contacts compared with numerous bibliographic references [167, 168, 150, 149, 169, 170, 171, 172]. 160
C.2 HV transfer characteristics of the RBMESFET at 425K for the close channel configuration with $V_{GS} = 5V$ in the red curve and for the on-state and Schottky diode configuration in the blue curve with $V_{GS} = -0.8V$. 161
C.3 Champ électrique soutenu versus surface d'électrode Schottky pour les contacts en molybdène de ce travail comparés à de nombreuses références bibliographiques [167, 168, 150, 149, 169, 170, 171, 172]. 166
C.4 Caractéristiques de transfert à haute tension du RBMESFET à 425K pour la configuration à canal fermé avec $V_{GS} = 5V$ dans la courbe rouge et pour la configuration à l'état ON et diode Schottky dans la courbe bleue avec $V_{GS} = -0.8V$. 167
C.5 Campo eléctrico soportado frente al área de los contactos Schottky para los contactos de molibdeno de este trabajo frente a numerosas referencias de la bibliografía [167, 168, 150, 149, 169, 170, 171, 172]. 171
C.6 Características de transferencia de alto voltage del RBMESFET a 425K para la configuración del canal cerrado con $V_{GS} = 5V$ en la curva roja y para el estado encendido y la configuración de diodo Schottky en la curva azul con $V_{GS} = -0.8V$. 172

List of Tables

1.1 Material properties relevant to power electronics for silicon, WBG materials and UWBG materials [8, 9, 10, 11]. Some of the physical properties presented depend on the doping level, crystal quality and the measurement or calculation technique used specificities, thus only a rough overall comparison is encouraged between the materials presented. 9
1.2 Benchmarks, benefits and challenges for the different demonstrated diamond power transistors. 20

2.1 Parameters used in the mobility model from ref. [122]. 27

Introduction

Global warming is the major threat and challenge our society has to deal with this century. The dramatic rise of energy consumption in developing countries, the exponential growth of the world population and the growing demand of electric energy for new technologies such as crypto-currencies pose a threat to the accomplishment of the reduction of greenhouse gases objectives for 2030-2050. One of the principal sources of greenhouse emissions is the fossil fuels combustion related to transportation and electric energy production. To sort out these emissions, either a radical change in the consumerist lifestyle of modern societies is adopted, or a set of technological solutions are found. For the latter, condensed matter and applied physics, material science and chemistry are the key to keep our world as we know it nowadays. New renewable or improved productive energy sources are needed as well as a more efficient energy grid connecting the sources with the end applications.

This new grid is in need for efficient power devices components to reduce energy losses during power conversion. In order to make those components more efficient, new materials with better properties than silicon have to be developed and adapted to the semiconductor technological industry. These new promising materials are known as wide band gap semiconductors such as silicon carbide (SiC) and gallium nitride (GaN) or ultra-wide band gap semiconductors such as gallium oxide (Ga_2O_3) or diamond. SiC and GaN are already commercialized despite being still under investigation. Ga_2O_3 and diamond are still at an earlier stage with the first devices being developed.

This thesis focus on diamond Schottky contact based devices for which several technological limitations have still to be solved. Diamond vertical diodes lack thick efficient drift layers epitaxy, successful etching procedures and reliable Schottky contacts in order to compete with other materials in the high and ultra-high voltage applications. On the other hand, diamond transistors suffer either from low stability, gate hysteresis or non practical normally-on characteristics. These limitations and drawbacks have to be solved to adequate diamond technology to the semiconductor industry and to unleash diamond full potential in order to drain attention from the market. The present work main task is to solve the recurrent Schottky contacts problematic and its implementation within an electronic and material science approach. Moreover, the advances achieved by the Schottky contacts studies are applied to the transistors and diodes aforementioned specific problematic to demonstrate the ultimate diamond devices potential. It is an ambitious and wide work which goals can be summarized around three main objectives:

- The optimization of metal-diamond properties from a electronic, physico-chemical

and material science point of view. Molybdenum and zirconium are the best candidates to fabricate good quality reproducible Schottky contacts on diamond and the understanding of their interfacial properties with respect to diamond will enlighten their road to implementation and their limitations for the end application.

- The design, fabrication and characterization of an optimized high voltage diamond vertical Schottky diode. Using the knowledge developed about the interfacial properties of the studied Schottky contacts, a high voltage Schottky diode will be fabricated to demonstrate the capabilities of diamond diodes for high voltage applications.

- The design, fabrication and characterization of a normally-off 1 kV diamond gate-drain Schottky MESFET. Also benefiting from the knowledge extracted from Schottky contact interfacial properties studies, a normally-off (RB)MESFET will be for the first time fabricated with a <1 kV blocking voltage target for implementation into a diamond converter.

The development of such studies and devices is carried out within the institute NEEL and the University of Cadiz under the financing of two different projects:

- The first one, the diamond-HVDC project. Its goal is the fabrication of HV diamond Schottky diodes for their integration inside a commutation cell. In collaboration with Laplace laboratory in Toulouse, SATIE in Versailles and the Grenoble Electrical Engineering Laboratory (G2Elab). My role have been the development of the diamond Schottky diodes in order to push their performances mainly by solving metal-diamond interfacial problems that lead to premature leakages though the components.

- The second one is the Green diamond European project. Composed of 12 institutions (CNRS, CEA, UCA, IMEC, IBS, CAMUTRONIC, UCL, UCAM, CNM, IAF and ESRF) and 3 companies (Tecnalia, Indra and Wavestone) from UK, Belgium, Spain, France and Germany. Its main goal is the fabrication of a HV diamond vertical transistor and its implementation into a full diamond converter. The massive challenge of this device fabrication lead to several developments but was ultimately limited by epitaxy and etching. An alternative solution was proposed, the fabrication of lateral MESFETs for their implementation into a full diamond converter. My purpose inside this project was to coordinate and participate on the vertical MOSFET fabrication and to design, fabricate (together with the UCL) and characterize a normally-off 1 kV diamond gate-drain Schottky lateral MESFET.

The ultimate goal for these projects is to fabricate ideal performing devices, to demonstrate diamond ultimate capabilities, and their integration into functional power electronic components. The knowledge and capabilities of such prestigious numerous institutions joined to solve the several challenges that still exist for diamond electronics. Particularly, the

diamond epitaxy plus power electronic knowledge and capabilities from the SC2G group inside NEEL institute in France and the powerful material science analysis techniques and the expertise from the UCA are put together during my PHD to address these challenges.

The manuscript consist of 6 chapters in which the state of the art is introduced, the theoretical framework explained and the experimental results presented:

- **Chapter 1**

  The first chapter introduces the challenges of power electronics by taking a look at the historic development of devices up to date. The notion of devices performances being limited by material properties is presented and discussed in the case of silicon devices. The advantages of using ultra wide band gap materials, in particular diamond, are reviewed. Lastly a summary of diamond growth, substrates, surfaces and the state of the art of diamond Schottky diodes and unipolar transistor is presented.

- **Chapter 2**

  The second chapter is dedicated to the theoretical framework used to quantitatively understand the performance of diamond devices. It covers from the basic comprehension of the band scheme of a Schottky contact and the development of the classical thermionic emission expression to the implementation of mobility, ionization, avalanche breakdown or leakage currents model adapted concretely to diamond. Lastly, the performance of Schottky contact based transistors and diodes is evaluated based on the aforementioned models.

- **Chapter 3**

  This third chapter is focused on the theoretical and experimental study of the interfacial properties of two Schottky metals and diamond: zirconium and molybdenum. For this study, a lateral diode sample is fabricated and their interfacial properties evaluated by transmission electron microscopy, X-ray photoelectron spectroscopy, kelvin probe atomic force microscopy and simulated thanks to density functional theory.

- **Chapter 4**

  In chapter number four, the main focus is the optimization of the electrical performance of Schottky diodes. The fabrication process for two different samples is presented. The first one is used to study parasitic leakage currents with the intention of mitigate them with different approaches. The second one implements the knowledge acquired into a thicker drift layer structure to push the OFF-state into the kV range.

- **Chapter 5**

  In the fifth chapter, a 1 kV normally-off Schottky drain (reverse blocking) MESFET design and fabrication is presented. The transistor characteristics are shown and compared to a numerical implemented 1D model. The high voltage and high temperature

characteristics of the transistor as well as for its Schottky gate are presented and analyzed. Lastly, its perspectives and future are discussed.

Chapter 1

Diamond Power Electronics: Material Properties and State of Art

This first chapter is dedicated to power devices history, current status and perspectives. Their operation as well as their performance link to semiconductor properties are revisited. The new ultra wide band gap materials properties and devices are presented, compared among them and to the commercially available devices and properties of silicon, SiC and GaN. Between all of them, diamond stands out, and its main properties and peculiarities are reviewed. Finally, the state of art of unipolar diamond diodes and transistors is presented.

1.1 Power electronics nowadays

The use of solid state electronic devices to control and convert electrical power from one form to another one to meet a specific need is known as power electronics (PE). Since its beginnings in the early XX century, with the invention of the mercury arc rectifier, to the later invention of the transistor in the Bell labs, power electronics has evolved until playing a key role in our lives nowadays. The enormous demand of electric energy in our societies, of the order of hundreds of TWh for EU countries[1], and the threat of global warming, requires the ability to sustainably produce it and an efficient system for its transmission and distribution. The current energetic model is based on centralized energy production in power plants followed by high voltage transmission to reduce conduction losses. These high voltages managed in tension lines and the huge variety of needs from final applications require the ability of power devices to transform the electric energy into a great range of different voltages and currents. Devices such as rectifiers and inverters for conversions between Alternative Current (AC) and Direct Current (DC), and converters for amplification and attenuation take care of this task.
The growing demand of energy has consequently risen the importance of power electronics and its global market size to 29k millions of euros in 2020. And yet, silicon devices are dominant in the power electronic market and are responsible for most of the energy losses over the whole energy chain [1]. This fact turns the current status of power electronics into a bottleneck for sustainable energy usage and a niche for future development. These losses come from the physical limitations of the materials used to engineer the devices. Devices can be understood as electrical switches, with the current flowing through during the on-state and blocked during the off-state. However, the on-state resistance, related to the material resistivity, dissipate heat due to Joule effect during current conduction, which is typically in the range of 1-100 A for power electronics. In the off-state, the maximum voltage blocked by the device (from hundreds of Volts to tens of kV) is related to the maximum electric field sustained by the material. Indeed, these two material properties are connected, resulting in a core trade-off for power electronics: on vs off state performance. An illustration of this trade-off is shown in figure 1.1 for a p-type Schottky diode. Besides conduction losses, switching losses coming from the fact that a device requires time to switch from on-state to off-state (and vice versa) are always present. These represent a major part of the total losses in power devices. In every switch, the gate capacitance for transistors or the junction capacitance for diodes has to be charged or discharged, and the charge/discharge current must flow through that element causing losses.

With the current silicon technology reaching its theoretical limits, the only road to improve the performance is to use new materials with better properties, and thus, better on vs off state trade-off. For instance, in high voltage applications, the low critical field of silicon (0.3 MV/cm) limits the maximum breakdown voltage of devices to <10 kV with

[1] https://yearbook.enerdata.net/

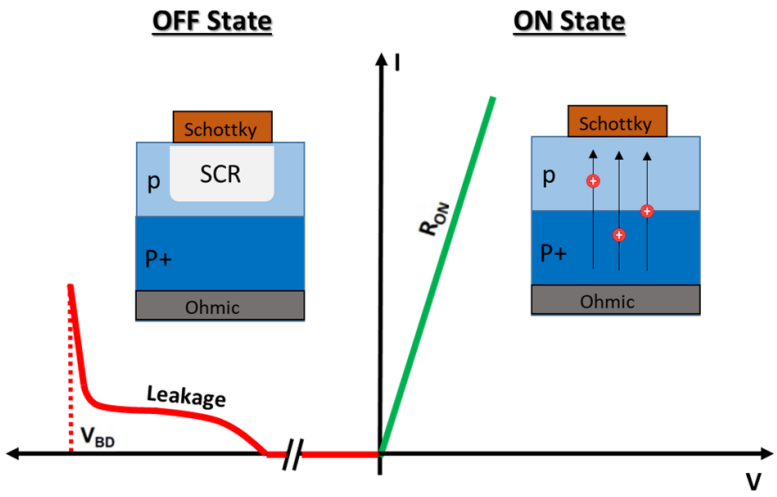

FIGURE 1.1: *On vs off state characteristics of a p-type Schottky diode. On the left, the off-state is characterized by the breakdown voltage V_{BD} and parasitic leakage current. The vertical diode shows the space charge region produced by the depletion under the Schottky. On the right, the on-state is schematized being characterized by the on-state resistance R_{ON}. The diode scheme shows the flow of holes (i.e. the sense of the current) from ohmic to Schottky.*

poor on-state performance [2] causing a good deal of energy losses. Already in the 1980s, semiconductor technology was mature enough to start working with wide band gap (WBG) semiconductors that could overcome silicon limitations thanks to their better properties, transferring the lead of development in power electronics to WBG materials science. At the present, silicon carbide and gallium nitride are the two first commercial competitors of silicon devices due to their higher critical field, mobility and thermal properties. SiC is already well-established for high voltage application [3]. A 2.8 MV/cm critical field together with a thermal conduction of 370 W/mK allow this material to overcome the limitations of silicon [4]. Its properties are displayed in Table 1.1. Junction barrier Schottky SiC diodes are commercially available (for voltages around 1-10 kV) and PIN diodes are very promising for higher voltages. Commercial SiC MOSFETs are competitive at blocking voltages <3 kV although the highest blocking voltage reported is about 15 kV [5, 6]. On the other hand, not as mature as SiC technology, GaN devices interest lies in the high voltage-high switching speed applications. With a better 3.3 MV/cm critical field but lower bulk mobility and thermal conductivity than SiC, as shown in the table 1.1, the advantage of GaN is the unique properties of its high mobility 2D electron gas. Because vertical GaN devices have not yet been produced on a commercial level, GaN devices available today are lateral high electron mobility transistors (HEMTs) rated at 600–650 V [7].

Power devices nowadays are, therefore, dominated by the mature silicon technology but evolving towards newer SiC and GaN technologies, especially at high voltage and switching frequency. With the increasing demand and push of these technologies, PE market is projected to grow up to 36k millions of euros by 2025. The increasing focus on the use of renewable power sources across the globe, electric vehicles, and increasing use of power

electronics in consumer electronics are the drive force for the growth of the market. [2]

1.2 UWBG semiconductors properties for power electronics

With the power electronics market already implementing GaN and especially SiC new technologies, a new door opened the route for further future power electronic development in the last years: Ultra wide band-gap (UWBG) materials. WBG materials as SiC and GaN benefit from a higher critical field than silicon due to a larger band-gap (~ 3 eV) that energetically hinders the avalanche breakdown from happening. However, a new set of materials with even wider band-gaps in the range of 4-6 eV known as UWBG materials can push this limit even higher demonstrating critical electric fields up to 10 MV/cm. This new generation of materials can sustain up to 3 times the critical electric field of SiC or GaN and therefore, devices based on UWBG can display lower on resistance due to higher doping while having the same blocking capabilities. Not only the on vs off state trade-off is better for these materials, but also the device size is smaller. These materials also benefit from high temperature operation since their intrinsic carrier concentration is extremely small and therefore there is not a limit to high temperature operation as in silicon. Furthermore, typical dopants used for UWBG semiconductors give rise to deep dopants level that benefit from high temperature operation, as carriers are partially frozen out at room temperature. With different levels of technology maturity, niche applications, and set of properties; listed in table 1.1 and represented in figure 1.2, the following materials are classified as UWBG semiconductors:

- **β-Ga_2O_3**

Its high critical electric field of 8 MV/cm and its affordable substrates projected to fall down to two time less than those of SiC are its main advantages. Its main drawbacks are: its very poor thermal conductivity, p-doping not been available and that it is worse than its competitors in terms of mobility [12, 13]. Anyways, the affordable cost of the substrates makes this material one of the UWBG semiconductors receiving most attention from researchers. Wafers are fabricated using simple melt-based crystal growth, while homoepitaxial films grown via metal-organic chemical vapor deposition (MOCVD) allow precise control of n-type doping, usually using Sn or Si with low activation energies of 30 to 80 meV [14, 15]. Unipolar MESFETs and depletion MOSFETs have been fabricated showing a record breakdown voltage of 2.3 kV and 1 A in the forward state, while Schottky diodes have shown to exhibit more than 1 kV of breakdown voltage [16, 17].

- **AlN**

It is attractive for high power and temperature applications due to its high critical electric field of 10 MV/cm and high thermal conductivity of 319 W/mK. On the other hand, its electron saturated velocity is lower while its e-h mobilities are comparable to those of gallium oxide. Moreover, due to the challenging growth and cost of substrates not much work

[2] https://www.marketsandmarkets.com/Market-Reports/power-electronics-market-204729766.html

Material	Silicon	SiC	GaN	β-Ga_2O_3	AlN	c-BN	Diamond
Bandgap (eV)	1.1	3.3	3.4	4.9	6.1	6.4	5.5
E_c (MV/cm)	0.3	2.8	3.5	8	10	8	10
μ_e ($cm^2/V \cdot s$)	1500	1000	2000	300	300	600	1000
μ_h ($cm^2/V \cdot s$)	480	120	200	14	14	-	2000
ϵ_r	11.8	9.8	9	9.9	8.5	4.5	5.5
λ ($W/cm \cdot K$)	150	370	253	20	300	1300	2300
$v_{sat}^{e-h}(10^7 cm/s)$	1 - 0.8	1.9 - 1.2	2.5	2	1.4	3	2.5 - 1.4
Available doping	p & n	p & n	p & n	Only n	p & n	p & n	p & n
Max. wafer diameter (")	>12	8	8	4	2	-	1
Wafer cost for max. size wafer ($\$/cm^2$)	0.1	1	6	100	200	-	>1000

TABLE 1.1: *Material properties relevant to power electronics for silicon, WBG materials and UWBG materials [8, 9, 10, 11]. Some of the physical properties presented depend on the doping level, crystal quality and the measurement or calculation technique used specificities, thus only a rough overall comparison is encouraged between the materials presented.*

has been reported on AlN electronics. 1 kV vertical Schottky diodes [18, 19] and >2.5 kV n-type MESFET have been demonstrated [20]. An encouraging result for AlN electronics is the progress shown in its MOCVD heteroepitaxial growth over sapphire [21, 22]. Nevertheless, this material seems to be at bay by the cheaper applications of gallium oxide and the superior properties and more mature technology of diamond.

- **c-BN**

It is by far the less studied UWBM until now but its extraordinary properties might attract more attention from researchers in the future. With the possibility of both p and n doping [23, 24], a high critical field of 10 MV/cm, very good thermal conductivity and the best theoretical saturated electron velocity of all the listed materials is the only material that rivals diamond in terms of properties [25, 26, 27]. However, the severe difficulties of the HPHT growth methods and the limited size of c-BN grains produced have limited its application to power devices. Up to now, only p-n junctions with diamond have been reported [28].

- **Diamond**

Besides being the hardest material, diamond is the crown jewel in UWBG semiconductors due to its superior properties for power electronics. It has high electron-hole mobility, high critical electric field low dielectric constant. Moreover, it surpasses all competitor materials in terms of thermal conductivity with the highest value reported for any material. The main

drawback is that both p and n type dopants give rise to relatively deep levels causing partial ionization at room temperature [29, 30]. However, the partial ionization can be easily mitigated for p-type diamond by working at high temperatures (550K) leading to outstanding on-state device performances. Also, substrates are expensive and limited in size, although an encouraging progression have been shown in the last decade [31]. Therefore, the future market of diamond devices seems to be focused to ultra-high power and high frequency and temperature applications [32]. The archived unipolar structures are summarized in subsections 1.4.1 and 1.4.2.

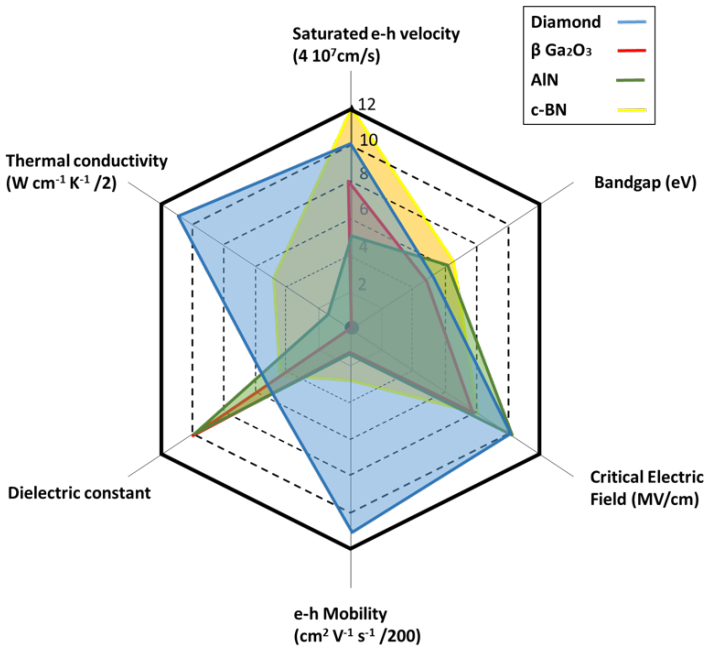

FIGURE 1.2: *UWBG materials properties comparison. Diamond takes advantage over competitors especially because of its thermal conductivity, mobility, saturation velocity and low dielectric constant.*

1.3 Diamond synthesis, wafers, dopants and surfaces

1.3.1 High-pressure high-temperature synthesis

The first synthesis of diamond dates back to 1955 based on the High Pressure High Temperature (HPHT) method [33] and it is still the main method used for substrates production nowadays. This method relies in belt press systems that compress above 5 GPa at temperatures of 1800K a sp^2 carbon source in order to enhance the phase change to sp^3 diamond by means of a diamond seed. The growth occurs from the seed to multiple crystallographic directions at the same time as shown in figure 1.3, and the most stable are (100), (110), (111) and (113). The three most important categories of HPHT-synthesized diamond are:

- **Type Ib**

Type Ib diamonds contain a high concentration of nitrogen impurities enough to be detected by infrared spectroscopies (around 5 ppm) in isolated substitutional sites. These type of substrates are used because of its insulating properties, as nitrogen is a deep donor (the ionization energy has been determined to be at 1.7 eV below the conduction band [34] in diamond. They are interesting as insulating substrates for lateral transistors and parallelized Schottky diodes [35].

- **Type IIa**

Type IIa diamonds have very low concentration of nitrogen and boron impurities. They usually display a p-type character with boron concentration around [B] = 10^{15} cm^{-3}. They are less available commercially but interesting for vertical transistors and Schottky diodes as their crystallographic quality is typically superior.

- **Type IIb**

Type IIb diamonds contain a high concentration of boron atoms [36]. They are sometimes used as active layers for the fabrication of vertical devices. However, the higher resistivity than metallic CVD grown heavily doped p++ diamond limits their uses to application where the current is not a key factor [37].

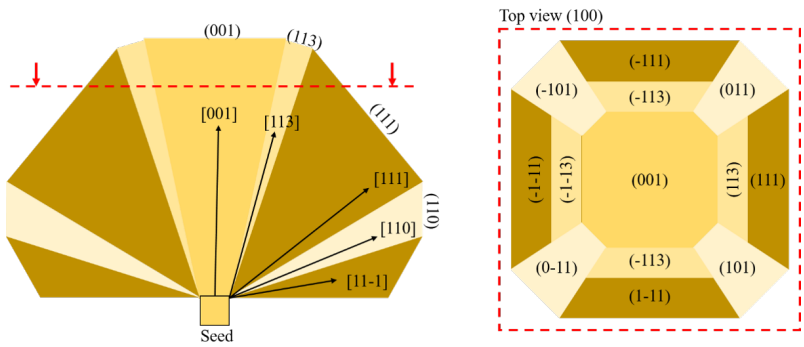

FIGURE 1.3: *Scheme showing the main growth directions appearing in high temperature high pressure (HPHT) diamond synthesis. Courtesy to Dr. Alba.*

1.3.2 Wafers

Diamond wafers are an essential part of the future of this UWBG semiconductor implementation in high power, high temperature and harsh environment applications. Both CVD and HPHT substrates are available commercially with sizes up to 4 mm and 10 mm radii and dislocation densities of 10^6 cm^{-2} and 10^2 cm^{-2} respectively. Due to their superior sizes and qualities, mostly HPHT electronic grade wafers are used for device development. In fact, HPHT technology is ready for 2" wafers production but there is no market for such layers nowadays. The absence of market drives a negative cyclic feed back effect: Substrate quality, reproducibility and size constrained by the small market limit device performances and projections resulting in the discouragement to invest in increasing wafers size and quality.

In this restrained context, it is urgent to manufacture devices that exceed the limits of silicon and SiC devices ín order to increase interest and investment for breaking the negative feedback cycle. With the rise of performances and eventually a large scale application, diamond market now driven by gem industry (and carat price not driven by the market) will split the two different and well-defined markets.
On the technological side, different solutions are in development to reduce cost and enlarge the size of diamond wafers. Between them we can find mosaic wafers produced by ion implantation, cleavage and then fused by CVD growth as demonstrated in ref. [38] or the "smartcut" process developed by CEA and CRNS [39, 40]. Another approach is heteroepitaxy [41, 42, 43], where CVD layers are grown in silicon, iridium or sapphire substrates. A summary of the diamond wafers state of the art approaches size, quality and cost and their future projections is presented in figure 1.4. These solution are very promising and their success could also allow diamond to expand its targets applications by reducing its cost. However, there is still a long way to go since they need to offer better crystalline quality and reproducibility.

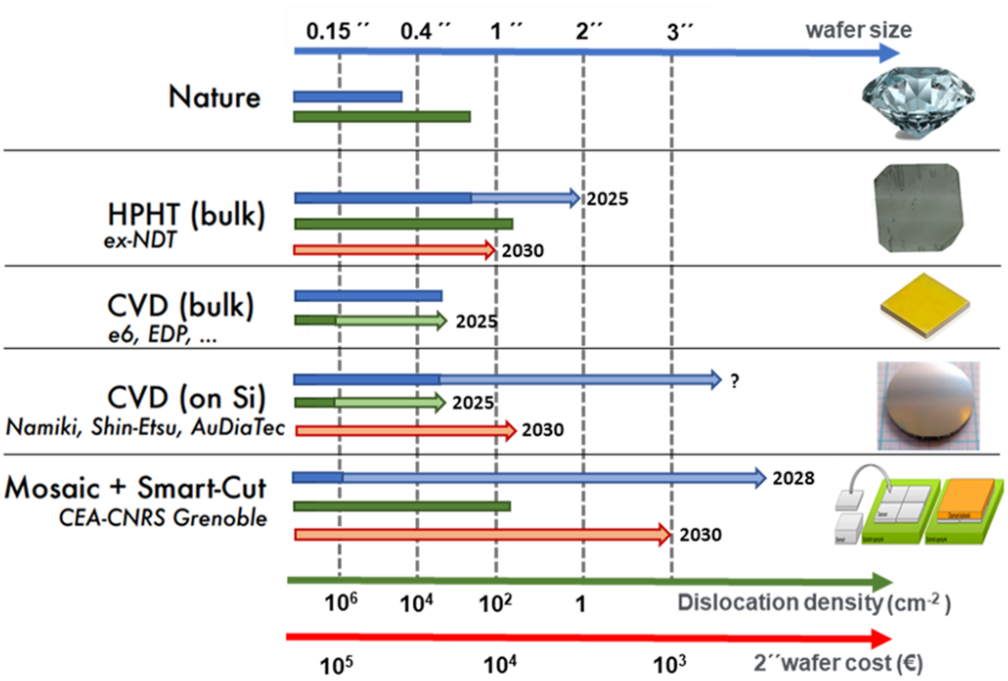

FIGURE 1.4: *Diamond wafer size, dislocation density and cost comparison for the different production methods and their expected future projection [44].*

1.3.3 Epitaxy & dopants

Diamond chemical vapor deposition (CVD) is the most relevant technique for the fabrication of electronic-grade diamond doped active layers. It started in the early 1980s [45] and its current precision in layers thickness and doping level, together with the wider doping range than HPHT, make this technique the core of devices development. It consists on the chemical

reaction of a gaseous carbon precursor (CH_4) with a diamond seed or substrate. In order to thermodynamically activate this reaction, an energy source a such as microwave, radio frequency or hot-filament are required. The focus of this thesis is microwave plasma (MP)CVD. In this technique, a low pressure hydrogen gas is ionized by means of a microwave source. This dissociate the H_2 molecules into H atoms that will interact with diamond surface by creating active sites or hydrogenating them ($C_{surf} + H \rightleftharpoons C-H$) as shown in figure 1.5 (i) and (ii). Once, the surface is partially activated (As the hydrogenation and site activation processes converge to a kinetic equilibrium) methane is also injected in the gas mixture. In the plasma, methane is able to react with hydrogen atoms to form CH_3 groups and hydrogen molecules ($CH_4 + H \rightleftharpoons CH_3 + H_2$). After, this CH_3 groups can bond to the active sites in the diamond surface (figure 1.5 (iii) and (iv)). Once the group is fixed, an hydrogen atom can react again with the CH_3 and leave a CH_2 linked to diamond liberating molecular hydrogen as a product (figure 1.5 (v) and (vi)). Lastly, another hydrogen atom can react with the CH_2 group liberating molecular hydrogen again and leaving the carbon integrated into a new diamond layer (figure 1.5 (vii) and (viii). New active sites can be again created by the hydrogen atoms allowing the process to go on in a cycle as long as required [46]. Additionally, the use of oxygen in the gaseous mixture is reported to reduce the defect formation as it increases hydrogen etching of amorphous carbon (and may even act as etchant itself) and improves the reaction of CH_3 with the surface, especially at initial growth stages [47, 48].

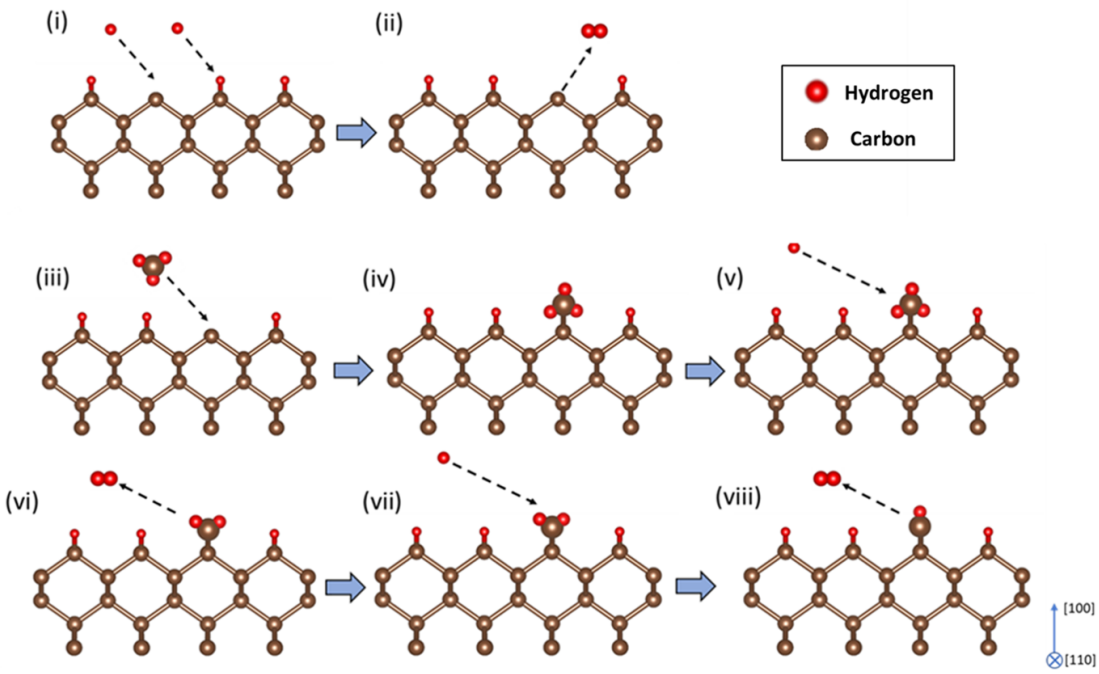

FIGURE 1.5: *Schematic process for diamond MPCVD epitaxy.*

The most common dopants in diamond are boron (p-type), nitrogen (n-type) and phosphorus (n-type). Boron is the most studied diamond dopant up to date. It can be incorporated by means of diborane (B_2H_6) or trymethylboron ($B(CH_3)_3$) with reproducibility.

It has the lowest ionization energy among effective diamond dopants (0.37 eV [49]). Its big ionization energy makes p-type diamond to suffer form partial ionization at RT. However, diamond can take advantage of the heat losses produced by working at high power as high temperature operation successfully mitigate the partial ionization. Its optimal working temperature is around 550K as the trade-off between mobility and carrier concentration is maximized [50]. At this temperature, diamond outperforms any other material for PE applications. The doping level and thickness control is well-developed but the appearance of defects limits the maximum high quality thickness available. Heavily doped layers are well studied showing a metallic transition at $3 \cdot 10^{20}$ cm^{-3} and a superconducting state at 10^{21} cm^{-3} at low temperature [51, 52]. The growth of phosphorus doped layers is based on the use of phosphine (PH_3). The incorporation is favoured in the (111) direction but has been also achieved in the (100) direction. However, heavily doped layers are only available in the (111) direction. The ionization energy is still under discussion: from 0.43 to 0.63 eV [53, 54].

1.3.4 Surfaces

Diamond surfaces are crucial for the development of devices as well, as they extremely affect their functioning and performance. In fact, diamond surfaces are very complex and phenomenologically rich as they display very different behavior depending on their termination and they still are a matter of debate after more than 20 years of research. As the eminent physicist Wolfgang Pauli once said "God made the bulk; the surface was invented by the devil" referring to the difficulties of the physico-chemical description of surfaces. In diamond, the most used and studied are (100) and (111) surfaces although although (113) and (110) surfaces [55, 56, 57, 58] are also under investigation. These diamond surfaces display similar electronic behaviour and their main difference is related to dopants incorporation during CVD growth. Some interfacial properties in devices such as density of interface states or band setting might slightly change with orientations but the dramatic electronic behaviour modifications appears as a result of the different surface terminations. The most used are hydrogen and oxygen; although other such as nitrogen, silicon, fluor or magnesium [59, 60, 61]) have been studied.

- **H-terminated**

Hydrogen terminated diamond surface present a 2x1 reconstruction in the (100) direction and a 1x1 reconstruction in the (111) direction. For both surfaces, it give rise to a 2D hole gas and negative electron affinities [62]. This 2D hole gas is understood as a result of a surface transfer doping phenomena, where the electrons from diamond valence band fall into energetically favorable unoccupied energy states widely attributed to adsorbed species on the H-terminated surface [63]. This process is illustrated in figure 1.6. This 2D hole gas shows high concentrations of 10^{12} to 10^{13} cm^{-2} but low mobilities of 50 cm^2/(V·s) compared to those measured for the bulk [64]. This is attributed to ionic scattering due to the proximity of the transferred negative charges to the 2D hole gas. However, the 2D hole gas can exist even after deposition of oxides thus enabling the possibility of fabricating devices. Better

mobilities up to 300 $cm^2/(V{\cdot}s)$ have been extracted for FETs in which the charge separation is archived [65, 66]. The hydrogen termination of diamond have been shown to be very stable up to temperatures of 1100K. At this temperature, hydrogen desorption takes place, and the (100) and (111) surfaces show 2x1 reconstructions [62]. However, as the 2D hole gas depends on the energy levels introduced by adsorbed species, its time and temperature stability have been a major challenge over the last decades. Its stability is compromised as early as 500K although it can be improved with the use of oxides up to 700K [67].

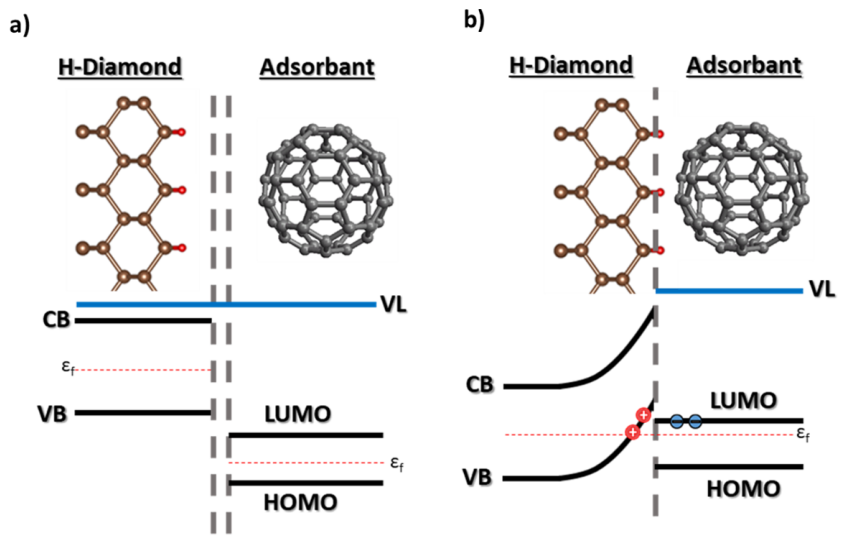

FIGURE 1.6: *Schematic illustration of the transfer doping process. a) On the left, the scheme and the energy bands of the H-terminated diamond in the (100) direction. On the right, a molecule before adsorption with its associated molecular orbitals. b) The molecule is adsorbed causing the electrons from diamond VB to be transferred to the LUMO orbitals leaving behind a 2D hole gas.*

- **O-terminated**

Oxygen-terminated surfaces display insulating behavior and positive electron affinity [68]. They are also very stable up to >700K [69]. The most common way up to oxidize diamond surface is by the use of UV ozone treatment [70] but many other methods are present in literature such as acid treatment, exposure to O_2 atmosphere or water vapor annealing [71]. As a matter of fact, all the studies in this thesis use the (100) oxygen-terminated surface based on UV ozone treatment due to its interesting surface passivating properties for bulk diamond conducting transistors and because it give rise to high Schottky barriers when in contact with metals. Concerning the surface reconstruction, a 1x1 pattern has been widely observed by electron diffraction techniques for the oxygenated (100) surface. However, electron diffraction is not able to discern the possible bonding configurations for this 1x1 reconstruction. Oxygen termination could exist in a variety of states: ether bridge (C-O-C), hydroxyl (C-OH), ketone (C=O), and most probably in a combination of all three [72, 73,

74] as represented in figure 1.7. There is still some controversy with some experimental and theoretical discrepancies pointing toward ether and hydroxyl groups as the most stable and energetically favorable [75].

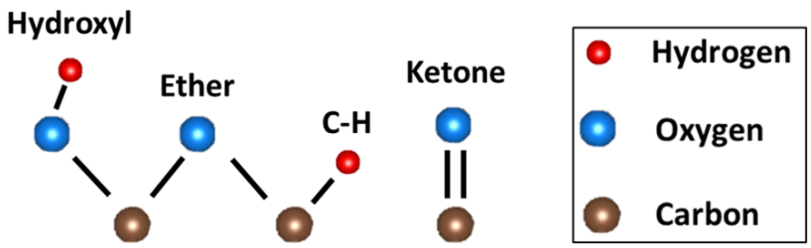

FIGURE 1.7: *Oxygen-terminated diamond possible surface groups.*

1.4 Diamond devices state of the art

In this section, the challenges and the state of art of diamond devices including diodes and transistors is summarized. The main focus are unipolar devices although some remarkable results from bipolar devices are included for comparison.

1.4.1 Schottky diodes

Diamond Schottky diodes have been fabricated since the 90's and are the most developed component nowadays. Due to its lower activation energy and the more difficult incorporation of phosphorous (especially in the (100) direction), most Schottky contacts are fabricated based on boron-doped diamond. This limitation has also impacted the fabrication of bipolar devices such as PN or PIN diodes where less devices have been reported [76, 32]. While Bipolar diodes target is ultra-high voltage and low-medium frequency, Schottky diodes are very promising for its fast switching capabilities and high voltages. In fact, optimized diamond Schottky diodes can ideally sustain up to 30 KV. Of course, this is still far away from the actual technology, but the high critical field of diamond might allow optimized Schottky diodes to work at ultra high voltages being competitive with bipolar diodes. Concerning Schottky diodes investigations, wide and deep research has led to impressive results reported over the last ten years. Different surface treatments and metals (W, WC, Zr, Pt, Mo, etc) have been explored with the purpose of reducing leakage currents and thus obtaining the best possible on vs off trade-off [77, 78, 79, 80, 81]. Diamond Schottky diodes able to sustain up to 10 kV [82] were reported by Volpe et al. Although noteworthy, the characteristics show a very resistive ($\sim 20\Omega/cm$) on-state. Moreover, a Zr-based Schottky diode were reported to sustain up to 1KV with a record critical electric field of 7.7 MV/cm [83]. This device had also an excellent on-state with an ideal performance for a punch-through device. However, the absolute lack of reproducibility transformed this result into a shooting star on the long night of non-ideal performing devices. Additionally, extend and exceptional research was reported by Dr. Umezawa, studying the influence of defects [84], Schottky metals

[85] and edge terminations [86] over the leakage current, and reporting a 5 A, >1 kV vertical diode [84] with Pt Schottky metal. High temperature (over 525K) and harsh environment operations have also been reported with diamond Schottky diodes [87] by Dr. Umezawa. On the other hand, heteroepitaxial Schottky diodes have also been fabricated [88, 41]. They show promising results but growth improvements to reduce dislocation density and to acquire optimized control are still required. Regarding architectures, the limited technology stage in terms of etching [89] and growth have led to different solutions (shown in figure 1.8). The non-availability of low resistance self-sustaining heavily boron-doped substrates makes the use of pseudo-vertical architectures the preferred solution. These structures show the best on-state performance but are limited for HV due to the maximum etch size (4-10 microns) available that is needed to access the p+ layer to fabricate the ohmic contact. Another original approach is the encapsulated CVD p+ growth as shown in figure 1.8 [90]. This structure allows to boost the p- drift layer thickness (up to 20-30 microns), only limited by maximum growth size, which is restricted by generation of defects. The road for improvement of these devices passes through the research of leakage current mechanisms and the possible ways to reduce them, edge terminations to avoid premature breakdown and the improvement in etching and epitaxy processes.

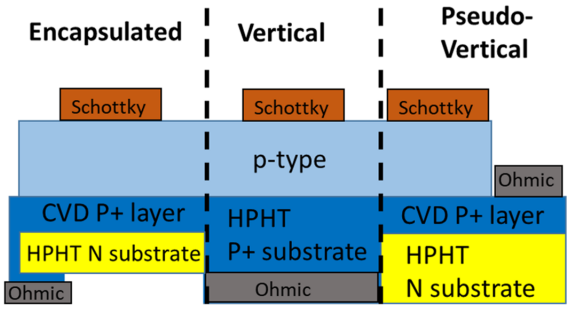

FIGURE 1.8: *Scheme for the different Schottky architectures. On the left, encapsulated type diode. The CVD p+ growth extend over the edge allowing its contact through the back face. On the center, the vertical structure. This structure tends to display a resistive on-state due to the thick and low conductive p+ HPHT substrate. On the right, the pseudo-vertical architecture. While this structure is very efficient in terms of performance, the early stage of diamond technology makes it very limited in drift layer thickness.*

1.4.2 Transistors

A big variety of transistors concepts have been proposed over the last years in order to benefit from the excellent properties of diamond: Metal semiconductor FET (MESFET), H-terminated FET (HFET), junction FET (JFET), inversion MOSFET and diamond deep depletion MOSFET (D3MOSFET) as shown in figure 1.9. A detailed review of diamond transistors can be found in [8, 91]. The early stage of diamond technology has limited transistors architectures mostly to lateral ones while the transition toward vertical architectures is expected to boost performance over the coming years as more optimized etching and growth

processes are developed. The main ideas and performances for the different transistors concepts follows and are summarized in the table 1.2:

- **H-FET**

Most of the fabricated transistors are lateral devices (MOSFET, MESFET and MISFET) based on the 2D hole gas existing on the H-terminated diamond. Compared to the surface, the transfer doping process in these FET happens thanks to free energy levels inside the oxide layer [92]. The proximity of the transferred charges and the 2D hole gas is one of the main factor reducing its mobility. Increasing their separation has been attributed to an increase of mobility up to 100 to 300 cm^2/Vs with carrier concentrations of $10^{12} - 10^{13} cm^{-2}$ [65, 66]. These transistors display a very good on-state, especially at RT, with record currents densities of > 1.3 A/mm [93] as they avoid the limitation caused by the high ionization energy of boron. A maximum breakdown field of 3 MV/cm has been estimated for these FET, far from the 10 MV/cm theoretical bulk critical field. An off-state record of 2 kV has been demonstrated. Moreover, current and power gains at a maximum frequency of operation up to 100 GHz range have been demonstrated [94, 95, 91, 96]. Normally-off H-FETs have also been fabricated by means of different solutions, either by partially oxidizing the gate interface [97], implanting nitrogen under the gate [98] or by using an oxide bilayer [99]. Time and temperature stability are their main drawback, although great progress have been accomplished over the last years relying on the use of different oxides for the transfer doping process with demonstrated working temperatures of 700K [67]. Furthermore, a vertical H-FET architecture was fabricated in the last years [100].

- **Depletion based FET**

FET transistors based on depletion comprehend JFET, MESFET and D3MOSFET. They all benefit from high temperature operation as a result of the boron activation energy. The off-state is accomplished by depleting the whole channel under the gate. In case of D3MOSFET, the off-state functioning is based on the deep depletion regime caused by the extremely long minority carrier generation time in diamond. Compared with MESFETs, it offers a higher doping, and thus better current, but their gates tend to generate high density of interface states and trapping/detrapping mechanisms which limit the switching capabilities. D3MOSFETs demonstrated drain current density of 10 mA/mm and an operating temperature of 523 K with a 175 V BV with an associated 5.4 MV/cm calculated maximum electric field [101]. On the other hand, MESFETs must have a lightly doped region in the channel to limit the gate leakage which occurs especially at high temperature. Several diamond MESFETs based on different Schottky metals (Mo, Pt, Al) have been demonstrated. A maximum current density of 1.2 mA/mm at high temperature (T=600 K) and high breakdown voltages above 2 kV were recorded. Diamond MESFETs based on reverse blocking (RB) configurations with a Schottky metal for the gate and the drain contacts have also been demonstrated. They exhibited a maximum BV of 3 kV and a maximum on-state current of 1 µA [102, 103]. Lastly, p-n+ junction with high BV up to 1 kV were used to fabricate diamond JFET by

Hoshino et al. [104, 105]. Both normally-on and normally-off devices have been demonstrated as well as unipolar and bipolar conductions. Unipolar normally-on devices display current densities of 10 A/cm^2 at RT and close to 450 A/cm^2 at 673 K. JFET able to block > 600 V with an associated breakdown field of > 6 MV/cm were demonstrated. Regarding Normally-off JFETs, they are fabricated by reducing either the doping concentration or the channel width in order to deplete the whole channel under the gate at 0V. These JFET display a much smaller current density due to the reduced thickness and increased resistivity of the channel [106].

- **Inversion MOSFET**

The first diamond inversion type lateral MOSFET based on phosphorous doped diamond and alumina as gate oxide was reported by Matsumoto et al. [107]. A maximum drain current density of 1.6 mA/mm and channel field effect mobility of 8 cm^2/V s were extracted. A second demonstration of inversion, this time in a freestanding heterohepitaxially grown diamond, was recently published by Zhang et al. [108]. These are proof of concept transistors fabricated for the demonstration of the inversion regime and so not designed to have high blocking voltages capabilities as there are no drift regions. The fabrication of such a power vertical transistor, still not achieved, was the main target of the GreenDiamond European project in which this thesis is comprehended. Due to the difficulties in the layers epitaxy, deep etching and gate trench etching the transistor fabrication was unsuccessful. Anyways, these efforts have led to great progresses in etching, trench fabrication and growth which will eventually allow the fabrication of such device.

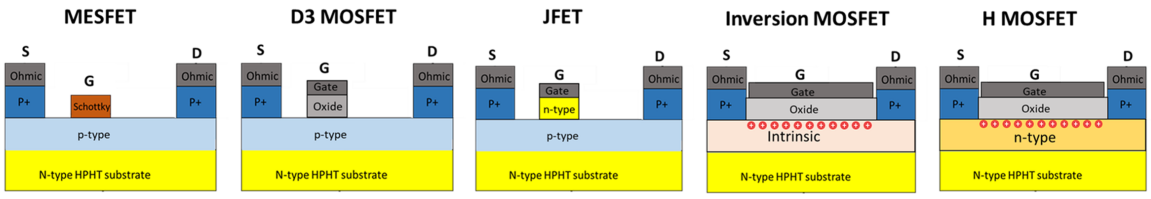

FIGURE 1.9: *Scheme of the different fabricated lateral unipolar transistors.*

1.5 Summary & conclusion

This chapter introduces the necessity of power devices market to find new alternatives to the silicon technology to ameliorate the performance of the semiconductor devices and reduce the power losses. In this context, the alternative of using ultra-wide band-gap materials have been presented as well as a review of their properties, benefits, drawback and fabricated devices. Between them, diamond stands out, with the best properties among ultra-wide band-gap semiconductors for power electronics. Diamond peculiarities such as epitaxy, dopants, wafers and surfaces have been introduced with special focus on their impact in the electrical properties of diamond. Lastly, the state of the art of diamond unipolar devices is revised. Diamond Schottky diodes are the most developed component up to date, with demonstrated

Transistor	MESFET	D3MOSFET	JFET	H-MOSFET
V_{max}	3kV	0.125kV	0.6kV	2kV
E_{max}	2.1 MV/cm	5.4 MV/cm	6 MV/cm	3.6 MV/cm
J_{max}	3 mA/mm	10 mA/mm	450 A/cm^2	1.3 A/mm
Benefits	Stable operation	Good current	Normally-off	Best current
	Radiation Hardness	Accumulation regime	Bipolar operation	Vertical structure
	HT operation	HT operation	HT operation	f_{max} > 100 GHz
Challenges	Schottky leakage	Oxide traps	n-type doping	Reliability

TABLE 1.2: *Benchmarks, benefits and challenges for the different demonstrated diamond power transistors.*

blocking capabilities up to 10 kV and 7.7 MV/cm. However, irreproducibilities and technological steps such as thick layers epitaxy or etching are still bottlenecks to reach the ultimate performance. On the other hand, diverse diamond transistors concepts are presented including: MESFET, D3MOSFET, JFET, Inversion MOSFET and H-MOSFET. The strong points and weaknesses of each transistor are reviewed. While the majority of diamond transistors are H-MOSFETs due its very good on-state performances based on the 2D hole gas formed on hydrogen-terminated surface, bulk conduction based transistors present a robust alternative for high temperature and harsh environment applications. In conclusion, diamond electronic devices are very promising for power electronics due to diamond outstanding properties. Nonetheless, several challenges have to be solved in order to extract diamond full potential. In this thesis, some of these challenges are addressed in the coming chapters.

Chapter 2

Schottky Contact-Based Diamond Devices: Physical Models and Technology

---

The focus of this chapter is to introduce the theoretical framework underlying Schottky contact-based devices. Diamond Schottky contacts modelization is presented based on an analytical description of Schottky barriers. The equations governing the forward and reverse conduction mechanisms through the Schottky barrier are introduced and solved numerically. The state of the art diamond resistivity and breakdown models are as well presented and discussed. These physical models are then used for the quantitative comprehension of diamond diodes firstly and diamond lateral MESFETs secondly.
On one hand, the different diode structures and their fabrication constraints and technological limitations are introduced. The impact of these constraints is illustrated as well as the optimal performance of diamond diodes. On the other hand, the RBMESFET concept is presented and a 1D model for the on-state current under the gradual channel approximation is developed. Its performance is analyzed relying on the developed physical models.

2.1 Metal-Semiconductor junctions

All semiconductor devices use metal-semiconductor contacts whether it is for injecting carriers with the lowest resistance as possible (ohmic) or for its rectifying properties (Schottky). The discovery of rectifiers dates back to 1874 by Ferdinand Brown and the first description of such junctions would not come up until the 1930's by Schottky [109]. The ideal Schottky model of a metal-semiconductor contact describe the junction in the framework of the band theory. In the figure 2.1 a), the semiconductor and metal bands are shown before contact. If we assume no interface layer and intimate contact is made between semiconductor and metal, the chemical potentials (here after referred as Fermi levels) of both materials will equilibrate due to the charge transfer of more energetic carriers into less energetic free states. This leads to a situation where the bands of the semiconductor are bend toward the interface with the metal. This curvature will thus respond to the difference of work functions. For a p-type semiconductor, an ohmic contact is formed when the metal work function (ϕ_m) is higher than that of the semiconductor (ϕ_s) whereas a Schottky is obtained in the opposite situation as shown in the fig. 2.1 b).

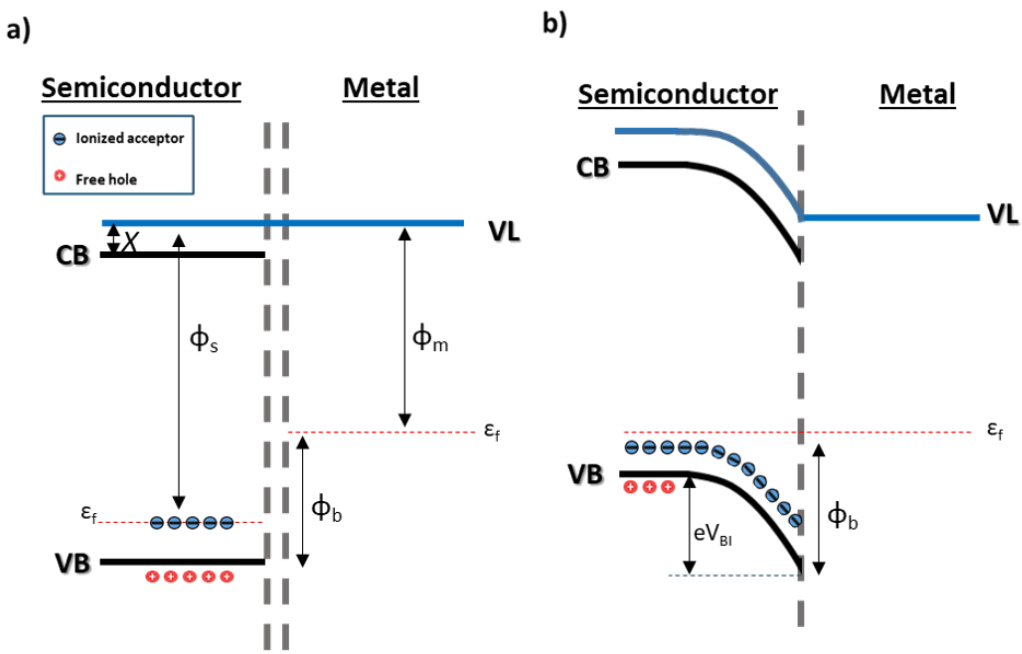

FIGURE 2.1: *Band structure of a metal/p-type semiconductor junction: a) before contact for a metal and a p-type semiconductor. b) After intimate contact at thermal equilibrium.*

In the latter case, a potential barrier arises for semiconductor holes due to the downward semiconductor band bending related to the negatively charged acceptor atoms left after the hole transfer. This space where the bands are bent pushing away semiconductor carriers is known as the depletion region. For the metal, an abrupt (Schottky) barrier ϕ_b prevent the injection of carriers to the semiconductor. The ideal Schottky Barrier Height (ϕ_b) is defined by the Mott equation:

$$\phi_b = E_g - (\phi_m - X_s) \tag{2.1}$$

where X_s, E_g and e are the electron affinity of semiconductor, its band-gap and the elementary charge. If a negative potential is now applied from metal to the p-type semiconductor, the potential barrier will be lowered. This situation is called forward bias. In forward bias, due to the lowered potential barrier, semiconductor carriers can be injected into the metal. On the other hand, a positive voltage drives to reverse bias. Ideally, a Schottky contact biased in reverse prevents the current flow through the junction as the potential barrier for holes grows. However, the carrier injection from the metal to the semiconductor is responsible for undesired leakage currents in this regime. The Schottky model provided a very intuitive and simple description of Schottky barriers but its predictive character for ϕ_b was later discovered to be far from ideal.

In the late 1930', the idea that the periodic arrangement of bulk atoms was broken at surfaces and interfaces creating surface states was introduced by Shockley [110]. This idea was applied by Bardeen to metal-semiconductor contacts in 1947 [111] in order to describe the complex behavior of these junctions driven by interfaces states produced by dangling bonds. Nowadays, it is wide known that these interface states can also arise from the tailoring of the metal electrons wave function in to the semiconductor (known as metal induces gap states or MIGS [112]) and from the disorder in the atomic arrangement is introduced at the interface (DIGS). Within Bardeen's model, the Schottky barrier between a metal and a semiconductor would not depend on the work function of the metal but on the interfacial states density and character. In Bardeen description, the contact behavior is driven solely by the interface states.

In the practice, the ϕ_b tends to be comprehended between the Mott-Schottky and the Bardeen descriptions. With the beginning of the experiments in silicon with different metals the pinning parameter was defined [113]. The pinning parameter $S = \frac{d\phi_b}{d\phi_m}$ is a compromise between the two description where if S=1 a perfectly Schottky interface is acquired while if S=0 the metal work function does not impact the ϕ_b. The pinning parameter was later demonstrated to have a strong relation with the ioniciy of the semiconductors [114].

Lastly, in the late 1980', Tersoff proposed a refined model based on the interface density of states distribution and their charge neutrality level. The charge neutrality level (CNL) is the key concept in the modelization of such interfaces and it is explained as follows. In the interface, where the bulk properties are broken due to disorder and non periodicity, states close to the conduction band present an acceptor like-behaviour while states close to the valence band present a donor-like behaviour. The CNL is the energy point where this states change from one to the other behaviour. Within Tersoff model, the CNL of the interface is argued to be the same as the branch points in the bulk semiconductor [115, 116, 117]. This model showed very good results in describing the properties of metal semiconductor contacts.

In the context of the MIGS model, the S value is determined only by the semiconductor in contact with the metal. However, different S values have been observed experimentally for the same combination of semiconductor and metal. In the more advanced DIGS model, where dangling bonds at the interface are considered as the origin of interface states, different interface states can be obtained from the same combination of metal and semiconductor by different interface treatments. The S values can differ due to the modification of density of states of the interface due to the treatment. However, the CNL is the same as that for the bulk semiconductor and it is independent of the S values [118]. The existence of bulk intrinsic CNL was demonstrated experimentally [119] showing that the dielectric properties of the interface and thus the S parameter can be changed with the interface treatment.

In summary, these theories provide a general framework for understanding the behavior of metal-semiconductor junctions, even if the CNL is a bulk property, each interface have its peculiarities resulting from passivation treatments and the deposition process of the metal. For obtaining precise predictions of the ϕ_b in a concrete junction, the microstructure of the interface have to be revealed with experimental techniques and the many body problem of electrons in the system have to be solved in order to accurately describe its interface.

2.2 Diamond Schottky contacts modelization

2.2.1 Forward state

In the forward state, the current flow is governed generally by two mechanism: Thermionic and diffusion. These mechanisms are described within the thermionic-emission-diffusion model (J_{TED}) proposed by Crowell and Sze in 1966 [120]:

$$J_{TED} = \frac{eN_v v_R}{\frac{v_R}{v_D} + 1} exp\left(-\frac{e\phi_b}{k_B T}\right)\left[exp\left(\frac{eV}{k_B T}\right) - 1\right] \tag{2.2}$$

where v_R is recombination velocity, v_D the effective carrier diffusion velocity , N_v the valence band effective state density and V the applied bias.
However, in the case of p-type diamond Schottky diodes $v_D >> v_R$ [83]. Therefore, the diffusion current is negligible and the thermionic dominant.

2.2.1.1 Thermionic emission

The thermionic current density can be expressed, following eq. 2.2, as:

$$J_{TE} = J_0^{TE}\left[exp\left(\frac{eV}{k_B T} - 1\right)\right] \tag{2.3}$$

Where J_0^{TE} is the saturation current density:

$$J_0^{TE} = \frac{eN_v v_R}{1+v_R} exp\left(\frac{-e\phi_b}{k_B T}\right) \tag{2.4}$$

But the maximum recombination velocity is related to the thermal velocity v_{th} [121]:

$$v_R^{max} = \frac{< v_{th} >}{4} = \frac{1}{4}\left(\frac{8k_B T}{\pi m^*}\right)^{(1/2)} \tag{2.5}$$

And therefore we can define the more commonly used equation:

$$J_0^{TE} = A^* T^2 exp\left(\frac{-e\phi_b}{k_B T}\right) \tag{2.6}$$

Where A^* is the effective Richardson's constant and for diamond $A^* \sim 90 Acm^{-2}K^{-2}$ [78]. If the Schottky barrier height is considered to vary with the forward bias due to image force lowering or the non-ideality of the interface: $\phi_{eff} = \phi_b - \Delta\phi_{bi}$. And if this variation of the ϕ_{eff} is linear with the bias, then $\Delta\phi_{bi} = (\Delta\phi_{bi})_0 + \beta V$ and thus ϕ_{eff} may be expressed as $\phi_{eff} = \phi_{b0} - (\Delta\phi_{bi})_0 - \beta V$ where $\beta = \frac{\partial\phi_{eff}}{\partial V}$. Thus the thermionic current density can be written as:

$$J_{TE} = J_0^{TE} exp(\frac{-eV\beta}{k_B T})\left[exp\left(\frac{eV}{k_B T} - 1\right)\right] \tag{2.7}$$

$$J_0^{TE} = A^* T^2 exp\left(\frac{-e(\phi_{b0} - (\Delta\phi_{bi})_0)}{k_B T}\right) \tag{2.8}$$

Alternatively, if $1/n = 1 - \beta$ is defined:

$$J_{TE} = J_0^{TE} exp(\frac{eV}{nk_B T})\left[1 - exp\left(\frac{-eV}{k_B T}\right)\right] \tag{2.9}$$

The ideality factor n incorporates unknown effects that make the device non ideal and that change the barrier height with the applied bias. For instance, a Schottky diode is unlikely to be uniform over its area. Barrier height inhomogeneities generally leads to n > 1 and tend to decrease with increasing temperature.
Lastly, if the effect of the series resistance of the diamond layer R_{ON} and V> $3k_B T/e$ are considered, the following expression is found:

$$J_{TE} = A^* T^2 exp(-\frac{e\phi_b}{k_B T}) exp(\frac{e(V - IR_{ON})}{nk_B T}) \tag{2.10}$$

2.2.1.2 Diamond resistivity physical models

In the previous section, the thermionic current flow through a Schottky barrier was derived. In the eq. 2.10, the contribution of the series resistance was also introduced in the expression to take into account the voltage drop in the diamond layer. Therefore, for successfully predict the characteristics of a diamond Schottky diode deriving the physical models for its

resistivity is necessary. The electrical resistivity for a general semiconductor will depend on the doping level and temperature and it is expressed as [122]:

$$\rho(T, N_A, N_D) = \frac{1}{(ep(N_A, N_D, T)\mu(N_A, N_D, T))} \tag{2.11}$$

Where μ(T, N_A, N_D) is the hole mobility of carriers and p(T, N_A, N_D) is the free hole density.

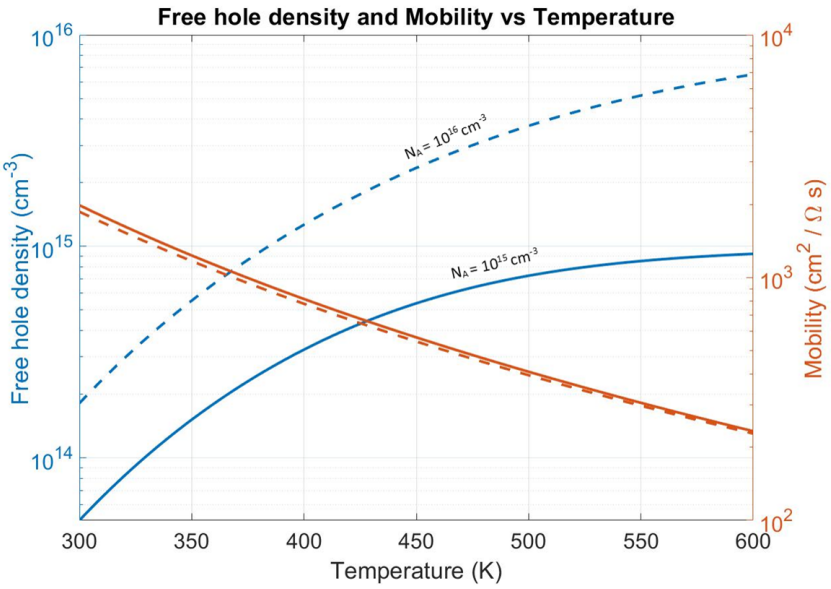

FIGURE 2.2: *Free hole density and mobility versus temperature. The discontinuous lines represent the mobility and free hole density for $N_A = 10^{16}\ cm^{-3}$ while the continuous for $N_A = 10^{15}\ cm^{-3}$.*

- **Free hole density**

Boron doped diamond has a big activation energy of $E_A = 380meV$ (up to a doping level of $10^{18}cm^{-3}$) and thus most of the carriers won´t be ionized at room temperature. For Schottky diodes, the used range of doping for the drift layer lies between 10^{15} to $5 \cdot 10^{16}cm^{-3}$, as further increase would rise the leakage current. In this doping range, diamond is a non degenerate semiconductor. The free hole concentration can be expressed as [122]:

$$p(T) = \frac{N_D + \phi_A}{2}\left(\sqrt{1 + \frac{4\phi_A(N_A - N_D)}{(N_A + N_D)^2}} - 1\right) \tag{2.12}$$

Where:

$$\phi_A = \frac{N_V(T)T^{3/2}exp(E_A/k_BT)}{4} \tag{2.13}$$

$$N_V(T) = \frac{1}{\sqrt{2}}\left(\frac{m_h m_0 k_B T}{\pi h^2}\right)^{3/2}; \tag{2.14}$$

with $m_h = 0.908$, the hole effective mass in diamond.
In figure 2.2, the hole concentration for uncompensated boron doped diamond with $N_A =$

$10^{16}cm^3$ and $N_A = 10^{15}cm^3$ is represented versus temperature. The hole concentration grows at high temperature due to the thermal ionization of boron. Also, the compensation effect tends to be reduced at high temperature as shown in figure 2.3.

- **Hole mobility**

The main scattering mechanism for bulk conduction are phonon and impurities scattering. The empirical model developed in [122] based on data extracted from Hall measurements [123] can be expressed as follows:

$$\mu(T) = \mu(300K)(\frac{T)}{300K})^{\beta} \tag{2.15}$$

$$\beta = \beta^{min} + \frac{-\beta^{min} + \beta^{max}}{1 + (\frac{N_A + N_D)}{300K})^{\gamma}_{\beta}} \tag{2.16}$$

$$\mu = \mu^{min} + \frac{-\mu^{min} + \mu^{max}}{1 + (\frac{N_A + N_D}{N_{\mu}})^{\gamma_{\mu}}} \tag{2.17}$$

And the parameters used in the model are presented in the Table 2.1 extracted from [122].

β^{max}	β^{min}	$N_{\beta}(cm^{-3})$	γ_{β}	μ^{max} (cm$^2/(V\cdot$ s))	μ^{min} (cm$^2/(V\cdot s)$)	N_{μ}	γ_{μ}
3.11	0	$4.1 \cdot 10^{18}$	0.617	2016	0	$3.25 \cdot 10^{17}$	0.73

TABLE 2.1: *Parameters used in the mobility model from ref. [122].*

From $N_A = 10^{16}cm^3$ to $N_A = 10^{15}cm^3$, the mobility has very weak dependence with doping level as shown in fig. 2.2. This is due to the dominance of scattering by phonons which is also responsible for the lower mobility at higher temperatures.
Using the models to calculate μ and p, the resistivity can be estimated as function of temperature, doping level and compensation. In fig. 2.3, the resistivity for a $N_A = 3 \cdot 10^{16}cm^3$ doped diamond layer is plotted versus temperature for different compensation ratios. At RT, the resistivity is dominated by the low hole concentration due to the low ionization and compensation. At high temperature, the resistivity decreases due to the ionization of dopants which tend to mitigate the effect of compensation. A higher temperature would eventually lead to an increase of resistivity due to the decrease of mobility and constant hole concentration.

2.2.2 Reverse state

A Schottky diode biased in reverse should ideally display an infinite resistance preventing the current from flowing through it. The two main phenomena that limit the off-state performance of a Schottky diode are the semiconductor breakdown and leakage currents. Breakdown happens when the critical field for avalanche is reached in the semiconductor layer,

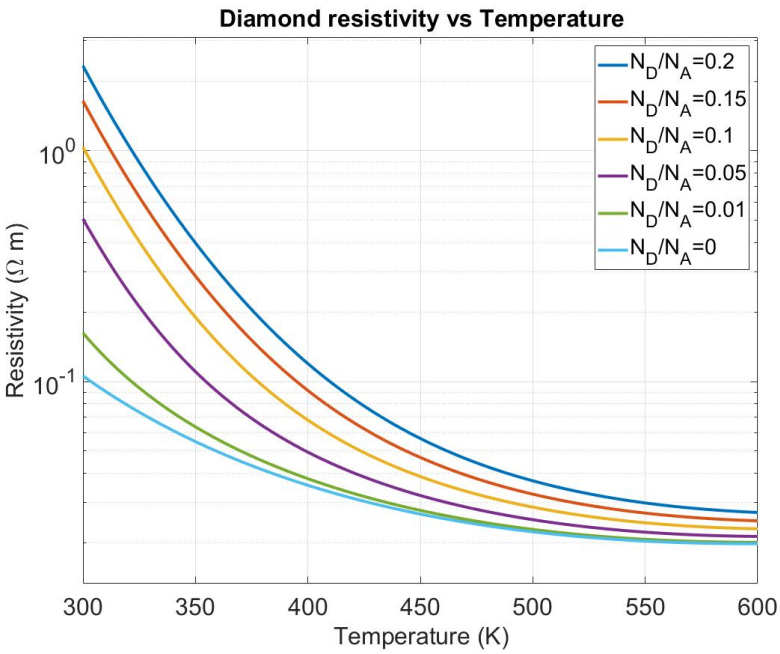

FIGURE 2.3: *Diamond resistivity versus temperature for* $N_A = 3 \cdot 10^{16} cm^{-3}$ *for different compensation ratios.*

usually at the interface, causing an irreversible damage to the device. On the other hand, undesired currents can flow through the Schottky barrier responding to various physical mechanisms. In order to model these phenomena, the Schottky barrier height, the electric field and the depletion region behaviours and dependencies versus the applied bias need to be described first.

2.2.2.1 Depletion region

When metal and diamond are brought into contact, the Fermi levels of both materials align at thermal equilibrium, in order for it to be the constant throughout the interface. The excess of holes from the p-diamond will diffuse into the metal leaving a region of net negative charge in the p-region, near the junction. As the holes diffuse, the ionized acceptors are left behind. The region near the junction interface is depleted of majority carriers, and is therefore referred to as the depletion region or space charge region (SCR). Following Poison's equation the electric field in the depletion region can be calculated as [124]:

$$\frac{dE}{dx} = \rho / (\epsilon_0 \varepsilon_s) \tag{2.18}$$

Therefore, considering a full depletion approximation where the semiconductor is considered to be depleted beside a distance W:

$$E = \int \frac{eN_A dx}{\varepsilon_s} = \frac{eN_A x}{\epsilon_0 \varepsilon_s} - \frac{eN_d W}{\varepsilon_s} = \frac{eN_A}{\epsilon_0 \varepsilon_s}(x - W) \tag{2.19}$$

As the electric field must be zero at the edge of the depletion region. The potential across the barrier can be obtained integrating the electric field:

$$\phi(x) = \int E(x)dx = \frac{eN_A}{2\epsilon_0\varepsilon_s}(x - W)^2 \tag{2.20}$$

If the origin of potential is set at x=0. Now the built-in voltage will be the total jump of the potential and can be expressed as:

$$V_{BI} = \frac{eN_A}{2\epsilon_0\varepsilon_s}W(V = 0)^2 \tag{2.21}$$

If we now apply the charge neutrality condition over the interface, the width of the space charge region for an arbitrary bias V applied:

$$W = \sqrt{\frac{2\epsilon_0\varepsilon_s(V_{BI} + V)}{eN_A}} \tag{2.22}$$

And the junction capacitance per area:

$$C = eN_A\frac{dW}{dV} = \sqrt{\frac{2(V_{BI} + V)}{e\epsilon_0\varepsilon_s N_A}} \tag{2.23}$$

If the reciprocal is squared:

$$C^{-2} = \frac{e\epsilon_0\varepsilon_s N_A}{2(V_{BI} + V)} \tag{2.24}$$

This last formula is useful for doping and V_{BI} determination in measurements. Plotting the inverse square of the capacitance versus the applied voltage the Mott-Schottky plot is obtained. The doping level depends linearly with voltage and the V_{BI} is related to the cut with the x-axis, thus they can be obtained by performing a simple linear fit.

2.2.2.2 Schottky barrier height

The charge transfer across the junction bends the bands of the semiconductor creating the SCR as explained in the last subsection. However, the Schottky barrier arises from the alignment of the semiconductor and metal electronic states. The Schottky barrier height (ϕ_b) is the energy difference between the semiconductor valence band (for p-type semiconductor) and the Fermi level at the interface. In order to accurately describe the potential energy across a Schottky barrier, it is important to introduce the image-force lowering effect.

When a carrier approaches the metal from the semiconductor, the electric field must be perpendicular to the interface. Therefore, the electric field can be calculated as if there were a positive charge of magnitude e located at the mirror-image of the carrier. Thus, when the carrier is at a distance x from the surface of the metal it experiences a Coulombic attraction towards the surface of the metal. Due to this effect the barrier height reduction near the

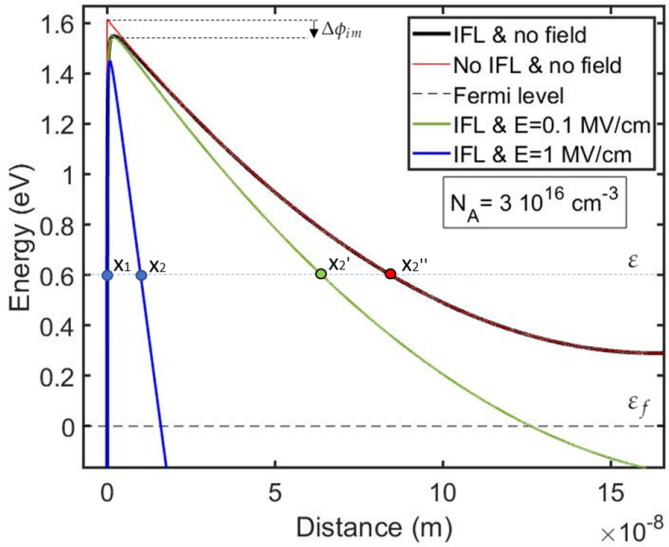

FIGURE 2.4: *Schottky barrier potential energy plot based on eq. 2.31 for a 1.6 eV Schottky barrier height, $N_A = 3 \cdot 10^{16} cm^{-3}$ with and without image force lowering and with and without electric field. The classical turning point are represented for an arbitrary energy ε.*

interface expressed as followed [125]:

$$\phi_{im} = \int -E(x)dx = \int -\frac{e}{4\pi\epsilon_0\varepsilon_s x^2}dx = \frac{-e}{16\pi\epsilon_0\varepsilon_s x} \tag{2.25}$$

At the maximum of the potential, the barrier lowering due to image force is thus:

$$\Delta\phi_{im} = \sqrt{eE_m/4\pi\epsilon_0\epsilon_s} \tag{2.26}$$

Where E_m is the electric field at the interface as deduced from eqs. 2.19 and 2.22:

$$E_m = \sqrt{2eN_A(V + V_{BI})/\epsilon_0\epsilon_s} \tag{2.27}$$

And lastly, using the eqs. 2.20 and 2.25 the total potential distribution across the barrier can be approximated as [126]:

$$\phi(x) = -\frac{e}{16\pi\epsilon_0\varepsilon_s x} + \frac{eN_A}{2\epsilon_0\varepsilon_s}(x - W)^2 \tag{2.28}$$

And if the origin of energy is set as the Fermi level:

$$\phi(x) = k_B T ln(N_V/p) + V_{BI} - \frac{e}{16\pi\epsilon_0\varepsilon_s x} + \frac{eN_A}{2\epsilon_0\varepsilon_s}(x^2 - 2xW) \tag{2.29}$$

Injecting the expression for W (eq. 2.22) and using the definition of the ϕ_b:

$$\phi(x) = \phi_b - \frac{e}{16\pi\epsilon_0\varepsilon_s x} + \frac{eN_A}{2\epsilon_0\varepsilon_s}(x^2 - 2x\sqrt{\frac{2\epsilon_0\varepsilon_s(V_{BI} + V)}{eN_A}}) \tag{2.30}$$

Where the first term is the ϕ_b, the second term is the image force lowering of the barrier and, the third term is the drop of potential in the SCR region due to the doping and the drop of potential due to the bias applied plus the contribution of the built-in voltage. The expression can be reformulated in terms of the electric field at the interface as using 2.27 yields:

$$\phi(x) = \phi_b - \frac{e}{16\pi\epsilon_0\varepsilon_s x} + \frac{eN_a x^2}{2\epsilon_0\varepsilon_s} - xE_m \tag{2.31}$$

The graphic representation of this potential is displayed in figure 2.4. This representation is able to capture the main phenomena under the Schottky barrier such as doping and image force lowering effects. Despite, the image force effect is generally not enough to explain the bias dependence of ϕ_b. Indeed, interface dipoles and states also contribute to change the ϕ_b and more complicated models could be developed to accurately describe the behavior of the ϕ_b versus the bias voltage. However, this picture provides a reasonably good description of the potential profile along Schottky barriers that will allow the evaluation of leakage currents flowing through them in the next subsection.

2.2.2.3 Leakage current model

There are two main mechanisms on which the carriers can rely to overcome the Schottky barrier: tunneling through the barrier and thermionic emission. Now that the potential distribution over the Schottky barrier is appropriately described by eq. 2.31, the leakage current density versus bias can be calculated for a given ϕ_b.
On one hand, the thermionic emission current density is expressed:

$$J_0^{TE} = A^* T^2 exp\left(\frac{e\phi_b - e\Delta\phi_{im}}{k_B T}\right) \tag{2.32}$$

As described in 2.10, but with the image barrier lowering described in the last subsection taken into consideration. The drift layer resistance is usually not taken into account as its contribution will not be relevant compared to the limiting emission mechanism.

On the other hand, the tunnel probability for an electron through a potential barrier under a Wentzel–Kramers–Brillouin (WKB)-type approximation, $T(\varepsilon)$ is given by:

$$T(\varepsilon) = [1 + exp(\frac{-2}{\hbar}\int_{x_1}^{x_2}\sqrt{2m(e\phi(x) - \varepsilon)}dx)]^{-1} \tag{2.33}$$

Where x_1 and x_2 are the classical turning points where $\varepsilon = e\phi(x)$ as shown in figure 2.4.

The current density due to tunneling through the barrier can be calculated integrating the product of the number of electron charges incident on the barrier per second per unit

area $N(T,\varepsilon)$ per the tunneling probability $T(\varepsilon)$ by means of the expression [127, 128]:

$$J = e\int_{-\infty}^{\varepsilon_{max}} T(\varepsilon)N(T,\varepsilon)\,d\varepsilon \tag{2.34}$$

Where ε_{max} is the top of the barrier. Considering a free electron model in the metal:

$$N(T,\varepsilon)d\varepsilon = 4\pi m h^{-3} k_B T \cdot ln[1 + exp(-\frac{\varepsilon - \varepsilon_f}{k_B T})]d\varepsilon \tag{2.35}$$

The tunneling current density yields [129]:

$$J = \frac{A^* T}{k_B}\int_{-\infty}^{\varepsilon_{max}} T(\varepsilon)\cdot ln[1 + exp(-\frac{\varepsilon - \varepsilon_f}{k_B T})]\,d\varepsilon \tag{2.36}$$

This expression can be easily solved numerically for a certain potential distribution over a Schottky barrier given by eq. 2.31.

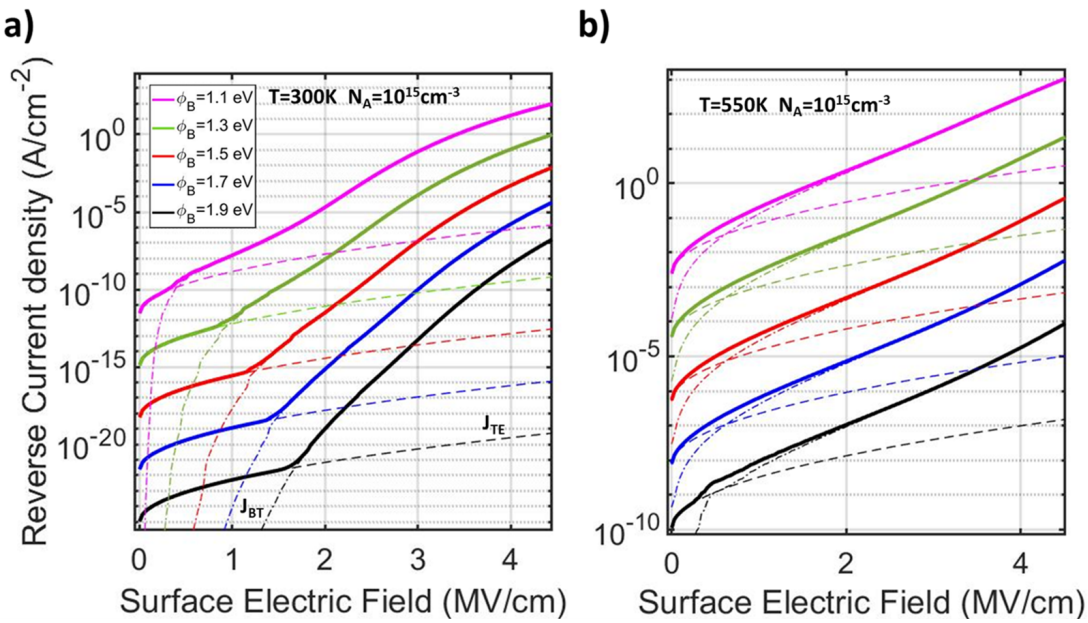

FIGURE 2.5: *Reverse leakage current density and its mechanisms represented for a $N_A = 10^{15}cm^{-3}$ and a temperature of a) 300K and b) 500K for a different set of ϕ_b values.*

- **Leakage current vs Schottky barrier height**

In the figure 2.5, the leakage current density and its mechanisms are represented for a $N_A = 10^{15}cm^{-3}$ and a temperature of a) 300K and b) 500K versus different values of the ϕ_b. The leakage current is dominated by thermionic emission at low fields and by tunneling at high fields. The leakage current densities represented at both temperatures are very sensitive to the variations of ϕ_b. At 300K, the leakage current density at 4 MV/cm is $10^{-7}A/cm^2$ for a ϕ_b of 1.9 eV while at the same field is $10^3 A/cm^2$ for a ϕ_b of 1.1 eV. Therefore, in order to be able to extract diamond properties, a high Schottky barrier forming metal needs to be found in order to have a good rectification ratio. However, diamond

full potential is only reached at high temperature due to the elevated ionization energy of boron dopants. At 550K, the leakage current grows earlier versus electric field due to the augmented thermionic emission. At high field, the tunneling current still dominates even if it is much less sensitive to temperature. At this temperature, the leakage current density at 4 MV/cm is $2 \cdot 10^{-5} A/cm^2$ for a ϕ_b of 1.9 eV while at the same field is $2 \cdot 10^3 A/cm^2$ for a ϕ_b of 1.1 eV. In order to have a rectification ratio of about 10^3 between 10 V in forward and 4 MV/cm in reverse for $N_A = 10^{15} cm^{-3}$ and 550K, a ϕ_b of at least 1.5 eV is needed, as the on-state current at 10 V for this doping is about $100 A/cm^{-2}$.

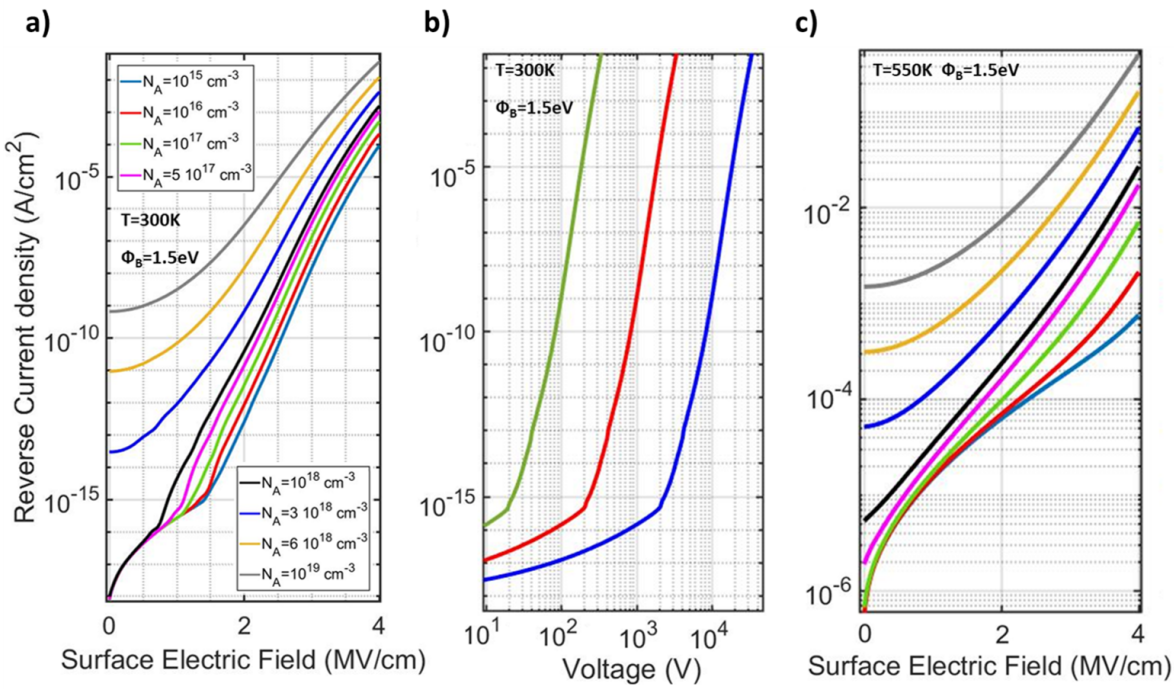

FIGURE 2.6: *Reverse leakage current density represented for a set of doping levels versus a) field and b) voltage at 300K and c) versus field at 550K for a ϕ_b of 1.5 eV.*

- **Leakage current vs doping**

The doping level is also an important parameter concerning the leakage current as it makes the barrier thinner as it grows thus affecting the tunneling leakage current. In the figure 2.6, the leakage current density is represented for a set of doping levels versus a) field and b) voltage at 300K and versus c) field at 550K for a ϕ_b of 1.5 eV. The leakage current is unaffected at low fields between doping levels of $10^{15} cm^{-3}$ to $10^{18} cm^{-3}$ due to the thermionic component being orders of magnitude higher than the tunneling. Only for the doping levels between $3 \cdot 10^{18} cm^{-3}$ and $10^{19} cm^{-3}$, the tunneling leakage surpasses the thermionic component making the total leakage dependent on doping at low fields. On the other hand, at a very high field of 4MV/cm, the leakage current density grows from $10^{-4} A/cm^2$ to $10^{-3} A/cm^2$ between doping levels of $10^{15} cm^{-3}$ and $5 \cdot 10^{17} cm^{-3}$. From there, the leakage current density escalates up to $2 \cdot 10^{-2} A/cm^2$ at 4 MV/cm and $10^{19} cm^{-3}$. Concerning the

leakage versus doping, it is represented in the figure 2.6 b) for a non-punch through design. The maximum voltage that a Schottky contact is able to maintain a leakage current level under $10^{-2} A/cm^2$ at 300K for a ϕ_b of 1.5 eV is 300V, 3 kV and 30 kV for doping levels of $10^{15} cm^{-3}$, $10^{16} cm^{-3}$ and $10^{17} cm^{-3}$ respectively. Lastly, the leakage versus field at 550K is represented in the figure 2.6 c). The leakage is very dependent on the doping at this temperature, specially at high field, growing from $8 \cdot 10^{-4} A/cm^2$ to $4 \cdot 10^{-1} A/cm^2$ at 4 MV/cm. Therefore, in order to work at elevated temperatures, low doping is beneficial for acquiring Schottky contacts with moderated leakage currents. On the other hand, at low fields, the leakage is independent of doping for doping levels smaller than $10^{17} cm^{-3}$.

- **Leakage current vs temperature**

In the figure 2.7, the leakage current density for a $N_A = 10^{15} cm^{-3}$ and ϕ_b of 1.5 eV for temperature of 300K, 400K and 500K. At low fields, the temperature has a very strong influence in the thermionic emission growing 10 orders of magnitude from 300K to 500K. The tunneling current is also influenced, but at very high field the current density for the three temperatures converge. This graph demonstrates that the leakage current is almost unaffected by temperature at high field being this very important for diamond Schottky diodes as their optimal working temperature is about 550K. However, in order to reach 8 MV/cm with a controlled level of leakage current density, a ϕ_b of 1.5 eV is not enough, displaying a current density level of $10^2 A \cdot cm^{-2}$. Anyways, for ultra high voltage applications and thus low doping levels ($< 10^{16} cm^{-3}$), the maximum electric field sustained by diamond is about 5.5 MV. This will be further explained in the following section where the avalanche breakdown models of diamond are presented.

In summary, in order to extract diamond full potential, a Schottky metal with a ϕ_b of at least 1.5 eV and good thermal stability up to 550K needs to be found. This set the framework for the search of a Schottky metal in this thesis. Also, due to the increased tunneling current at high doping level, diamond Schottky contacts should be limit to a doping range of $10^{17} cm^{-3}$. With these requirements, diamond Schottky-based devices sustaining up to 4 MV/cm could be fabricated with low leakage currents. In the case of a doping level of $N_A = 10^{15} cm^{-3}$, this would allow a non punch through Schottky diode at 10 kV to work with a good rectification ratio.

2.2.2.4 Avalanche breakdown

In the case where no leakage current is present through the device or its contribution is rather small, the off-state will be limited by the breakdown of diamond itself though a mechanism called avalanche. The avalanche breakdown is a process in which the carriers in a semiconductor are subjected to a great electric field and subsequently they collide with other atoms ionizing them (impact ionization). This releases more carriers which accelerate and ionize more atoms, in an avalanche like chain reaction. Due to the nature of this avalanche mechanism, UWBG semiconductors and in particular diamond can sustain

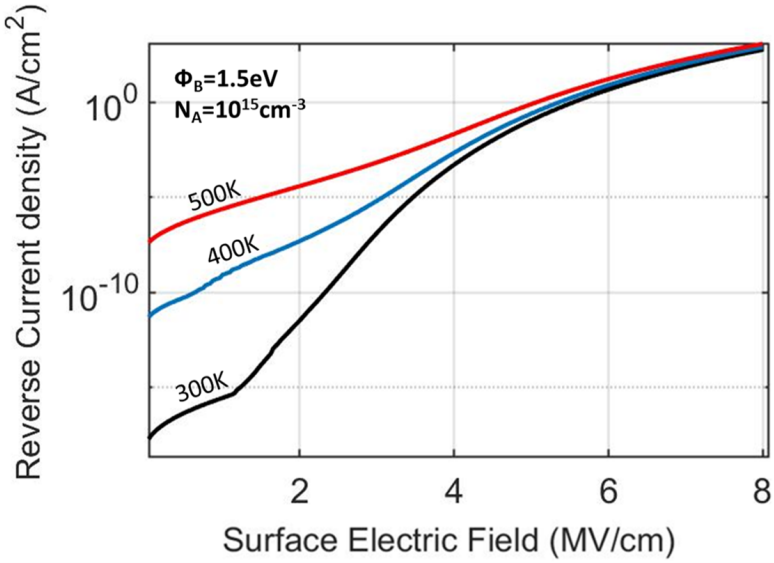

FIGURE 2.7: *Reverse leakage current density for a $N_A = 10^{15} cm^{-3}$ and ϕ_b of 1.5 eV for temperature of 300K, 400K and 500K.*

very high fields due to their enormous band-gap. The avalanche mechanism multiply any small current by a factor M. This factor as a function of the position in the depletion region in boron doped diamond is given by [50]:

$$M(x) = 1 + \int_0^x \alpha_n M(x)\, dx + \int_0^W \alpha_p M(x)\, dx \tag{2.37}$$

Where α_n and α_p are the impact ionization coefficients for electrons and holes. eq. 2.37 has the following solution:

$$M(x) = \frac{exp(\int_0^x (\alpha_n - \alpha_p)\, dx)}{1 - \int_0^W \alpha_p exp(\int_0^{x'} (\alpha_n - \alpha_p)\, dx')\, dx} \tag{2.38}$$

And the breakdown happens when the multiplication factor tends to infinity i.e. when the denominator becomes zero. The denominator integral can be approximated considering a geometric average of the impact ionization rate of electrons and holes $\alpha = sqrt\alpha_n\alpha_p$ so that it becomes zero when:

$$\int_0^W \alpha dx = 1 \tag{2.39}$$

However, there is no precise extraction of diamond ionization rate coefficients in literature. This is due to the difficulty to measure the critical field, as the early stage of technology does not allow the fabrication of test structures without edge effects and leakage currents yet. In this work, the ionization rates fitted to experimental data at RT by Dr. Hirawa and Prof. Kawarada are used [50]:

$$\alpha = \frac{9.44\, 10^4}{10^{0.5}} exp(\frac{1.9\, 10^{7.5}}{|E|}) \tag{2.40}$$

In figure 2.8, the breakdown field and voltage are represented versus the doping level for

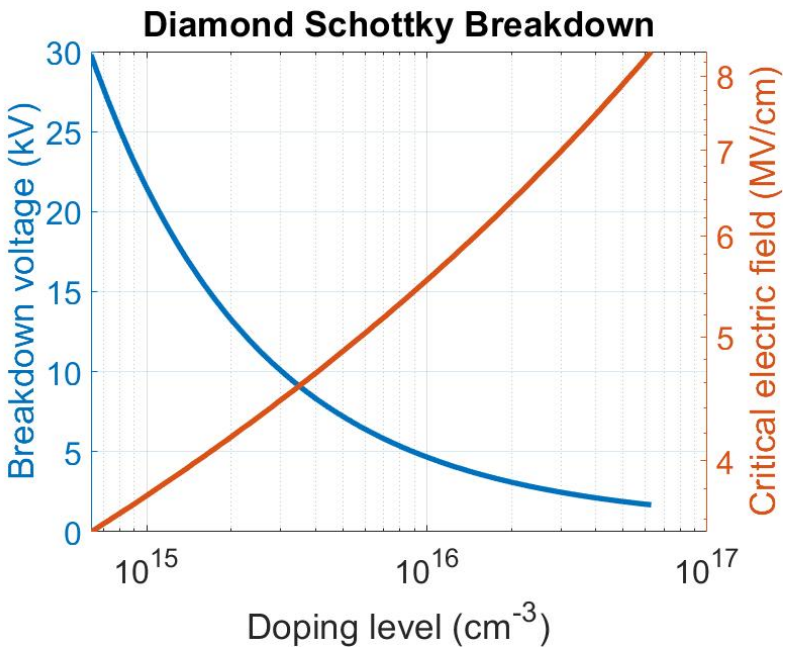

FIGURE 2.8: *Avalanche breakdown field and voltage versus doping level for boron doped diamond based on ref. [50] for a non punch through design.*

a diamond Schottky diode in a non punch trough design. The critical field grows with the doping level from 3.8 MV/cm at $N_A = 10^{15}\ cm^{-3}$ to 5.6 MV/cm at $N_A = 3 \cdot 10^{16}\ cm^{-3}$. For comparison, the critical field of SiC changes from 2 MV/cm at $N_A = 10^{15}\ cm^{-3}$ to 2.83 MV/cm at $N_A = 3 \cdot 10^{16}\ cm^{-3}$, much lower than those of diamond [130]. Conversely, the breakdown voltage decreases with the doping level as the SCR thickness is reduced for the same voltage. While at $N_A = 10^{15}\ cm^{-3}$ a very high blocking capability of 21.4 kV is displayed, at $N_A = 3 \cdot 10^{16}\ cm^{-3}$ only 4.7 kV are sustained.
The latter calculations demonstrate the outstanding potential for the off-state capabilities of diamond outperforming those of the off-state of SiC. Based on them, the performances of Schottky contact based devices are evaluated in the following sections. Also, the technological constrains and bottlenecks to reach such ideal performance are introduced hereafter.

2.3 Ohmic contacts in diamond

In the section 2.1, the formation of an ohmic contact was introduced as a result of the metal work function being higher than the semiconductor´s. However, this is never the case in case of UWBG materials and diamond among them, mostly due to pinned interfaces. Alternatively, an ohmic contact can be achieved by narrowing the depletion layer width of a contact by using heavily doped layers. By using a heavily doped layer, the barrier thickness decrease, as it depends on the inverse square root of the doping, boosting the tunneling current through the barrier (as illustrated in the figure 2.6) and thus creating an ohmic contact. In diamond, titanium contacts deposited on a heavily BDD layer is a well established method

of obtaining contacts with ohmic behaviour. These contacts present good adhesion, reproducibility and good thermal stability. In order to reduce the contact resistances, an annealing treatment is used to form a TiC layer that increase the adhesion and reduce the barrier height, increasing furthermore the tunneling process and reaching contact resistances down to $10^{-7}\Omega \cdot cm^2$ [131, 132].

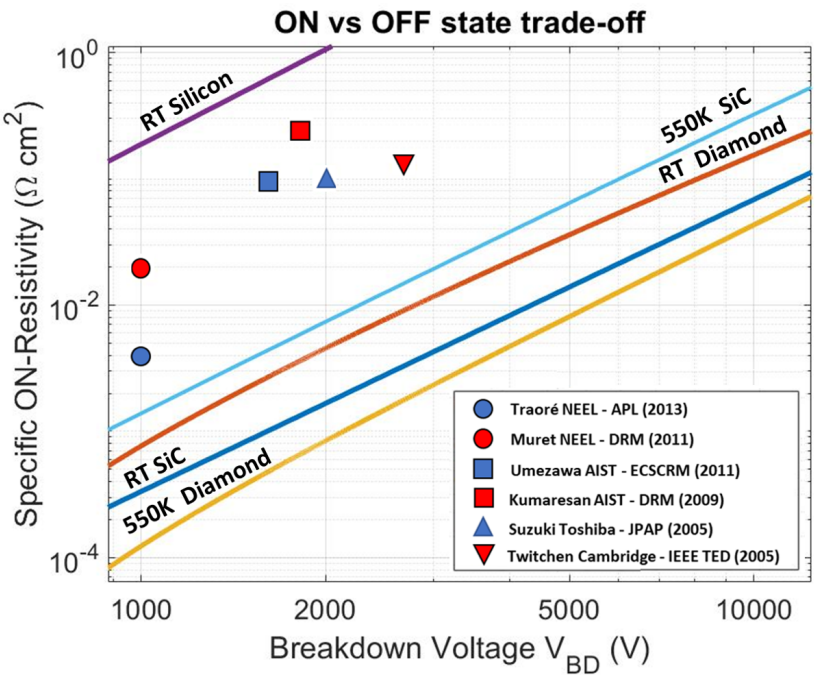

FIGURE 2.9: *Specific on-state resistivity vs breakdown voltage for a non-punch through diamond Schottky diode at RT and 550K. For comparison, the trade-off is also represented for Si at RT, based on [133], and calculated for SiC at RT and 500K based on [134] for mobility and [130] for the doping dependence of the critical electric field. Some of the best experimental results from diamond Schottky diodes are also represented for comparison from [83, 135, 136, 79, 137].*

2.4 P-type diamond Schottky diodes

2.4.1 Non-Punch Through Performance

The last section was dedicated to the understanding and modelization of Schottky contacts to provide the necessary tools for the design and the analysis of diamond Schottky diodes. Based on these tools, the ideal performance of diamond Schottky diodes can be evaluated in terms of on vs off state trade-off performance. The ideal Schottky diode on-state performance will be limited by the drift layer on-state resistance. p+ doped diamond layer or ohmic contact resistance are negligible versus the drift layer resistance in this case. On the other hand, the off-state is limited by the breakdown phenomena and, usually at earlier voltages, by leakage current. However, if a high enough Schottky barrier is considered in

order to prevent leakage currents, the off-state performance will be limited ultimately by the avalanche breakdown. Based on these considerations, the minimum specific on-state resistivity versus the breakdown voltage is displayed in figure 2.9 for a non-punch trough (NPT) design for the typical doping level range for Schottky diodes. The specific on-state resistance ($R_{ON} = \rho W_{max}$) is calculated multiplying the resistivity extracted from eq. 2.11 [122] per the depletion layer thickness at V_{BD}. The V_{BD} is calculated based on the critical field model based on eq. 2.39.

At a doping level of $N_A = 3 \cdot 10^{15}\ cm^{-3}$, the on-state resistance at RT is 0.16 $\Omega \cdot cm^2$ and 0.044 $\Omega \cdot cm^2$ at 550K while sustaining 10 kV. On the other hand, 1 kV is sustained using $N_A = 2.1 \cdot 10^{17}\ cm^{-3}$ with 0.76 $m\Omega \cdot cm^2$ at RT and 0.12 $m\Omega \cdot cm^2$ at 550K. The trade-off is ameliorated at higher temperatures due to the increased carrier density, however, the temperature dependence of the critical electric field is not considered in the used model [50]. For the sake of comparison, the trade-off is also represented in figure 2.9 for Si based on [133] and calculated for SiC at RT and 500K based on [134] for mobility and [130] for the doping dependence of the critical electric field. Diamond at its optimal temperature ($\sim$ 550K) outperform SiC at RT. This is especially relevant since the working temperatures are usually higher than RT in power electronics and HT reduces the on-state performance of SiC by reducing its mobility thus augmenting the performance gap between diamond and SiC. Despite this ideal limit, the off-state performance of most diamond Schottky diodes is limited by leakage currents.

2.4.2 Technological constraints and their limitations to performance

Beside the theoretical performance of diamond Schottky diodes, there are several technological limitations that make impossible to fabricate optimized structures yet. The main bottlenecks for the ideal Schottky structure fabrication are:

- **Deep etching**

Due its immense hardness and its chemical inertness, conventional etching methods from semiconductor industry are not easily transferred to diamond. Most of the efforts to develop a successful diamond etching are based on the use of reactive ion etching (RIE) [138, 139, 140]. However, in order to acquire selectivity the traditional photoresists masks cannot be used due to their short lifetime in the plasma. Thus the only solution for selective diamond etching is to use metallic or oxide mask. These however, can generate defects as particles of the mask are usually sputtered across the etched surface. This leads to the formation of irregular surfaces with spikes or pillars that are not suitable for diamond electronics. Considerable progress have been made over the last years, an etching procedure based on an aluminum mask and a cyclic Ar/O_2 and Ar/Cl_2 RIE process able to etch about ten microns without apparent surface modification was demonstrated [89]. However, this procedure involves the use of thick (1 micron) mask layers and very long etching times with etching rates of 45 nm/min. For ultra high voltage Schottky diodes, etching depths of the

order of 100 microns are needed, therefore the etching technology of diamond is still immature for the needs of power electronics. At the Institute NEEL, the maximum optimized etching is about 2 microns based on a SF_6 RIE that make use of a 300 nm nickel mask.

- **Epitaxy**

The epitaxy of the drift layer is another limiting factor due to the very long time needed for growing thick diamond layers. Generally, epitaxy of diamond layers with boron doping concentration in the range of 10^{15} to 10^{17} cm^{-3} is well established with growth rate about 1 to 10 microns/hour. However, the generation of defects in thick epitaxy limits the maximum layer thicknesses. The maximum layer thickness demonstrated at NEEL institute is a 20 micron layer [90] with prolonged epitaxy time (24h). On the other hand, low methane concentration is associated with reduced defects density [141]. However, reducing the C/H ratio impacts the growth rate thus aggravating the time cost problem. Concerning heavily doped layers, there are critical boron concentrations and thicknesses for dislocations generation. On (100) diamond, the critical boron concentration is 3.2 to 2.5 10^{21} cm^{-3} and on the (111) diamond 6.5 to 17 10^{20} cm^{-3} [142, 143]. Besides these boron concentrations, a plastic relaxation is favored at a certain thickness through dislocations to adapt the in-plane lattice space of both the substrate and the epilayer. Another important aspect is the substrate quality. Defects coming from the substrate can propagate through the grown layer dramatically giving rise to killer defect that are dramatic for device performances [144, 145].

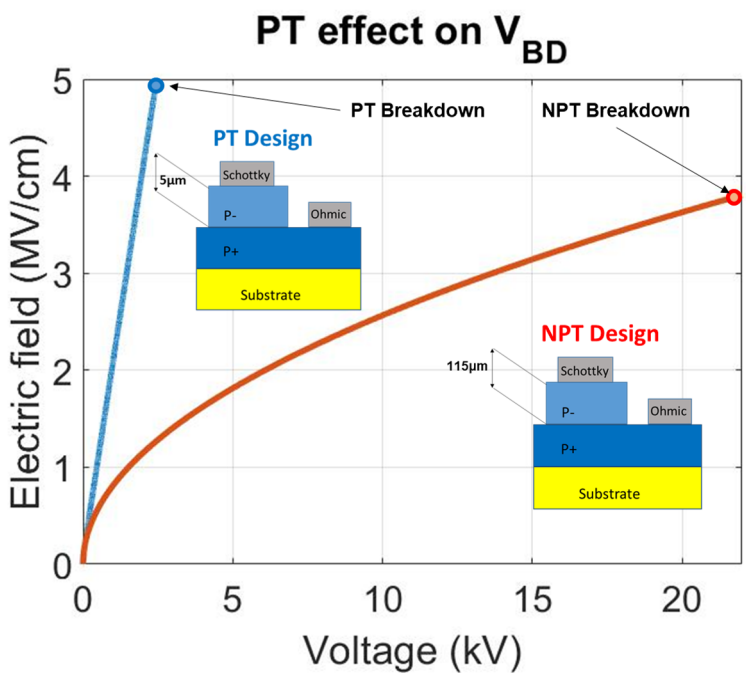

FIGURE 2.10: *E_{max} vs V_{BD} comparison between a NPT design and a 5 µm PT design with $N_A = 10^{15} cm^{-3}$.*

Due to these two limitations and because the depletion region thicknesses at V_{BD} for 10^{15} cm^{-3} is around 115 microns and for 10^{16} cm^{-3} is about 17 microns, most of the fabricated

Schottky are in punch though (PT) configuration. In this configuration the electric field cannot relax entirely in the drift layer because the SCR reaches the end of the drift layer at a certain voltage below the breakdown voltage. From this point, the SCR cannot expand anymore and therefore $E_m = V/t_{drift}$. Thus, the electric field at the interface grows linearly with the applied voltage instead of growing with its square root. However, due to the reduced thickness, the critical field is augmented as $W = t_{drift}$ in eq. 2.39 [146]. Similarly, the on-state resistance of the device is also reduced due to a reduced thickness. Even though the critical field is increased, the device in PT reaches the VBD earlier than the NPT designs. This dramatically reduce the maximum reachable breakdown voltage for the range of available drift layer thickness. The trade-off between on and off state is generally worsen using PT configurations as a result of all the aforementioned opposed effects. In the figure 2.10, the effect of a PT design is illustrated. For a drift layer with a 10^{15} cm^{-3} doping level and 5 microns, the pinch-off voltage is about 40V. From this voltage the electric field escalates linearly until reaching the critical field of 4.95 MV/cm at 2.5 kV while for the NPT design the breakdown happens at 21.4 kV. This is a particular useful example that shows the voltage range limitations imposed by the fabrication constrains. However, the on-state resistance of the NPT is $0.71\Omega \cdot cm^2$ while for the PT structure is 0.031 $\Omega \cdot cm^2$ as the drift layer thickness is severely reduced. For the sake of the comparison, the Baliga figure of merit (BOG = V_{BD}^2/R_ON) is 645 MW$/cm^2$ for the NPT design and 201.6 MW$/cm^2$ for the PT design illustrating the worsened trade-off [147]. Its worth noting that a PT design can be used to improve the trade-off by appropriately choosing the thickness and doping level of the drift layer reducing up to a $\sim$ 10% the on-state resistance [148]. However, the fabrication constraints does not allow fabricating such optimized PT structures.

With the aim of mitigating the effect of thin drift layers, an original approach is taken in this work. By growing encapsulated p+ layers as presented in figure 1.8, no etching is needed for the fabrication of pseudovertical Schottky diodes. This approach removes the etching limitation to the thickness, allowing the maximum drift layer to be ideally up to 20 microns. This can partially reduce the effects of PT since the electric field relaxes in the drift layers up to a very high voltage happens and the structure is finally pinched-off.

- **Schottky contacts fabrication and its interface functionalization**

Several metals and terminations have been used to fabricate p-type Schottky contacts as introduced in Sec. 1.4.1. However, they display premature leakage currents than those predicted by the model developed in the section 2.2.2.3, these reduce the off-state performance of Schottky diodes. These leakage current are usually highly irreproducible in similar samples and even within contacts in the same sample. They can be originated from two different sources: i) Defects under the contact that can open a path for current greatly reducing the Schottky barrier locally. They can be controlled relatively easy but their density limits the contacts size [90]. And ii) Barrier inhomogeneities and electric field crowding at the edge of the contact. Even if the contact ϕ_b measured by I-V or C-V is high enough to prevent leakage currents, if there are local variations to the barrier, the current can still find a path to leak

through this locally lower barrier areas. Moreover, the edge of the contacts is in practice never atomically flat and this can lead to electric field crowding due to spike effects. This latter phenomena makes the electric field to increase faster and uncontrolled versus bias, giving a possible qualitative explanation for the irreproducibilities systematically observed in leakage currents [77, 78].

This is a big limit to performance since the diodes never reach their ideal performance due to premature leakage, thus decreasing further the maximum breakdown voltage and trade-off reachable with these devices. In order to obtain reliable Schottky diodes, an appropriate metal and surface treatment are needed and to find them is one of the main targets of this work. Finding a high ϕ_b forming metal is also conditioned by its thermal stability, because to extract diamond full potential these contacts need to be able to operate at it diamond optimal temperature ($\sim$ 550K). Its worth noting that several edge terminations such as field plates and metal rings have been used to reduce electrical field crowding with promising but non-optimized results [149, 150, 151, 152, 86].

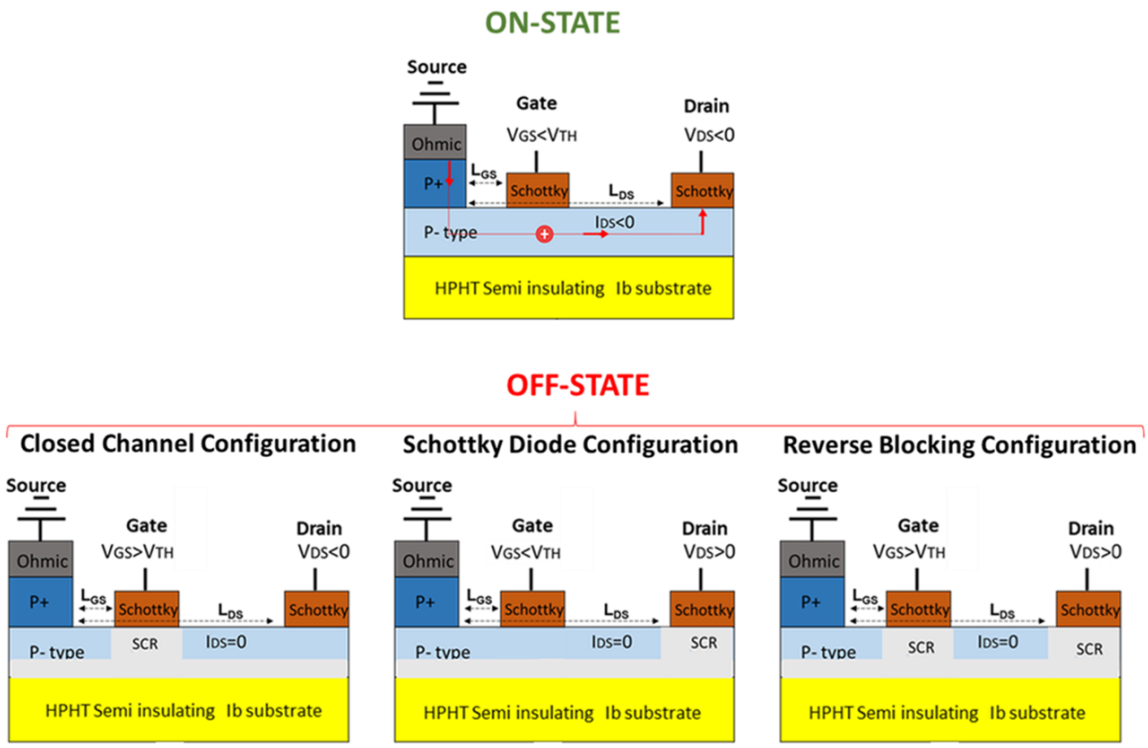

FIGURE 2.11: *Scheme of the possible configurations of the RBMESFET. On the top, the on-state configuration with the current flowing from source to drain. On the bottom, the three off-state configurations: i) Close channel, ii) Schottky diode and iii) Reverse blocking configurations.*

2.5 P-type diamond reverse blocking MESFET

2.5.1 Concept and functioning

Metal-semiconductor field effect transistor (MESFET) is a unipolar device based on a majority carrier conducting channel. Its reverse blocking variant uses both gate and drain Schottky electrodes and ohmic source. This variant main advantage is that it present a better leakage current control due to the Schottky drain electrode, and this allow the transistor to sustain higher voltages. Its main counterpart is that the current is only able to flow in one sense due to the diode character of the drain. The scheme of the possible configurations of a lateral p-type RBMESFET is shown in figure 2.11. For a p-type RB MESFET, applying a negative drain bias V_{DS} induce a hole flow from source to drain, i.e. negative drain current I_D, while for a positive V_{DS} the current is blocked by the reverse state of the Schottky drain. The Schottky gate is designed to modulate the channel thickness by controlling the SCR underneath. Therefore, operating the gate in its reverse state permit to control the I_D. These transistors have been fabricated in the so called normally-on mode in which the channel is open unless a certain positive bias is applied and turns off the device.

For MESFET specifically, but in general for all diamond depletion based FET´s, the fabrication imply the use of a semi-insulating type IIb substrate. These substrates are nitrogen-doped with a donor concentration around $N_D = 10^{19} cm^{-3}$. The expected depletion width within the epilayer at the interface between the substrate and the epilayer can be calculated using:

$$t_{PN} = 2\sqrt{\frac{\epsilon_0 \epsilon_s k_B T}{2e^2 N_D (1 + N_A/N_D)} log(\frac{N_A N_D}{n_i^2})} \tag{2.41}$$

where n_i is the intrinsic carrier concentration.

The SCR spreads almost completely in the p-channel due to a higher doping level of the substrate. Therefore, the effective channel thickness is reduced by the pn junction SCR: $t_{eff} = t_p - t_{PN}$.

2.5.1.1 On-state

The on-state characteristics of a RBMESFET are those of a lateral Schottky diode with an on-resistance modulated by the Schottky gate. The thermionic current density governing the Schottky drain is, using the expression developed in last section and injecting the channel gate-modulated resistance as $R_{CH}(V_{DS}, V_{GS})$:

$$I_{TE}(V_{DS}, V_{GS}) = SA^* T^2 exp(-\frac{e\phi_b}{k_B T}) exp(\frac{e(V_{DS} - IR_{ch}(V_{DS}, V_{GS}))}{nk_B T}) \tag{2.42}$$

Therefore to model the current for a RBMESFET, the channel resistance dependence on the gate BIAS need to be described. Under the gradual-channel approximation and assuming an abrupt SCR and no source to gate current; the SCR width at a distance x from the

source and can be approximated to:

$$t_G(x) = \sqrt{\frac{2\epsilon_0\epsilon_s(V_{BI} - V(x) + V_{GS})}{eN_A}} \tag{2.43}$$

where V(x) is the potential distribution along the channel. This expression assumes that the whole channel is covered by the gate electrode, which is in practice not true. However, the rest of the channel is also depleted by the oxygen termination of diamond that causes a downward band bending and its SCR size is still unreported. On the other hand, the SCR width considered is only due to the gate and not due to the Schottky drain. This is again because in the practice those SCR do not add up since there is a distance between them and thus the drain SCR does not contribute to the current modulation in the channel. A representation of the followed scheme for the on-current derivation is shown in figure 2.12

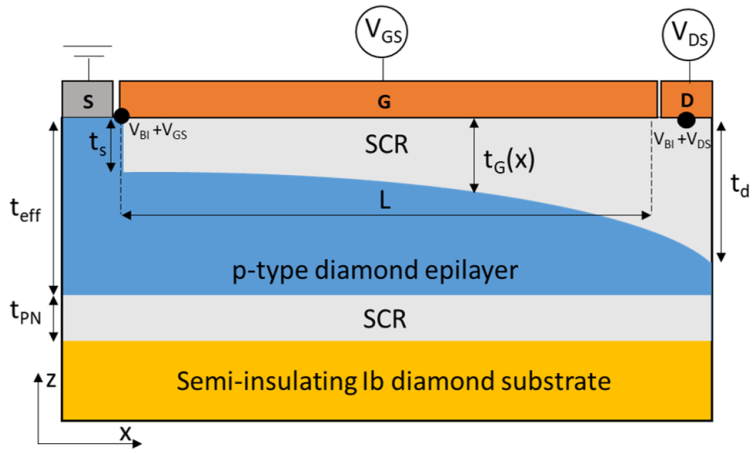

FIGURE 2.12: *RBMESFET scheme used for the modelization of the on-current.*

The resistance of an infinitesimal channel length can thus be expressed:

$$dR = \frac{\rho dx}{(t_{eff} - t_G(x))W_{ch}}. \tag{2.44}$$

Where W_{ch} is the channel width. The current has to be constant through the channel thus $dV = I_{ch}dR$. Where I_{ch} is a hypothetical current limited only by the channel resistance and not by the drain rectifying behaviour. Using this expression and eq. 2.44:

$$I_{ch}dx = \rho(t_{eff} - t_G(x))W_{ch}dV \tag{2.45}$$

Differentiating eq. 2.43:

$$\frac{dt_G}{dV} = -\frac{\epsilon_s\epsilon_0}{eN_A t_G}. \tag{2.46}$$

and substituting dV in eq 2.45 yields a first order differential equation that can be solved for the depletion thickness as a function of the position:

$$I_{ch}dx = -\frac{e^2 \mu p N_A W_{ch}}{\epsilon_s \epsilon_0}(t_{eff} - t_G)t_G dt_G \tag{2.47}$$

Integrating from source to drain:

$$I_{ch}\int_0^L dy = -\frac{e^2 \mu p N_A W_{ch}}{\epsilon_s \epsilon_0}\int_{t_S}^{t_D}(t_{eff} - t_G)t_G dt_G \tag{2.48}$$

Where L is the gate length, t_s is the SCR width at the source and t_D the SCR width at the drain given by eq. 2.43. Assuming that gate and drain Schottky metals are the same, the potential needs to take into account the potential drop for the Schottky drain $V(L) = V_{DS} + V_{BI}$. The SCR width under source and drain for a RBMESFET are thus:

$$t_S = \sqrt{\frac{2\epsilon_s \epsilon_0 (V_G + V_{BI})}{eN_A}}, \qquad t_D = \sqrt{\frac{2\epsilon_r \epsilon_0 (-V_{DS} + V_G)}{eN_A}} \tag{2.49}$$

and therefore:

$$\boxed{I_{ch}(V_{DS}, V_{GS}) = -I_p\left[-\frac{V_{BI} + V_{DS}}{V_p} - \frac{2}{3}\left(\frac{-V_{DS} + V_{GS}}{V_p}\right)^{3/2} + \frac{2}{3}\left(\frac{V_{BI} + V_{GS}}{V_p}\right)^{3/2}\right].} \tag{2.50}$$

Where:

$$I_p = \frac{\mu p N_A W_{ch} e^2 t_{eff}^3}{2L\epsilon_s \epsilon_0}, \qquad V_p = \frac{eN_A t_{eff}^2}{2\epsilon_s \epsilon_0} \tag{2.51}$$

and after pinch-off:

$$I_{ch,sat}(V_{GS}) = -I_p\left[\frac{1}{3} - \frac{V_{bi} + V_{GS}}{V_p} + \frac{2}{3}\left(\frac{V_{bi} + V_{GS}}{V_p}\right)^{3/2}\right]. \tag{2.52}$$

Thus the channel resistance is:

$$R_{ch}(V_{DS}, V_{GS}) = \left[\frac{I_{ch}(V_{DS}, V_{GS})}{V_{DS}}\right]^{-1}. \tag{2.53}$$

And injecting this expression in eq. 2.42, the RBMESFET transfer characteristics can successfully be represented. Typical I-V characteristics of a RBMESFET are shown in figure 2.13, where the drain current as a function of drain voltage for different gate voltages is plotted at RT. In fig. 2.14, the transfer characteristics of a RBMESFET are represented for a fixed V_{GS} versus temperature.

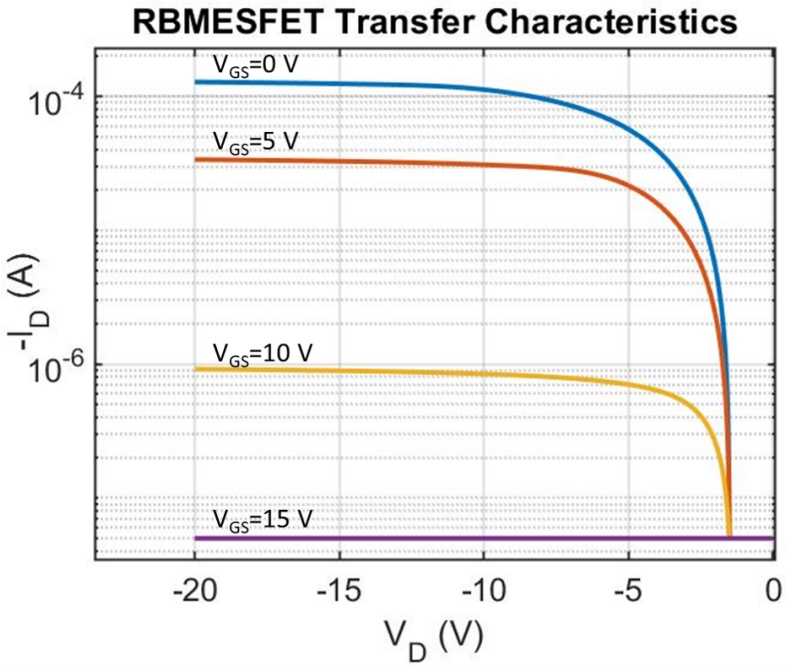

FIGURE 2.13: *Transfer characteristics of a RBMESFET with* $\phi_b = 1.6V$, $n = 1.4$, $N_A = 3 \cdot 10^{16}\ cm^{-3}$, $t_{eff} = 500nm$, $W_c = 650\mu m$ *and* $L_c = 68\mu m$ *for* V_{GS} *=0 to 15V every 5V step.*

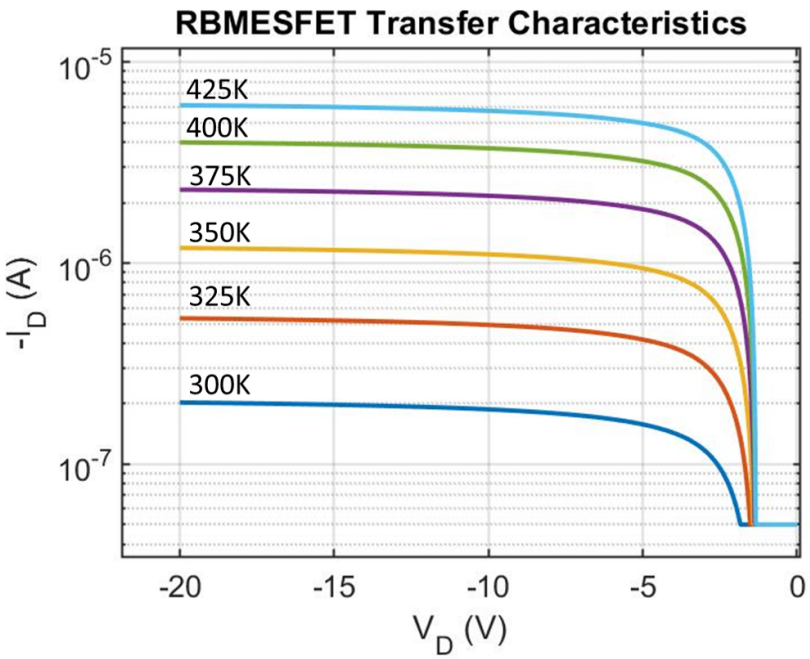

FIGURE 2.14: *Transfer characteristics of a RBMESFET with* $\phi_b = 1.6V$, $n = 1.4$, $N_A = 3.5 \cdot 10^{16}\ cm^{-3}$, $N_A/N_D = 0.2$, $t_{eff} = 180nm$, $W_c = 650\mu m$ *and* $L_c = 68\mu m$ *for* $V_{GS} = -1.2V$ *for temperatures between 300K and 425K with a 25K step.*

2.5.1.2 Off-state

The off-state of a RBMESFET is composed of three different configurations as shown in figure 2.11: i) $V_{GS} > V_{TH}$ and $V_{DS} < 0$ referred as close channel configuration. This configuration is similar to the off-state of a conventional MESFET. ii) $V_{GS} < V_{TH}$ and $V_{DS} > 0$ referred as Schottky configuration. In this configuration the transistor works as a lateral Schottky diode biased in reverse. iii) $V_{GS} > V_{TH}$ and $V_{DS} > 0$ referred as reverse blocking configuration. In this particular configuration the transistor displays its best off-state performance joining the last two configurations in order to block the current flow. Again as in a Schottky diode, the two main limits to the off-state of a RBMESFET are leakage current and avalanche breakdown. However, depending of the configurations, the leakage and the electric field relaxation will occur differently. In the close channel and reverse blocking configurations, the leakage current will most likely occur through the gate, while for the Schottky diode configuration it will happen through the drain. In any case, the leakage current can be described by eqs. 2.36 and 2.32. Analogously, the electric field in these configurations would again obey eq. 2.27 and the SCR will expand as 2.22, but the relaxation will happen between gate and drain. Moreover, the maximum breakdown voltage sustained by the RBMESFET will obey eq. 2.39. Alternatively, the RBMESFET in the Schottky configuration will behave just like a lateral diode where both the leakage current and the electric field relaxation happen from drain to source.

2.5.2 Normally-off character

In this thesis the aim is to fabricate a normally-off transistor because, in terms of safety, normally-off FET operation is usually required for power electronic applications. Moreover, due to the outstanding radiation hardness demonstrated by diamond MESFET [87], digital electronics in harsh environments could make use of such transistor if it displays normally-off operation. In general, MESFET transistors are normally-on: The Schottky gate can be operated only in reverse mode, depleting the channel in order to close it. However, if a p-diamond layer doping level and thickness is precisely engineered, the SCR on the source can be exactly as thick as the drift layer and a small forward voltage can be applied to the gate, just below the threshold voltage of the Schottky diode in order to reduce the SCR extension and open the channel. Thus, in order to have a normally-off RBMESFET with $V_{TH} = 0V$, then $t_{eff} = t_s(V_G = 0)$ and therefore the pinch-off voltage (V_p) must be similar to the Schottky built-in voltage as it is deduced from substituting eq. 2.49 on eq. 2.51. The major challenge in the fabrication of such a normally-off transistor is thus to target the correct layer thickness with the precise targeted doping level.

2.5.3 Non-Punch Though Performance

As stated in the last two sections, an ideal RB MESFET on-state will be limited by the layer resistivity, while its off-state will be limited by its drift layer critical field. In order to evaluate the performance, a simple picture can be obtained considering the case of no contact

resistance, R_{ON} can be taken as:

$$R_{ON} = R_{ch}|_{\frac{dR_{ch}}{dV_{DS}}=0}^{V_{GS}^{max}} \tag{2.54}$$

This is, the minimum resistance of the channel (i.e. the channel resistance at the saturation point) for the maximum negative V_{GS} that can be applied before reaching the turning-on point of the gate (The V_{GS} value at which the I_G current is relevant compared to the I_D). In order to compare between devices, its convenient to define an active area normalized resistance, the specific on-resistance $R_{ON,S}$, which for lateral devices is defined by:

$$R_{ON,S} = R_{ON} L_{SD} W_{ch} \tag{2.55}$$

And the off-state breakdown voltage its again given by eq. 2.39. If we assume the devices to be optimized so that the W_{ch} has the SCR size at breakdown voltage and t_{eff} to be closed at a reference threshold voltage no matter the doping level, the trade-off versus on and off states can be represented as shown in figure 2.15. Obviously, the performance of the device will depend on the threshold voltage selected. For the sake of comparison in figure 2.15 normally-off performances at RT and 500K are compared to a 15 V threshold voltage normally-on performance at RT. The performance is much worse for the normally-off MESFET due to the thinner channel. This is the cost of having a normally-off operation, while the device is lateral, only a very thin layer will contribute to the on-state current. However, this drawback of the normally-off operation can be solved by using a vertical architecture.

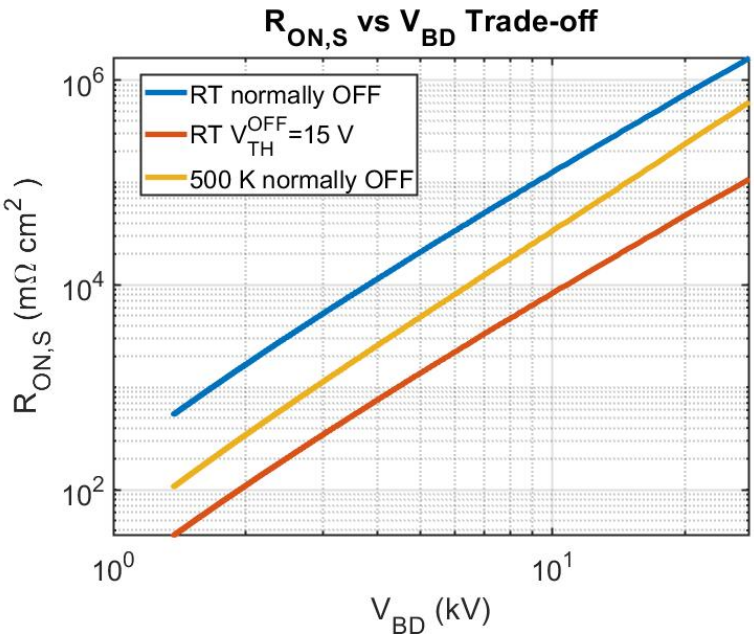

FIGURE 2.15: *On vs off state trade-off for a NPT RBMESFET with $\phi_b = 1.6V, n = 1.4$, no compensation, $Wc = 650\mu m$ and $Lc = 68\mu m$ with normally-off character at RT and 500 K and normally-on character with $V_{TH}^{ON} = 15V$ at RT.*

If a lateral square device is considered:

$$R_{ON,S}^{Lat} = R_{ON} L_T W_C \sim R_{ON} L_T^2 \tag{2.56}$$

And for a squared vertical device with the same resistance the specific on-resistance is:

$$R_{ON,S}^{Vert} = R_{ON} W_C t_{ch} \sim R_{ON} L_T t_{ch} \tag{2.57}$$

The lateral versus vertical comparison thus yields:

$$\frac{R_{ON,S}^{Vert}}{R_{ON,S}^{Lat}} = \frac{t_{ch}}{L_T} \xrightarrow{normally-off} \frac{\sqrt{\frac{2\epsilon_0 \varepsilon_s (V_{BI})}{eN_A}}}{\sqrt{\frac{2\epsilon_0 \varepsilon_s (V_{BI} + V_{BD})}{eN_A}}} \sim \sqrt{\frac{V_{BI}}{V_{BD}}} \tag{2.58}$$

This would yield a performance boost of about or about 12 times for the RBMESFET with $V_{TH} = 15V$ while giving about 40 times better performance for the normally-off RBMESFET for a doping level of $3 \cdot 10^{16} cm^{-3}$ reducing the gap between them in a vertical architecture. In fact, for a vertical normally-off MESFET, a boost up to 20 to 100 times lower specific resistances in the rage of doping level of $10^{15} cm^{-3}$ to $10^{17} cm^{-3}$ used for Schottky contact based devices is expected versus lateral devices.

2.6 Conclusion

In this chapter, the theoretical framework and the state of art practical bottlenecks for the p-type diamond Schottky based power devices have been introduced and discussed. Diamond on-state performance is determined by its resistance, which is shown to be minimized at elevated temperatures (550K) due to the ionization of boron impurities. Concerning the off-state, two limiting mechanisms have been introduced and discussed: leakage currents and avalanche breakdown. The latter is introduced within a state of art model provided by Dr. Hirawa [50]. Within these realistic models, the ultimate diamond capabilities are shown to outperform those of SiC specially at high temperature. On the other hand, leakage currents are a recursive problem for diamond Schottky contacts limiting the off-state performance. In order to evaluate the requirements to prevent it, a novel model for the leakage current in diamond have been developed and its dependencies versus temperature, doping and ϕ_b discussed. The necessity of finding a high barrier forming metal is emphasized by the latter. In order to extract diamond full off-state potential, a metal that forms a ϕ_b of at least 1.5 eV is needed for preventing leakage currents at high temperature and at the enormous electric field that diamond can sustain.
Once that such metal is found, diamond Schottky diodes sustaining up to tens of kV could be fabricated. Despite, some other problematic derived from the thin drift layers used, due

to the the difficult and long-lasting epitaxy and etching, are present and their impact to performance are discussed extensively in this chapter. A partial solution for the latter will be taken in this thesis, the encapsulated pseudovertical architecture, that allows to access the p+ back contact without etching boosting the maximum drift layer thickness and pushing the off-state performance. By taking this approach and committed to the search of a thermally stable high ϕ_b forming metal, a reproducible Schottky barrier diode that demonstrate kV range blocking voltage will be fabricated and presented in chapter 4.
Concerning diamond transistors, the concept of a reverse blocking MESFET is introduced and its working modes explained. The on-state current is model through a 1D approximation within the gradual channel approximation. The off-state is evaluated thanks to the developed models for the avalanche breakdown. Lastly, the performance of such transistor is evaluated and the benefits and advantages of a normally-off transistor presented. Special emphasis is put in the performance of the vertical architecture of such transistor that will allow to boost the on-state current by up to 100 times when vertical architectures can be fabricated thanks to the progress in the etching and epitaxy technology.

Chapter 3

Diamond-metal interface: The search for an ideal Schottky metal

---

A theoretical and experimental investigation of the electronic and physico-chemical properties of molybdenum and zirconium lateral Schottky diodes is presented in this chapter. The microstructure and chemical composition of the contacts is revealed by transmission electron microscopy and x-ray photoelectron spectroscopy and is correlated to the electrical characteristics of the diodes. The potential profile along the edges of the contacts is measured with Kelvin probe force microscopy showing the contacts built-in voltage and the oxygen-terminated diamond band bending. Lastly, an AB-initio investigation of the electronic properties of the oxygen-terminated surface and its interface with molybdenum is presented.

3.1 LD1 sample fabrication

The main objective of the investigation presented in this chapter is to develop both a qualitative and quantitative understanding of diamond lateral Schottky diodes. This comprehends the electrical behaviour of the Schottky contact operated laterally and its link to material science, as well as the role of the surface properties and the back p-n junction produced within the drift layer and the substrate. This knowledge is fundamental in order to design lateral transistors later on in this work and also to provide an insight in the behaviour of the Schottky metal contacts and its relation with the microstructure. One lateral diode sample noted LD1 has been fabricated based on a Sumitomo Ib multisectorial (100) oriented substrate. The followed fabrication process is designed to be as simple as possible, since the performance of the diodes is not the main target here, but the study of their microstructural properties and its link to the electrical behaviour. The MPCVD epitaxy of the p epilayer was performed in a home made reactor at the institute NEEL, which can grow from heavily to slightly doped layer. The general fabrication process requires a clean environment since the smallest contamination can lead to failure, for this purpose, all the fabrication steps (i.e. lithography, metal evaporation, etc.) have been performed in NanoFab clean-room. The full scheme of the fabrication process for the sample LD1 is presented in figure 3.1, the steps are detailed hereafter:

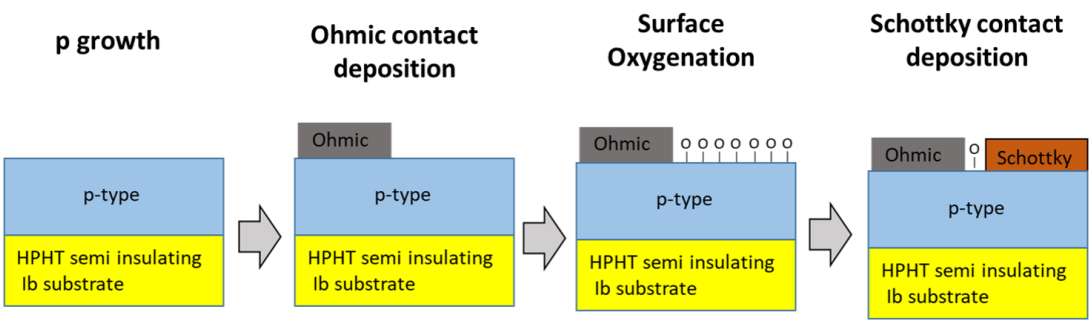

FIGURE 3.1: *Schematic fabrication process for the lateral diamond Schottky diode sample LD1. The first step is the epitaxy of the drift layer. Once the epitaxy is finished, the ohmic contacts are fabricated following the usual lithography plus lift-off process, followed by a thermal treatment at 750 K to reduce the contact resistance. The top surface is then treated by means of an ozone plasma in order to acquire an oxygen-terminated surface. A laser lithography process is again used to define the Schottky electrodes, followed by the deposition of the molybdenum and zirconium Schottky metal stacks.*

3.1.1 p-type drift layer epitaxy

The sample LD1 is set inside a home made reactor for a 2h H_2 plasma treatment after a triacid (sulfuric, nitric and percloric in volumic proportions 3:4:1 at 600K) cleaning treatment. This H_2 plasma treatment has the double purpose of cleaning and smoothing the sample surface

as well as acquiring a stable plasma ball centered on the sample with a constant temperature. The pressure used is 33 Torr and a 200 sccm flow with a microwave power of 240 W. After, methane and a mix of H_2, oxygen and diborane after a double dilution process are injected in the mixture reaching temperatures of 1200K. The parameters for the epitaxy are: CH_4/H_2=1%, O_2/H_2=0.25% and B/C = 60 ppm for a target doping level of $1.5{\cdot}10^{16} cm^{-3}$. The epitaxy lasts 110 min reaching a thickness of ∼900 nm. The rugosity of the surface is about 0.8 nm as measured by profilometry. Low concentration of defects are found by optical microscope inspection of the sample LD1, reassuring the good quality of the grown drift layer.

3.1.2 Ohmic contact fabrication

Ohmic contacts are fabricated based on a stack of titanium (30 nm), platinum (30 nm) and gold (30 nm) for the sample LD1. Titanium is used for its adhesion and low barrier due to the formation of a TiC layer at diamond interface, platinum is used to avoid gold diffusion and gold is chosen for its conductivity, stainless and wire-bonding ease. It is evaporated after a standard lithography and lift-off process engineered thanks to a laser lithography. As the ohmic electrode is evaporated directly on the low doped diamond drift layer, it is designed to cover as much as area as possible since a small contact would have Schottky contact behaviour. After metal the deposition, the sample LD1 is annealed at 830K in ultra-high vacuum in order to enhance the formation of TiC at the titanium-diamond interface for ameliorating the adhesion and lowering the contact resistances. Anyways, the ohmic electrode is expected to be greatly resistive as no p+ diamond layer was grown underneath.

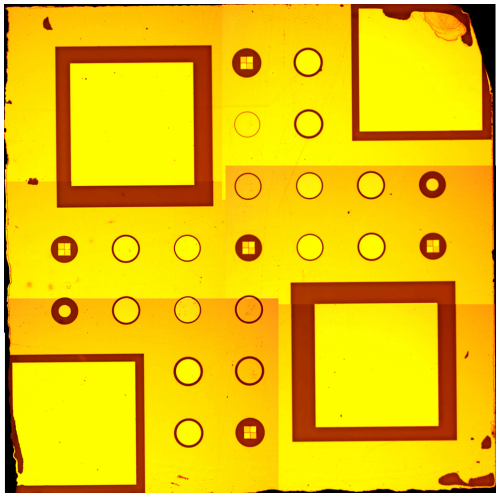

FIGURE 3.2: *Optical microscope image of the LD1 sample after the full fabrication process.*

3.1.3 Schottky contact fabrication

After the ohmic contact fabrication, an ozone plasma treatment is performed in order to oxidize the LD1 sample surface. The treatment consist on a 2 hours plasma at a pressure of

500 mbar. The ozone plasma is achieved by using a a Xenon EXCIMER UV lamp at 172 nm. After, a lithography process to define the electrodes is performed and a subsequent ozone treatment is again performed to ensure the surface oxygenation. Then, metal stacks based on zirconium (30 nm), platinum (30 nm) and gold (30 nm) are deposited by e-gun evaporation under high vacuum. After, a stack of molybdenum (30 nm), platinum (30 nm) and gold (30 nm) is deposited with the same procedure in order to compare their behaviour in the same sample. An image of the sample LD1 after the full fabrication process is presented in figure 3.2. The whole surface is covered by the ohmic contact except for the circular 100 micron radii molybdenum and zirconium Schottky contacts with different spacing ranging from 5 to 20 microns and the 500 micron side square molybdenum and zirconium contacts. An additional ozone plasma treatment is again used after contact fabrication once a first electrical characterization of the contacts is performed in order to evaluate its impact on the electrical response of the diodes.

3.2 Lateral diodes characteristics

The I-V characteristics for a molybdenum contact and a zirconium contact with 100 microns radius and 5 microns spacing before and after an O_3 surface passivation treatment are presented in the figure 3.3. Concerning the molybdenum contact, the on-state characteristics are slightly affected by the ozone treatment with the Schottky barrier and ideality factor passing from 2.08 eV and 1.02 to 1.70 eV and 1.08 as deduced from fitting the on-state characteristic to 2.10. Also, the resistance resistance rise from 145 MΩ to 177 MΩ. On the other hand, the zirconium contact displays a Schottky barrier of 1.86 eV and an ideality factor of 1.03 before the surface passivation. A strong change in the characteristics after the passivation is observed with a high ideality factor of 1.32 and a low Schottky barrier of 1.36 eV. The zirconium contacts are probably affected by the ozone treatment leading to a chemical composition change that dramatically affects their behaviour. Again, an increase in the on-state resistance after the passivation treatment is observed, changing from 157 MΩ to 204 MΩ after the passivation.

In both diodes, the current level is limited by the ohmic contact resistance as the resistance of the drift layer is expected in the 10-100 kΩ range. The change in the resistance after the ozone treatment is attributed to the modification of the ohmic contact resistance. Most probably, due to the Schottky barrier under the titanium electrode due to the absence of a p+ layer, the current is flowing thanks to a surface related process that is affected by the passivation. Otherwise, the off-state characteristics of the molybdenum contact remain unaffected up to 100 V by the passivation with the leakage current still under the detection limit. However, the zirconium contact show an improve after passivation making the leakage current to disappear after passivation. The passivation treatment is probably benefiting both zirconium and molybdenum off-state performances although the latter did not display leakage currents even before the treatment and thus a robust demonstration for this hypothesis is still needed and will be presented in chapter 4.

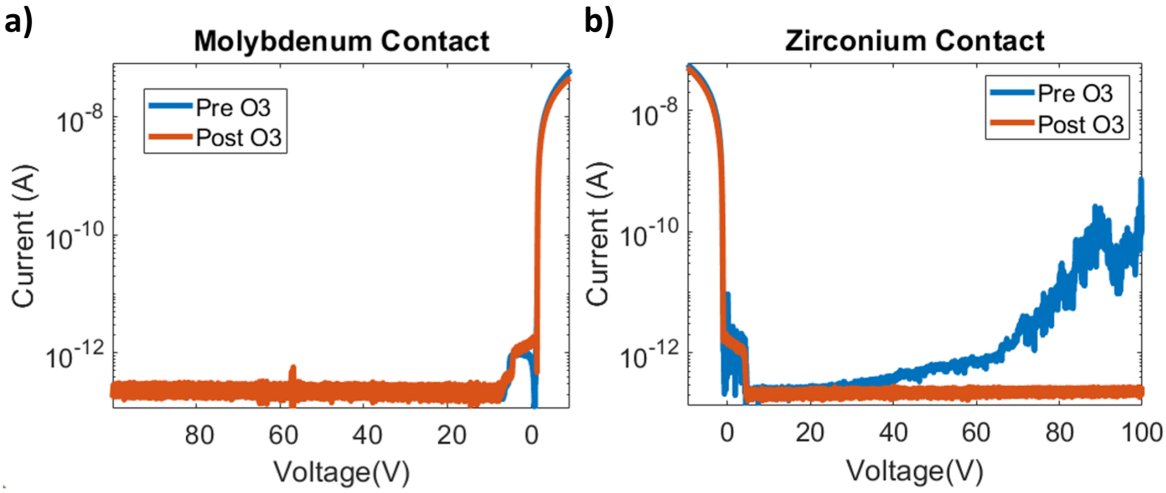

FIGURE 3.3: *I-V measurements for a molybdenum contact and a zirconium contact with 100 micron radius and 5 microns spacing before and after the O_3 surface passivation treatment.*

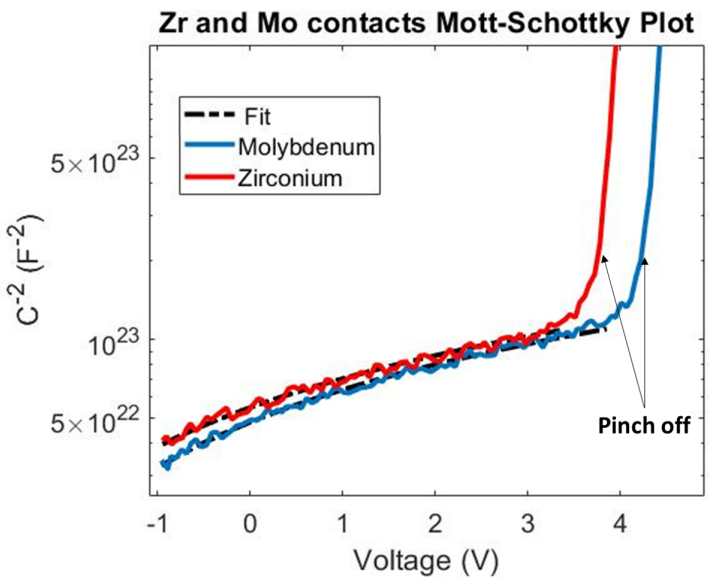

FIGURE 3.4: *Mott-Schottky plot for C-V measurements performed on a molybdenum contact and a zirconium contact with 100 micron radius and 5 micron spacing. The $N_A - N_D$ value deduced from both curves is $1.6 \cdot 10^{16}$ cm^{-3}. However, the V_{BI} for the molybdenum contact is 3.0 eV while for the zirconium contact is 3.4 eV. The depletion region reaches the substrate SCR at 3.8 V for zirconium and at 4.2 V for molybdenum. The deduced channel thickness is 900 nm, 400 nm being always depleted due to the p-n junction between drift layer and substrate.*

The Mott-Schottky plot for the C-V measurements at 100 Hz performed on a molybdenum and a zirconium contacts with 100 micron radius and 5 microns spacing after passivation are presented in the figure 3.4. The low frequency used for these measurements is chosen in order to avoid the series resistance high pass filter effect on the C-V characteristics. The C^{-2} curves were fitted to the equation 2.24 in the range -1V to 3 V in order to determine $N_A - N_D$ value. The $N_A - N_D$ is similar for both contacts yielding a value of $1.6 \cdot 10^{16}\ cm^{-3}$. However, the V_{BI}, deduced from the intercept with the x-axis, for the molybdenum contact is 3.0 eV while for the zirconium contact is 3.4 eV. The difference between the built-in voltages extracted from I-V and C-V are attributed to Schottky barrier patchiness over the contacts areas. The depletion region reaches the substrate SCR at 3.8 V for zirconium and at 4.2 V for molybdenum. Therefore, the deduced channel thickness is 900 nm using equation 2.22, 400 nm being always depleted due to the p-n junction between drift layer and substrate according to eq. 2.41. Such a thin drift layer is not benefiting the on-state characteristics of the diodes, but as discussed earlier, this is not the objective of this sample. In fact, this sample is used to calibrate the growth rate and doping of the drift layer epitaxy plus the V_{BI} of the contacts to be able to fabricate a normally-off device later on in the chapter 5. In the sample LD1, a pinch-off voltage of $\sim 4V$ is archived, meaning the epitaxy time must be slightly reduced to reach a pinched-off layer at 0V in order to get a normally-off transistor. Lastly, the passivation treatment seems to affect positively to the blocking capacities of the contacts although zirconium revealed sensitive to oxidation degrading its on-state characteristics.

3.3 TEM study of the interface

In the previous section, the electrical characteristics of lateral zirconium and molybdenum contacts were presented. The off-state characteristics improved thanks to a ozone passivation treatment performed after contact fabrication although the zirconium contact on-state was degraded reducing the Schottky barrier and augmenting the ideality factor. As both of these metal are susceptible to oxidation, a material science study is thus necessary to verify the chemical composition, crystallography and quality of the interface in order to validate this approach and understand the role of the microstructure on the ultimate electrical characteristics. For this, a transmission electron microscopy (TEM) study of the interfaces between the metals and diamond is presented in this chapter. As diamond hardness makes impossible the preparation of TEM samples by the conventional procedure, a lamella was nano-engineered for each contact by means of a focus ion beam (FIB) based on Ga+ ions in a Scios 2 DualBeam at the University of Cadiz for their subsequent study by TEM.

- **Molybdenum**

Two high resolution transmission electron microscopy (HRTEM) images of the diamond-molybdenum interface are presented in the figure 3.5. The micrograph presented in the figure 3.5 a) shows diamond on the left and molybdenum on the right. It also shows the fast Fourier transform (FFT) performed on the three blue square regions in order to check the

crystalline quality of diamond and the crystalline phase of molybdenum. In the FFT region 1, diamond (0 1 1) pole is displayed corresponding to a face centered cubic (fcc) lattice with L/M=1.157, very close to the theoretical value of 1.156. The molybdenum layer presents a policrystalline character with a typical grain size of about 5 nm. In the FFT performed on regions 2 and 3, which are molybdenum well resolved grains, the (0 0 1) pole and the (-1 1 1) pole of molybdenum are observed with M′/M=1.01 and L′/L= 1.001 respectively. This confirms the expected body centered cubic (bcc) phase of molybdenum at RT.

In the figure 3.5 b), a zoomed-in micrograph from a different region of the lamella is presented. In this image, the microscope is set to show a focused image of the interface for a more careful evaluation. Diamond in the left and molybdenum in the right join in a now clearly sharp interface in which some well ordered molybdenum grains are resolved at the interface. A strong bright line of about two atomic planes between diamond and molybdenum is observed just at the interface. This can be attributed to the diffraction from the electron beam at the interface or to the chemical bonding between the two materials involving oxygen, i.e., a compositional contrast.

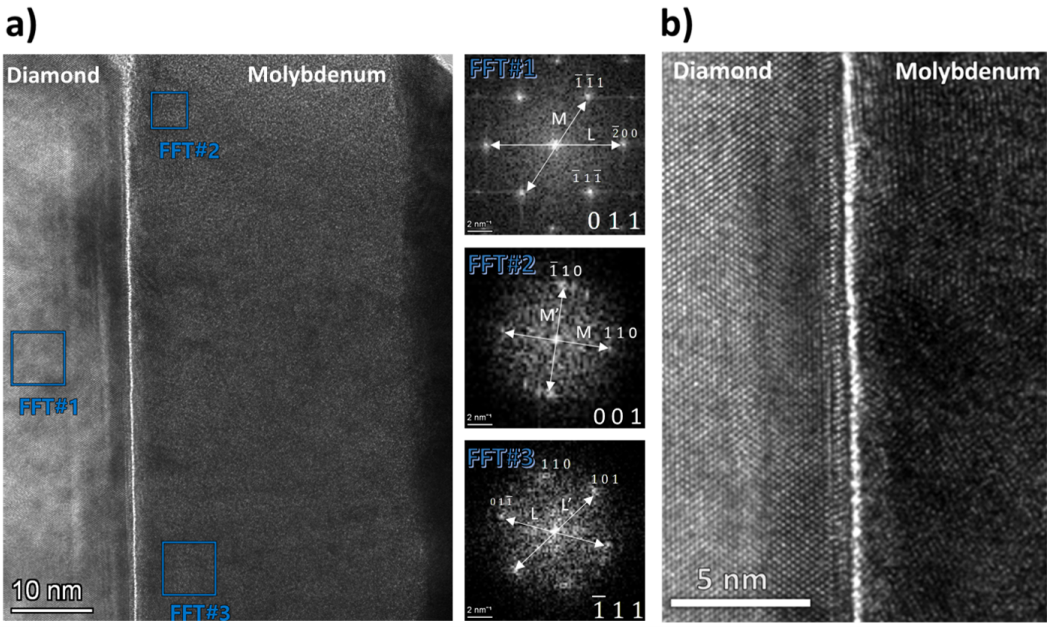

FIGURE 3.5: *a) High resolution transmission electron microscopy image of the diamond-molybdenum interface. The micrograph presented shows diamond on the left and molybdenum on the right with their associated fast Fourier transform for their phase identification. b) Zoomed-in high resolution transmission electron microscopy image of the diamond-molybdenum interface.*

In order to study the chemical composition of molybdenum itself and its interface with diamond scanning transmission electron microscopy images in the high angular annular dark field (STEM-HAADF) and electron dispersive x-rays (EDX) studies were performed on the lamella. In the figure 3.6 a), TEM, STEM-HAADF and EDX-calculated compositional images from the same region in the lamella are presented with diamond on the left followed by

the Mo/Pt/Au metal stack and the FIB deposited platinum during the lamella preparation on the right.

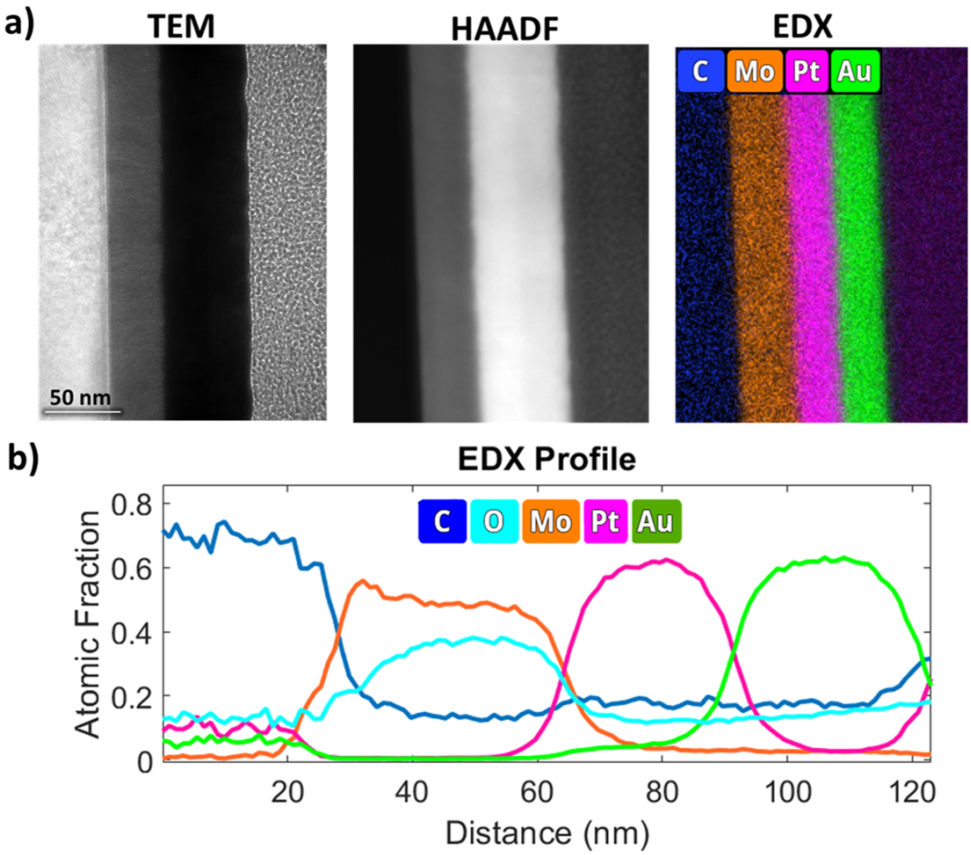

FIGURE 3.6: *a) TEM, STEM-HAADF and EDX-calculated compositional images from the same region in the lamella with diamond on the left followed by the Mo/Pt/Au metal stack and the FIB deposited platinum during the lamella preparation on the right. b) Atomic fraction profile across the stack calculated based on a Brown-Powell ionization cross section model to each EDX spectrum from the previous EDX image.*

The TEM image provide good contrast between diamond and molybdenum but platinum and gold from the contact appear darker due to their heavy and similar atomic masses. The different contrast between the platinum from the contacts and the preparation arise from the different crystallographic phase and thickness. Contrary, in the HAADF image, the signal is stronger for the heavier elements as the signal comes from the scattered electrons. Anyways, the platinum and gold layers appear unresolved again. From these two images, a stack thickness of 90 nm is deduced as expected from the fabrication target. Lastly, in the STEM-EDX image all the stack is well resolved as is it constructed from the analysis of the EDX spectrum obtained at each point. Since the EDX spectrum is characteristic for each element as it arise from X-ray emission caused by high energetic electronic transitions from deep core electrons, it provides a great tool for not only imaging the full stack but also to quantify the chemical composition. By applying a Brown-Powell ionization cross section model to each spectrum an atomic fraction profile across the stack is calculated and

presented in 3.6 b). The profile shows clearly distinguished regions for diamond carbon, molybdenum, platinum and gold. The full profile shows carbon and oxygen contamination at a level of around 15% to 20%. This is related to the FIB preparation of the lamella and its posterior exposition to air prior to the TEM study. However, it can be considered as a background when making up conclusions about the metal stack. The molybdenum in the stack is partially oxidized with a relative concentration of oxygen about 40% once the background carbon and oxygen are removed. This high value must be carefully considered as the metal was exposed to air prior to the TEM study. Surprisingly the concentration of oxygen is reduced towards diamond interface even though an oxygen termination was present in diamond prior to the contact deposition. Concerning platinum and gold, no oxidation is observed besides contamination but some interdiffusion is clearly present even if the sample LD1 was never subjected to high temperature.

- **Zirconium**

Two high resolution transmission electron microscopy (HRTEM) images of the diamond-zirconium interface are presented in the figure 3.7.

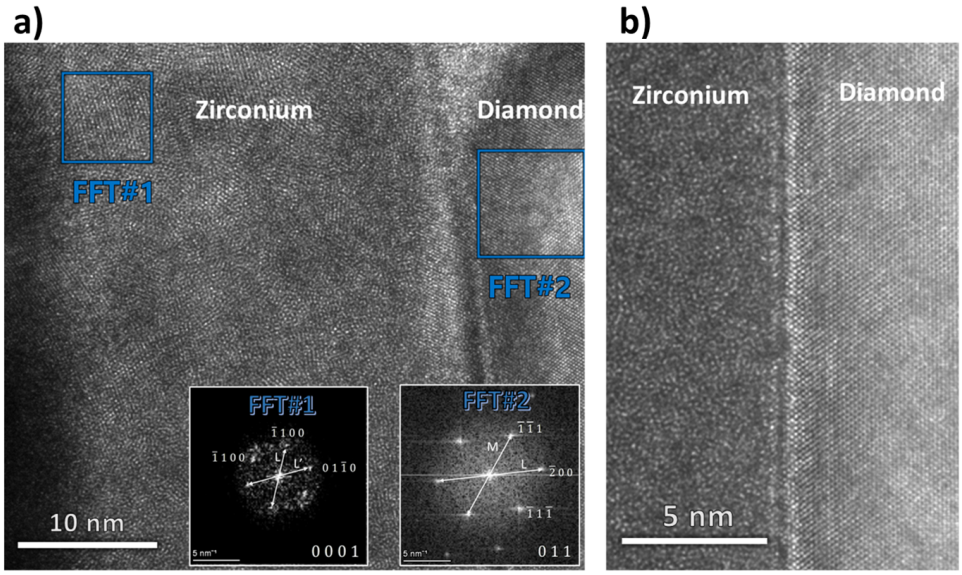

FIGURE 3.7: *a) High resolution transmission electron microscopy image of the zirconium-diamond interface. The micrograph presented shows zirconium on the left and diamond on the right, with their associated fast Fourier transform performed on the blue regions. b) Zoomed-in high resolution transmission electron microscopy image of the zirconium-diamond interface.*

The micrograph presented in the figure 3.7 a) shows diamond on the right and zirconium on the left. Fast Fourier transform (FFT) were performed on the two blue square regions in order to check the crystalline quality of diamond and zirconium. In the FFT region 2, diamond (0 1 1) pole is displayed corresponding to a fcc lattice with L/M=1.167, close to the theoretical value of 1.156. The zirconium presents a policrystalline phase with a typical grain size of about 3 nm. In the FFT performed on region 1, which is a zirconium well resolved

grain, the (0 0 0 1) pole of zirconium is observed with an L′/L= 1.01. This is compatible with the expected hexagonal close package (hcp) phase of zirconium at RT.

In the figure 3.7 b), a zoomed-in micrograph from a different region of the lamella is presented. In this image, rather than focusing on the zirconium grains in order to resolve their phases, the microscope is set to show a focused image of the interface for a more careful evaluation. Diamond in the right and zirconium in the left join in a now clearly sharp interface. In this micrograph the interface show a slight contrast at the interface through the first 3-4 diamond atomic planes. This contrast could be due to composition, i.e., oxygen placed at the interface, or diffraction at the interface. Anyways, a more profound and detailed analysis needs further experimental evaluation.

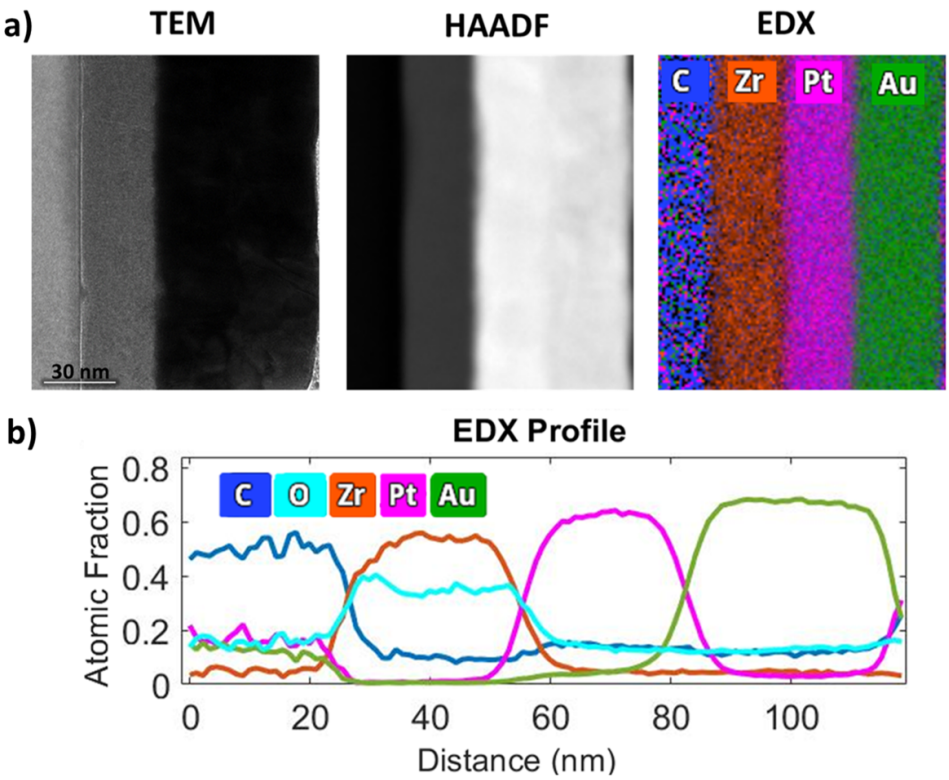

FIGURE 3.8: *a) TEM, STEM-HAADF and EDX-calculated compositional images from the same region in the lamella with diamond on the left followed by the Zr/Pt/Au metal stack. b) Atomic fraction profile across the stack calculated based on a Brown-Powell ionization cross section model to each EDX spectrum extracted from the previous EDX image.*

In order to study the chemical composition of zirconium itself and its interface with diamond scanning transmission electron microscopy images in the high angular annular dark field (STEM-HAADF) and electron dispersive x-rays (EDX) studies were performed on the lamella. In the figure 3.8 a), TEM, STEM-HAADF and EDX-calculated compositional images from the same region in the lamella are presented with diamond on the left followed by the Zr/Pt/Au metal stack. The TEM image provide good contrast between diamond and molybdenum but platinum and gold from the contact both appear darker due to their big

and similar atomic masses. Contrary, in the HAADF image, the signal is stronger for the heavier elements as the signal comes from the scattered electrons. Anyways, the platinum and gold layers appear unresolved again. From these two images, a stack thickness of 90 nm is deduced as expected from the fabrication target.

Lastly, in the STEM-EDX calculated compositional image all the stack is well resolved as is it constructed from the analysis of the EDX spectrum obtained at each point. By applying a Brown-Powell ionization cross section model to each spectrum an atomic fraction profile across the stack is calculated and presented in 3.8 b). The profile shows clearly distinguished regions for diamond carbon, zirconium, platinum and gold. The full profile shows carbon and oxygen contamination at a level of around 15% to 20%. This is related to the FIB preparation of the lamella and its posterior exposition to air prior to the TEM study. However, it can be considered as a background when making up conclusions about the metal stack. The zirconium in the stack is partially oxidized with a relative concentration of oxygen about 35% to 40% once the background carbon and oxygen is removed. This high value must be carefully considered as the metal was exposed to air prior to the TEM study. Importantly, the concentration of oxygen is higher towards diamond interface reaching up to 45% of oxygen on zirconium. This might explain the high measured value for the built-in voltage from the C-V measurements, the degradation of the I-V characteristics and the contrast from the TEM micrograph at the interface. Concerning platinum and gold, no oxidation is observed besides contamination but some interdiffusion is again clearly present.

3.4 XPS studies of the interface

TEM results provided an insight into the contacts chemical composition and microstructure. However, the FIB preparation and its posterior exposition to air made the results lest robust due to the possible modification of the contact properties. Therefore, the analysis would benefit from a comparison of the chemical composition of the contacts provided by TEM with a different technique leading to a more solid understanding of the nature of the contacts. For this purpose, an XPS depth profile have been performed in the zirconium and molybdenum contacts thanks to an Ar+ milling at low voltage (0.5V) with zalar compucentric rotation. This allow to study the metal stack composition and its interface with diamond without exposing it to air. However, the Ar+ irradiation is known to lead to carbonization of metals and thus special care must be taken to analyze the results and their comparison with TEM results.

On the other hand, XPS can also be used to measure the Schottky barrier of the contacts which provide an interesting comparison with the electric measurements. Again, using a depth profile is chosen for the Schottky barrier measurement since measuring it directly on a zirconium or molybdenum electrode would lead to their oxidation after air exposition dramatically changing their properties.

- **Molybdenum**

A molybdenum 500x500 micron contact from the sample LD1 has been sputtered using 0.5 kV Ar+ ions at 33° incidence angle with respect to the sample surface while Zalar compucentric sample rotation was performed. Sputtering was carried out in-situ in the spectrometer to alternately etch the contact until reaching its interface with the diamond layer and record an XPS spectrum each 30 seconds. By using the relative sensitive factor (RSF) provided by the manufacturer of the XPS equipment, the relation between the different elements present in the molybdenum contact stack was extracted for each of the recorded spectra. The resulting chemical profile of the molybdenum contact stack is displayed in the figure 3.9. In the chemical profile, the interfaces between the Au/Pt/Mo are well defined. In contrast with the EDX results, no interdiffusion is observed between the gold and the platinum layers. Therefore, the EDX observed interdiffusion is not such, but probably the modification of the contact during the FIB preparation by dragging platinum and gold atoms through the stack. Concerning the molybdenum, it present a constant 20% of oxygen trough the layer thus confirming the results provided by EDX. However, quantitatively a significantly big difference is observed with EDX providing a 40% oxidized layer. The difference is explained by the air exposition of the lamella before the TEM study. The XPS chemical profile is thus more reliable and accurate in this case. On the other hand, a decrease of the oxygen concentration in the molybdenum down to a 15% is observed towards its interface with diamond in the XPS chemical profile. This is surprising due to the oxygen termination of diamond prior to the contact fabrication, but it matches perfectly what was observed in the EDX profile.

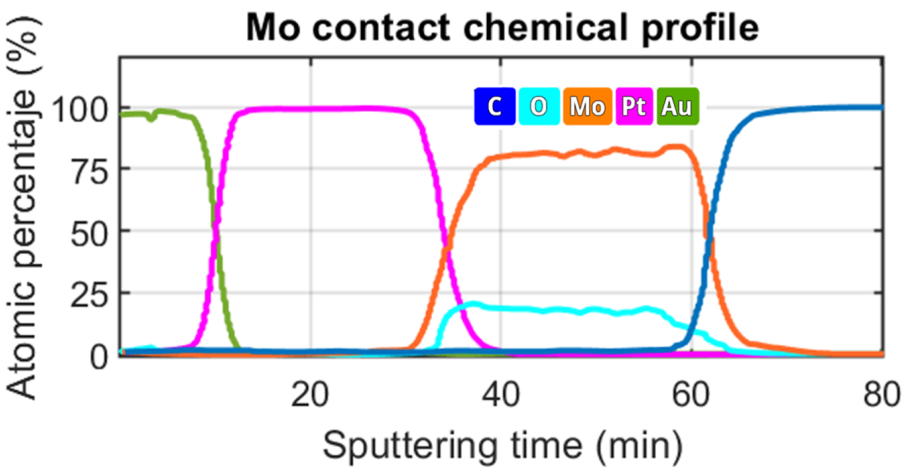

FIGURE 3.9: *Chemical profile of the Au/Pt/Mo contact on diamond extracted from spectra alternately recorded each 30 seconds while sputtering etching using 0.5 kV Ar+ ions at 33° incidence angle with respect to the sample surface with Zalar compucentric rotation is performed.*

In order to determine the Schottky barrier height by XPS, the characteristics core level spectra of diamond (C(1s)) and molybdenum (Mo(3d)) and the VB region were recorded during the sputtering inside the molybdenum layer, at its interface with diamond and at diamond after no molybdenum was left. The aforementioned XPS spectra are represented

in the figure 3.10.

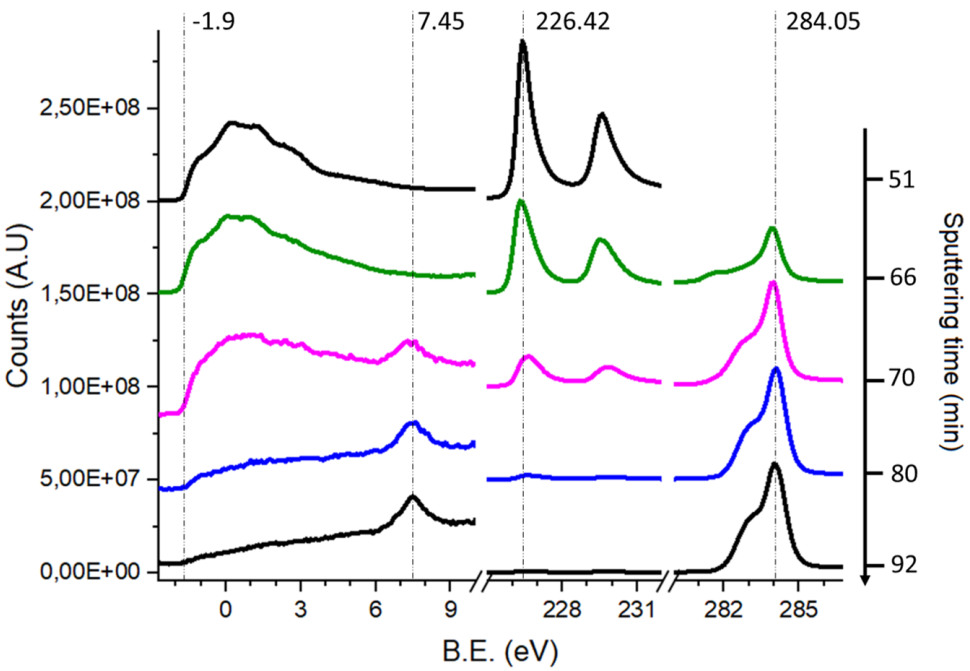

FIGURE 3.10: *Representative regions of the spectra (C(1s), Mo(3d) and VB) recorded at different sputtering times between 51 and 92 min. The molybdenum layer (51 min), its interface with diamond (66 and 70 min) and pure diamond (80 and 92 min) are distinguished. Only the position of the peaks are representative while the height of the peaks are chosen in order to ameliorate the reader comprehension of the spectra.*

On the top, after 51 min of sputtering, the VB and Mo(3d) spectra of the molybdenum at the half of the molybdenum layer are displayed. Importantly, no carbon signal was detected here and thus, the spectrum can be associated with a fully molybdenum layer. The Mo(3d) presents two well splitted peaks, as expected for metallic molybdenum, with the lower energy peak at 226.43 eV. Also, the VB shows the characteristic features of molybdenum. Closer to the interface after 66 min of sputtering, The VB, Mo(3d) and C(1s) spectra were recorded. The VB still shows the characteristics features of molybdenum with no sign from diamond VB. The Mo(3d) core level still appears at a very close energy of 226.39 eV. The C(1s) shows now a peak characteristic of diamond at 283.92 eV. However, in the C(1s) there is a contribution at lower energies of 281.71 eV typically associated with a molybdenum carbide which might have formed during the sputtering process. The carbon feature appearing only as a core level and not in the VB even if the depth sensitivity of core levels are lower due to the less energetic electrons is explained by the predominant signal of molybdenum and the significantly bigger cross section of the VB electrons of the metal. The third spectrum at 70 min, presents again the molybdenum characteristics features in the VB but this time overlapped with diamond VB with a characteristic peak at 7.45 eV related to Ar+ implantation in diamond [153]. The Mo(3d) peaks are slightly displaced toward higher energies with the lower energy peak appearing at 226.60 eV. The C(1s) contribution from

diamond still appears at 281.68 eV but the second peak is displaced toward higher energies around 282.88 eV, this peak can be related to sp^2 carbon probably related to implantation damage [154]. The fourth and fifth spectra at 80 min and 92 min are characteristics of pure diamond after Ar+ milling. The VB of Ar+ implanted diamond with the Ar+ implated peak at 7.45 eV and the VBM at -1.9 and the C(1s) with diamond characteristic peak at 284.05 eV plus the graphitized carbon peak at 282.90 eV are observed while no significant signal of molybdenum is. The calculation of the ϕ_b based on the measurements performed throughout the molybdenum layer and its interface with diamond is performed with the following formula [155]:

$$\phi_b = C(1s)_{interface} - (C(1s) - VBM)_{diamond} - Mo(3d)_{interface} - Mo(3d)_{metal} \tag{3.1}$$

Where $C(1s)_{interface}$ is the position of the C(1s) peak associated with diamond recorded at the interface, $(C(1s) - VBM)_{diamond}$ is the VBM to C(1s) associated with diamond distance recorded in pure diamond and $Mo(3d)_{interface}$ and $Mo(3d)_{metal}$ are the position of the molybdenum core levels position recorded at the interface and metal respectively.

Based on the measurements, the position of the $C(1s)_{interface}$ is 283.92 eV as deduced from the spectrum recorded at 66 min where no Ar+ implantation sign is present at the VB. The $(C(1s) - VBM)_{diamond}$ distance extracted from spectra taken at 80 min or 92 min is 285.95 eV. The molybdenum core level positions are 226.60 eV at the 66 min spectrum and 226.62 eV at the 51 min spectrum. Therefore, based on these values and applying 3.1 a ϕ_b of 2.01 eV is deduced. This value is certainly compatible with the value deduced from the I-V characteristics.

However, the $(C(1s) - VBM)_{diamond}$ distance of 285.95 eV is significantly higher than values observed in literature for H-diamond around ∼284 eV [156, 154], which should be about the same as for the O-terminated diamond. If the literature value is used, a ϕ_b value as low as 0.06 eV is deduced. The Ar+ milling might have modified the interface properties even as soon as after 66 min where no sign of implantation were detected in the VB making the ϕ_b determination not robust. Further studies based on big molecules (like C_{60}) sputtering through molybdenum contacts or XPS spectrum acquisition directly on an in-situ deposited molybdenum over oxygen-terminated diamond (to prevent the metal oxidation) could provide a good comparison to ensure the deduced value is reliable.

- **Zirconium**

Similarly to what was presented in the previous section, a zirconium contact has been sputtered using 0.5 kV Ar+ ions at 33° incidence angle with respect to the sample surface while Zalar compucentric sample rotation was performed. Sputtering was carried out in-situ in the spectrometer to alternately etch the contact until reaching its interface with the diamond layer and record an XPS spectrum each 30 seconds. By using the relative sensitive factor (RSF) provided by the manufacturer of the XPS equipment, the relation between the different elements present in the zirconium contact stack was extracted for each of the

recorded spectra. The resulting chemical profile of the zirconium contact stack is displayed in the figure 3.11. In the chemical profile, the interfaces between the Au/Pt are well defined with no interdiffusion observed between the gold and the platinum layers. Again, the EDX observed interdifussion is not such, but probably the modification of the contact during the FIB preparation. On the other hand, platinum is observed all throughout the zirconium layer. This is similar to what is observed in the EDX results but again is attributed to an specificity of the measurement technique rather that to the diffusion of platinum diffusion in the zirconium. Most probably the Ar+ sputtering must have dragged some platinum atoms inside the zirconium layer. Concerning the oxidation of zirconium, it present a constant 20% of oxygen trough the layer with a slightly higher concentrations toward its interface with diamond. However, quantitatively there is a significant difference between EDX providing a 40% oxygen in zirconium an the XPS results. The difference is explained by the air exposition of the lamella before the TEM study. The XPS chemical profile is again more reliable and accurate in this case. The consistent result of a higher concentration of oxygen at zirconium interface with diamond is a plausible explanation for the on-state degradation of the contacts presented in the section 3.2, as the ozone passivation treatment might have further oxidized its interface with diamond causing a drop in the ϕ_b and a rise in the ideality factor and built-in voltage.

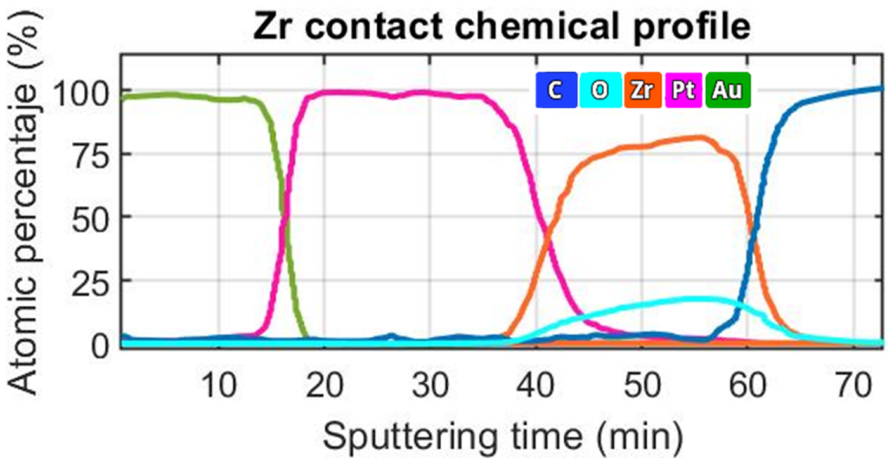

FIGURE 3.11: *Chemical profile of the Au/Pt/Zr contact on diamond extracted from spectra alternately recorded each 30 seconds while sputtering etching using 0.5 kV Ar+ ions at 33° incidence angle with respect to the sample surface with Zalar compucentric rotation is performed.*

In order to determine the Schottky barrier height by XPS, the characteristics core level spectra of diamond (C(1s)) and zirconium (Zr(3d)) and the VB region were recorded during the sputtering throughout the zirconium layer, at its interface with diamond and at diamond after no zirconium is present. The aforementioned spectra are shown in figure 3.12. On the top, after 50 and 52 min of sputtering, the VB and Zr(3d) spectra of the zirconium at approximately half the depth of the zirconium layer are presented. Importantly, no carbon signal is detected here and thus, the spectrum can be associated fully with a pure zirconium

layer. Only in the 52 min spectra, a very small contribution of the C(1s) is detected at 281.3 eV corresponding to a zirconium carbide probably formed due to the Ar+ sputtering. The Zr(3d) presents two well splitted peaks in both spectra, as expected for metallic zirconium, with the lower energy peak at 178.32 eV. Also, the VB shows the characteristic features of zirconium. Closer to the interface after 58 min of sputtering, The VB, Zr(3d) and C(1s) spectra were recorded. The VB still shows the characteristics features of zirconium with no sign from diamond VB. The Zr(3d) core level still appears at a very close energy of 178.08 eV. The C(1s) shows now a peak characteristic of diamond at 284.22 eV. However, in the C(1s) there are at least two contributions at lower energies at 280.70 eV and 283.4 eV probably associated with a zirconium carbide and a sp^2 carbon respectively. The carbon feature appearing only as a core level and not in the VB even if the depth sensitivity of core levels are lower due to the less energetic electrons is explained by the predominant signal of zirconium and the significantly bigger cross section of the VB electrons of the metal. The fourth spectrum at 88 min, presents the characteristics features of pure diamond after Ar+ milling. The VB of Ar+ implanted diamond with the Ar+ implanted peak at 7.32 eV and the VBM at -1.9 and the C(1s) with diamond characteristic peak at 283.94 eV plus the graphitized carbon peak at 282.89 eV are observed while no significant signal of zirconium is present.

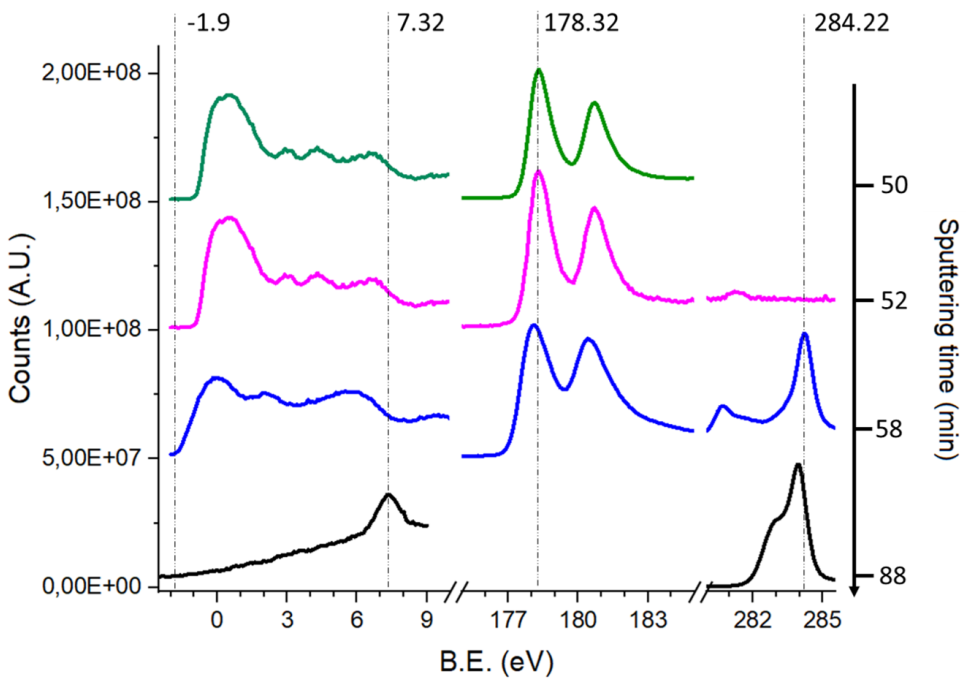

FIGURE 3.12: *Representative regions of the spectra (C(1s), Zr(3d) and VB) recorded at different sputtering times between 50 and 88 min. The zirconium layer (50 and 52 min), its interface with diamond (58 min) and pure diamond (88 min) are distinguished. Only the position of the peaks are representative while the height of the peaks are chosen in order to ameliorate the reader comprehension of the spectra.*

The calculation of the ϕ_b based on the measurements performed throughout the zirconium layer and its interface with diamond is performed based on the same formula introduced earlier 3.1 adapted to zirconium:

$$\phi_b = C(1s)_{interface} - (C(1s) - VBM)_{diamond} - Zr(3d)_{interface} - Zr(3d)_{metal} \tag{3.2}$$

Based on the measurements, the position of the $C(1s)_{interface}$ is 284.22 eV as deduced from the spectrum recorded at 58 min where no Ar+ implantation sign is present at the VB. The $(C(1s) - VBM)_{diamond}$ distance extracted from spectra taken at 88 min is 285.84 eV. The zirconium core level positions are 178.32 eV at the 50 min spectrum and 178.08 eV at the 58 min spectrum. Therefore, based on these values and applying 3.1 a ϕ_b of 1.86 eV is deduced. This value is significantly higher than the value deduced from the I-V characteristics.

However, the $(C(1s) - VBM)_{diamond}$ distance of 285.84 eV is significantly higher than values observed in literature around ∼284 eV [156, 154], which should be about the same as for the O-terminated diamond. If the literature value is used, a ϕ_b value as low as 0.02 eV is deduced. The Ar+ milling might have modified the interface properties even as soon as after 58 min where no sign of implantation were detected in the VB making the ϕ_b determination not robust. As proposed for molybdenum contacts, further studies based on big molecules (like C_{60}) sputtering through molybdenum contacts or XPS spectrum acquisition directly on an in-situ deposited zirconium over oxygen-terminated diamond (to prevent the metal oxidation) could provide a good comparison to ensure the deduced value is reliable.

3.5 Kelvin probe studies

The precedent studies based on TEM and XPS gave an insight on the microstructure and chemical composition of the contacts, focused in the metal-diamond interface, which can be used to explain and understand their electrical characteristics. However, a fundamental part of the contacts that can be a major factor governing leakage currents is their edges. On the section 3.2, the use of an additional ozone passivation treatment was demonstrated to reduce leakage currents. This fact is probably associated with parasitic leakage currents following a path not only through the metal-diamond interface but mediated through the diamond surface at the edge of the contact where the Schottky barrier might be lower locally.

In order to study the lateral potential distribution of the Schottky contacts, Kelvin probe force microscopy (KPFM) was performed on the edge of the zirconium and molybdenum contacts. In this technique, the position of the Fermi level versus the vacuum level is mapped at the nanoscale level thanks to a nanometric probe. When the probe contacts the material, the Fermi levels of both align and the contact potential difference (CPD) can be measured. The CPD is related to the Fermi level of the material as it is the difference in work functions between the probe and the material. If the work function of the probe is known, the work function of the material can be mapped with accuracy. Furthermore, by

applying KPFM on the lateral space charge region of a contact, the potential energy distribution of the depletion region of a Schottky contact can be mapped. This is illustrated in figure 3.13.

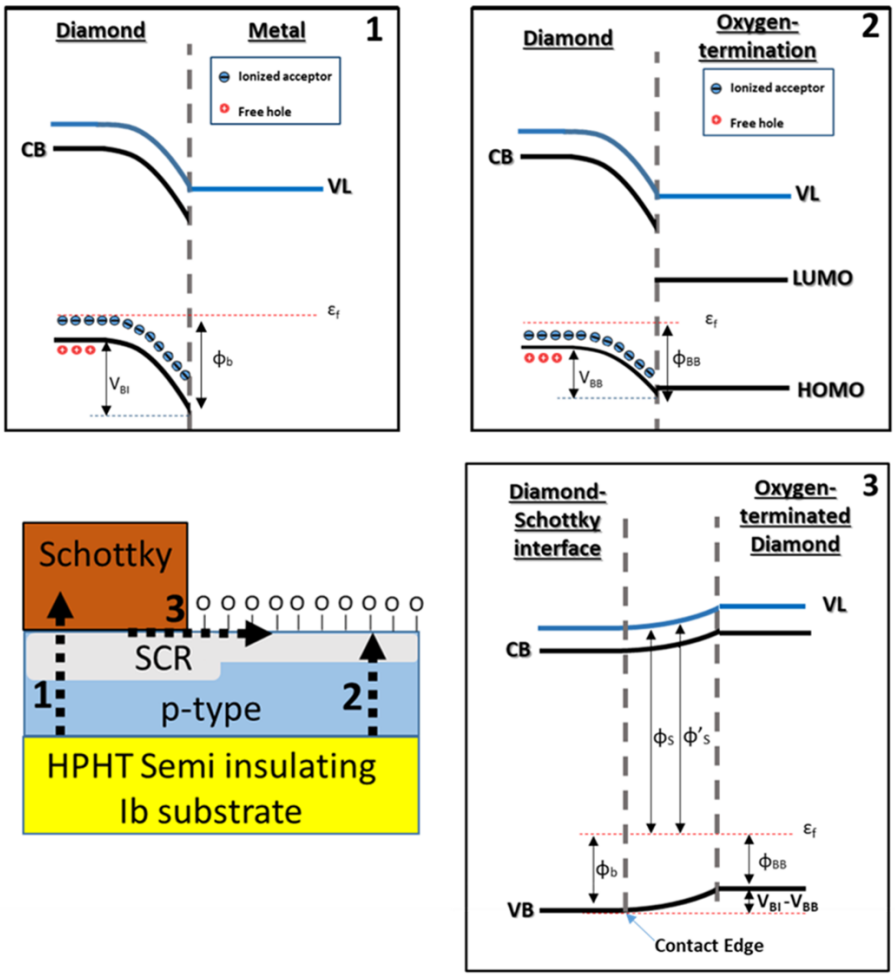

FIGURE 3.13: *Band scheme of three different profiles in a Schottky contact. 1) The vertical band scheme of a diamond-metal junction. 2) The vertical band scheme of diamond and its oxygen-terminated surface. 3) The lateral band scheme along diamond-metal interface up to its oxygen-terminated surface. In this band scheme, the diamond bands are bent from their position at the interface of the Schottky contact to the position at the oxygen-terminated surface. As this band bending happens laterally over the interface-surface, the work function of diamond depends on the lateral distance, enabling to observe the lateral depletion region of the contact by KPFM.*

In the figure 3.13, three different potential profiles are schemed. The first is the classical scheme of a Schottky barrier extensively explained in the section 2.1. The second is the potential energy distribution in diamond and its O-terminated surface, where the surface density of states pin the Fermi level causing a downward band bending V_{BB} and giving rise to a positive electron affinity. The third is an scheme of the lateral potential energy distribution along the Schottky metal-diamond interface and diamond oxygen-terminated

surface. On the interface, the diamond VB is located at a Schottky barrier height ϕ_b distance with respect to the Fermi level. This is, the position of the VB is determined by the V_{BI} plus the distance of the VB to the Fermi level in diamond bulk ϕ_f. At the diamond oxygen-terminated surface, the diamond VB is located at a distance ϕ_{BB}, i.e., the V_{BB} produced by the oxygen termination plus the distance of the VB to the Fermi level in diamond bulk ϕ_f. Between these two configurations, at the edge of the contact, the bands will bend from the former to the latter scenario. As the Fermi level remains constant through this band bending, the work function will vary when passing from one to the other configuration. This fact is interesting because using KPFM the work function variation can be measured and thus the lateral depletion region can be observed.

- **Molybdenum**

In the figure 3.14 a), the atomic force microscopy image of a molybdenum Schottky contact with diamond in the left and the Mo/Pt/Au contact stack in the right is presented.

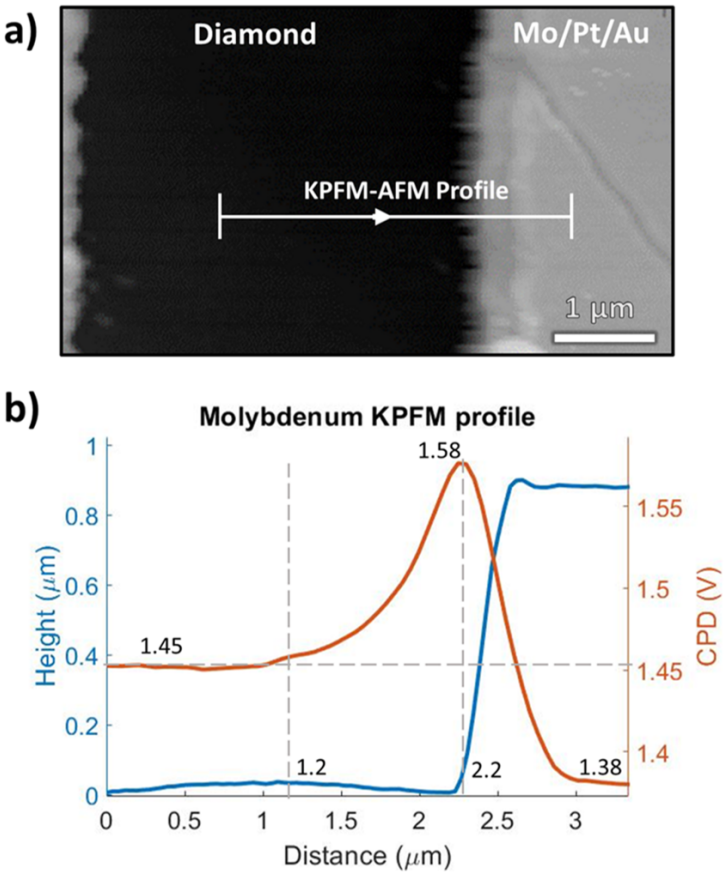

FIGURE 3.14: *a) Atomic force microscopy image of a molybdenum Schottky contact with diamond in the left and the Mo/Pt/Au contact stack in the right. b) The KPFM (red) and AFM (blue) profiles along the diamond surface and the Mo/Pt/Au contacts in the region specified in the figure a).*

The figure 3.14 b), presents the KPFM (red) and AFM (blue) profiles along the diamond surface and the Mo/Pt/Au contact in the region specified in the figure 3.14 a). The AFM

profile shows a contact thickness of 90 nm in agreement with the XPS and TEM results. On the other hand, the KPFM profile shows three very distinct features. On the left, the oxygen-terminated diamond shows a constant CPD level at 1.45 V from 0 to 1.2 microns. From there, a rise of the CPD is observed up to 1.58 V at 2.2 microns. This rise is associated with the lateral potential distribution of the depletion region caused by the molybdenum Schottky contact. Beyond, the CPD decreases down to a value of 1.38 V on the top gold layer of the Mo/Pt/Au stack.

On one hand, the difference of CPD between the gold layer and the oxygen-terminated diamond out of the molybdenum Schottky depletion layer is 0.07 V. Considering a value for the air exposed gold work function of 4.62 eV [157], a work function for the p-type oxygen-terminated diamond of 4.69 eV is deduced. Taking the value of 1.7 eV for the electron affinity measured on p-type oxygen-terminated diamond [72], a distance between the Fermi level and the VB at the surface of $\phi_{BB} = 2.46$ eV is deduced by applying $\phi_{BB} = E_g + X - \phi_s$. The Fermi level to VB distance at the bulk for the $N_A - N_D$ value deduced for this sample is $\phi_f = 0.3eV$. Therefore, a band bending of $V_{BB} = 2.16$ with a depletion width of 287 nm for the doping level of this sample is deduced. This is the first value of the V_{BB} of the (100) oxygen-terminated p-type diamond ever reported to the author knowledge.

On the other hand, the built-in potential of the Schottky contact can be estimated from the maximum value of the CPD at the edge of the contact. A value for the built-in voltage of $V_{BI} = 2.03eV$ and a value for the Schottky barrier height of $\phi_b = 2.33eV$ are deduced with a direct comparison with the oxygen-terminated diamond. This result is surprising since it means that the oxygen termination potential depleting holes is higher than that of the molybdenum Schottky contact. Since the edge of the contact is known to be a major factor governing leakage currents, this result shows that the ozone passivation treatment can effectively suppress leakage currents by neglecting the possibility of surface related leakage currents. Also, the discrepancies between the value deduced for the V_{BI} in the C-V measurements and the present measurements could be explained by the fundamental vertical vs lateral nature of each of them. Although ideally their values should be the same, a higher oxidation of the metal in its edges could definitively affect to the value measured by KPFM. Furthermore, the lateral depletion caused by the Schottky contact relaxes over 1 micron up to getting to the constant value of the oxygen-terminated diamond. This value is extremely large for the doping level and built-in voltage deduced where a depletion of about 280 nm should ideally be expected. Possibly, the longer distance over which the depletion from the Schottky relaxes is related to the superposition of the built-in potential of the Schottky with the band bending produced in the oxygen-terminated diamond surface.

- **Zirconium**

In the figure 3.15 a), the atomic force microscopy image of a zirconium Schottky contact with diamond in the left and the Zr/Pt/Au contact stack in the right is presented. The figure 3.15 b), presents the KPFM (red) and AFM (blue) profiles along the diamond surface and the Zr/Pt/Au contact in the region specified in the figure 3.15 a). The AFM profile

shows a contact thickness of 90 nm in agreement with the XPS and TEM results. On the other hand, the KPFM profile shows three very distinct features. On the left, the oxygen-terminated diamond shows a constant CPD level at 1.41 V from 0 to 2 microns. From there, a decrease of the CPD is observed down to 0.61 V at 2.6 microns. This decrease is related to the lateral potential distribution of the depletion region caused by the zirconium Schottky contact. Beyond, the CPD decreases down to a value of 1.35 V on the top gold layer of the Zr/Pt/Au stack.

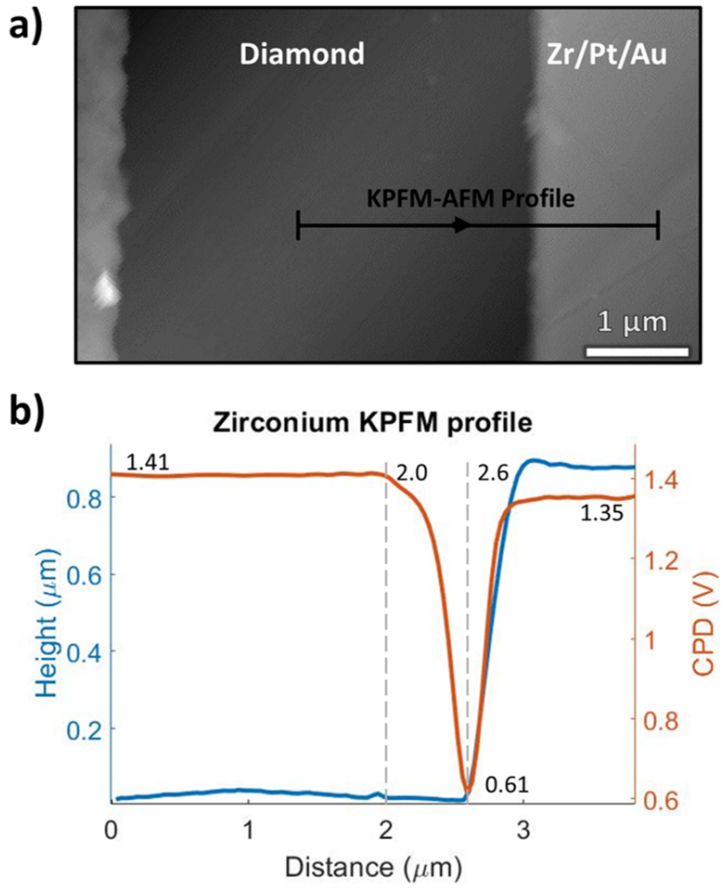

FIGURE 3.15: *a) Atomic force microscopy image of a zirconium Schottky contact with diamond in the left and the Zr/Pt/Au contact stack in the right. b) The KPFM (red) and AFM (blue) profiles along the diamond surface and the Zr/Pt/Au contacts in the region specified in the figure a).*

On one hand, the difference of CPD between the gold layer and the oxygen-terminated diamond out of the zirconium Schottky depletion layer is 0.06 V, very close to what was observed in the molybdenum contact. Considering again a value for the air exposed gold work function of 4.62 eV [157], a work function for the p-type oxygen-terminated diamond of 4.68 eV is deduced. A distance between the Fermi level and VB at the interface of $\phi_{BB} =$ 2.47 eV is thus extracted in great agreement with what was deduced for the molybdenum contact KPFM measurement.

On the other hand, from the minimum value of the CPD at the edge of the contact, the

built-in potential of the Schottky contact can be estimated. A value for the built-in voltage of $V_{BI} = 2.96eV$ is deduced with a direct comparison with the oxygen-terminated diamond surface. This value is not far away from what is deduced from the C-V measurements in contrast to what was observed in the molybdenum contact. Such a high value of the V_{BI} necessary must be related to the formation of an oxidized layer at the zirconium-diamond interface in which a significant value of fixed charges are located. This last statement is supported by TEM and XPS extracted chemical profile, as an increase of the oxygen concentration in the zirconium layer is observed toward the interface. For zirconium, in contrast with molybdenum, the V_{BI} of the Schottky is higher than the V_{BB} of the oxygen-terminated diamond. This could establish a major difference in terms of surface related leakage currents for which zirconium could be more prone, since the potential distribution around the Schottky contact would not block the leakage through the edges of the contact. In fact, earlier leakage-related breakdown phenomena were measured consistently for zirconium diodes than for molybdenum diodes in the sample VD1 presented in the following chapter 4.

Furthermore, the lateral depletion caused by the Schottky contact relaxes over 600 nm up to getting to the constant value of the oxygen-terminated diamond. This value is again larger than the expected value of about 330 nm and is again attributed to the superposition of the built-in potential of the Schottky contact with that of the oxygen-terminated diamond.

3.6 DFT simulation of the interface

The previous sections were dedicated to the experimental investigation of the molybdenum and zirconium Schottky contacts. These results allowed to establish a correlations between the chemical composition of the contacts and their electrical performance. Furthermore, the degradation of the zirconium contacts was explained as a result of the high concentration of oxide in the interface affecting the on-state characteristics. Lastly, the potential profiles along the contacts edge showed the great passivation capabilities of the oxygen-terminated diamond and its possible role in the leakage currents through the edge of the contacts in zirconium.

In this section, an AB initio study of (100) oxygen-terminated diamond and molybdenum Schottky contacts follows, in other to complement the experimental results with detailed calculations. The zirconium interface was no longer investigated as the chosen candidate to fabricate HV Schottky diodes in this work is molybdenum due to the better demonstrated properties than zirconium. Moreover, a clear picture of zirconium degradation was shown and is no longer interesting comparing the experimental results with theoretical calculations.

Concerning the oxygen-terminated surface, some previous studies have shown its possible stable structures and electronic behaviour [68, 73]. Anyways, as a part of the molybdenum oxygen-terminated diamond interface construction, these calculations are reproduced in this work and compared to those of literature. The molybdenum interface with diamond

is then studied providing an insight on its bonding type and configuration and the potential profile that allows to calculate the theoretical Schottky barrier.

The AB initio calculations were performed within the framework of the density functional theory (DFT) with projected augmented wave (PAW) fully-relativistic (taking into account the spin-orbit interaction) ultrasoft pseudopotentials determined with Bessel functions used as the basis. The exchange–correlation interaction was taken into account within a Perdew-Zunger local density approximation (LDA). The electron wave functions were expanded in terms of plane waves with the energy up to 48 Ry and the Kinetic energy cut-off for charge density and potential was set to 450 Ry. In the self consistent calculations, the level of convergence of the total energy was specified at 10^{-8} Ry. Integrating over the Brillouin zone was conducted by Monkhorst–Pack's method of special points. All computations were performed with the use of the QuantumEspresso software [158, 159, 160].

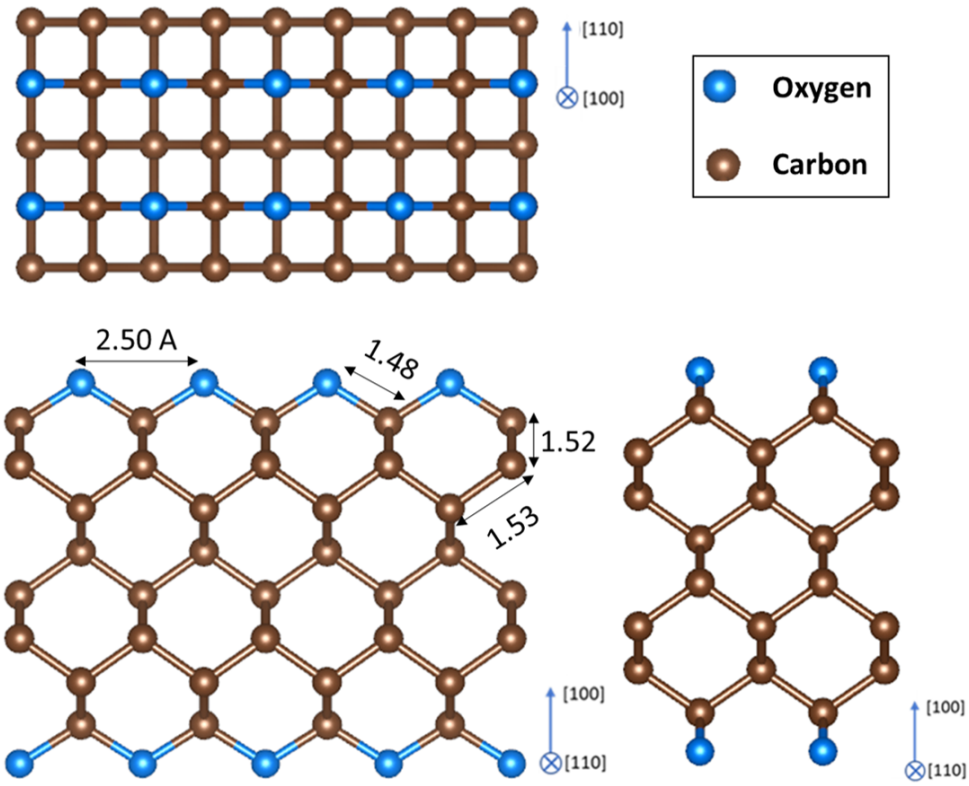

FIGURE 3.16: *(100) O-terminated diamond relaxed slab based on ketone 1x1 reconstruction. The highlighted distances between the atoms are in 3D (not projected) and are displayed in angstrom.*

3.6.1 (100) O-terminated diamond

The process followed to build the O-terminated diamond surface was the following. First, diamond unit cell was constructed using the experimental lattice constant (3.567 angstrom). This cell was relaxed in order to obtain the minimum stress as possible. A lattice constant of 3.534 angstroms was found. The density of states as well as the mean potential were

extracted for the optimized diamond unit cell. A distance from VBM to the bulk mean potential of 26.06 eV was calculated. After this, the diamond unit cell was replicated 2 times in the y direction, 4 in the x direction and 6 in the z direction in order to obtain a slab. In this slab, oxygen atoms were added following a 1x1 reconstruction pattern on both surfaces of the slab. The constructed cell was then further elongated in the z-direction in order to add 40 angstroms of vacuum between slab and slab in the calculation in order to neglect slab to slab interactions. The constructed structure was then relaxed leaving the cell intact and allowing the oxygen and their adjacent two carbon layers to move toward their equilibrium positions following a Broyden–Fletcher–Goldfarb–Shanno (BFGS) quasi-newton algorithm. The relaxation was stopped once a minimum force of $<10^{-4}$ Ry/Bohr was reached. The optimized structure and their distances are shown in the figure 3.16. The result is consistent with an ether bonding pattern of the oxygen in diamond surface and their distances are in extremely well agreement with literature results [73].

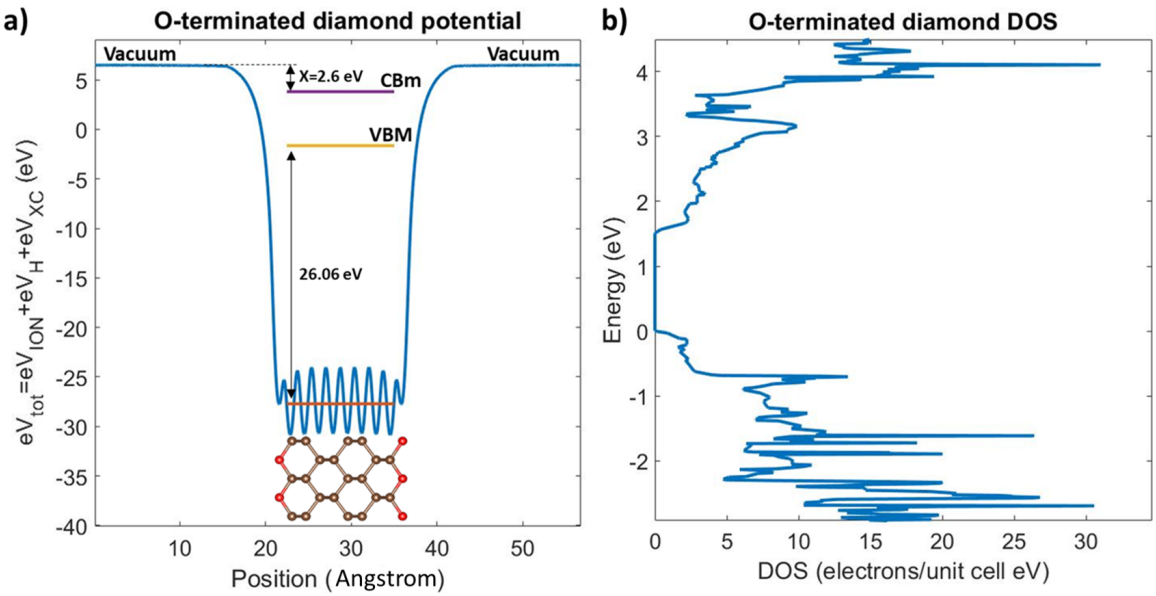

FIGURE 3.17: *a) 2D (x-y plane) averaged potential energy distribution along the (100) O-terminated diamond slab. b) Density of states in the vicinity of the band-gap region calculated for the (100) O-terminated diamond slab.*

Having optimized the structure, a self consistent calculation with a k-mesh of 6x10x1 and a non-self consistent calculation with k-mesh of 9x15x1 were performed. The former calculation was used to derive the slab potential. By using the mean value of the potential inside diamond slab, which is constant and can be used as a reference, a value for the bulk diamond VBM to mean potential calculated in the diamond unit cell of 26.06 eV was applied in order to locate the VBM position within the potential in figure 3.17 a). By the comparison of the CBM (VBM plus experimental gap) and the vacuum level, an electron affinity value of 2.6 eV is deduced. This is in very good agreement with previous calculation further confirming the robustness of our approach [68]. Moreover, the Fermi level calculated in the non self consistent calculation was set in the figure as the origin of energy. An E_f to VBM

distance of ϕ_{BB}=1.65 eV was deduced. This means that for a $N_A - N_D = 1.6 \cdot 10^{16}\ cm^{-3}$ where the Fermi level is at 0.3 eV above the VBM, a V_{BB} of 1.35 eV is deduced. This is a rather lower value compared to the one deduced by KPFM and it might be a result of the complex composition of the O-terminated surface where ketone and hydroxile groups may be as well present. Also, adsorbed molecules on this surface might play a role by adding additional levels in the vicinity of the band-gap that can exchange charges with diamond VB increasing this potential in a similar fashion of what has been demonstrated for H-diamond.

Lastly, from the non self consistent calculation, the oxygen-terminated diamond density of states (DOS) in the vicinity of the VB were extracted. The oxygen-terminated diamond calculated DOS are represented in figure 3.17 b). The results shows a surface band-gap of 1.52 eV, considerably reducing the calculated bulk diamond band-gap of 4.15 eV at the surface. Anyways, the presence of a band-gap in this surface confirms the good capabilities from the oxygen termination of diamond as a passivation layer.

3.6.2 (100) molybdenum - (100) O-terminated diamond interface

Once the oxygen-terminated diamond surface has successfully been simulated, the construction with its interface with molybdenum follows. First, the molybdenum unit cell based on the bcc structure, as deduced from the TEM results, and its experimental lattice parameter were relaxed in order to obtain the minimum stress. A lattice parameter of 3.12 angstroms was found, very close to the experimental lattice parameter of 3.15 angstroms. Self consistent and non self consistent calculations with a k-point mesh of 20x20x20 where performed in order to extract the molybdenum bands scheme and density of states in order to compare with experimental and theoretical calculations. The results, not shown here for their lack of interest, reproduced with good accuracy the expected molybdenum bands and density of states. After, a molybdenum slab with 12 layers was constructed expanding the relaxed molybdenum cell in the (100) z-direction. A 30 angstroms vacuum was also inserted between slabs in order to prevent slab-slab interactions. In this molybdenum slab, a self consistent calculation with 16x16x1 k-mesh was performed in order to calculate the averaged potential distribution and thus deduce the work function. A value of ϕ_m=3.7 eV was extracted from the calculations, similar to values found in literature [161].

Then the assembly of the interface follows. It starts by choosing a number of integers of the molybdenum unit cell so that it matches in the x-y plane that of the oxygen-terminated diamond within a reasonable value. In the present study, a 4x4x3 expansion of the (100)-oriented molybdenum cell was used to fit (100)-oriented diamond oxygen-terminated based on the structure developed in last subsection with a cell expansion of diamond of 5x5x4. The (110) pole of diamond was aligned with the (100) pole of molybdenum in agreement with the TEM results. The mismatch between the 4x4x3 (100) molybdenum supercell and the (100) O-terminated diamond supercell based on a 5x5x4 expansion of the diamond cell in the x and y directions is only about 0.14%. The distance of the molybdenum slab with respect to diamond was chosen to be 2 angstroms, were no bonds are formed according to their respective electron shell sizes. In order to prevent slab-slab interactions, a distance for the

vacuum between slab and slab of >35 angstroms was added. The structure was then relaxed over the z-coordinate letting the two layers of molybdenum atoms closer to the interface, the oxygen atoms and the closer layer to the interface of carbon atoms to relax within the BFGS quasi-newton algorithm. The structure was considered relaxed when a force lower than <0.01 Ry/Bohr was achieved. The relaxed structure is presented in the figure 3.18. With the optimized cell, a self consistent calculation with a k-mesh of 6x6x1 was performed.

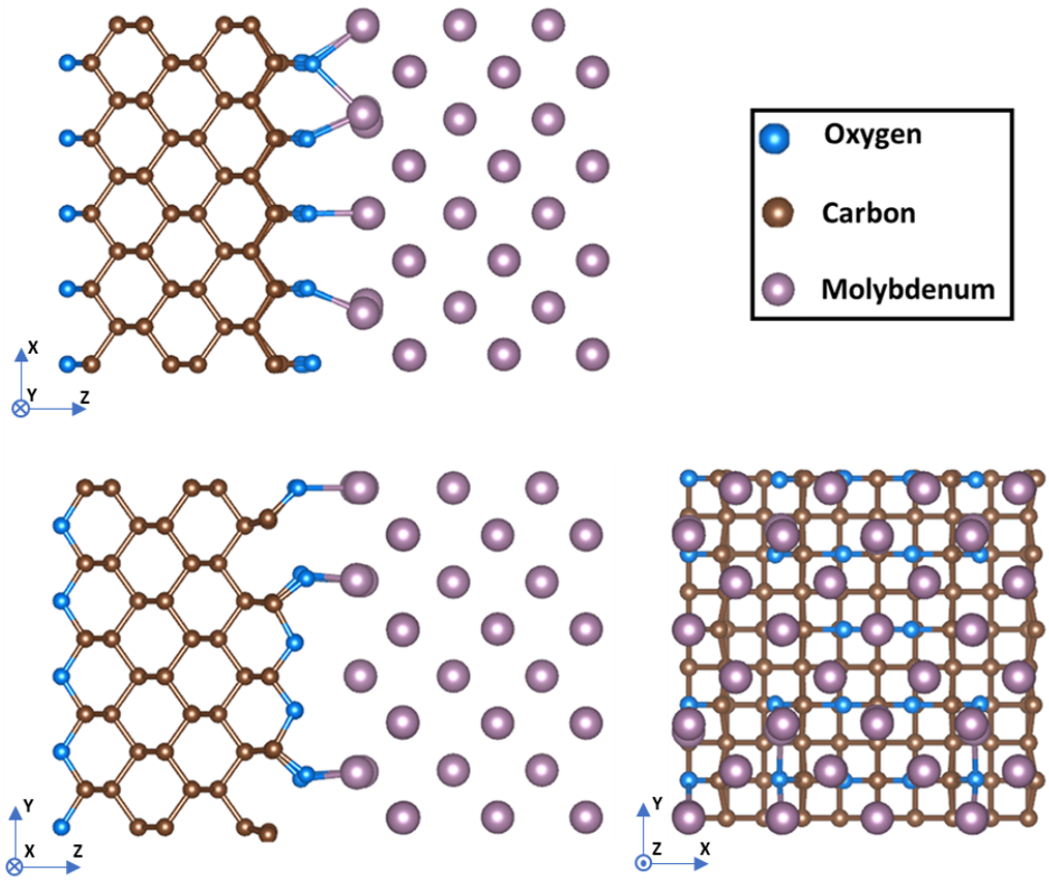

FIGURE 3.18: *Relaxed slab of (100) molybdenum interface with (100) O-terminated diamond. The full slab is composed of 346 atoms.*

In the figure 3.19, the electron localization function derived from the latter calculation is presented projected on the y-z and x-z planes of the unit cell. The electron localization function is represented in RGB, i.e., high probability of finding an electron is represented in red, blue means low probability and between them there is green. On top, the molybdenum three layers closer to the interface can be observed. The molybdenum atoms are surrounded from a delocalized electron cloud characteristic from the metallic bonding type in this compound. On the bottom, the carbon four layers closer to the interface can be observed. The electron localization function in this region shows great probability of finding electrons where the strong directional bonds of diamond are located, while is very low everywhere else, indicating a covalent bonding character as expected for diamond. The most interesting part from this plot is the interface, where the oxygen atoms from diamond surface termination

meet molybdenum. The ether configuration of the oxygen in diamond (100) surface is broken for two out of every five oxygen atoms. These oxygen atoms are pushed toward the molybdenum interfacial atoms remaining only bonded to one carbon with a covalent bond, while they now present an ionic-like bonding with the molybdenum interfacial atoms. The ionic-like character of this bonding can be deduced from the oriented electron halos from the more electronegative oxygen pointing toward the molybdenum atoms at the inteface, while the latter, being electropositive, show low probability regions pointing toward the oxygen atoms.

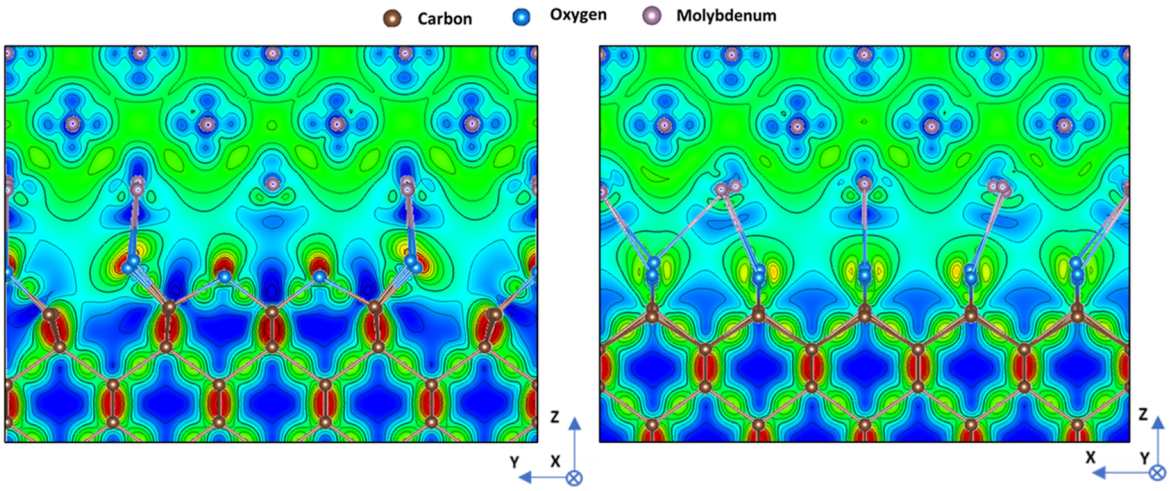

FIGURE 3.19: *Electron localization function calculated for the interface of (100) molybdenum and (100) oxygen-terminated diamond projected along the x-direction on the y-z plane of the unit cell in the left and along the y-direction on the x-z plane of the unit cell in the right. The red colors in the graph show high probability electron regions, while the blue colors show low probability regions.*

The self consistent calculation was also used to derive the potential across the slab. The 2D (x-y plane) averaged potential from the slab is presented in the figure 3.20. A dipole correction was used during the scf calculation in order to cancel the dipole present in the structure assuring a flat vacuum potential. On the left, the diamond potential is found to be constant inside the slab. Closer to the interface, the last carbon layer shows a shallower potential well as expected from its bond with oxygen and the latter presents a pronounced less profound well similar to what was observed in the figure 3.17. From there, a great peak is found at the interface of the oxygen-terminated diamond and molybdenum followed by the potential inside the molybdenum layers. By using the mean value of the potential inside diamond slab, which is constant and can be used as a reference, the previous value for the distance from the VBM to mean potential calculated in the diamond unit cell was applied in order to locate the VBM position within the 2D averaged potential over the slab. The diamond VBM distance to the Fermi level (set as the energy origin in the figure 3.17) is indeed the Schottky barrier ϕ_b. A value of 2.44 eV is deduced from this calculation. Similarly, the Schottky barrier height can be calculated following the formula:

$$\phi_b = X + E_g - \Delta E - \phi_m \tag{3.3}$$

Where X is the electron affinity of the oxygen-terminated diamond, E_g is diamond band-gap, ΔE is the shift between the vacuum levels in the slab and ϕ_m is the molybdenum work function.

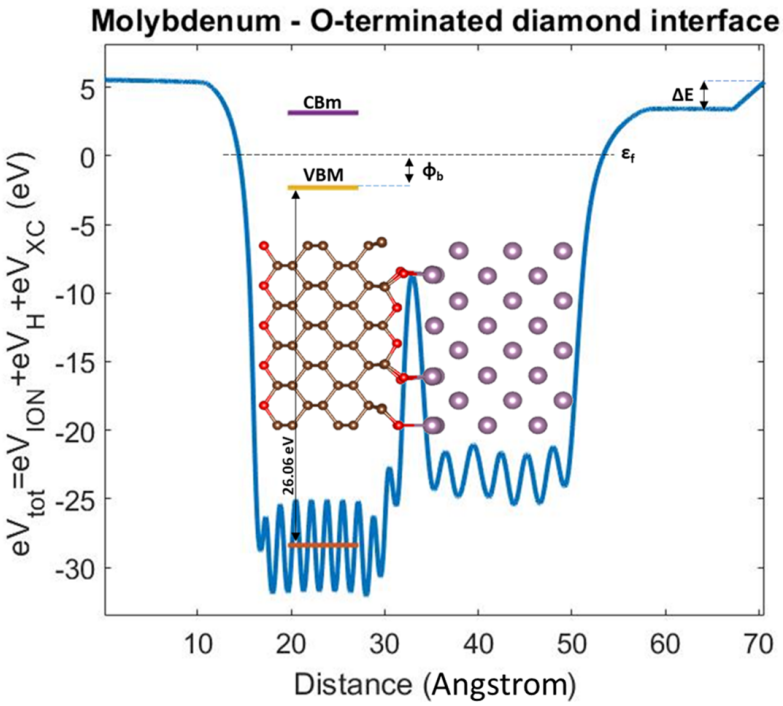

FIGURE 3.20: *2D (x-y plane) averaged potential energy distribution calculated on relaxed slab of the interface of (100) molybdenum and (100) oxygen-terminated diamond.*

Using the values for the previous calculations of X=2.6 eV, ΔE=1.94 eV, ϕ_m=3.7 eV and the experimental band-gap of diamond 5.5 eV a value for ϕ_b of 2.46 eV is deduced in great agreement with the previous calculated value. The deduced value for the ϕ_b is higher than the value deduced for the I-V measurements. This difference can arise from the policrystalline character of the molybdenum layer. In fact, the (100) molybdenum surface displays the lowest work function of all of its surfaces giving rise to a higher ϕ_b. If the real contact is composed between differently oriented grains as deduced by TEM, one should expect local variations of the barrier and thus a lower barrier deduced from I-V measurements. On the other hand, the ϕ_b value deduced from KPFM coincides with great accuracy with the value from the present calculation. The value deduced from KPFM is local, as it arises from the contact between the tip and the material, but in a hundreds of nanometers scale. The great agreement might indicate that at this scale and next to the contact edge, the predominant orientation of the molybdenum grains with respect to diamond is the (100). Lastly, the C-V measurements value of the ϕ_b deduced is higher than the value from the presented calculation. The C-V deduced ϕ_b is a non-local value and its origin is the predominant ϕ_b in area

under the contact. As explained before, the high value was attributed to the charged traps at the interface due to the oxidation of the metal observed by XPS and TEM. However, the calculation did not account for the metal oxidation explaining thus the difference between the theoretical and experimental approaches.

3.7 Conclusion

In this chapter, a dedicated experimental investigation of the molybdenum and zirconium Schottky contacts was presented. The TEM and XPS results allowed to establish a correlation between the chemical composition of the contacts and their electrical performance. The ozone passivation, demonstrated to be crucial in reducing leakage currents, was shown to oxidize the molybdenum and zirconium layers. While this did not greatly affect the molybdenum on-state characteristics, the degradation of the zirconium contacts was explained as a result of the high concentration of oxygen in the interface. On the other hand, the potential profiles along the contacts edges extracted from KPFM proved the great passivation capabilities of the oxygen-terminated diamond. These measurement yielded a $\phi_{BB} = 2.46$ for the (100) oxygen-terminated p-type diamond. This is the first ever reported value and it will contribute to the design and comprehension of Schottky diodes and bulk conducting transistors where oxygen termination is fundamental. The KPFM measurements also allowed the estimation of the molybdenum and zirconium Schottky barriers and built-in potentials. While the molybdenum V_{BI} was shown to be lower than the oxygen-terminated V_{BB}, the opposite situation was found for zirconium. This might play an important role in governing leakage currents through the edge of the contacts and a plausible explanation for the better off-state characteristics of molybdenum than zirconium (which is further studied in the following chapter 4) was offered based on these measurements. Lastly, AB initio calculations to investigate both the oxygen-terminated surface of diamond and its interface with molybdenum were performed. The theoretical calculation presented qualitative agreement with the experimental KPFM results yielding a Schottky barrier height for molybdenum of ϕ_b=2.45 eV. Also, the bonding pattern between molybdenum and oxygen-terminated diamond was revealed to consist of an ionic-like oxygen-molybdenum bonding.

Chapter 4

Vertical Schottky diodes: interface solutions and HV implementation

---

This chapter is dedicated to the fabrication and characterization of vertical Schottky diodes. A first sample (VD1) is used to find successful metal-diamond Schottky contacts in terms of barrier, leakage and thermal stability. Two candidates are evaluated in the first sample: zirconium and molybdenum. Applying the knowledge developed from these studies in the first sample, a second sample (VD2) with a specific design for high voltage (>1.1 kV) applications has successfully been fabricated and characterized.

4.1 VD1 & VD2 samples fabrication process

In this chapter, two different diamond Schottky diodes samples (VD1 and VD2) with pseudo-vertical encapsulated architecture are designed, fabricated and characterized. This architecture was preferred over the classical pseudo-vertical one as the latter is constrained by the etching depth and can eventually suffer from surface modifications during the etching process. On the other hand, the encapsulated design is only limited by epitaxy. However, the pseudo-vertical encapsulated architecture is a newer structure in which the growth parameters still need to be optimized. The fabrication process of the samples VD1 and VD2 have multiple points in common but will differ at the drift layer epitaxy. The samples have been fabricated based on New Diamond Technologies (NDT) IIa non-intentionally p-doped multisectorial (100) oriented substrates repolished by Syntek due to their overall better crystalline qualities than competitors companies. The MPCVD epitaxy of the p+ and p epilayers were performed in the same home made reactor at the institute NEEL, which can grow from heavily to slightly doped layer. The non-intentionally doped layer was grown using a Plassys BJ 150 reactor, which is a dedicated reactor in order to avoid boron contamination. The general fabrication process requires a clean environment since the smallest contamination can lead to failure, for this purpose, all the fabrication (i.e. lithography, metal evaporation, etc.) have been performed in NanoFab clean-room. The fabrication procedure is illustrated in figure 4.1 and elapses as follows.

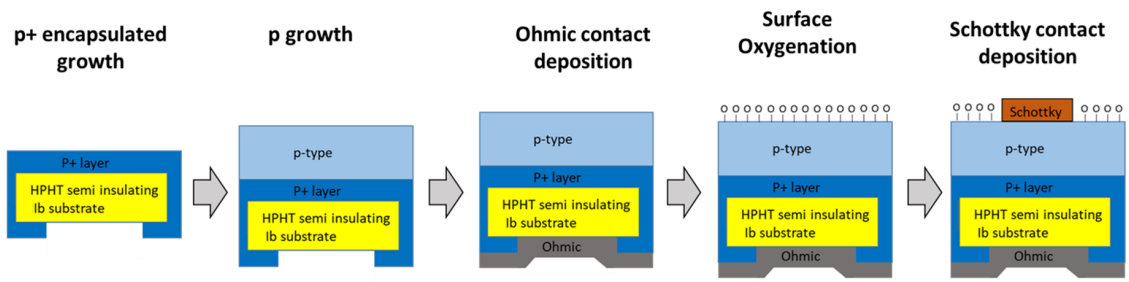

FIGURE 4.1: *Schematic fabrication process for an encapsulated diamond Schottky diode. The first step is the epitaxy of the encapsulated p+ layer. After the p+ layer, the epitaxy of the p-type drift layer follows. Once the epitaxy of both layers is finished, the ohmic metals are evaporated on the back face followed by a thermal treatment to reduce the contact resistance. The top surface is then treated by means of an ozone plasma in order to acquire an oxygen-terminated surface. A photolitography is then used to define the Schottky electrodes, followed by the deposition of the Schottky metal stack.*

4.1.1 Encapsulated p+ layer epitaxy

The first step for both samples is the encapsulated p+ layer epitaxy. The process is carried out individually for each of them. Each sample is set inside the reactor for a 2h H_2 plasma treatment after a triacid (sulfuric, nitric and percloric in volumic proportions 3:4:1 at 600K) cleaning treatment. This H_2 plasma treatment has the double purpose of cleaning and

smoothing the sample surface as well as acquiring a stable plasma ball centered on the sample with a constant temperature. The gas pressure used is 21 Torr as well as 200 sccm flow with a microwave power of 240 W reaching temperatures over 1150K. The lower gas pressure and thus bigger plasma ball used in the encapsulated p+ epitaxy (about 2 cm) than in usual ones is meant to ensure the growth in the samples edges and back face. In this growth, the sample is placed over a smaller dummy diamond rotated by 45 degrees in order to allow the plasma access the back face. After 2h of H_2 plasma, methane and a diluted mix of H_2 and diborane are injected in the mixture reaching temperatures of 1200K. The concentration of the injected gases followed the proportions CH_4/H_2=4% and B/C = 533 ppm. The epitaxy lasts 90 minutes, a significantly long time, to assure the p+ growth over the edges and back faces with a nominal thickness on the top face of 3 microns. These conditions give rise to heavily doped layers just beyond metallic transition with encapsulation over the edges and the back face of the substrate as shown in figure 4.2. After the epitaxy, the samples are again cleaned with a triacid treatment to remove any surface graphitization left from the growth process.

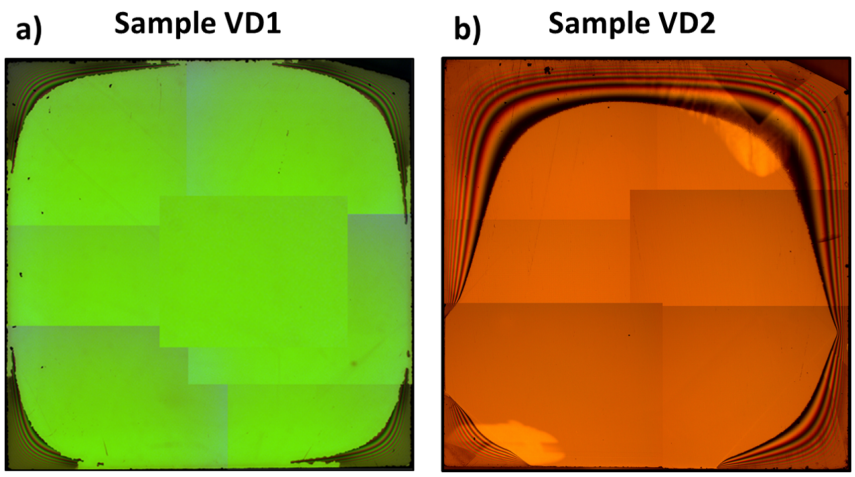

FIGURE 4.2: *Optical image of the back face of samples a) VD1 and b) VD2. The p+ encapsulation can be observed on the corners of both samples.*

4.1.2 p-type drift layer epitaxy

The next step is the samples drift layer epitaxy. The procedures, targeted thicknesses and doping levels differ between the samples:

1. **Sample VD1:** The sample is again set inside the same reactor for a 2h H_2 plasma treatment. The pressure used is 33 Torr and a 200 sccm flow with a microwave power of 240 W. After, methane and a mix of hydrogen, oxygen and diborane after a double dilution process are injected in the mixture reaching temperatures of 1200K. The parameters for the epitaxy are: CH_4/H_2=1%, O_2/H_2=0.25% and B/C = 60 ppm for a target doping density of $3{\cdot}10^{16} cm^{-3}$. The epitaxy lasts 90 min reaching a thickness of

$\sim$ 430 nm. The rugosity of the surface is about 0.6 nm as measured by profilometry. Low concentration of defects are found by optical microscope inspection of the sample reassuring the good quality of the grown drift layer.

2. **Sample VD2:** The sample is set inside the Plassys BJ 150 reactor for a 2h H_2 plasma treatment with a microwave power of 2500 W. The pressure used is 150 Torr and a 200 sccm flow. After, methane is injected in the mixture for a non intentionally doped growth reaching temperatures of 1080K. The concentration of methane for the epitaxy is CH_4/H_2=4%. The growth lasts 12 hours reaching nominally 8-10 microns. A high amount of defects are present in the sample due to the prolonged epitaxy.

4.1.3 Ohmic contact fabrication

Ohmic contacts are fabricated based on a stack of titanium (30 nm), platinum (30 nm) and gold (30 nm) for both samples. Titanium is used for its adhesion and low barrier due to the formation of a TiC layer at diamond interface, platinum is used to avoid gold diffusion and gold is chosen for its conductivity, stainless and wire-bonding ease. Because of the encapsulated architecture, the stack is directly evaporated on the back face with no need of lithography process. After metal the deposition, the samples are annealed at 830K in ultra-high vacuum in order to enhance the formation of TiC at the titanium-diamond interface for ameliorating the adhesion and lowering the contact resistances.

4.1.4 Schottky contact fabrication

The first step in the Schottky contact fabrication is to perform an ozone plasma treatment, in order to oxidize the samples surfaces. The treatment consist on a 2 hours plasma at a pressure of 500 mbar. The ozone plasma is achieved by using a a Xenon EXCIMER UV lamp at 172 nm. After, a lithography process to define the electrodes is performed and a subsequent ozone treatment is again performed to ensure the surface oxygenation. Then, metal stacks based on molybdenum or zirconium (30 nm), platinum (30 nm) and gold (30 nm) are deposited by e-gun evaporation under high vacuum. The sample VD2 is based entirely on molybdenum while the sample VD1 has molybdenum and zirconium electrodes (fabricated using the described process for each of the metals) in order to compare their behaviour in the same sample. For sample VD2, the ozone plasma treatment is again used after contact fabrication while for sample VD1, this treatment is performed after a first electrical characterization in the contacts in order to evaluate its impact on the electrical response of the diodes. An image of both samples after the full fabrication process is presented in figure 4.3.

4.2 Sample VD1

The sample VD1 has the purpose of study molybdenum and zirconium Schottky contacts in order to find a suitable metal for high voltage applications. For this purpose, a relatively

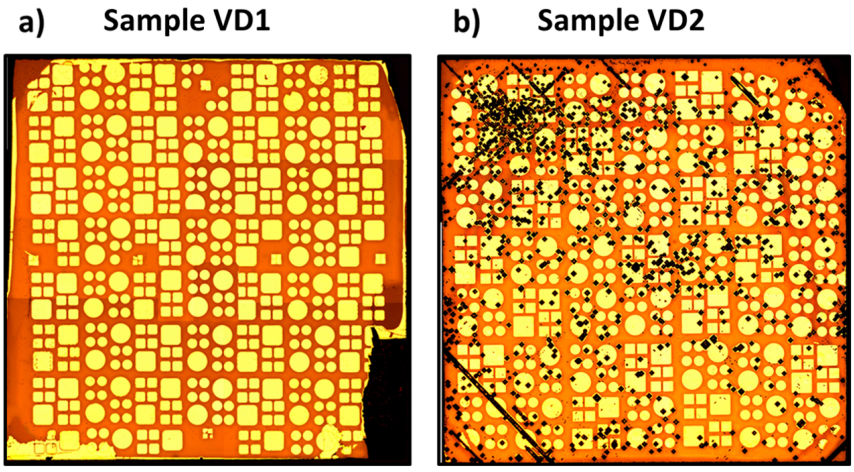

FIGURE 4.3: *Optical image of the top face of samples a) VD1 and b) VD2 after the full fabrication process. The sample VD1 is composed of molybdenum and zirconium electrodes, its drift layer its thin ($\sim$ 430nm) and has a doping level of $N_A = 3 \cdot 10^{16} cm^{-3}$. The sample VD2 is only composed of molybdenum electrodes. Its drift layer is a thick non-intentionally doped layer with expected residual concentration of boron of $N_A \sim 2 \cdot 10^{15}$ cm^{-3}. A notable concentration of hillocks and round defects are present on the top surface. These are attributed to the prolonged epitaxy process both for the p+ and non-intentionally doped layers.*

high doping level (for Schottky diode applications) of $N_A = 3 \cdot 10^{16} cm^{-3}$ was targeted in order to study the contacts behaviour under challenging conditions. The targeted thickness is 430 nm to guarantee a not 0 V pinched-off layer to be able to determine the $N_A - N_D$ value with C-V measurements, but thin enough to reach an early pinch-off (< 10 V) in order to study the leakage currents at high field at relatively low voltages. The molybdenum and zirconium contacts electrical measurements to determine the on-state and off-state behaviour, reproducibility, temperature dependence and thermal stability are presented hereafter.

4.2.1 I-V characteristics

The I-V characteristics for a molybdenum and a zirconium 50 microns radius circular Schottky contacts are presented in figure 4.4 a) and b) respectively. These contacts show a representative behaviour of what molybdenum and zirconium contacts show in the sample VD1. First, the contacts were measured right away after fabrication (red curve). They both show leakage current exploding at around 40 V in reverse. The zirconium contact also shows a slower exponential increase of the leakage current starting from 20 V in reverse. These are premature leakage currents flowing at (1D estimated) low field that cannot be explained using the model developed in the section 2.2.2.3 without considering electric field crowding at the edge of the contacts and or barrier inhomegeneities. In order to try to improve the performance of the diodes, the sample was then subjected to an additional ozone treatment to repassivate the surface. The characteristics of the same contacts after the treatment are again

presented in figure 4.4 a) and b) respectively (blue curves). The leakage current, although still present, is significantly reduced for both of the contacts. This is a demonstration of the crucial importance of surface passivation for preventing leakage currents through the contacts. This effect was consistently observed throughout the whole set of measured contacts.

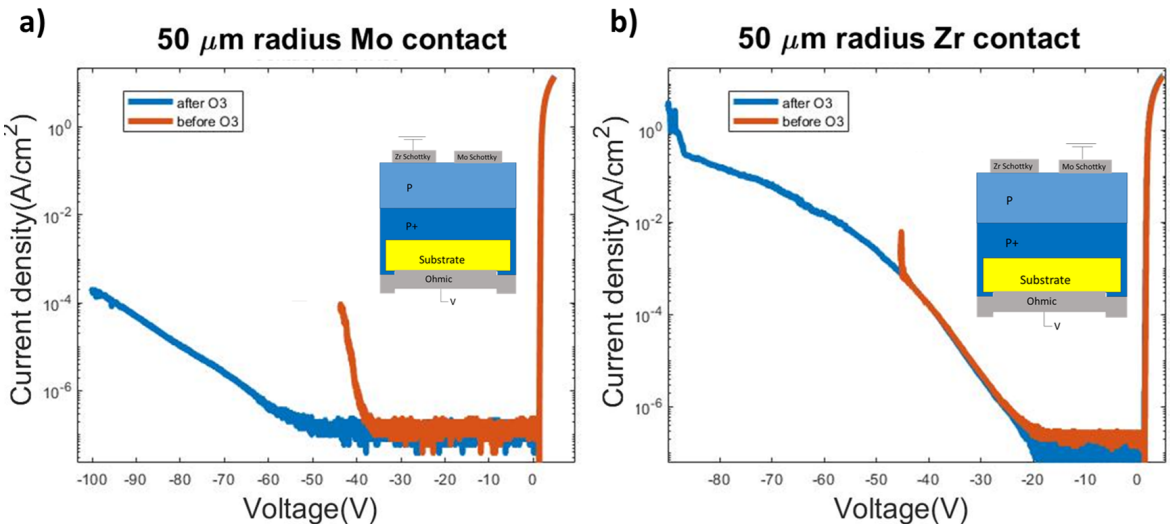

FIGURE 4.4: *I-V characteristics for a) 50 microns molybdenum contact and b) 50 microns zirconium contact before and after an ozone passivation treatment carried out after the sample VD1 fabrication.*

The molybdenum contact on-state characteristic remain unaffected displaying identical curves before and after the passivation. The molybdenum on-state behavior for a set of 8 different contacts after passivation is represented in figure 4.5 a). They show a very similar behavior with a turning-on voltage (the earliest voltage at which the forward current is measured) of 1.35 V. Adjusting the experimental data to the expression 2.10, values for the Schottky barrier height of 1.9 eV , for the ideality factor of 1.11 and for the on-state active normalized resistance of $\sim 0.2\ \Omega{\cdot}cm^2$ are found. Contrary, the zirconium contact on-state is slightly changed reducing the turning-on voltage from 1.34 V to 1.25 V, which is related to a Schottky barrier decrease. The zirconium on-state behavior for a set of different contacts after passivation is represented in figure 4.5 b). They also show a similar behavior with the turning-on voltage at 1.23 V (except the contact c1Rs2 with 1.16 V) and by fitting the experimental data to the expression 2.10, values for the Schottky barrier height of 1.54 eV, for the ideality factor of 1.50 and for the on-state active normalized resistance of $\sim 0.2\ \Omega{\cdot}cm^2$ are found. The on-state behaviour of zirconium contacts seems to be affected by the passivation treatment probably due to the metal oxidation causing a very high ideality factor and a decreased Schottky barrier height. The characteristics of the molybdenum and zirconium contacts remain unaffected by their shapes although a bigger size is usually accompanied by an earlier leakage current. Despite, the present study of the contacts focus solely on circular 50 micron radius contacts.

On the other hand, the on-current is not limited by the p-type drift layer resistance.

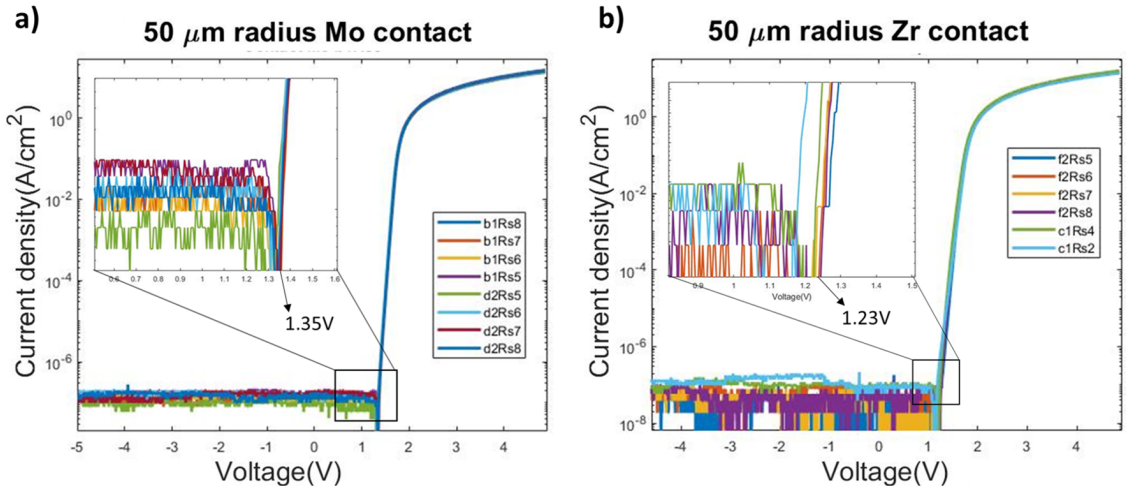

FIGURE 4.5: *I-V characteristics for a set of different 50 microns contact for a) molybdenum and b) zirconium after an ozone passivation treatment carried out after the sample VD1 fabrication.*

The calculated normalized area resistance according to the model described in sec. 2.11 for the measured $N_A - N_D$ (see next subsection) and a layer thickness of 450 nm is $\sim$ 5 10^{-4} $\Omega{\cdot}cm^2$ far below 0.2 $\Omega{\cdot}cm^2$. This high on-state diode resistance could be related to the p+ resistance. The p+ thickness on the edge of the substrate could be way lower than desired as its growth process is not still well controlled. This could result in a high resistive p+ layer explaining the on-state characteristics. In fact, one possible factor for the unsuccessfully encapsulation process in this sample is the orientation of the used substrate. The edges of the sample are (110) oriented while the top and back surfaces are (100). A significantly low boron incorporation or and growth rate due to the crystallography of the edge is a plausible explanation for the unsuccessfully on-state of this sample.

The overall comparison between zirconium and molybdenum contacts favor the choose of molybdenum due to the slightly higher on-state reproducibility, higher Schottky barrier, lower ideality factor and in case of the shown contact in figure 4.4, lower leakage current.

4.2.2 C-V characteristics

The Mott-Schottky plots based on the capacitance measurements at 100 kHz performed on a molybdenum and a zirconium 50 microns radius Schottky contacts are presented in figure 4.6 a) and b) respectively. A linear fit has been performed in the region -1 to 4 V in order to determine the $N_A - N_D$ value and the V_{BI} of each Schottky contact according to formula 2.24. The fit provides a value of $N_A - N_D = 3.9 \cdot 10^{16}\ cm^{-3}$ for both contacts being consistent with the nominal value of doping level expected and being reproducible throughout the sample. However, the built-in voltage deduced for molybdenum is 3.6 V and for zirconium 7.1 V. The built-in voltage is related with the Schottky barrier by $V_{BI} = \phi_B - \phi_f$, where $\phi_f = k_B T ln(N_V/p)$ is the distance from the Fermi level to the valence band far way from the interface, and for the doping level of this sample $\phi_f = 0.29eV$. Both molybdenum and

zirconium built-in voltages values are significantly big compared to the deduced Schottky barrier by the fit performed to the forward characteristics. There are several differences from the V_{BI} extraction between I-V and C-V, being the latter less sensitive to inhomogeneities. For instance, if two Schottky contacts of different barrier height are connected in parallel, the I-V curve is dominated by the lower Schottky barrier height while the C-V is dominated by whichever occupy a wider area. Nonetheless, the huge difference in the values points toward some fixed charges accumulated in the interface or in a partially oxidized region of the contact such as in a MOS capacitor.

On the other hand, due to the thin p-type drift layer of $\sim 430nm$, the layer becomes fully

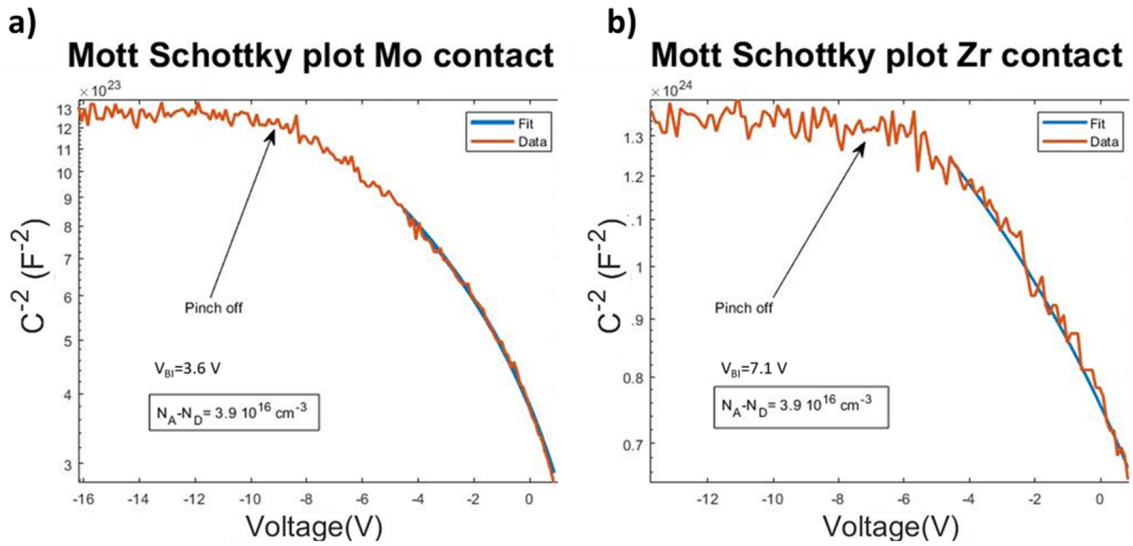

FIGURE 4.6: *Mott-Schottky plot for a) a 50 microns molybdenum contact and b) a 50 microns zirconium contact. Both curves are measured after the ozone passivation treatment carried out after the sample fabrication.*

depleted in the case of the molybdenum contact at around 9V in reverse and at 5.5V in reverse for the zirconium contact. This difference match surprisingly well the differences observed in the V_{BI}. As the layer is more depleted initially for zirconium, the SCR reach at an earlier voltage the p+ layer underneath.

4.2.3 Thermal stability

As important as the ability to block the current in reverse or the on-state reproducibility, the thermal stability for the contacts need to be studied in order to be able to operate them at the ideal working temperature for diamond ($\sim 500K$). The I-V characteristics at RT for a molybdenum and a zirconium 50 microns radius Schottky contacts are presented in figure 4.7 a) and b) respectively after 400 K and 500 K annealing and before the annealing. The molybdenum electrode remains almost unaffected by the thermal treatment with the ideality factor being constant at around 1.1 and a small barrier reduction from 1.9 eV to 1.81 eV after the 500

K thermal treatment under high vacuum. This behaviour is consistently observed throughout the molybdenum contacts in this sample. On the other hand, the zirconium electrode is significantly degraded by the thermal treatment with a great barrier reduction from 1.56 eV to 1.07 eV after the 500 K thermal treatment under high vacuum with a very high augmentation of the ideality factor from 1.5 to 2.23, the latter being extremely high. This behaviour is in contrast with the results provided by [83] with zirconium contacts, and the different thermal stability of the zirconium contacts in this thesis is attributed to the diverse fabrication process. Despite, degradation has also been reported for zirconium contacts in [90]. Probably the sum of the passivation and thermal treatment is responsible for the degradation of the zirconium contact. This degradation is similar in the rest of the measured zirconium contacts in this sample. The degradation of zirconium contacts and the thermal stability of molybdenum are one of the main reasons to opt for the latter in the rest of the devices fabricated in this work.

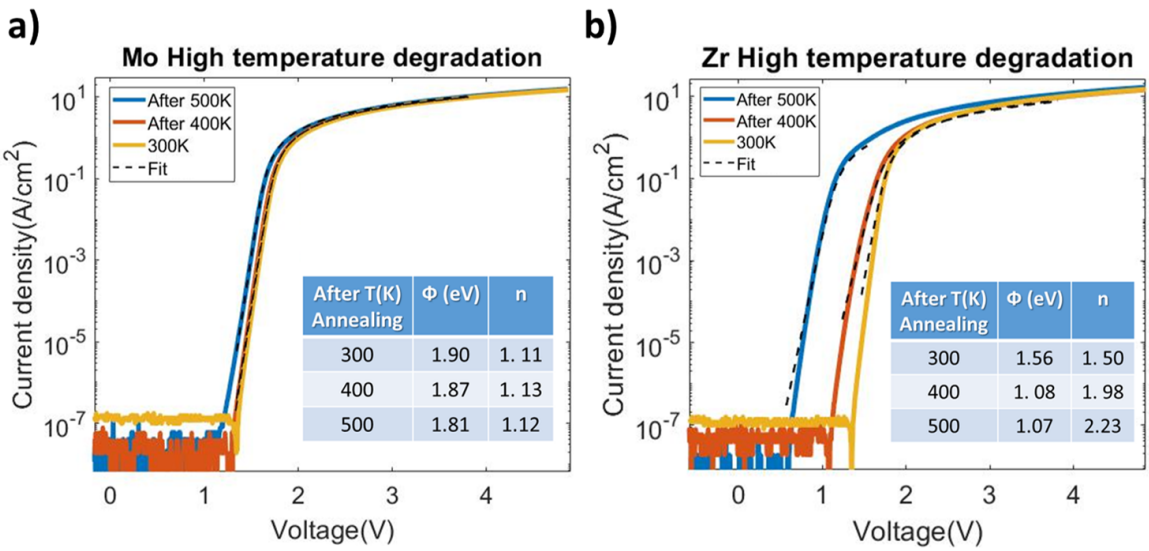

FIGURE 4.7: *I-V characteristics at RT for a) a 50 microns molybdenum and b) a 50 microns zirconium contact before and after a 400 K and 500 K thermal treatments.*

4.2.4 I-V characteristics at high temperature

The I-V characteristics at RT, 400 K and 500 K for a molybdenum 50 microns radius Schottky contact are presented in figure 4.8 after the contact passivation and the annealing treatment. The I-V characteristics from the zirconium contact are not represented in this case due to the lack of interest as they were severely degraded due to the latter treatment. The contact Schottky barrier of the represented molybdenum contact increases from 1.81 eV at RT to 1.94 eV at 500 K while the ideality factor is reduced from 1.12 to 1.02. This trend can be explained by the fact that a inhomogeneus Schottky barrier would display higher Schottky barrier height and lower ideality factor as the Fermi function blur due to the higher temperature because higher barriers can be overcome by thermionic effect and less non-thermionic

emission processes are involved in the current flow through the contact. This behaviour further support the hypothesis of patchiness of the molybdenum contacts in agreement with the conclusion extracted from RT C-V and I-V measurements.

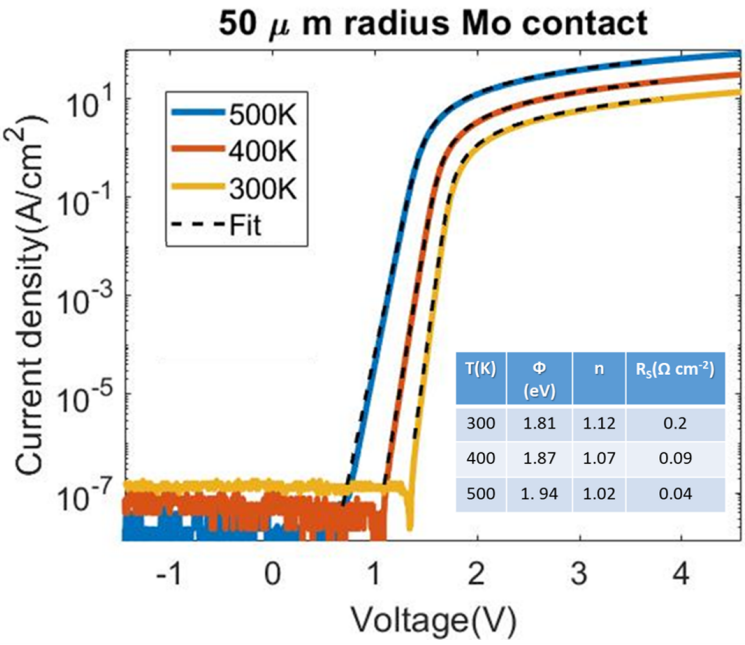

FIGURE 4.8: *I-V versus temperature characteristics for a 50 microns molybdenum contact after ozone passivation and thermal treatments carried out after the sample fabrication.*

The on-resistance diminish as the temperature rise, reaching 0.04 $\Omega{\cdot}cm^2$ at 500 K. The calculated normalized area resistance from the drift layer according to the model described in sec. 2.11 at 500 K is $\sim 1\ 10^{-4}\ \Omega{\cdot}cm^2$. Therefore, as mentioned in the subsection 4.2.1, the resistance is not dominated by the drift layer resistance. As explained, the most probable cause is the thin character of the p+ growth in the sample edges. However, the temperature dependence of the on-state resistance is not compatible with a p+ layer dominated resistance. The increase of the on-state current can only be explained if the limiting resistance is coming from a low doped layer as it would benefit from thermal ionization of boron acceptors. The substrate is a non-intentionally doped layer grown by HPHT from New Diamond Technologies company which typically display a doping level of $N_A \sim 10^{15}\ cm^{-3}$. In fact, the most plausible explanation is that the current is thus flowing though the substrate at least at high temperature. The on-state resistance of the sample is thus the parallel resistance from the p+ layer in the edge and the substrate $R_{ON}^{-1} = R_{p+_{edge}}^{-1} + R_{subs}^{-1}$, the latter clearly dominating at higher temperatures.

4.2.5 High field off-state I-V characteristics

The I-V characteristics at RT from 5 V in forward to -100 V in reverse for a set of molybdenum and zirconium circular 50 microns radius Schottky contacts are presented in figure 4.9 a) after the contact passivation and thermal treatment for molybdenum and b) after the

contact passivation and before thermal degradation for zirconium. In the case of molybdenum, out of the 8 represented contacts, 6 reach 90 V in reverse with at least a rectification ratio of 3 orders of magnitude and no degradation after the measurement. For 4 contacts, the leakage current seems to converge to 10^{-2} A/cm^2 in which seems to be a similar leakage mechanism. For the two best contacts, the leakage current starts increasing at 60 and 80 V in reverse respectively and remains substantially low at 100 V. However, for 5 of these contacts, the leakage current explodes at a certain voltage increasing very fast yielding an irreversible degradation of the contacts. The mechanisms governing the leakage remain unidentified but the most probable explanation is the tunneling plus thermionic emission through an inhomogeneous Schottky barrier with electric field crowding at the edge of the contacts, as this would explain the high irreproducibility between similar contacts. The latter phenomenon in which the contacts are degraded is probably related to the hard breakdown in a local spot in the contact perimeter where a very high field is reached. In fact, even the best contact displays a leakage current level expected for a Schottky contact with an effective barrier around ∼1.2 eV as calculated using the leakage current model from subsection 2.2.2.3 and represented in the figure 2.5. This is still improvable as it is a lower value for the Schottky barrier deduced from I-V forward characteristics, but is already a very promising result. To put this in context, the electric field at the interface at 100V is around 2.25 MV/cm due to the thin p-type drift layer (calculated with eq. 2.22 until the pinch-off voltage and using V/t_p after as in figure 2.10.). Therefore, half of the contacts reaching $\sim 2MV/cm$ with at least 3 orders of magnitude rectification ratio and the best contact reaching 2.25 MV/cm with almost no leakage current must be seen as a great success. Furthermore, the doping level used in this sample is particularly high for a Schottky diode and this is another factor for increasing the leakage current. If this result is now translated to a non punch through Schottky diode with a doping level of $N_A - N_D = 7 \cdot 10^{14}$ cm^{-3} where the maximum critical field of diamond is 3.6 MV/cm, more than the 60% of diamond electric field could be exploited.

For the zirconium contacts, the leakage current increases significantly faster with only half of the contacts giving a higher rectification ratio than 3 orders of magnitude at 50V in reverse. At higher voltages, all of the contacts are irreversibly degraded after the leakage escalates rapidly versus voltage at a certain voltage between 30 V and 80 V in reverse. The overall behaviour is similar to what is found in the molybdenum contacts but the leakage increases faster and at earlier voltages. This difference between molybdenum and zirconium in the same sample can be attributed to the more inhomogeneous barrier for zirconium as the electric field crowding effect is expected to be similar for both electrodes with the same fabrication process. Of course, the irreproducibility in the leakage behavior between zirconium contacts again points toward the electric field crowding at the edge of the contacts being a major factor but only this fact cannot explain the difference between the two metals.

The overall comparison favor molybdenum over zirconium again, showing smaller leakage currents even if molybdenum has been submitted to a thermal treatment and zirconium has not. The noteworthy results obtained from molybdenum contacts open the route to the

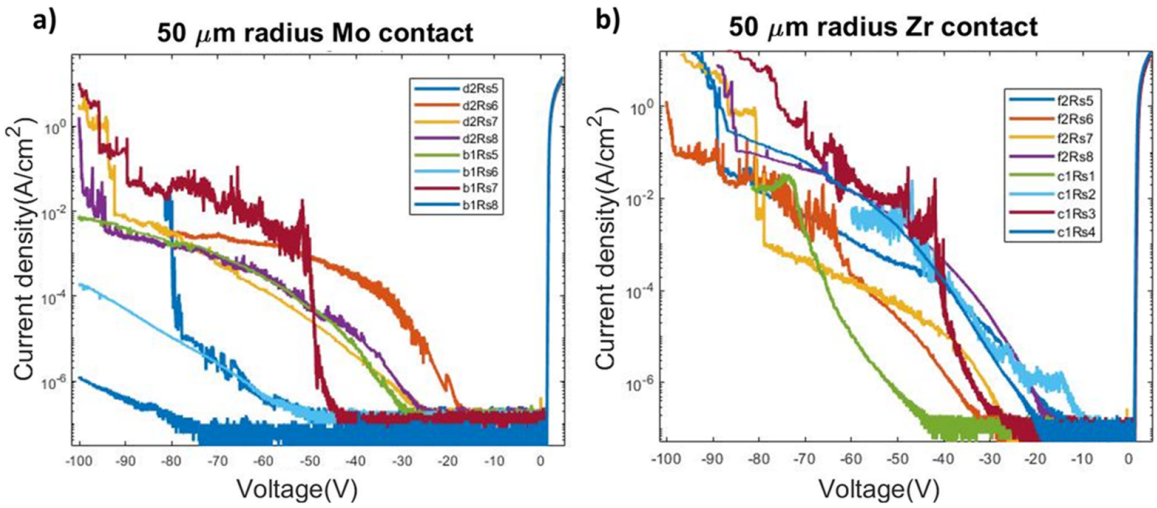

FIGURE 4.9: *I-V characteristics for a set of different 50 microns contact for a) molybdenum and b) zirconium after an ozone passivation and annealing treatment carried out after the sample fabrication for molybdenum and before the annealing for zirconium.*

fabrication of HV optimized molybdenum based Schottky diodes structures where around 60% of the critical field of diamond can be exploited with reproducibility even without the use of edge terminations structures.

4.2.6 Sample VD1 conclusion

The main objective of this sample was to test molybdenum and zirconium as Schottky forming metals on diamond in order to find a successful candidate. Whereas zirconium exhibited a high ideality factor and relatively low ϕ_b and was degraded both by the passivation and thermal treatments, molybdenum presented a low ideality factor, a high ϕ_b and remained unaffected by the surface passivation and almost unaffected by the thermal treatment up to 500 K. Molybdenum presented as well a higher blocking capacity with a record contact sustaining 2.25 MV/cm with almost no leakage current. The main conclusion for this sample is thus, that the fabrication process followed based on molybdenum produced reliable contacts for high voltage Schottky contacts-based devices. As a secondary conclusion, the on-state performance of the sample was not as successful as desired as the current level was limited by the failed p+ growth on the edge of the sample. This problem should be relatively easy to solve by using (100) edge oriented substrates and optimized growth conditions.

4.3 Sample VD2

The purpose of sample VD2 is to integrate the developed fabrication process based on molybdenum into an optimized diode structure able to reach the kV range blocking voltage. For this purpose, a non-intentionally doped ($N_A \sim 2 \cdot 10^{15}\ cm^{-3}$) and thick (8-10 microns)

layer was targeted in order to provide the successful molybdenum contacts a favorable environment to reach a high blocking voltage. These two parameters guarantee the electrical field to grow significantly slower versus voltage than in sample VD1, providing a better blocking voltage capability. The molybdenum diodes electrical measurements to determine the on-state and off-state behaviour, reproducibility and temperature dependence are presented hereafter.

4.3.1 I-V characteristics

The low voltage I-V characteristics of 7 different 50 microns radius circular molybdenum Schottky contacts are presented in figure 4.10. These 7 contacts show a representative behavior of what is found in the sample. Even though the sample VD2 seems very inhomogeneous by a simple optical inspection with round defects and hillocks as it is shown in figure 4.3, the on-state characteristics of the molybdenum contacts show the same behaviour not being affected by defects or the position in the sample. They display a turning-on voltage at 1.22 V and performing a fit to the expression 2.10, values for the Schottky barrier height of 1.51 eV, ideality factor of 1.72 and on-state active normalized resistance of $\sim 3\Omega{\cdot}cm^2$ are found. Not evident in figure 4.10, a double barrier is present in the characteristics of the molybdenum Schottky contacts. The second barrier turn-on voltage appears at $\sim 1.5V$. This second barrier is very reproducible for all of the contacts and its origin remains unknown. As the metal deposition process is exactly the same as in sample VD1, the evidence points toward the diamond layer epitaxy. A possible explanation is a homogeneous distribution of non-visible near surface defects that can impact the barrier causing patchiness leading to this phenomenon. Therefore, the discrepancies found between the (lower) ϕ_b and (higher) ideality factor from samples VD2 versus sample VD1 are attributed to this double barrier in sample VD2.

On the other hand, the on-current is not limited by the p-type drift layer resistance, this behaviour was also observed in sample VD1. The calculated normalized area resistance according to the model described in sec. 2.11 for the measured $N_A - N_D$ profile (see next subsection) and a layer thickness between 5-10 micron is around $\sim 2-3\ 10^{-2}\ \Omega{\cdot}cm^2$ far below 3 $\Omega{\cdot}cm^2$. This higher resistance is again attributed to the p+ unsuccessful growth on the (110) edges of the sample. The p+ thickness on the edge of the substrate could be lower than desired as its growth process is not still well controlled. This could result in a high resistive p+ layer explaining the on-state characteristics. However, the 10 times higher resistance of sample VD2 versus sample VD1 is somewhat a downside for this hypothesis since the resistance should be about the same.

4.3.2 C-V characteristics

The Mott-Schottky plot based on the capacitance measurement at 100 kHz performed on a molybdenum 100 microns radius Schottky contact is presented in the figure 4.11 in the black curve up to 100V in reverse. As it is shown, the C^{-2} curve does not show a linear behaviour

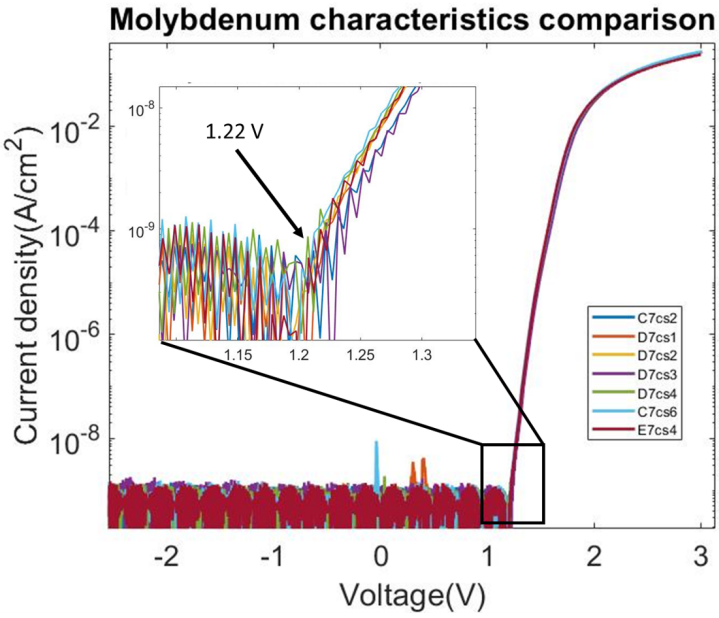

FIGURE 4.10: *I-V characteristics for seven 50 microns radius molybdenum contacts from different regions in the sample VD2 showing a reproducible behaviour with a turning-on voltage of 1.22V.*

implying a varying $N_A - N_D$ profile along the depletion width under the contact. Moreover, the curve does not show signs of pinch-off even at 100V due to the thick drift layer. The exact thickness remains thus unknown as the limit of the experimental capabilities is 100 V but a nominal value of 8-10 μm is expected from the growth conditions. A fit has been performed all over the 100V in order to determine the $N_A - N_D$ profile and the V_{BI} of the Schottky contact. The fit consist on a succession of iterative linear fits according to equation 2.24 with a variable slope and it is plotted in figure 4.11 in blue. It provides a range of values from $N_A - N_D = 2 \cdot 10^{15}\ cm^{-3}$ at the surface up a value of $N_A - N_D = 9 \cdot 10^{15}\ cm^{-3}$ at 4.5 and is consistent throughout different regions of the sample. This doping profile is characteristic of non-intentionally doped layers grown on heavily doped layers, the latter act as a boron source resulting in a decaying boron concentration versus thickness. The depth of the SCR is calculated based on the expression 2.22. The $N_A - N_D$ is represented as well in figure 4.11 in the red curve. The built-in voltage is deduced from the fit intercept with the x-axis and yields a value of 4V. The values is significantly big compared to the deduced Schottky barrier by the fit performed to the forward characteristics. However, the value is close to what is observed for a similar contact in sample VD1. Therefore, as in sample VD1, the big value of the built-in voltage is attributed to fixed charges located near the interface in an oxidized region of the molybdenum.

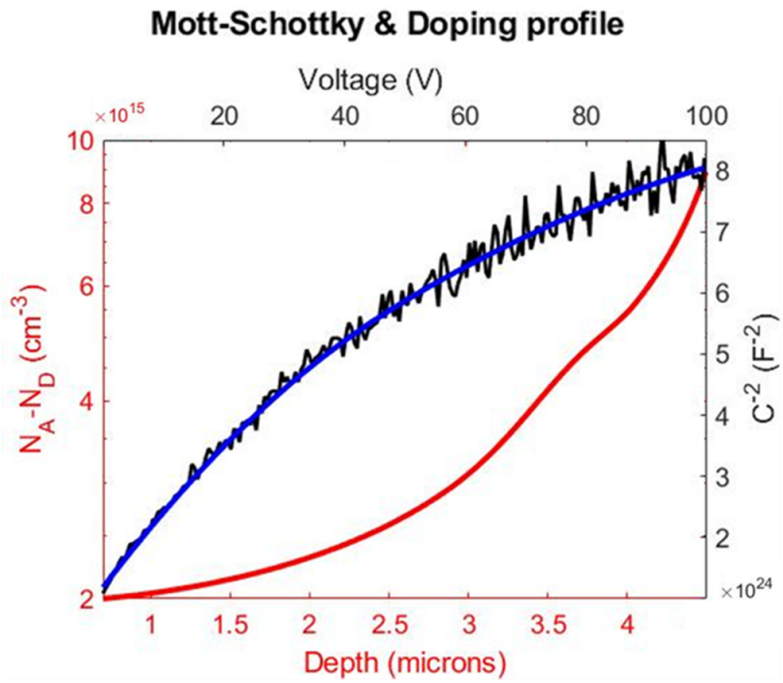

FIGURE 4.11: *Mott-Schottky plot showing the measured data and a fit performed based on eq. 2.24 and the $N_A - N_D$ depth profile for a 100 micron radius molybdenum Schottky contact.*

4.3.3 I-V characteristics at high temperature

The I-V characteristics at RT, 400 K and 500 K for a molybdenum 50 microns radius Schottky contact are presented in figure 4.12. The contact Schottky barrier increases from 1.51 eV at RT to 1.76 eV at 500 K while the ideality factor grows from 1.72 to 2.08. The double barrier phenomenon becomes clearly evident as the temperature increases at around 1.5V. Interestingly, it does not seem to be affected by the temperature change as the current level of the three curves represented converge around this value. The high ideality factor extracted and the variation of the barrier versus the temperature are attributed to the second barrier that make the fit according to the expression 2.10 relatively inaccurate and unreliable. On the other hand, the turn on voltage is reduced as the temperature increases changing from 1.2 V at RT to 0.9 V at 500 K due to the blurred distribution of carriers.

The on-resistance diminish as the temperature rise, as expected for a slightly p-doped layer, reaching 0.5 $\Omega{\cdot}cm^2$ at 500 K. The calculated normalized area resistance according to the model described in sec. 2.11 at 500 K for the doping profile and the nominal thickness is around $\sim 7\ 10^{-3}\ \Omega{\cdot}cm^2$. Again the expected resistance is way lower than the measured value and its temperature dependence points toward a slightly doped layer limiting the on-state current. However, the 10 times higher resistance at RT and 500 K than in sample VD1 is difficult to explain as their similar substrates are expected to behave alike.

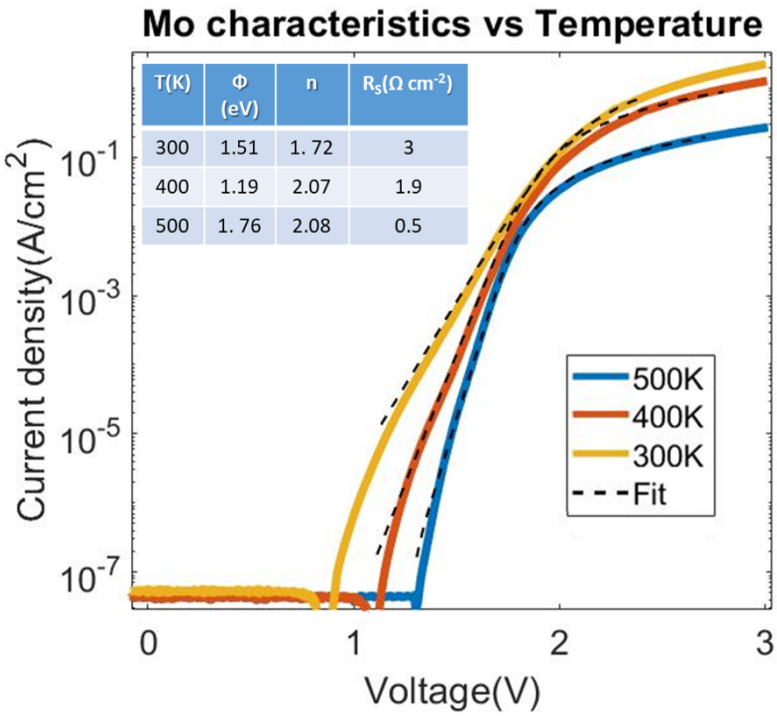

FIGURE 4.12: *I-V versus temperature characteristics for a 50 microns radius molybdenum contact. The curves were fitted according to eq. 2.10 in order to extract the ϕ_b and ideality factor values displayed.*

4.3.4 High field off-state I-V characteristics

The reverse I-V characteristics at RT up to 1.1 kV for a set of five circular 50 microns radius and two 100 microns radius molybdenum Schottky contacts are presented in figure 4.13. Two 50 micron contacts display no detectable leakage current up to 1.1 kV. The rest of the 50 micron contacts show a rapidly increasing leakage current at 1kV, 0.68kV and 0.64 kV irreversibly degrading the contact blocking capabilities after the high voltage stress. These five contacts show a big dispersion in the blocking voltages and the set is representative of what is found in the sample, with typical blocking voltages ranging from 0.6 kV to <1.1 kV. The irreproducibilities found in the sustained voltages for similar contacts probably respond to two different factors: i) The presence of defects under the contact. Although it did not seem affect the on-state characteristics, the off-state characteristics could still be impacted as the electric field distribution or the leakage current mechanism can be modified by the presence of defects. However, no general trend for contacts with hillocks or round defects underneath to have earlier breakdown voltages was observed. ii) The electric field crowding at the edge of the contacts due to spike effect at the electrode edge imperfections that are created irremediably during fabrication. As in sample VD1, this factor seems to be the most reasonable explanation for the dispersion found in the blocking voltages. Moreover, the two represented 100 micron radius contacts are able to sustain 0.88 kV and 1 kV. These two latter contact have the best blocking capabilities found between all the tested contacts for this size. As expected, an average performing 50 micron radius contact yields a higher blocking

voltage than an average 100 micron radius contact. This fact can be explained by the higher probability of having a killing defect or a marked fabrication related deficiency prone to generate electric field crowding operating at high voltage. These two contacts had multiple hillocks underneath and still display a very impressive breakdown voltages.

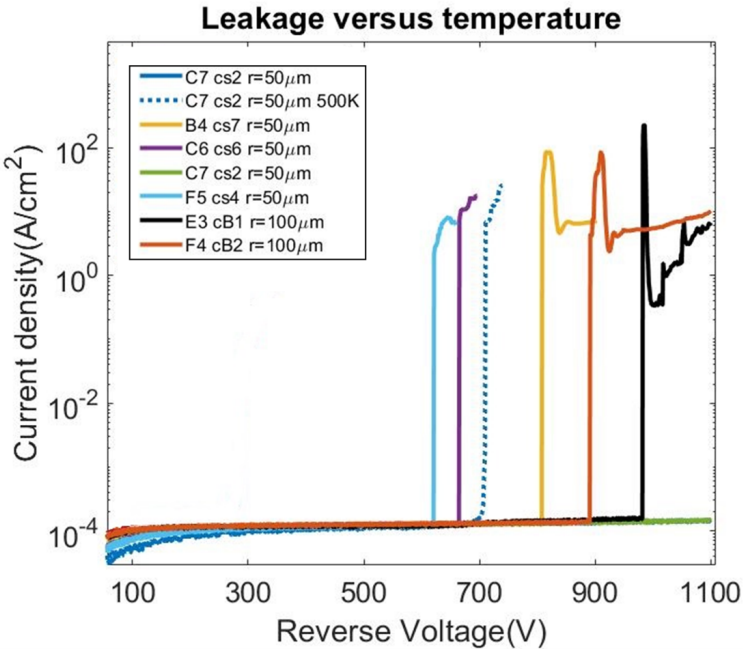

FIGURE 4.13: *Reverse I-V characteristics up to 1.1 kV at RT for a set of five circular 50 microns radius and two 100 microns radius molybdenum Schottky contacts. Two 50 micron contacts display no detectable leakage current up to 1.1 kV. The rest of the 50 micron contacts show a rapidly increasing leakage current at 1kV, 0.68kV and 0.64 kV irreversibly degrading the contact blocking capabilities after the high voltage stress. Also, the reverse I-V characteristics up to 1.1 kV at 500 K are represented for one the best performing circular 50 microns radius molybdenum Schottky contact (C7 cs2) sustaining 0.7 kV.*

In order to evaluate the off-state performance of the contacts, an estimation of the electric field sustained is necessary. However, due to the thick layer, the C(V) did not reach the p+ layer and elipsometry measurements were also unsuccessful for the same reason. Moreover, the full $N_A - N_D$ profile is also unknown and only the first 4.5 microns are accurately measured as presented in the subsection 4.3.2. However, as a big increase of the $N_A - N_D$ value from $2 \cdot 10^{15}\ cm^{-3}$ to $8 \cdot 10^{15}\ cm^{-3}$ is found and because it is only expected to increase with depth, the electric field a the surface is relatively insensitive to the layer thickness. As an upper limit, if the layer is considered to be pinched-off at 100V, the electric field at 1.1 kV is 2.7 MV/cm. On the other extreme, if a constant $N_A - N_D$ value is assumed after the first 4.5 microns (where the measured profile is used) and the diode is considered to be NPT, the electric field at 1.1 kV is 2.23 MV/cm. Therefore, the best performing contacts were at least able to sustain 2.23 MV/cm while the 0.64 kV blocking contact at least 1.65 MV/cm. These result are remarkable since even having a very defective drift layer, the contacts were able

to match the electric field sustained in the sample VD1. Also noteworthy is the ability of the best 100 micron radius contact to sustain 1 kV, even if it has both round defects and hillocks, which is at least 2.14 MV/cm.

The reverse I-V characteristics of one the two best performing diode (C7 cs2 with >1.1 kV blocking voltage at RT) is also represented also at 500 K in figure 4.13 for comparison. At 500 K, the leakage current increase rapidly at around 700 V irreversibly degrading the contact. The high temperature (500 K) operation of this diode reduced its blocking voltage capabilities at least a 36% with a lower estimation of 1.73 MV/cm at the surface. Contrary, its on-state capabilities augmented severely as explained in the subsection 4.3.3. The Baliga figure of merit of the best contact operating at 500 K is thus 1 MW/cm^2, still far way from diamond potential due to the low performing on-state.

4.3.5 EBIC & cathodoluminiscence characterization

In order to analyze the role of round defects and hillocks present on the sample VD2 on the off-state characteristics cathodoluminiscence (CL) and electron beam induced current (EBIC) were performed. In the figure 4.14 a), the 5k exciton CL spectrum measured on the sample VD2 at 10 kV is represented. The spectrum remained unchanged independently of the position in the sample and whether if defects were present or not. The peaks at 236.2 nm, 243.9 nm, 237.1 nm and 233.9 nm are due to free exciton emissions associated with a transverse optical (TO), transverse optical plus center zone (TO+O), longitudinal optical (LO) and transverse acoustic (TA) phonons respectively. On the other hand, the peaks at 237.5 nm, 245.2 nm, 250.8 nm and 231.2 nm are associated with bound exciton emissions mediated with a TO, TO+O, TO+2O phonons and no phonon (NP) recombination respectively [162, 163]. The active boron concentration can be calculated based on the ratio between FE^{TO} and BE^{TO} peaks. This is due to the fact that the higher concentration of boron atoms the more improbable is the emission from free excitons as they would easily interact with boron atoms becoming bound excitons before recombination. The active boron concentration extracted from the ratio between the FE^{TO} and BE^{TO} peaks is $3 \cdot 10^{15}\ cm^{-3}$ according to ref. [164]. This is consistent with what is observed in the C-V measurements with a low concentration of nitrogen species being responsible for a 30% compensation in the region close to the surface, as the approximate depth of the pear generated by electrons in the material is of the order of 0.3 micron at 10 kV [165].

In the figure 4.14 b), the 5K CL visible range spectrum (from 250 nm to 620 nm) measured on three regions of the sample VD2 at 10 kV is represented. The spectra is normalized respect to the FE^{TO} peak as it height and morphology similar in all of them. Three curves are represented: i) in yellow, the spectrum for a defect free sample region, ii) in red, the spectrum obtained from a round defect and iii) the spectrum obtained from a hillock. The broadband around 535 nm present in the ii) and with stronger intensity in iii) is known as A-band emission. It is observed to be located in all type of dislocations in diamond. Evidence in literature suggest it is due to nitrogen aggregates with variable spacing along the dislocation lines [166]. The emission peak at 415 nm and the following peaks superimposed on the

band-A emission are identical to the ' N3 ' system emission, which is a well known system due to nitrogen. It is found for the three spectra but its broadened for the hillock spectrum. The well known emission system (H3) associated with nitrogen is found at 505-510 nm with very low intensities for all three spectra [166]. A zerophonon line due to donor acceptor recombination at 466 nm and the following peaks appear due to coupling with phonons with similar shape and intensity for the three spectra. No nitrogen incorporation was intended in this sample and its probably associated with nitrogen contamination in the epitaxy reactor. Moreover, the stronger A-band emission from the hillock spectrum suggest that these kind of defects impact the electrical properties of the diamond layer. On the other hand, the round defect significantly less strong emission A-band suggest that the impact of these defects on the electrical characteristics is lower than those of hillocks.

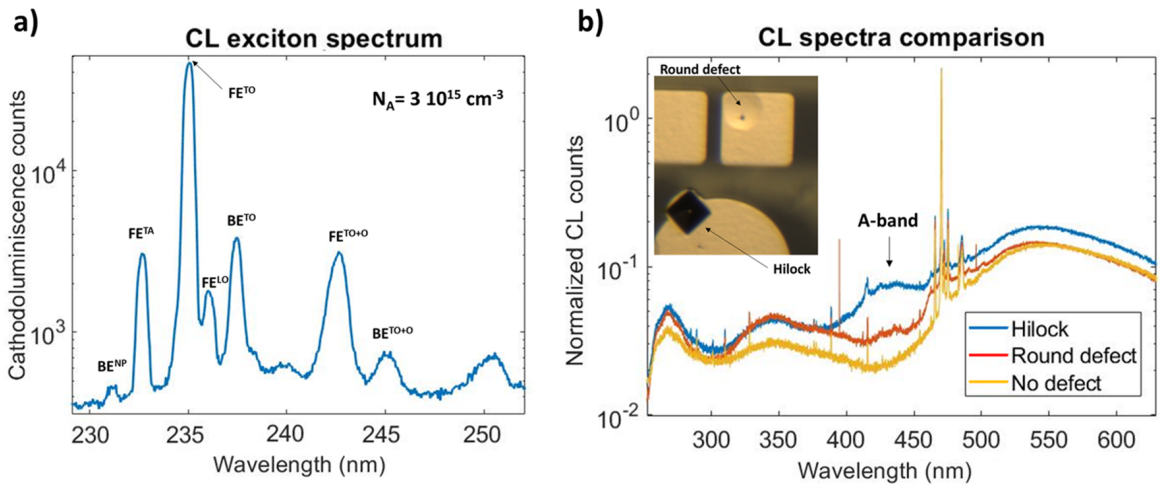

FIGURE 4.14: *a) The 5k exciton CL spectrum measured on the sample VD2 at 10 kV is represented. The spectrum remained unchanged independently of the position in the sample and whether if defects were present or not. The active boron concentration extracted from the ratio between the FE^{TO} and BE^{TO} peaks is $3 \cdot 10^{15}$ cm^{-3} according to ref. [164]. b) The 5K CL visible range spectrum (from 250 nm to 620 nm) measured on three regions of the sample VD2 at 10 kV is represented. The spectra is normalized respect to the FE^{TO} peak as it height and morphology is similar in all regions. Three spectra are represented: i) in yellow, the spectrum for a defect free sample region, ii) in red, the spectrum obtained from a round defect and iii) the spectrum obtained from a hillock.*

In the figure 4.15 a) the scanning electon microscopy (SEM) micrograph of a 100 micron side square Schottky contact is presented. The imperfections due to fabrication are highlighted with black arrows with special emphasis in a zoomed-in region showing the typical morphology of these fabrication related defects. The EBIC image obtained at 30 kV and 200 V reverse bias in the same contact is presented superimposed to the previous SEM micrograph in the figure 4.15 b). Electron beam created electron hole pair are separated and drifted to opposite directions due to the electric field produced by the applied bias to the Schottky contact. This allow the identification of two different features at the edge of the

contact: i) the surrounding brighter halo all around the contact which is associated with the depletion region produced at this high reverse bias. The width of the depletion region extracted from the image is 6.9 microns which is compatible with the calculated depletion width for a $N_A - N_D$=2.5 $\cdot$ 10^{15} cm^{-3} layer at 200 V, in agreement with the near surface value extracted from C-V measurements. ii) Several hot-spots are detected in the contact edge displaying remarkable brighter spike-shaped regions. These hot spots are coincident with the remarked fabrication imperfections thus supporting the hypothesis formulated in the subsection 4.3.4 that the irreproducibilities on the blocking voltage capabilities probably come from electric field crowding on the edge of the contacts due to fabrication related defects.

In the figure 4.15 c) the scanning electon microscopy (SEM) micrograph of a different 100 micron side square Schottky contact is presented. Inside the contact a squared hillock is observed and two round defects are also present but are not evident in the SEM micrograph and they are identified thanks to an optical microscope image (not shown here). The EBIC image obtained at 30 kV and 150 V reverse bias in the latter contact is presented superimposed to the previous SEM micrograph in the figure 4.15 d). No sign of the round defects is detected with EBIC while the hillock show a strong EBIC signal specially on the aristas. This could be explained by two hypothesis: i) the Schottky barrier in the aristas of the hillock is lower than in the rest of the contact enhancing the premature leakage current and or ii) There is electric field crowding at the aristas of the hillock thus magnifying the electric field and causing and earlier voltage leakage. These results are as well consistent with the CL characterization as the hillocks were associated with a stronger A-band emission. On the other hand, the no clear correlation between the breakdown voltages of the Schottky diodes and the presence of hillocks might be a result of the dominant leakage current due to electric field crowding at the edge microfabrication defects versus the leakage current passing through the hillocks. The latter contribute to the leakage process as demonstrated by EBIC results but the breakdown phenomena shown in figure 4.13 is surely related to a high current flowing through small spots on the edge of the contacts, where the contact properties might be degraded by the self-heating and the avalanche phenomenon is produced.

4.3.6 Sample VD2 conclusion

The main objective of this sample was to demonstrate the high voltage capabilities of the molybdenum Schottky contacts. This has been accomplished as numerous >1 kV 50 micron radius contacts were found in the sample. Moreover, a 100 micron radius contact sustaining 1 kV was demonstrated as well. These results are even more impressive if we consider the amount of defects present in the drift epilayer. The contacts sustained a low estimate record of 2.1 MV/cm and 1.8 MV/cm for the 50 micron and 100 micron radius contacts at RT respectively. Moreover, the best 50 micron radius contact sustained up to 700 V at 500 K. On the other hand, the diodes on-state performance is far from ideal due to the limited (110) oriented edge p+ growth. The Baliga figure of merit of the best contact at 500 K BFOM=$V_{BD}^2/(R_{ON}S)$ is about 1 MW/cm^2. This value is still far from the ideal value for

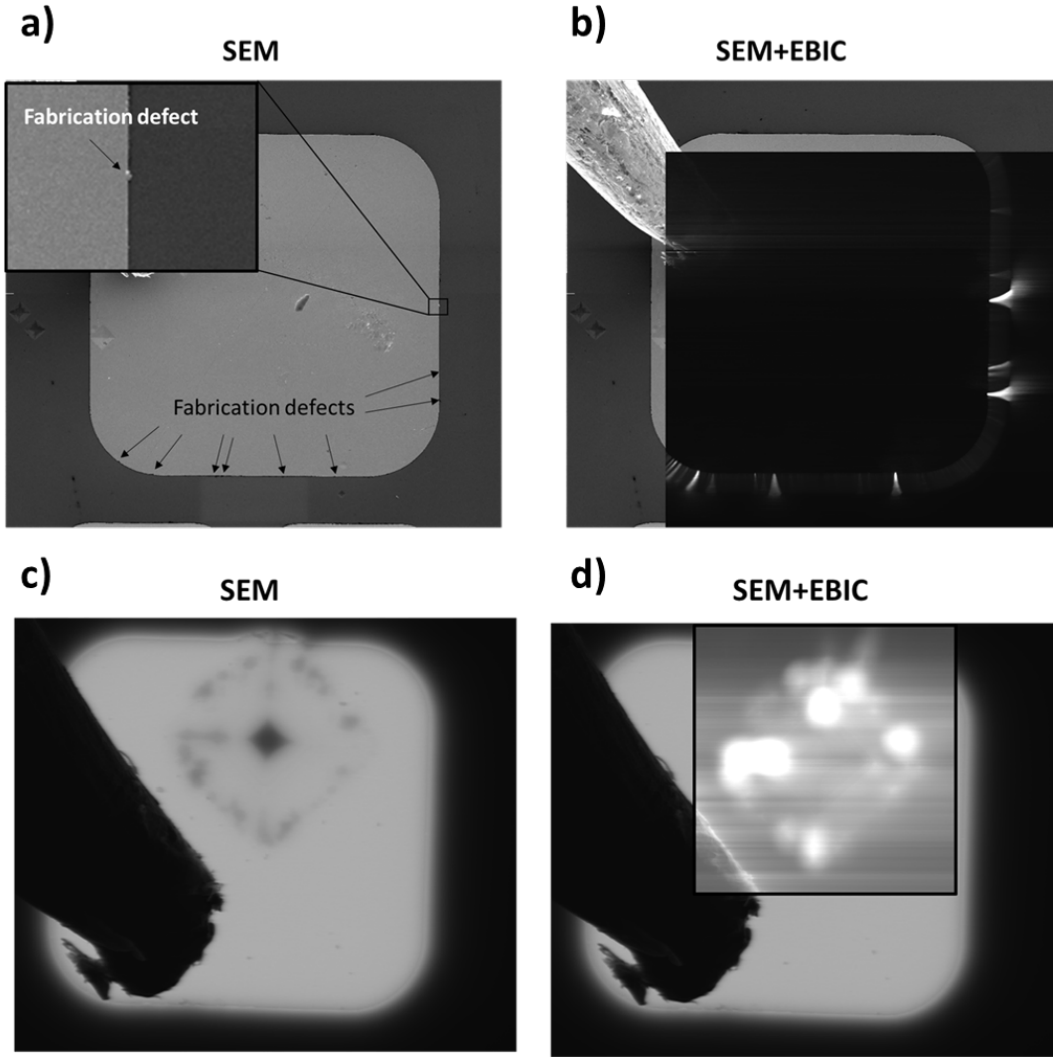

FIGURE 4.15: *a) and c) present the scanning electon microscopy (SEM) micrograph of two 100 micron side square Schottky contact. In a), the imperfections due to fabrication are highlighted with black arrows with special emphasis in a zoomed-in region showing the typical morphology of these fabrication related defects. In c) a squared hillock is observed inside the contact. b) and d) present the EBIC images obtained at 30 kV and 200 V and 150 V in reverse bias superimposed to the previous SEM micrographs a) and c) respectively. In b) the SCR region and hotspots are identified at the near edge region of the contact. In d) the hillock show a strong EBIC signal especially on the aristas.*

diamond but the on-state problematic can be solved by using other architectures or optimizing the p+ encapsulated growth. This results open the road to get reproducible results in diamond Schottky contacts with $\sim 2MV/cm$ sustaining contacts even in highly defective samples and no edge terminations.

4.4 Summary and Conclusions

In this chapter, two different Schottky diode samples were fabricated in order to find a good metal candidate for diamond Schottky diodes and for developing a kV range diode based on the findings. The sample VD1 demonstrated the success of the fabrication process used, based on molybdenum, with the crucial importance of the surface passivation treatment for the high blocking voltage capabilities. The superiority of this molybdenum versus zirconium as Schottky contact was demonstrated as the former had higher Schottky barrier, lower ideality factor, better thermal stability and better blocking voltage capabilities. Over half of the contacts presented in the sample VD1 were able to sustain 2.25 MV/cm with at least 3 magnitude orders of rectification ratio in a sample with a very high doping for Schottky applications ($N_A = 3 \cdot 10^{16}\ cm^{-3}$). This fact demonstrate the potential of this metal for Schottky diodes fabrication with consistent high blocking voltage capabilities. Its application in low doped diamond epilayers could consistently sustain as much as a 60% of low doped diamond breakdown field. The sample VD2 implemented the developed fabrication process of molybdenum base Schottky contact into an HV design. It successfully demonstrated >1kV breakdown voltage capabilities with contacts sustaining (a low estimate) electric field of 2.2 MV/cm. This sample drift layer epitaxy produced numerous hillocks and round defects which makes even more noteworthy the contacts performance. The role of these defects was studied and only the hillocks contributed to the leakage currents through the contacts. Although the sample irregularity and high concentration of defects, the irreproducibility in the breakdown voltages was attributed to the electric field crowding on the edge of the contacts and this hypothesis was supported by EBIC measurements. On the other hand, the samples suffered from a very limited on-state. This was attributed to the unsuccessful growth of p+ diamond over the (110) oriented edges of the sample. An optimization of this problem is still required and could easily reduce 2 orders of magnitude in the on-resistance leading to a Baliga figure of merit of $\sim 100MW/cm$.

Comparing the contacts area vs sustained field of sample VD1 and VD2 versus other results in literature can help the understanding of the great success accomplished in this study. In figure 4.16, the sustained electric field versus Schottky electrode area for this work molybdenum contacts from sample VD1 and VD2 is compared with numerous bibliographic references [167, 168, 150, 149, 169, 170, 171, 172]. In the case of sample VD1 contacts, the doping level is substantially higher than any other presented and no termination structures were used. Despite, the performance of molybdenum in this sample is unarguably between the top performances on literature with more room for improvement if lower doping and termination structures are used. In fact, the best contact presented no leakage currents at

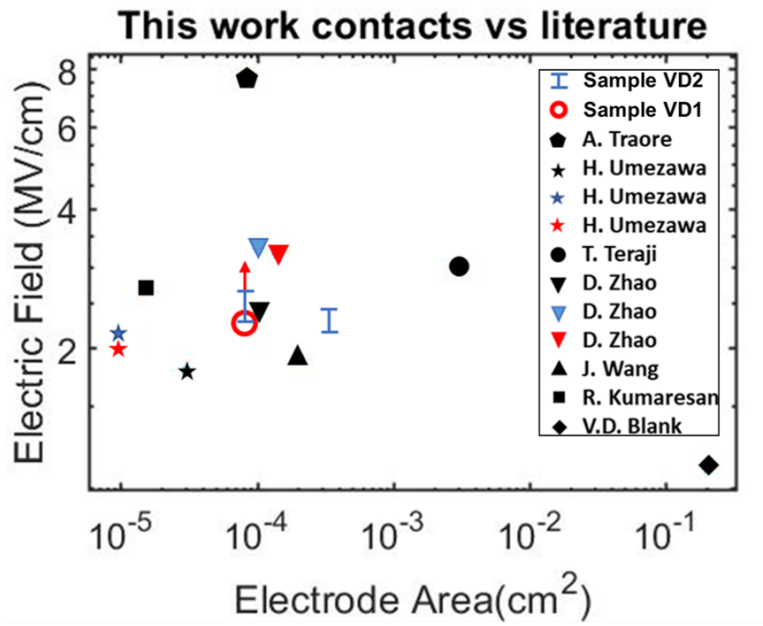

FIGURE 4.16: *Sustained electric field versus Schottky electrode area for this work molybdenum contacts compared with numerous bibliographic references* [167, 168, 150, 149, 169, 170, 171, 172]

2.25 MV/cm while the bibliography data correspond to the breakdown. If this diode was pushed further it could support higher electric field but this was not done in order to not deteriorate it. Only the zirconium electrode published by Dr. Traore remains at a considerable distance for the same area. On the other hand, in sample VD2 the best trade-off is found for a 100 micron radius contact sustaining 1kV; which is at least 2.14 MV/cm. This contact is also noteworthy as it extends the results from the VD1 sample to a four times bigger area showing the second best electric field sustained for similar or higher areas.

In conclusion, the molybdenum Schottky contacts developed in this work demonstrated consistently suitable performances for extracting diamond HV potential at high temperature. One of the main constrains for HV diamond Schottky was the leakage current appearing in most Schottky contacts as explained in the subsection 2.4.2. This was addressed in this chapter and by following the fabrication process developed here, future diamond Schottky diodes will be able to unleash its full potential.

4.5 Road-map

Even if a partial solution to leakage currents, a major problem for Schottky diodes, was demonstrated in this chapter; the future for the HV Schottky diodes will be attached to the development of the epitaxy. Thicker drift layers ($\sim 100\mu m$) are needed in order to be able to fabricate NPT devices allowing the fabrication of diodes in the 10 kV range. Moreover, the reduction of killer defects in thick layers will allow the optimal performance with higher

yield in the fabricated samples. The etching process development will also make a big advance for classical pseudovertical architectures freeing the thickness limitations of diodes together with making available the parallelization of diodes resulting in better on-state performances. Also, the use of edge terminations structures will also ameliorate the off-state reproducibility between different contacts. All these advances would allow the fabrication of diamond diodes that reach consistently higher breakdown voltages than now (as high as 10 kV) with close to ideal performances making use of the developed molybdenum contacts. A plausible road-map for developing consistent 10 kV Schottky diodes based on the contacts developed in this work and the encapsulated pseudo-vertical architecture is:

1. **Encapsulated P+ epitaxy:** The development of a stable process that yields low resistive heavily doped layers with appropriate encapsulation is needed. Special attention has to be taken on the crystallographic orientation of the edge as it can heavily impact the outcome.

2. **Drift layer epitaxy:** A consistent procedure to grow $\sim 100\mu m$ thick layers needs to be developed within a reasonable amount of time. The reduction of dislocations in these layers would allow the best off-state outcomes from Schottky contacts.

3. **Edge termination structures:** The adaptation of field metal rings for instance, would allow the field crowding at the edge of contacts to be severely reduced homogenizing performances between contacts.

4. **Etching:** A procedure to etch up to $\sim 100\mu m$ is still unavailable due to the low selectivity of the used metallic masks. Its development would allow the parallelization of diamond diodes.

Chapter 5

1 kV Normally-off Lateral Reverse-Blocking MESFET

The design, fabrication and characterization of a 1 kV lateral diamond normally-off reverse blocking (RB)MESFET ready for its integration into a full diamond converter is presented in this chapter. The design of such transistor is based on the knowledge developed from Schottky studies from previous chapters. The fabrication is a collaborative effort within the framework of the Green Diamond European project. The full characterization of the sample is presented, comprehending the transfer characteristics, gate characteristics, temperature response and stability and blocking voltage capabilities.

5.1 Design

The design of a transistor consist on the determination of the geometries and material properties that have to be used to achieve a certain performance and it must consider the fabrication constrains, physical models and ease for its posterior integration. The aim of the design presented here is to sketch out a layout and find the optimal parameters to fabricate a lateral normally-off Reverse Blocking (RB) MESFET with 1 kV capabilities for its integration into a diamond power converter. The first step is to determine the drift layer maximum doping level enough to sustain the desired target of 1 kV, as the doping level is directly related to the breakdown voltage and a higher doping translates into a better on-state performance. Due to the lateral nature of the transistor and the possible impact on the breakdown capabilities of various 2D effects such as electric field crowding, the targeted V_{BD} is set to 3 kV instead of 1 kV to have a comfortable margin. The maximum doping level able to sustain 3 kV in a NPT design is $3 \cdot 10^{16} cm^{-3}$ according to eq. 2.39 and therefore this value is targeted for the drift layer. The device is designed in a NPT configuration benefiting from its lateral geometry that leads to no fabrication constraint for archiving this. A gate width L_G of 30 microns and a distance between gate and drain L_{GD} of 30 micron (much bigger than the maximum SCR width at V_{BD} for the targeted doping level) were designed, based on the reported results from Dr. Driche where the best blocking capabilities were obtained for this distance in a similar sample [103]. Also, for a comfortable fabrication a distance of L_{GS} of 8 microns was selected. Of course, the ideal design would minimize the L_{GS}, L_G and L_{GD} distances for maximizing the on-state performance. However, all the transistors integrated in the sample RB will be identical for integration purposes and this gives very small error margin to fabrication and undesired effects. Therefore about 75% of the on-state performance was sacrificed in order to aim for the maximum yield of working devices by taking reasonably higher L_{GS}, L_G and L_{GD} distances.

In terms of safety, normally-off FET operation is usually required for power electronic applications. In general, MESFET transistors are normally-on: The Schottky gate can be operated only in reverse mode, depleting the channel in order to close it. However, if a p-diamond layer doping level and thickness is precisely engineered on top of a n-type diamond substrate, the SCR can be exactly as thick as the drift layer and a small forward voltage can be applied to the gate, just below the threshold voltage of the Schottky diode in order to reduce the space charge region extension and open the channel. The major challenge in the fabrication of such a normally-off transistor is thus to target the correct layer thickness with the precise targeted doping. Based on knowledge acquired in our previous works with molybdenum Schottky contacts on p-type diamond, the SCR thickness has been estimated for both the Schottky gate using eq. 2.22 and the back p-n junction between the p-drift layer and the n-type substrate using eq. 2.41, ideally to offer a normally-off channel. Therefore, for the doping level targeted, a drift layer thickness of 450 nm is required to have the layer fully depleted layer at 0V and thus a normally-off device. However, this makes the requirements

in the control of doping and thickness of the layer very demanding given the relative immaturity of previous diamond device fabrication technology. Recent progress in the precise control of epitaxial growth of lightly boron doped diamond layers on single crystal substrates in the NEEL Institute has now made the growth of such structures possible.

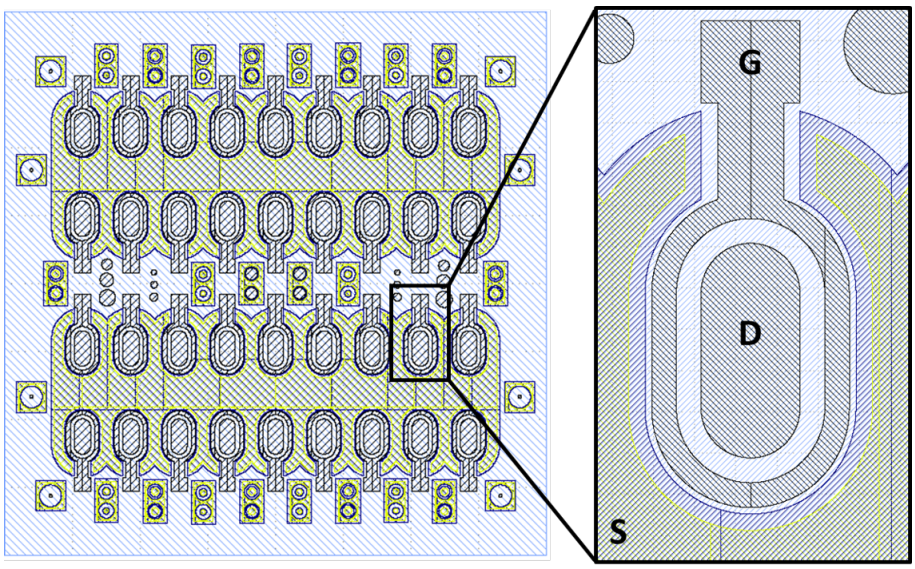

FIGURE 5.1: *RBMESFET designed layout using circular architecture, common source electrodes and $L_{GS} = 8\mu m$, $L_G = 30\mu m$ and $L_{GD} = 30\mu m$ with minimum pad size of 100x120 microns. The light blue represents the p-type drift layer while the darker blue represents the p+ selectively grown layer under the yellow ohmic electrode. The black electrodes account for the Schottky drain and gate. Several circular TLM structures and Schottky contacts are also present in the layout for testing purposes.*

On the other hand, with the aim of reducing the contact resistance, a selectively grown heavily boron doped layer was added beneath the source. The pad sizes for source, gate and drain were designed to be always bigger than 120x100 microns in order to ease the posterior wire-bonding required for integration. With respect to the shape of the devices, circular architecture was preferred owing to the absence of angles for facilitate p+ growth and for electric field management reasons. An image of the proposed layout based on all of these considerations is presented in the figure 5.1.

5.2 RB sample fabrication process

The designed RBMESFET was fabricated in the framework of the GreenDiamond European project with the purpose of its later integration in a full diamond converter. The fabrication process was a co-joint work between various of the partners of the project. The sample (hereafter referred as sample RB) was fabricated based on Sumitomo type IIb semi-insulating substrates repolished by the Prof. Cimalla at the Fraunhofer Institute in Germany. All the CVD

layers were grown in the same home-made reactor at the institute NEEL. The lithographies and evaporations for metallic masks and contacts were performed in the cleanroom of the University college of London by Dr. Pakpour-Tabrizi. The full fabrication procedure is illustrated in figure 5.2. It proceed as follows: i) p drift layer growth, ii) metal mask deposition, iii) p+ selective growth, iV) ohmic contact fabrication and v) Schottky contact fabrication.

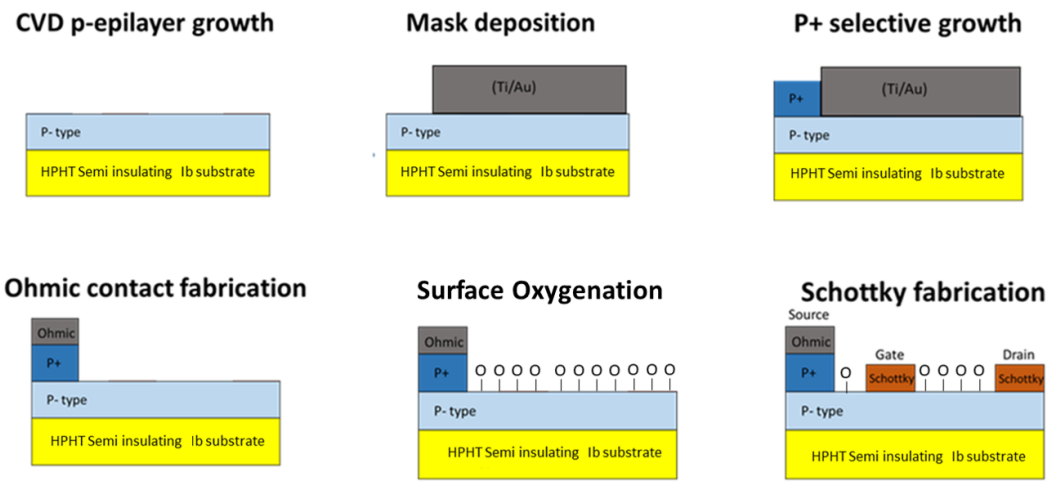

FIGURE 5.2: *RBMESFET fabrication process scheme.*

5.2.1 Drift layer epitaxy

The type Ib substrate is set inside the reactor for a 2h H_2 plasma treatment. The pressure used is 33 Torr and a 200 sccm flow with a microwave power of 240 W. After, methane and a mix of hydrogen, oxygen and diborane after a double dilution process are injected in the mixture reaching temperatures of 1200K. The parameters for the epitaxy are: CH_4/H_2=1%, O_2/H_2=0.25% and B/C = 60 ppm. The epitaxy lasts 90 min reaching 450 nm and a doping level of $N_A = 3.5 \cdot 10^{16} cm^{-3}$ as confirmed from elipsometry and cathodoluminescence respectively [164]. The rugosity of the surface was keep relatively low as $R_a = 2.61 nm$ was measured by phase shifting interferometry. Rugosity and doping level determination are presented in figure 5.3. Low concentration of defects were identified optically except from an agglomeration in two corners of the sample probably related to the substrate quality.

5.2.2 Metallic mask fabrication and p+ selective growth

After p-type layer epitaxy and its subsequent triacid cleaning treatment, a hard metallic mask is deposited on the sample for accomplishing a p+ selective growth. This mask is 400 nm thick and it is based on Ti for its good adhesion to diamond finished with a thin layer (5 nm) of gold. The mask is fabricated using the standard procedure of spin coating a light sensitive resist, its exposition to light thanks to a laser lithography, chemical development of the resist, metal evaporation and lift-off. The sample is then set inside the reactor for a short 15 min H_2 plasma treatment. This treatment has to be shorter than in any other

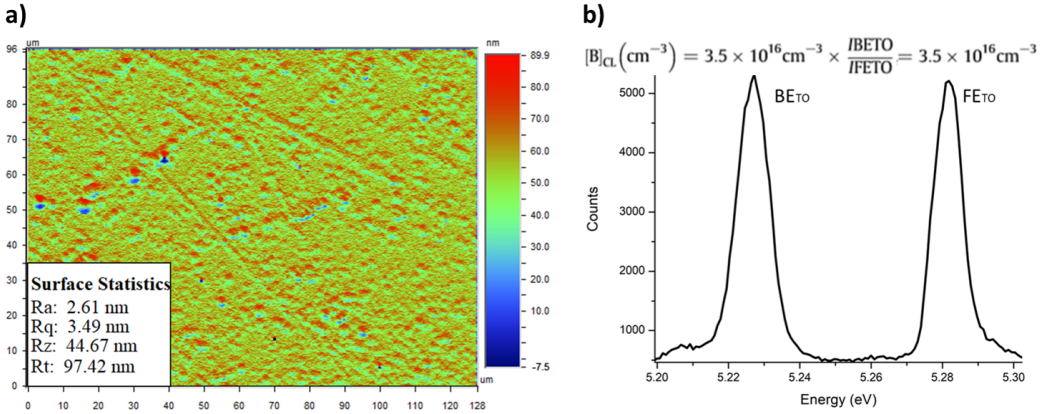

FIGURE 5.3: *a) Phase shift interferometry of the sample RB after the drift layer epitaxy. The rugosity of the surface remained similar to the substrate before the epitaxy. b) CL 5K exciton spectra showing FE^{TO} and BE^{TO} peaks. The ratio between the two peaks is associated with a doping level of $N_A = 3.5 \cdot 10^{16}\ cm^{-3}$ [164].*

growth in order not to damage the mask. A pressure of 33 Torr and a 200 sccm flow are used, reaching temperatures over 1150K. Just after, methane and a diluted mix of H_2 and diborane are injected in the mixture reaching temperatures of 1200K with concentrations of B_2H_6/H_2 of 1200 ppm and CH_4/H_2 of 4%. These conditions give rise to a heavily doped layer beyond metallic transition. The growth lasts 3 minutes for a thickness of 120 nm as measured by optical profilometry. Surprisingly, for most of the growths performed, the mask was completely removed after the growth in most of the sample. However, no p+ growth related to this phenomena was found thus suggesting that the mask was lifted due to thermal compression when cooling down the sample after the growth in the chamber. After the growth, the sample is again cleaned with acqua regia to remove the rest of the metal mask and a triacid treatment to remove possible graphitization on the surface. An optical image together with a phase shift interferometry (PSI) image of a feature of the p+ growth is shown in the figure 5.4.

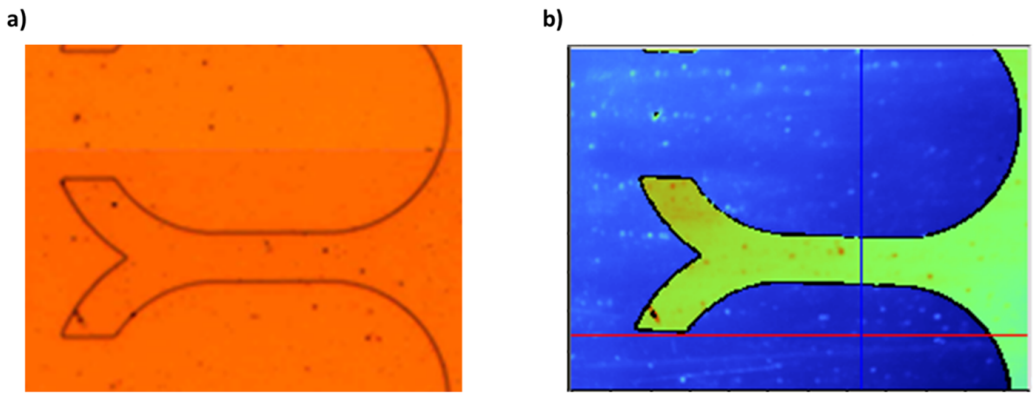

FIGURE 5.4: *a) Optical image of a p+ feature of the sample RB . b) Phase level interferometry image of the same feature.*

5.2.3 Contacts fabrication and surface oxygenation

Ohmic contacts were selectively deposited on top of the p+ growth based on a stack of titanium (30 nm), platinum (30 nm) and gold (270 nm) making use of lift-off photo-lithography process procedure described earlier in the subsection 3.1.2 and followed by a 750 K annealing to reduce the contact resistance. A thick gold layer was deposited in this device in order to facilitate the wire-bonding process. A 300°C, low pressure ozone treatment was then applied to diamond surface in order to make it oxygen-terminated for its passivation and Schottky contacts fabrication. Again a standard lift-off photo-lithography process was used to pattern sputtered molybdenum, this defined the Schottky drain and gate contacts. Schottky contacts are composed only with molybdenum (300 nm) due to a constraint in the evaporation. The final micrograph of the sample RB is presented in figure 5.5.

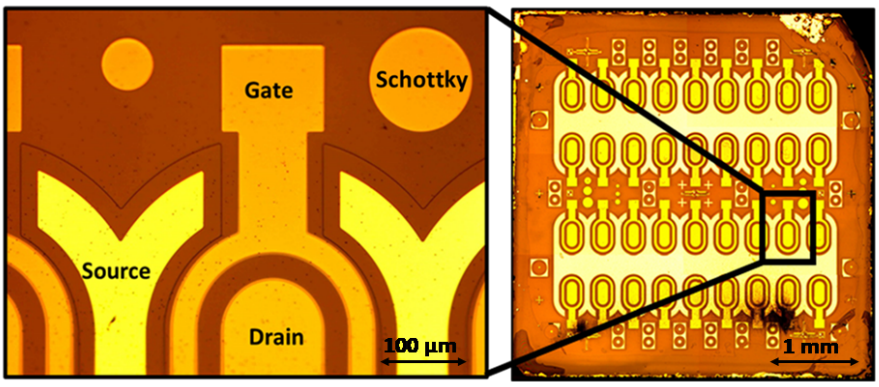

FIGURE 5.5: *Optical image of the fabricated sample RB: Device picture showing the ohmic source over the p+ diamond layer and the molybdenum Schottky drain, gate and test structure on the left. On the right, a full picture of the sample.*

5.3 Sample characterization

5.3.1 p+ layer and contact resistivity

Achieving a low ohmic contact resistance is fundamental for extracting the best performance of the present device, as it can be a limiting factor for the on-state performance. In order to minimize its resistance contribution, a selective p+ layer epitaxy was performed prior to the ohmic contact fabrication as explained earlier, in order to shrink the SCR width increasing the tunneling current. This approach was evaluated before the final sample fabrication presented in this chapter in a test sample, with the aim of acquiring low resistive contacts not limiting the final device performance. The full test sample geometry and layout is not specified here for its lack of interest but its epitaxy and metallic mask conditions are similar to the ones described earlier for the sample RB presented in this chapter. The viability of the approach and the contact resistance and the p+ resistivities are determined in this section using the Transmission Line Method (TLM) on this test sample, by measuring the

resistance between contacts for varying distances. A linear geometry was considered due to its simpler analysis and lower spacing. The TLM structure is 500 microns width and its p+ thickness is 120 nm (as in the sample RB) with variable distances between contacts of 50 and 400 microns.

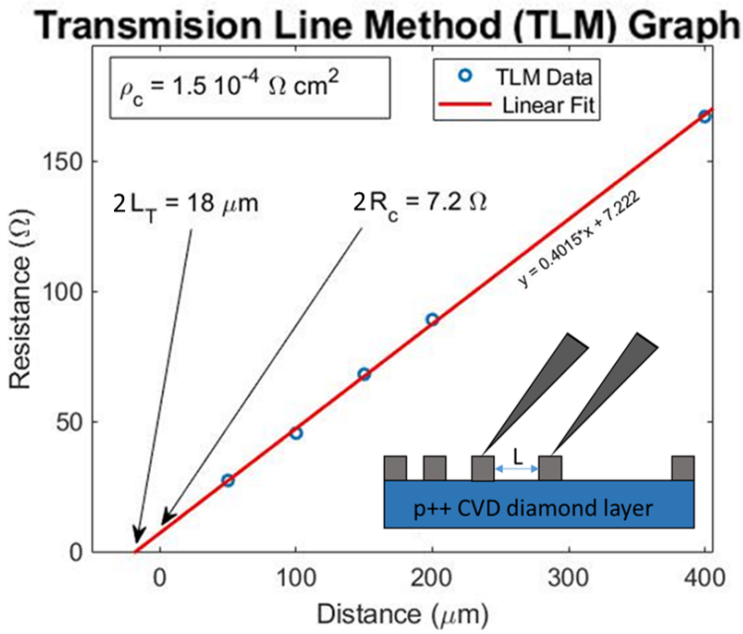

FIGURE 5.6: *Transmission Line Method (TLM) on a test sample to determine the p+ and contact resistivities.*

The resistivity of the 120 nm heavily doped layer, extracted from the resistance versus distance plot shown in figure 5.6, is 20 mΩ·cm. This value is much lower than the expected p-type channel layer resistivity, around $\sim 2\Omega\cdot$cm at 500 K and no compensation. Therefore, using this recipe, the p+ resistance will be negligible for the transistor performance as a result of its lower resistivity and smaller current path length versus the drift layer. The extracted resistivity is compatible with a doping density around $5 \cdot 10^{20}\ cm^3$.

The contact resistance R_C extracted is 3.6Ω at RT from the y-intercept in figure 5.6, attributed to the metal/diamond interface resistance as the the metal contribution is expected to be orders of magnitude lower and it is thus negligible. The contact resistivity is thus:

$$\rho_C = R_C L_T W_C \tag{5.1}$$

Where W_C is the width of the contact and L_T is the transfer length, as in a lateral geometry the current is flowing only through the edge of the contact up to the transfer length. Using $L_T = 9\mu m$, $W_C = 500\mu m$, a contact resistivity of $\rho_C = 1.5 \cdot 10^{-4}\ \Omega \cdot cm^2$ is obtained. Despite being a high value for the contact resistance compared with similar growths performed at our lab and bibliographic references, it is sufficiently low to not affect RBMESFET on-state performance. Therefore, this approach is validated and it used in the final sample RB fabrication as described earlier. Furthermore, the on-state current expression 2.42 derived in the second chapter is based on the hypothesis of negligible ohmic contact and p+

resistances, which is in agreement with the presented results.

5.3.2 Transfer characteristics at RT

In figure 5.7, room temperature measurements of the drain current I_{DS} are shown for V_{DS} = -25V to V_{DS} = +25V, with the gate voltage ranging from V_{GS} = 0V to -1.2V. For V_{GS} = 0V no drain current is observed, hence the transistor is normally-off; the threshold voltage (V_{TH}) is thus V_{TH}=0 V as current starts flowing at higher negative values of V_{GS}. The upper level of the gate voltage is limited to -1.2 V because the gate-source Schottky region becomes conductive leading to excessive I_{GS}. While the transistor is off at V_{TH}=0, it reaches $\sim$ 1.5 $\mu A/$mm at $V_{GS} = -0.8V$ and $V_{DS} = -25V$. The leakage current under reverse bias conditions is less than the detection limit of the system (pA). Due to its RB nature, the transistor characteristics are described by the thermionic emission of the Schottky drain with a gate and drain modulated channel resistance. The turn-on voltage for the Schottky drain is $V_{DS} = -0.8V$. From this voltage, the current increases limited by thermionic emission until the channel (variable) resistance becomes relevant and, at greater V_{DS}, dominant. Due to the normally-off character of the transistor with $V_{TH} = 0V$, the pinch-off voltage (V_p) must be similar to the Schottky contacts built-in voltage $V_p = 1.72V$ (see next section). Therefore, the channel is pinched-off for the V_{DS} values where I_D starts to be also limited by the channel resistance.

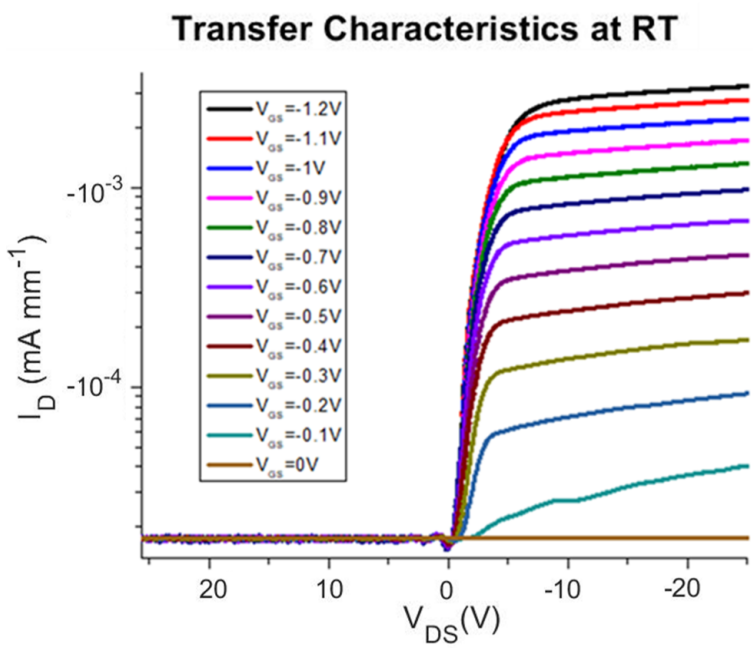

FIGURE 5.7: *Room temperature transfer characteristics for the normally-off RBMESFET at different gate voltages. The transistor is off at V_{GS}=0 and reaches $\sim$ 1.5 μ A/mm at V_{DS}=-25 V and V_{GS}=-0.8 V. No leakage current is observed in reverse.*

The drain current density, in the $\mu A/mm$ range is modest, but this is to be expected given the activation energy of 0.37eV for boron acceptor states at the doping level present in the

channel; indeed, at the room temperature measurements reported in figure 5.7 less than 1% of the boron acceptor states will be activated and contributing to conduction. Furthermore, the normally-off character implemented allows a very thin effective channel thickness that impact the on-state performance of the device. Anyways, according to the model 2.42, such current level is to be expected for a high compensation in the drift layer of around 20%. It can be observed that the values of current density at RT and $V_{GS} = -0.8V$ from figure 5.7 match those of the figure 2.14 if the current is divided by the channel length (68 microns). However, such high compensation value is unexpected. In fact, due to the very thin channel, the abrupt SCR approximation might be not accurate as the current is flowing over a very thin region of the sample between the Schottky and PN junction SCRs. This fact might explain the need of using such a high unexpected value of compensation to obtain a similar current level from the 1D model compared with the experimental data.

This successful implementation of a normally-off regime RBMESFET here is obtained by combining the top depletion region induced by the Schottky gate contact with the back depletion region induced by the p-n junction between the n-type substrate and the p-type channel. The thickness and the doping level of the epilayer were carefully chosen such that the channel would be exactly depleted at 0V to archive the off condition but still having control of the channel at negative V_{GS}. The effective transconductance in the saturation regime is calculated as 16 μS/mm for V_{GS} = -1V. This value is similar to the value obtained by Umezawa et al. [102] for a normally-on diamond MESFET, with an effective measured room temperature transconductance of 10 to 18 μS/mm depending on L_{DG} distance, and with those of Liu et al. [173, 174].

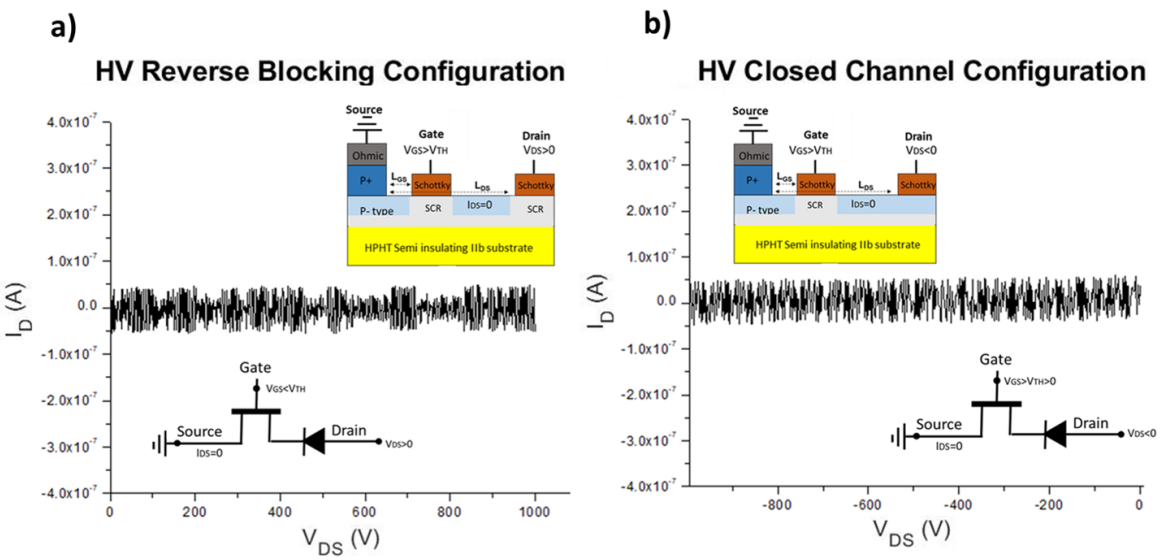

FIGURE 5.8: *High voltage transfer characteristics for the a) closed channel configuration and b) reverse blocking configuration of the RBMESFET both sustaining 1 kV.*

The off-state characteristics at high voltage (HV) for the device are presented in the figure 5.8. In the figure 5.8 (a), the reverse blocking configuration ($V_{GS} = 5V$ and $V_{DS} > 0$)

characteristics up to $V_{DS} = 1kV$ are presented with no breakdown or leakage current detected up to the detection limit (10 pA). Similarly, in the figure 5.8 (b), the closed channel configuration ($V_{GS} = 5V$ and $V_{DS} < 0$) characteristics up to $V_{DS} = -1kV$ are presented with no breakdown or leakage current detected. Its characteristics after the HV test were again measured with the same conditions as in figure 5.7 showing the same results guaranteeing that the stress caused by the HV did not degrade the properties of the device. The transistor is thus able to block 1 kV in both configurations successfully accomplishing its objective, sustaining an 1D estimated electric field (using eq. 2.27) of 1.5 MV/cm. Higher voltage measurements were not performed in order not to break the device for its future implementation in a power converter. The breakdown voltage was only reached during the 1 kV test for a single device in the sample RB, as the leakage current between source-gate increased rapidly at 750 V degrading its behaviour irreversibly.

5.3.3 Gate characteristics

The molybdenum Schottky gate used here allows the control of the channel conductivity in the device by depletion of channel carriers. The gate-source I-V and C^{-2}-V (at 1kHz) characteristics of the Schottky gate are shown in figure 5.9, measured at RT. The C^{-2} curve is expected to show a linear behavior in the depletion region of the C-V curve described by eq. 2.24. At 0V the channel is completely depleted under the gate and as $+V_{GS}$ increases further depletion happens laterally from around the gate perimeter. As V_{GS} becomes increasingly negative, lateral expansion is absent and the vertical depletion, directly under the Schottky contact represents the entirety of the space-charge-region (SCR), itself diminishing with increasing negative V_{GS}. In the Mott-Schottky plot (fig. 5.9), both lateral and vertical depletion capacitance regions under the gate can be distinguished and are fitted with dashed lines. Taking a linear fit for the capacitance over the first (laterally dominated) region considering the gate perimeter and channel thickness, a doping level of $4 \cdot 10^{16}\ cm^{-3}$ can be deduced. In the range of voltages lower than 0V, from $\sim$ -0.4 to -0.9 V, the vertical depletion regime in which the SCR expands directly under the Schottky gate is distinguished (the second dotted region). Here, a linear fit shows a free carrier density of $\sim 10^{16}\ cm^{-3}$ from the slope and a V_{BI} = 1.72V is deduced from the intercept with the x-axis. For this doping level, the distance from the Fermi level to the valence band of diamond is ϕ_f = 0.29 eV. The Schottky barrier height deduced from the built-in voltage is thus 2.01 V. The strong difference between the V_{BI} found in this sample and those of chapter 3 and 4 is attributed to the different oxygen functionalization method used.

If an n-type carrier density of $\sim 10^{19}\ cm^{-3}$ for the (N-doped) substrate and the deduced carrier level of the p-type layer, a 280 nm SCR can be estimated for the p-n junction that forms between the channel epilayer and the substrate. From the extracted value of V_{BI}, a Schottky SCR of 170 nm is estimated at 0V. Therefore, as the Schottky SCR joins the p-n SCR at approximately 0V a total p-type layer thickness of 450 nm is extracted. This calculation can only be an estimate since the actual carrier concentration in the n-type substrate at the temperatures concerned is unknown, given the E_A for substitutional N of $\sim$1.7eV and an

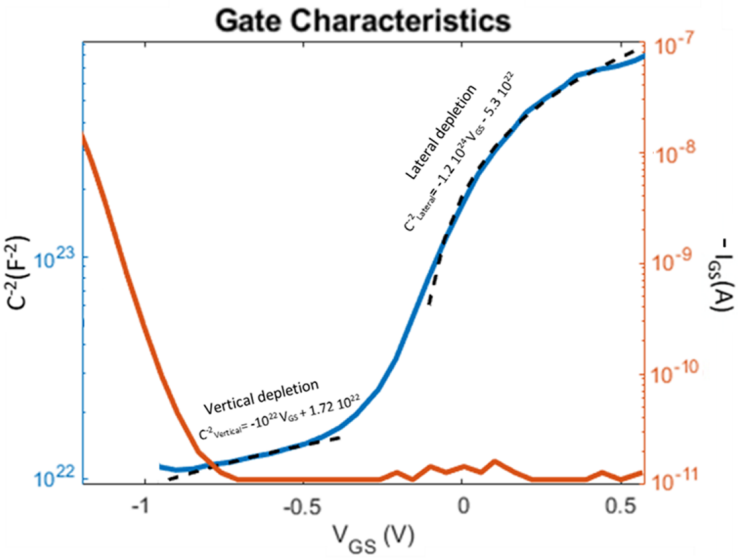

FIGURE 5.9: *I-V characteristics (in red) and Mott-Schottky plot (in blue) for the molybdenum Schottky gate. Lateral and vertical depletion capacitance under the gate are fitted with dashed line. $N_A - N_D$ extracted from the slope of the C^{-2} plot is 10^{16} cm^{-3} for the vertical depletion region and $4 \cdot 10^{16}$ cm^{-3} for the lateral. From the intercept with the x axis a V_{BI}= 1.72V is extracted.*

unknown level of defect-induced compensation. However, the high difference in doping level between drift layer and substrate makes this depletion region rather independent of small variations to the substrate doping and compensation levels. With regard to the I_{GS} data in figure 5.9 (red line), the Schottky gate shows no measurable leakage current at positive bias, while the current at negative bias starts increasing above -0.75V, reaching -10nA ($\sim$ 10% of the on-channel current) at $\sim$1.2V. From this I-V curve, an ideality factor of $\sim$1.67 and a Schottky barrier height of $\sim$1.02 eV are deduced. The disparity between the barrier height derived from capacitance and current measurements is attributed to homogeneities over the interfacial region; the capacitance extraction tends to give an averaged value while the current extraction will be influenced by regions which display a lower barrier. These are likely attributable to local inhomogeneities of the interface chemical bonding configuration between O-terminated diamond and molybdenum. The ideality factor of 1.67 may arise due to the formation of an ultra-thin insulating layer between diamond and molybdenum. However, here this relatively high ideality factor can be an advantage for the Schottky gate, as it allows the V_{GS} values to be high (up to -1.2V) toward the Schottky on-state, effectively retracting the space charge region under the gate and opening the channel without having a high value of I_{GS}. The disparity between the measured values $N_A - N_D$ values is most probably due to the small fitting range and its dispersion discourage the comparison with the $N_A - N_D = 3.5 \cdot 10^{16}$ cm^{-2} value extracted from cathodoluminescence to figure out the compensation level.

The forward gate current I_{GS} is shown in figure 5.10 for different temperatures up to 400K. While the turn-on voltage at RT is -0.75V as mentioned above, it decreases up to -0.4 V

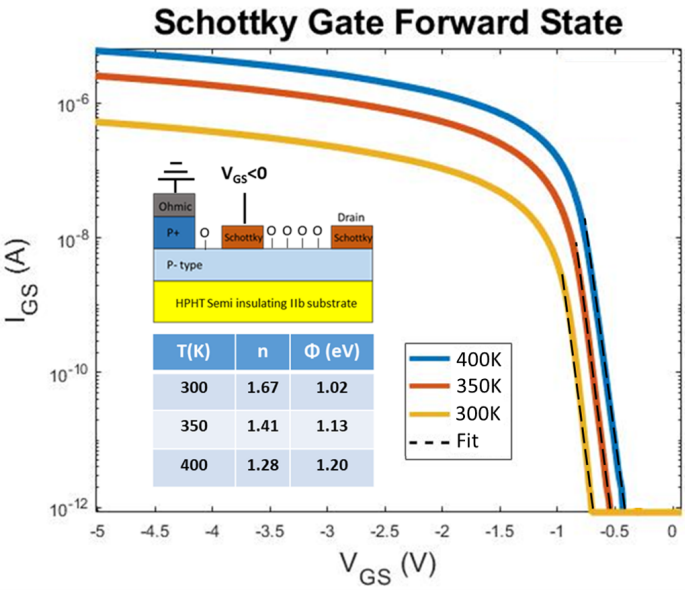

FIGURE 5.10: *I_{GS} versus V_{GS} represented at RT, 350 K and 400K. The ideality factor decreases from 1.67 at RT to 1.28 at 400K while the barrier increases from 1.02 eV to 1.2 eV.*

at 400K due to an enhanced thermionic effect. This fact will limit the maximum negative V_{GS} available to -0.8V in order not to increase the I_{GS} substantially while operating the transistor at high temperature. The ideality factor and the Schottky barrier of the gate are also shown in 5.10 for the different temperature used. A decrease in the ideality factor from 1.67 at RT to 1.28 at 400K and an increase of the barrier from 1.02 eV to 1.2 eV are extracted from the I_{GS} curves by fitting eq. 2.10. These results further support the hypothesis of a locally inhomogeneous Schottky barrier, since the increase in the thermal energy allow diamond holes to overcome higher barriers presents at the interface thus resulting in a higher barrier extracted at higher temperatures. Analogously, the ideality factor is reduced toward n=1 with increased temperatures as the thermionic mechanism becomes increasingly dominant making the Schottky barrier variation with the forward bias inappreciable.

5.3.4 Transfer characteristics vs temperature

As noted above, the boron dopant atoms become activated as acceptor states with an energy of ∼0.37 eV. Thus, to improve the device output performance, measurements at higher temperatures have been made. The drain current I_{DS} has been measured in the range 300K to 425K, again for V_{DS} = -25V to V_{DS} = +25V, with a fixed gate voltage of V_{GS} = -0.8V. This data is plotted in figure 5.11 a). Once again FET I-V curves can be understood as lateral Schottky diodes with gate and drain modulated channel resistance. At elevated temperatures, increased diamond conductivity and earlier drain turn-on voltages are recorded due to carriers thermal ionization and increased thermionic emission, respectively.

The devices remain normally-off in character, with no measurable leakage current up to 425K in reverse bias. Whereas at V_{GS} = - 0.8V at room temperature an I_{DS} of around 1.5

µA/mm was observed, the same V_{GS} value now yields an I_D of ∼70µA/mm at 425K. The maximum transconductance in the saturation regime at this temperature is $260\mu S/mm$ as it can be observed in figure 5.11 b), where the transconductance is plotted versus temperature at $V_{DS} = 10V$. This is a high value for this normally-off device with bulk conduction; for example, even for a normally-on MESFET, Umezawa and co-workers [102] reported a significantly lower transconductance of $61\mu S/mm$ at 573K. This is attributed to the superior doping level used in this work sample while the value of the Schottky barrier for the molybdenum gate used here, and the molybdenum contact stability at high temperatures contribute to this success. For comparison a significantly higher transconductance value of 11 mS/mm has been reported for a normally-off H-terminated device [97]. This form of device with surface-transfer doping, whereby surface diamond electrons accumulate in the (adsorbate or metal oxide covered) C-H layer leads to a 2D-like p-layer in the diamond surface which is inevitably easier to deplete than a channel region comprising a fraction of a micron of p-type material. However, reproducibility, long term stability and propensity to thermal degradation issues hamper the application of devices using surface-transfer doping.

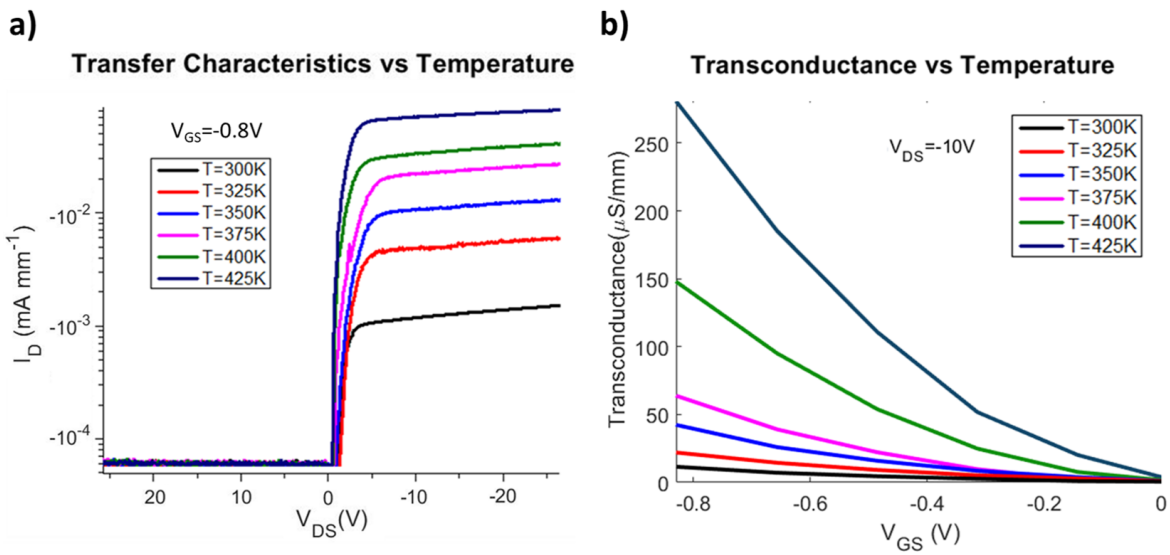

FIGURE 5.11: *a) Transfer characteristics for the normally-off RBMESFET at V_{GS}=-0.8V versus temperature. No leakage current is observed in reverse BIAS. The current at 425K is increased by a factor ∼ 40 compared to RT reaching $70\mu A/mm$ at -25V. b) Transconductance vs V_{GS} plot for the normally-off RBMESFET at $V_{DS} = 10V$ versus temperature.*

The improvement in the current level when higher temperatures are used is primarily due to the ionization of boron acceptor impurities in the p-layer and the reduced compensation effect; the boron impurity level is rather deep (0.37eV) and not fully ionized at RT, as mentioned above. This increase in the on-current can be explained by the semi-empirical mobility model plus the carrier density increase at higher temperatures. The operation at high temperature shows the potential for boron-doped diamond bulk conduction while the gate control over the channel remains stable. This fact shows the significant advantage of

working with a bulk-type conduction for high temperature operation versus H-terminated diamond (surface-transfer doping) FETs, which typically display thermal instability.

Quantitatively, the increment of around 40 times the current level experiments when reaching 425 K is rather high. In fact, this could be again a sign of compensation as the temperature tend to mitigate its effects leading to a more pronounced temperature dependence of the conductivity of the layer. In the figure 2.14, the theoretically expected current level versus temperature is plotted using the device parameters using the model developed 2.42. A compensation of 20% is able to explain up to a 30 times increase over this range of temperatures. This further support the hypothesis formulated earlier were a high compensation might be responsible for the obtained current level. However, the slight discrepancies between the model and the experimental data might come from the consideration of a sharp SCR and a fully channel gated transistor.

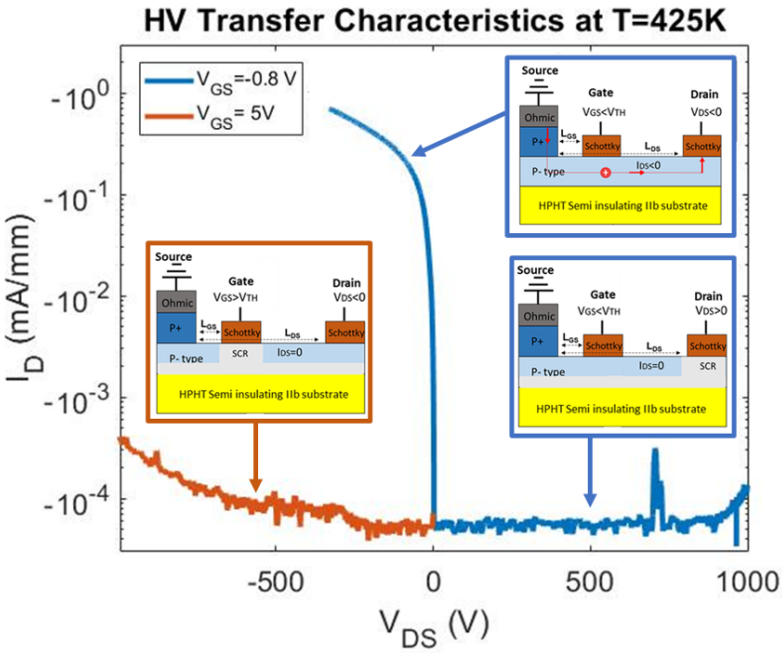

FIGURE 5.12: *HV transfer characteristics for the RBMESFET at 425K for the close channel configuration with $V_{GS} = 5V$ in the red curve and for the on-state and Schottky diode configuration in the blue curve with $V_{GS} = -0.8V$.*

Moreover, the HV transfer characteristics of the RBMESFET at 425K are presented in the figure 5.12. On one hand, the I_D measured from -300 V to 1kV at a V_{GS}=-0.8 V is displayed as the blue curve. This curve passes through the open channel configuration in which the on-state is observed, similar to what is represented in figure 5.11 a), to the Schottky diode configuration which remains stable without leakage current up to 1 kV. Also, the off-state behaviour in the closed channel configuration at 425 K is represented with the red curve. A blocking voltage capability of 1 kV is again sustained. Not presented here, but as well sustaining 1 kV is also the RBMESFET configuration. These result are noteworthy since the 1 kV requirement is sustained not only at RT as shown in 5.8 but at the best working temperature for the on-state of the device.

5.3.5 Higher temperature effects

Due to the followed fabrication process, no etching step was needed to engineer the device reducing possible failures and performances degradation. However, during characterization it became evident that leakage currents between the source of the transistor and the back face of the sample are always present in the level of μA. This leakage current is attributed to the p+ slight encapsulation of the sample edges, making the current able to flow from the ohmic source to the p layer through its p+ underneath and then flow through the edge of the sample again through p+. This would explain the current level as the resistance would be dominated during the p-type layer conduction. This hypothesis was indeed confirmed after further test samples were fabricated since no leakage was recorded between top and bottom sample faces prior to the p+ growth. The consequences of this fact are that all the electrical measurements performed in the sample were carried out with a floating substrate. At relatively low temperatures such as those used in figure 5.11 a), no important effect is expected since the type Ib substrate is insulating and thus the p-n junction SCR does not respond to variations of V_{GS} or V_{DS}. However, once the temperature reach 450K the substrate start to be conductive as the nitrogen dopant is ionized. This effect becomes dramatic for higher temperature operation of the transistor and its represented in the figure 5.13.

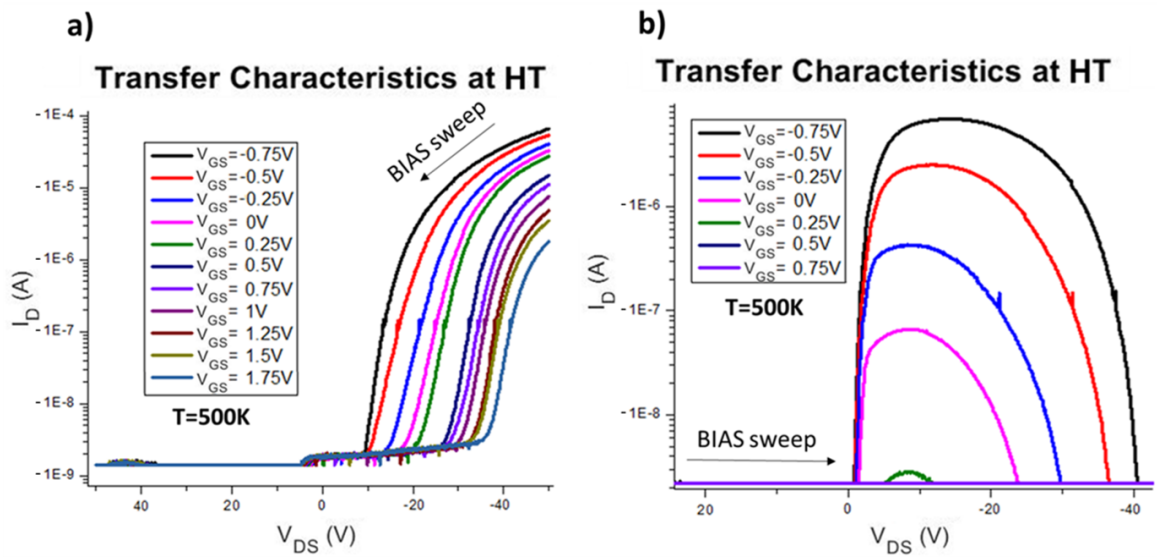

FIGURE 5.13: *Transfer characteristics for the RBMESFET at 500K for negative to positive V_{DS} sweep in (a) and viceversa in (b). The high temperature operation ionize the substrate dopants causing the values of V_{GS} and V_{DS} to affect the SCR of the back p-n junction preventing the normal transistor operation.*

In figure 5.13 (a) and (b) the transfer characteristics of the RBMESFET are represented at 500K for negative to positive BIAS sweep and viceversa respectively. The high temperature operation ionize the substrate dopants causing the values of V_{GS} and V_{DS} to affect the SCR of the back p-n junction preventing the normal transistor operation. For negative to positive BIAS sweep, the transistor effectively opens but before the sweep is over the p-n

SCR respond to the negative V_{DS} closing the channel at V_{DS}>10V. The turn on V_{DS} voltage is controlled by the BIAS sweep speed as the response time from the SCR is of the order of seconds at this temperature. Moreover, the normally-off behaviour is lost as evidenced in figure 5.13 (a) due to the non controlled variations of the p-n SCR. For a positive to negative BIAS sweep, the current grows up to a maximum value around V_{DS} = -10 V depending on the V_{GS} and then closes again due to the negative V_{DS} affecting the p-n SCR during the sweep. A quantitative explanation of this phenomena would need time-dependent 2D simulations and is not intended in this manuscript due to its lack of interest as this undesirable effect can be solved during fabrication. Anyways, this effect is dramatic for the RBMESFET as the best working temperature for the p-type diamond layer is around 500K for its doping level and the on-state of the device is limited to 425K operation.

5.3.6 Failure analysis

The fabricated sample RB is composed of 36 RBMESFET transistors with two sets of 18 sharing a common source. The normally-off transfer characteristics and gate control over the channel were presented in lasts sections with successful operation up to 425K. However, more than half of the fabricated transistors does not work due to different fabricational associated failures. In figure 5.14, the micrograph of the sample RB is again presented highlighting the working and non working transistors plus showing a zoomed micrograph of two non-working devices. The different failures that lead to not working transistors are:

1. Gate to drain or source to drain shortcut due to a undesired p+ growth under the mask. This is illustrated in the left device of the figure 5.14 zoomed micrograph for the case of a gate to drain shortcut.

2. Leaky gate or drain again due to a undesired p+ growth under the mask. This is illustrated in the left device of the figure 5.14 zoomed micrograph for the case of a leaky gate. In fact, this device shows a near-ohmic behaving drain thus performing rather closely to an hybrid MESFET - RBMESFET.

3. Fully depleted layer at maximum negative V_{GS} applicable. In these cases, the small variations of thickness and doping level along the full sample make the threshold voltage to vary sufficiently so that the channel cannot be opened with the V_{GS}.

Also noteworthy is that the thickness and doping variations along the sample RB yield most of the working devices to be normally-on with a V_{TH}<0.75V and only the three devices near the bottom-left corner showed similar characteristics with a normally-off behaviour. This should not be regarded as a disappointment due to the extreme precision needed for accomplishing such reproducibility. Indeed, a 0.75 V threshold voltage instability is explained by 30 nm variation in the layer thickness (considering a constant doping level of $N_A = 3.5 \cdot 10^{16} cm^{-3}$ with no compensation) and thus, only a 6% p-type layer thickness dispersion is found throughout the sample in the working devices. This is a rather small layer inhomogeneity even without considering possible substrate effects on the V_{TH} that could

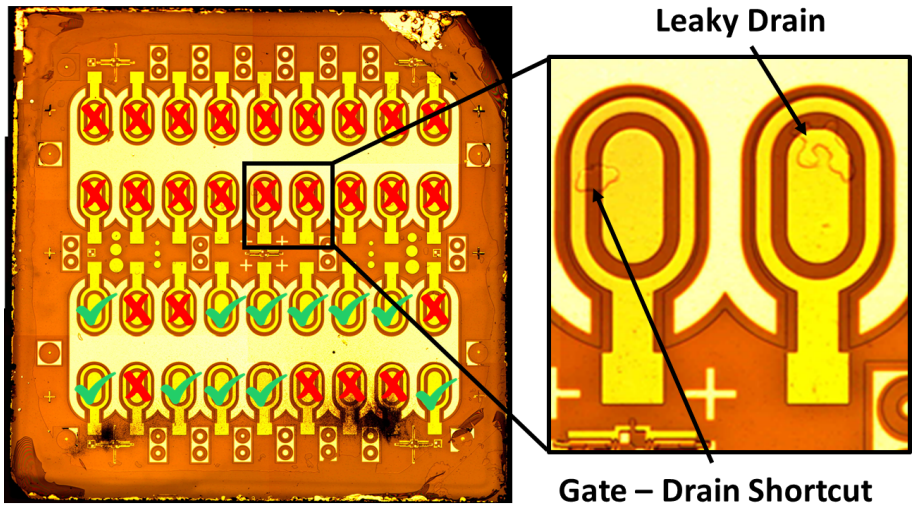

FIGURE 5.14: *Micrograph of the sample RB showing the working transistors in the sample and the p+ features that create leaky drains and gate-drain shortcuts.*

also be responsible for those variations. Pushing the limits of reproducibility and precision in diamond epitaxy and wafers fabrication are still mandatory for accomplishing a 100% yield sample, but a clear demonstration of the advances in diamond technology and future are represented here by these accomplishments.

5.4 Conclusion and future steps

A >1kV normally-off lateral reverse-blocking (Schottky Drain) MESFETs based on molybdenum Schottky contacts on O-terminated boron doped diamond have been fabricated. Precise control over epilayer thickness and doping level have been achieved such that full depletion of the channel arises without an applied gate bias with the possibility to open the channel at negative V_{GS}. The devices display undetectable leakage current and a current of 1.5 µA/mm in the on-state at RT. Importantly, the transistor blocking capabilities were evaluated to be >1kV even at its maximum working temperature of 425K displaying no leakage current and after the HV stress, presenting non-changed reproducible characteristics. Higher temperature characterization (425K) reveals augmented transistor on-state capabilities due to fuller ionization of the boron dopant atoms, with the transistor reaching a current level of 70 $\mu A/mm$ and a transconductance of 260$\mu S/mm$. However, its working temperature is limited to 425K, below the optimal 500-550K, due to the non-grounded p-n junction between the p-type drift layer and the semi-insulating Ib substrate. Anyways, the high breakdown voltage, the relatively high temperature operation capabilities, normally-off behavior and diamond inherent radiation hardness as a semiconductor, make these devices an excellent approach towards the goal of achieving diamond transistors for high temperature, high voltage and harsh environment applications.

Some easy adjustments in device such as the optimization of the metallic mask and p+ growth would give rise to a higher yield of working devices throughout the sample. This optimization should also focus on the removal of the consistently observed undesired p+ growth on the substrate edges. Alternatively, an etching step could be added in order to isolate the path of the current for the suppression of leakage between source and substrate back face to effectively ground the substrate opening the route for higher temperature operation. In addition, the introduction of field plates to the design may beneficially affect the field profile in the Schottky contact regions allowing higher blocking voltage capabilities. Further improvements should focus in the development of vertical structures of this device. For normally-off MESFETs, where the channel thickness is designed to be extremely small, the benefits toward a vertical architecture are enormous resulting in up to 100 times lower specific resistances.

Conclusions and perspectives

The potential of diamond for power electronics was introduced in chapter 1 with special emphasis in its outstanding properties, diamond peculiarities and demonstrated devices. The optimization of diamond components is crucial for their future roadmap for power electronics, as a true demonstration of diamond potential still lacks, and it will attract interest from research and companies into it further pushing the development of devices and eventually ending up in their commercialization. In this context, this thesis was dedicated to the development of Schottky barrier diodes and Schottky based transistors (MESFET) based on p-type diamond to demonstrate diamond unleashed performance. The main conclusions from this work are reviewed hereafter:

- **Chapter 2**

  The theoretical framework and the state of art practical bottlenecks for the p-type diamond Schottky based power devices were introduced and discussed in this chapter. Diamond on-state resistance was shown to be minimized at elevated temperatures (550K). Concerning the off-state, two limiting mechanisms have been introduced and discussed: leakage currents and avalanche breakdown. Within the implemented models, the ultimate diamond capabilities were shown to outperform those of SiC specially at high temperature. On the other hand, leakage currents are evaluated within a novel model for the leakage current in diamond. In order to extract diamond full off-state potential at its optimal temperature, a metal that forms a ϕ_b of at least 1.5 eV is needed for preventing leakage currents at high temperature. Once that such metal is found, diamond Schottky diodes sustaining up to tens of kV could be fabricated. Concerning diamond transistors, the concept of a reverse blocking MESFET was introduced and its working modes explained. The on-state current is modelized through a 1D approximation within the gradual channel approximation. Lastly, the performance of such transistor is evaluated and the benefits and advantages of a normally-off transistor presented.

- **Chapter 3**

  A dedicated experimental investigation of the molybdenum and zirconium Schottky contacts was presented in this chapter. The TEM and XPS extracted compositional profile was correlated to zirconium and molybdenum Schottky contact electrical performance. The ozone passivation, demonstrated to be crucial in reducing leakage currents, was shown to oxidize the molybdenum and zirconium layers. While this did not greatly affect the molybdenum on-state characteristics, the degradation of the

zirconium contacts was explained as a result of the high concentration of oxygen in the interface. On the other hand, the potential profiles along the contacts edges extracted from KPFM proved the great passivation capabilities of the oxygen-terminated diamond yielding a $\phi_{BB} = 2.46$ for the (100) oxygen-terminated p-type diamond. The measurements also showed that the molybdenum V_{BI} is lower than the oxygen-terminated V_{BB} while the opposite situation was found for zirconium. Lastly, AB initio calculations to investigate the molybdenum and oxygen-terminate diamond showed a Schottky barrier height for molybdenum of ϕ_b=2.45 eV and revealed ionic-like oxygen-molybdenum bonding at the interface.

- **Chapter 4**

  Two different Schottky diode samples were fabricated in this chapter. The first sample demonstrated the success of the fabrication process used, based on molybdenum, with the crucial importance of the surface passivation treatment for the blocking voltage capabilities. The superiority of this molybdenum versus zirconium as Schottky contact was demonstrated as the former had higher Schottky barrier, lower ideality factor, better thermal stability and better blocking voltage capabilities. The second sample implemented the developed fabrication process of molybdenum base Schottky contact into an HV design. It successfully demonstrated >1kV breakdown voltage capabilities with contacts sustaining (a low estimate) electric field of 2.2 MV/cm. The molybdenum Schottky contacts developed in this work demonstrated consistently suitable performances for extracting diamond HV potential at high temperature. The leakage current phenomenon was addressed in this chapter and by following the fabrication process developed here, future diamond Schottky diodes will be able to use as much as a 60% of low doped diamond breakdown field.

- **Chapter 5**

  A >1kV normally-off lateral reverse-blocking (Schottky Drain) MESFETs based on molybdenum Schottky contacts on oxygen-terminated boron doped diamond was fabricated and characterized in this chapter. High temperature characterization (425K) revealed the augmented transistor on-state capabilities, with the transistor reaching a current level of 70 $\mu A/mm$ and a transconductance of 260$\mu S/mm$. However, its working temperature is limited to 425K, below the optimal 500-550K, due to the non-grounded p-n junction between the p-type drift layer and the semi-insulating Ib substrate. Anyways, the high breakdown voltage, the relatively high temperature operation capabilities, normally-off behavior and diamond inherent radiation hardness as a semiconductor, make these devices an excellent approach towards the goal of achieving diamond transistors for high temperature, high voltage and harsh environment applications.

The perspectives of this work are separated for diodes and transistors:

- **Schottky diodes perspectives**

Even if a partial solution to leakage currents, a major problem for Schottky diodes, was demonstrated; the future for the HV Schottky diodes will be attached to the development of the epitaxy. Thicker drift layers ($\sim 100\mu m$) are needed in order to be able to fabricate NPT devices allowing the fabrication of diodes in the 10 kV range. Moreover, the reduction of killer defects in thick layers will allow the optimal performance with higher yield in the fabricated samples. The etching process development will also make a big advance for classical pseudovertical architectures freeing the thickness limitations of diodes together with making available the parallelization of diodes resulting in better on-state performances. Also, the use of edge terminations structures will also ameliorate the off-state reproducibility between different contacts. All these advances would allow the fabrication of diamond diodes that reach consistently higher breakdown voltages than now (as high as 10 kV) with close to ideal performances making use of the developed molybdenum contacts.

- **MESFET perspectives**

  The removal of the consistently observed undesired p+ growth on the substrate edges will allow MESFETs to work at much elevated temperatures displaying much better on-state performances. An additional etching step can suppress the leakage between source and substrate back face to effectively ground the substrate. In addition, the introduction of field plates to the design will allow higher blocking voltage capabilities. Further improvements should focus in the development of vertical structures of devices. For normally-off MESFETs, where the channel thickness is designed to be extremely small, the benefits toward a vertical architecture are enormous resulting in up to 100 times lower specific resistances.

In summary, the progress made during this thesis in the optimization of Schottky contacts allowed to push the off-state and reproducibility of vertical diamond Schottky diodes. Future diodes will benefit from the shown results, as the application of the Schottky contacts developed in this thesis together with thicker diamond drift layers could achieve the benchmark of sustaining 10 kV. On the other hand, the demonstration of a >1kV normally-off lateral reverse-blocking (Schottky Drain) MESFETs was the first of its kind. The unusual characteristics of this transistor show the precision acquired in diamond epitaxy technology. A future transition toward vertical transistors using the developed technology will unleash diamond MESFET potential performance.

Bibliography

[1] J. Millan, P. Godignon, and A. Perez-Tomas. "Wide Band Gap Semiconductor Devices for Power Electronics". In: *Automatika* (2012), pp. 107–116. DOI: 10.7305/automatika.53-2.177.

[2] L. M. Tolbert. "Power Electronics for Distributed Energy Systems and Transmission and Distribution Applications: Assessing the Technical Needs for Utility Applications". In: (2005). DOI: 10.2172/885985. URL: https://www.osti.gov/biblio/885985.

[3] E. A. Jones, F. F. Wang, and D. Costinett. "Review of Commercial GaN Power Devices and GaN-Based Converter Design Challenges". In: *IEEE Journal of Emerging and Selected Topics in Power Electronics* (2016), pp. 707–719. DOI: 10.1109/JESTPE.2016.2582685.

[4] T. Kimoto. "Material science and device physics in SiC technology for high-voltage power devices". In: *Japanese Journal of Applied Physics* 54 (2015), pp. 040–103. DOI: 10.7567/JJAP.54.040103.

[5] A. Pala et al. "10 kV and 15 kV silicon carbide power MOSFETs for next-generation energy conversion and transmission systems". In: *IEEE Energy Conversion Congress and Exposition (ECCE)* (2014), pp. 449–454. DOI: 10.1109/ECCE.2014.6953428.

[6] T. Kimoto et al. "Progress and Future Challenges of SiC Power Devices and Process Technology". In: (2017), pp. 3–6. ISSN: 01631918. DOI: 10.1109/IEDM.2017.8268360.

[7] X. She et al. "Review of Silicon Carbide Power Devices and Their Applications". In: *IEEE Transactions on Industrial Electronics* 64 (2016), pp. 8193–8205. DOI: 10.1109/TIE.2017.2652401.

[8] N. Donato et al. "Diamond power devices: state of the art, modelling, figures of merit and future perspective". In: *Journal of Physics D: Applied Physics* 53.9 (Dec. 2019), p. 093001. DOI: 10.1088/1361-6463/ab4eab. URL: https://doi.org/10.1088/1361-6463/ab4eab.

[9] Y. Zhang, A. Dadgar, and T. Palacios. "Gallium nitride vertical power devices on foreign substrates: a review and outlook". In: 51.27 (June 2018), p. 273001. DOI: 10.1088/1361-6463/aac8aa. URL: https://doi.org/10.1088/1361-6463/aac8aa.

[10] R. R. Sumathi. "Review—Status and Challenges in Hetero-epitaxial Growth Approach for Large Diameter AlN Single Crystalline Substrates". In: 10.3 (Feb. 2021), p. 035001. DOI: 10.1149/2162-8777/abe6f5. URL: https://doi.org/10.1149/2162-8777/abe6f5.

[11] J. Y. Tsao et al. "Ultrawide-Bandgap Semiconductors: Research Opportunities and Challenges". In: *Advanced Electronic Materials* 4.1 (2018), p. 1600501. DOI: https://doi.org/10.1002/aelm.201600501. eprint: https://onlinelibrary.wiley.com/doi/pdf/10.1002/aelm.201600501. URL: https://onlinelibrary.wiley.com/doi/abs/10.1002/aelm.201600501.

[12] N. Yadava and R. K. Chauhan. "Review—Recent Advances in Designing Gallium Oxide MOSFET for RF Application". In: *ECS Journal of Solid State Science and Technology* (2020), p. 065010. DOI: 10.1149/2162-8777/aba729.

[13] S. B. Reese et al. "How Much Will Gallium Oxide Power Electronics Cost?" In: *FUTURE ENERGY* 3 (2019), pp. 903–907. DOI: 10.1016/j.joule.2019.01.01.

[14] S.I. Stepanov et al. "GALLIUM OXIDE: Properties and applications - A review". In: *Reviews on Advanced Materials Science* 44 (2016), pp. 63–83.

[15] Z. Feng et al. "MOCVD homoepitaxy of Si-doped (010) -Ga2O3 thin films with superior transport properties". In: *Applied Physics Letters* 114 (2019). DOI: 10.1063/1.5109678.

[16] J. Yang et al. "2.3 kV Field-Plated Vertical Ga2O3 Schottky Rectifiers and 1 a Forward Current with 650 V Reverse Breakdown Ga2O3 Field-Plated Schottky Barrier Diodes". In: *2018 76th Device Research Conference (DRC)*. 2018, pp. 1–2. DOI: 10.1109/DRC.2018.8442188.

[17] K. Konishi et al. "1-kV vertical Ga2O3 field-plated Schottky barrier diodes". In: *Applied Physics Letters* 110.10 (2017), p. 103506. DOI: 10.1063/1.4977857.

[18] H. Fu et al. "Demonstration of AlN Schottky Barrier Diodes With Blocking Voltage Over 1 kV". In: *IEEE Electron Device Letters* 38.9 (2017), pp. 1286–1289. DOI: 10.1109/LED.2017.2723603.

[19] H. Okumura et al. "AlN metal–semiconductor field-effect transistors using Si-ion implantation". In: *Japanese Journal of Applied Physics* 57.4S (Mar. 2018), 04FR11. DOI: 10.7567/jjap.57.04fr11. URL: https://doi.org/10.7567/jjap.57.04fr11.

[20] P. Reddy et al. "Schottky contact formation on polar and non-polar AlN". In: *Journal of Applied Physics* 116.19 (2014), p. 194503. DOI: 10.1063/1.4901954.

[21] A. Knauer et al. "Correlation of sapphire off-cut and reduction of defect density in MOVPE grown AlN". In: *physica status solidi (b)* 253.5 (2016), pp. 809–813. DOI: https://doi.org/10.1002/pssb.201600075.

[22] T. Y. Wang et al. "Defect annihilation mechanism of AlN buffer structures with alternating high and low V/III ratios grown by MOCVD". In: *CrystEngComm* 18 (2016), pp. 9152–9159. DOI: 10.1039/C6CE02130A.

[23] T. Taniguchi et al. "Appearance of n-Type Semiconducting Properties of cBN Single Crystals Grown at High Pressure". In: *Japanese Journal of Applied Physics* 41.Part 2, No. 2A (Feb. 2002), pp. L109–L111. DOI: 10.1143/jjap.41.l109. URL: https://doi.org/10.1143/jjap.41.l109.

[24] X. Zhang and J. Meng. *Chapter 4 - Recent progress of boron nitrides*. Ed. by Meiyong Liao, Bo Shen, and Zhanguo Wang. 2019. DOI: https://doi.org/10.1016/B978-0-12-815468-7.00004-4. URL: https://www.sciencedirect.com/science/article/pii/B9780128154687000044.

[25] P. Siddiqua, Michael S. Shur, and Stephen K. O'Leary. "Electron transport within bulk cubic boron nitride: A Monte Carlo simulation analysis". In: *Journal of Applied Physics* 128.18 (2020), p. 185704. DOI: 10.1063/5.0013183.

[26] W. J. Zhang et al. "Nucleation, growth and characterization of cubic boron nitride (cBN) films". In: *Journal of Physics D: Applied Physics* 40.20 (2007), pp. 6159–6174. DOI: 10.1088/0022-3727/40/20/s03. URL: https://doi.org/10.1088/0022-3727/40/20/s03.

[27] N. Sanders and E. Kioupakis. "Phonon- and defect-limited electron and hole mobility of diamond and cubic boron nitride: A critical comparison". In: *Applied Physics Letters* 119.6 (2021), p. 062101. DOI: 10.1063/5.0056543. eprint: https://doi.org/10.1063/5.0056543. URL: https://doi.org/10.1063/5.0056543.

[28] T. Sekiguchi, S. Koizumi, and T. Taniguchi. "Characterization of p–n junctions of diamond and c-BN by cathodoluminescence and electron-beam-induced current". In: *Journal of Physics: Condensed Matter* 16.2 (Dec. 2003), S91–S97. DOI: 10.1088/0953-8984/16/2/011. URL: https://doi.org/10.1088/0953-8984/16/2/011.

[29] J. P. Goss et al. "Vacancy-impurity complexes and limitations for implantation doping of diamond". In: *Phys. Rev. B* 72 (3 July 2005), p. 035214. DOI: 10.1103/PhysRevB.72.035214. URL: https://link.aps.org/doi/10.1103/PhysRevB.72.035214.

[30] K. Thonke. "The boron acceptor in diamond". In: *Semiconductor Science and Technology* 18.3 (Feb. 2003), S20–S26. DOI: 10.1088/0268-1242/18/3/303. URL: https://doi.org/10.1088/0268-1242/18/3/303.

[31] M. Liao, B. Shen, and Z. Wang. "Chapter 2 - Semiconductor diamond". In: *Ultra-Wide Bandgap Semiconductor Materials*. Materials Today. Elsevier, 2019, pp. 111–261. ISBN: 978-0-12-815468-7. DOI: https://doi.org/10.1016/B978-0-12-815468-7.00002-0. URL: https://www.sciencedirect.com/science/article/pii/B9780128154687000020.

[32] S. Koizumi et al. *Power Electronics Device Applications of Diamond Semiconductors*. Woodhead Publishing, 2018.

[33] F. P. Bundy, H. T. Hall, and H. M. Strong. "Man-Made Diamonds". In: *Nature* 176 (1995), pp. 51–55. DOI: 10.1038/176051a0.

[34] S.A. Kajihara, A. Antonelli, and J. Bernholc. "Impurity incorporation and doping of diamond". In: *Wide-Band-Gap Semiconductors*. Ed. by Chris G. Van de Walle. Amsterdam: Elsevier, 1993, pp. 144–149. ISBN: 978-0-444-81573-6. DOI: https://doi.org/10.1016/B978-0-444-81573-6.50023-2. URL: https://www.sciencedirect.com/science/article/pii/B9780444815736500232.

[35] G. Perez. "Caractérisation de diodes Schottky en diamant de structure pseudo-verticale". PhD thesis. Communauté Université Grenoble Alpes, 2018.

[36] C. Fernández-Lorenzo et al. "Multi-technique analysis of high quality HPHT diamond crystal". In: *Journal of Crystal Growth* 353.1 (2012), pp. 115–119. ISSN: 0022-0248. DOI: https://doi.org/10.1016/j.jcrysgro.2012.05.007. URL: https://www.sciencedirect.com/science/article/pii/S0022024812003296.

[37] A. Zaitsev. *Optical Properties of Diamond, A Data Handbook*. Ed. by Springer. 2010. ISBN: 9783642085857.

[38] H. Yamada et al. "Fabrication of 1 Inch Mosaic Crystal Diamond Wafers". In: *Applied Physics Express* 3.5 (Apr. 2010), p. 051301. DOI: 10.1143/apex.3.051301. URL: https://doi.org/10.1143/apex.3.051301.

[39] J. Widiez et al. "Fabrication of Silicon on Diamond (SOD) substrates by either the Bonded and Etched-back SOI (BESOI) or the Smart-Cut™ technology". In: *Solid-State Electronics* 54.2 (2010). Selected Full-Length Extended Papers from the EUROSOI 2009 Conference, pp. 158–163. ISSN: 0038-1101. DOI: https://doi.org/10.1016/j.sse.2009.12.012. URL: https://www.sciencedirect.com/science/article/pii/S0038110109003554.

[40] J.C. Piñero et al. "Lattice performance during initial steps of the Smart-Cut™ process in semiconducting diamond: A STEM study". In: *Applied Surface Science* 528 (2020), p. 146998. ISSN: 0169-4332. DOI: https://doi.org/10.1016/j.apsusc.2020.146998. URL: https://www.sciencedirect.com/science/article/pii/S0169433220317554.

[41] J.C. Arnault et al. "Epitaxial diamond on Ir/ SrTiO3/Si (001): From sequential material characterizations to fabrication of lateral Schottky diodes". In: *Diamond and Related Materials* 105 (2020), p. 107768. ISSN: 0925-9635. DOI: https://doi.org/10.1016/j.diamond.2020.107768. URL: https://www.sciencedirect.com/science/article/pii/S0925963519309720.

[42] K. Ichikawa et al. "High crystalline quality heteroepitaxial diamond using grid-patterned nucleation and growth on Ir". In: *Diamond and Related Materials* 94 (2019), pp. 92–100. ISSN: 0925-9635. DOI: https://doi.org/10.1016/j.diamond.2019.01.027. URL: https://www.sciencedirect.com/science/article/pii/S0925963518307477.

[43] M. Schreck et al. "Multiple role of dislocations in the heteroepitaxial growth of diamond: A brief review". In: *physica status solidi (a)* 213.8 (2016), pp. 2028–2035. DOI: https://doi.org/10.1002/pssa.201600119. eprint: https://onlinelibrary.

wiley.com/doi/pdf/10.1002/pssa.201600119. URL: https://onlinelibrary.wiley.com/doi/abs/10.1002/pssa.201600119.

[44] E. Gheeraet. "GreenDiamond – Diamond Power Electronics: Achievements and Prospects". In: Brussels, 2020.

[45] M. Kamo et al. "Diamond synthesis from gas phase in microwave plasma". In: *Journal of Crystal Growth* 62.3 (1983), pp. 642–644. ISSN: 00220248. DOI: 10.1016/0022-0248(83)90411-6.

[46] J.C. Arnault, S. Saada, and V. Ralchenko. "Chemical Vapor Deposition Single-Crystal Diamond: A Review". In: *physica status solidi (RRL) – Rapid Research Letters* (). DOI: https://doi.org/10.1002/pssr.202100354. eprint: https://onlinelibrary.wiley.com/doi/pdf/10.1002/pssr.202100354. URL: https://onlinelibrary.wiley.com/doi/abs/10.1002/pssr.202100354.

[47] J. A. Mucha, D. L. Flamm, and D. E. Ibbotson. "On the role of oxygen and hydrogen in diamond-forming discharges". In: *Journal of Applied Physics* 65.9 (1989), pp. 3448–3452. DOI: 10.1063/1.342635.

[48] S. J. Harris and A. M. Weiner. "Effects of oxygen on diamond growth". In: *Applied Physics Letters* 55.21 (1989), pp. 2179–2181. DOI: 10.1063/1.102350.

[49] J.P. Lagrange, A. Deneuville, and E. Gheeraert. "Activation energy in low compensated homoepitaxial boron-doped diamond films1Paper presented at the Diamond 1997 Conference.1". In: *Diamond and Related Materials* 7.9 (1998), pp. 1390–1393. ISSN: 0925-9635. DOI: https://doi.org/10.1016/S0925-9635(98)00225-8. URL: https://www.sciencedirect.com/science/article/pii/S0925963598002258.

[50] A. Hiraiwa and H. Kawarada. "Figure of merit of diamond power devices based on accurately estimated impact ionization processes". In: *Journal of Applied Physics* 114.3 (2013), p. 034506. DOI: 10.1063/1.4816312.

[51] J. Bousquet et al. "Phase diagram of boron-doped diamond revisited by thickness-dependent transport studies". In: *Phys. Rev. B* 95 (16 Apr. 2017), p. 161301. DOI: 10.1103/PhysRevB.95.161301. URL: https://link.aps.org/doi/10.1103/PhysRevB.95.161301.

[52] E. Bustarret et al. "Dependence of the Superconducting Transition Temperature on the Doping Level in Single-Crystalline Diamond Films". In: *Phys. Rev. Lett.* 93 (23 Dec. 2004), p. 237005. DOI: 10.1103/PhysRevLett.93.237005. URL: https://link.aps.org/doi/10.1103/PhysRevLett.93.237005.

[53] T. Makino et al. "Strong Excitonic Emission from (001)-Oriented DiamondP-NJunction". In: *Japanese Journal of Applied Physics* 44.No. 38 (Sept. 2005), pp. L1190–L1192. DOI: 10.1143/jjap.44.l1190. URL: https://doi.org/10.1143/jjap.44.l1190.

[54] S. Koizumi et al. "Growth and characterization of phosphorous doped {111} homoepitaxial diamond thin films". In: *Applied Physics Letters* 71.8 (1997), pp. 1065–1067. ISSN: 00036951. DOI: 10.1063/1.119729.

[55] M. A. Pinault-Thaury et al. "Phosphorus-doped (113) CVD diamond: A breakthrough towards bipolar diamond devices". In: *Applied Physics Letters* 114.11 (2019), p. 112106. DOI: 10.1063/1.5079924. eprint: https://doi.org/10.1063/1.5079924. URL: https://doi.org/10.1063/1.5079924.

[56] A. Tallaire et al. "Growth of thick and heavily boron-doped (113)-oriented CVD diamond films". In: *Diamond and Related Materials* 66 (2016), pp. 61–66. ISSN: 0925-9635. DOI: https://doi.org/10.1016/j.diamond.2016.03.020. URL: https://www.sciencedirect.com/science/article/pii/S0925963516300929.

[57] Y. Balasubramaniam et al. "Thick homoepitaxial (110)-oriented phosphorus-doped n-type diamond". In: *Applied Physics Letters* 109.6 (2016), p. 062105. DOI: 10.1063/1.4960970. eprint: https://doi.org/10.1063/1.4960970. URL: https://doi.org/10.1063/1.4960970.

[58] V. Mortet et al. "Properties of boron-doped (113) oriented homoepitaxial diamond layers". In: *Diamond and Related Materials* 111 (2021), p. 108223. ISSN: 0925-9635. DOI: https://doi.org/10.1016/j.diamond.2020.108223. URL: https://www.sciencedirect.com/science/article/pii/S0925963520307780.

[59] A. Stacey et al. "Nitrogen Terminated Diamond". In: *Advanced Materials Interfaces* 2.10 (2015), p. 1500079. DOI: https://doi.org/10.1002/admi.201500079. eprint: https://onlinelibrary.wiley.com/doi/pdf/10.1002/admi.201500079. URL: https://onlinelibrary.wiley.com/doi/abs/10.1002/admi.201500079.

[60] A. K. Schenk et al. "The surface electronic structure of silicon terminated (100) diamond". In: *Nanotechnology* 27.27 (May 2016), p. 275201. DOI: 10.1088/0957-4484/27/27/275201. URL: https://doi.org/10.1088/0957-4484/27/27/275201.

[61] K. M. O'Donnell et al. "Extremely high negative electron affinity of diamond via magnesium adsorption". In: *Phys. Rev. B* 92 (3 July 2015), p. 035303. DOI: 10.1103/PhysRevB.92.035303. URL: https://link.aps.org/doi/10.1103/PhysRevB.92.035303.

[62] H. Kawarada. "Hydrogen-terminated diamond surfaces and interfaces". In: *Surface Science Reports* 26.7 (1996), pp. 205–259. ISSN: 0167-5729. DOI: https://doi.org/10.1016/S0167-5729(97)80002-7. URL: https://www.sciencedirect.com/science/article/pii/S0167572997800027.

[63] P. Strobel et al. "Surface transfer doping of diamond". In: *Nature* 430.18 (2004), pp. 439–441. DOI: 10.1038/nature02751.

[64] K. G. Crawford et al. "Surface transfer doping of diamond: A review". In: *Progress in Surface Science* 96.1 (2021), p. 100613. ISSN: 0079-6816. DOI: https://doi.org/10.1016/j.progsurf.2021.100613. URL: https://www.sciencedirect.com/science/article/pii/S0079681621000010.

[65] Y. Sasama et al. "Charge-carrier mobility in hydrogen-terminated diamond field-effect transistors". In: *Journal of Applied Physics* 127.18 (2020), p. 185707. DOI: 10.1063/5.0001868. eprint: https://doi.org/10.1063/5.0001868. URL: https://doi.org/10.1063/5.0001868.

[66] M. Kasu et al. "Fabrication of diamond modulation-doped FETs by NO2 delta doping in an Al2O3 gate layer". In: *Applied Physics Express* 14.5 (Apr. 2021), p. 051004. DOI: 10.35848/1882-0786/abf445. URL: https://doi.org/10.35848/1882-0786/abf445.

[67] A. Vardi et al. "A Diamond:H/MoO3 MOSFET". In: *IEEE Electron Device Letters* 35.12 (2014), pp. 1320–1322. DOI: 10.1109/LED.2014.2364832.

[68] M. J. Rutter and J. Robertson. "Ab initio calculation of electron affinities of diamond surfaces". In: *Phys. Rev. B* 57 (15 Apr. 1998), pp. 9241–9245. DOI: 10.1103/PhysRevB.57.9241. URL: https://link.aps.org/doi/10.1103/PhysRevB.57.9241.

[69] R. E. Thomas, R. A. Rudder, and R. J. Markunas. "Thermal desorption from hydrogenated and oxygenated diamond (100) surfaces". In: *Journal of Vacuum Science & Technology A* 10.4 (1992), pp. 2451–2457. DOI: 10.1116/1.577983. eprint: https://doi.org/10.1116/1.577983. URL: https://doi.org/10.1116/1.577983.

[70] T. Teraji, Y. Koide, and T. Ito. "Schottky barrier height and thermal stability of p-diamond (100) Schottky interfaces". In: *Thin Solid Films* 557 (2014). The 8th International Conference on Silicon Epitaxy and Heterostructures (ICSI-8) and the 6th International Symposium on Control of Semiconductor Interfaces (ISCSI-VI), pp. 241–248. ISSN: 0040-6090. DOI: https://doi.org/10.1016/j.tsf.2013.11.132. URL: https://www.sciencedirect.com/science/article/pii/S0040609013020075.

[71] R. Yoshida et al. "Formation of atomically flat hydroxyl-terminated diamond (111) surfaces via water vapor annealing". In: *Applied Surface Science* 458 (2018), pp. 222–225. ISSN: 0169-4332. DOI: https://doi.org/10.1016/j.apsusc.2018.07.094. URL: https://www.sciencedirect.com/science/article/pii/S0169433218319925.

[72] F. Maier, J. Ristein, and L. Ley. "Electron affinity of plasma-hydrogenated and chemically oxidized diamond (100) surfaces". In: *Phys. Rev. B* 64 (16 Oct. 2001), p. 165411. DOI: 10.1103/PhysRevB.64.165411. URL: https://link.aps.org/doi/10.1103/PhysRevB.64.165411.

[73] S. J. Sque, R. Jones, and P. R. Briddon. "Structure, electronics, and interaction of hydrogen and oxygen on diamond surfaces". In: *Phys. Rev. B* 73 (8 Feb. 2006), p. 085313. DOI: 10.1103/PhysRevB.73.085313. URL: https://link.aps.org/doi/10.1103/PhysRevB.73.085313.

[74] J. Navas et al. "Oxygen termination of homoepitaxial diamond surface by ozone and chemical methods: An experimental and theoretical perspective". In: *Applied Surface Science* 433 (2018), pp. 408–418. ISSN: 0169-4332. DOI: https://doi.org/10.1016/j.

apsusc.2017.10.065. URL: https://www.sciencedirect.com/science/article/pii/S0169433217329987.

[75] S. Torrengo et al. "XPS and ToF-SIMS investigation of nanocrystalline diamond oxidized surfaces". In: *Applied Surface Science* 276 (2013), pp. 101–111. ISSN: 0169-4332. DOI: https://doi.org/10.1016/j.apsusc.2013.03.041. URL: https://www.sciencedirect.com/science/article/pii/S0169433213005096.

[76] M. Dutta et al. "High Voltage Diodes in Diamond Using (100)-A nd (111)-Substrates". In: *IEEE Electron Device Letters* 38.5 (2017), pp. 600–603. ISSN: 07413106. DOI: 10.1109/LED.2017.2681058.

[77] P. Muret et al. "Potential barrier heights at metal on oxygen-terminated diamond interfaces". In: *Journal of Applied Physics* 118.20 (2015). ISSN: 10897550. DOI: 10.1063/1.4936317.

[78] H. Umezawa et al. "Leakage current analysis of diamond Schottky barrier diode". In: *Applied Physics Letters* 90.7 (2007), p. 073506. DOI: 10.1063/1.2643374.

[79] R. Kumaresan et al. "Device processing, fabrication and analysis of diamond pseudo-vertical Schottky barrier diodes with low leak current and high blocking voltage". In: *Diamond and Related Materials* 18.2-3 (2009), pp. 299–302. ISSN: 09259635. DOI: 10.1016/j.diamond.2008.10.055.

[80] T. Iwasaki et al. "Direct nanoscale sensing of the internal electric field in operating semiconductor devices using single electron spins". In: *ACS nano* 11.2 (2017), pp. 1238–1245.

[81] J.C. Piñero et al. "Atomic composition of WC/ and Zr/O-terminated diamond Schottky interfaces close to ideality". In: *Applied Surface Science* 395 (2017). Progress in Applied Surface, Interface and Thin Film Science and Solar Renewable Energy News IV, pp. 200–207. ISSN: 0169-4332. DOI: https://doi.org/10.1016/j.apsusc.2016.04.166. URL: https://www.sciencedirect.com/science/article/pii/S0169433216309552.

[82] P.N. Volpe et al. "High breakdown voltage Schottky diodes synthesized on p-type CVD diamond layer". In: *Physica Status Solidi (a)* 207.9 (2010), pp. 2088–2092. ISSN: 18626300. DOI: 10.1002/pssa.201000055. URL: http://onlinelibrary.wiley.com/doi/10.1002/pssa.201000055/.

[83] A. Traore. "High Power Diamond Schottky Diode". PhD thesis. Université de Grenoble, 2014.

[84] H. Umezawa et al. "Defect and field-enhancement characterization through electron-beam-induced current analysis". In: *Applied Physics Letters* 110.18 (2017), p. 182103. DOI: 10.1063/1.4982590. eprint: https://doi.org/10.1063/1.4982590. URL: https://doi.org/10.1063/1.4982590.

[85] A. Nawawi et al. "Characterization of vertical Mo/diamond Schottky barrier diode from non-ideal I–V and C–V measurements based on MIS model". In: *Diamond and Related Materials* 35 (2013), pp. 1–6. ISSN: 0925-9635. DOI: https://doi.org/10.1016/j.diamond.2013.03.002. URL: https://www.sciencedirect.com/science/article/pii/S0925963513000460.

[86] K. Driche et al. "Electric field distribution using floating metal guard rings edge-termination for Schottky diodes". In: *Diamond and Related Materials* 82.January (2018), pp. 160–164. ISSN: 09259635. DOI: 10.1016/j.diamond.2018.01.016. URL: https://doi.org/10.1016/j.diamond.2018.01.016.

[87] H. Umezawa et al. "Characterization of X-ray radiation hardness of diamond Schottky barrier diode and metal-semiconductor field-effect transistor". In: *2017 29th International Symposium on Power Semiconductor Devices and IC's (ISPSD)*. 2017, pp. 379–382. DOI: 10.23919/ISPSD.2017.7988983.

[88] H. Kawashima et al. "Electronic properties of diamond Schottky barrier diodes fabricated on silicon-based heteroepitaxially grown diamond substrates". In: *Applied Physics Express* 8.10 (2015). ISSN: 18820786. DOI: 10.7567/APEX.8.104103.

[89] M.L. Hicks, Alexander C. Pakpour-Tabrizi, and Richard B. Jackman. "Polishing, preparation and patterning of diamond for device applications". In: *Diamond and Related Materials* 97 (2019), p. 107424. ISSN: 0925-9635. DOI: https://doi.org/10.1016/j.diamond.2019.05.010. URL: https://www.sciencedirect.com/science/article/pii/S0925963519302201.

[90] J. Letellier. "Diamond Schottky diodes improvement to pave the way to high power electronic application". Theses. Université Grenoble Alpes, Dec. 2019. URL: https://tel.archives-ouvertes.fr/tel-02929023.

[91] H. Umezawa. "Recent advances in diamond power semiconductor devices". In: *Materials Science in Semiconductor Processing* 78 (2018). Wide band gap semiconductors technology for next generation of energy efficient power electronics, pp. 147–156. ISSN: 1369-8001. DOI: https://doi.org/10.1016/j.mssp.2018.01.007. URL: https://www.sciencedirect.com/science/article/pii/S1369800117322217.

[92] H. Kawarada et al. "Durability-enhanced two-dimensional hole gas of C-H diamond surface for complementary power inverter applications". In: *Scientific Reports* 7 (2017). DOI: 10.1038/srep42368.

[93] K. Hirama et al. "Diamond field-effect transistors with 1.3 A/mm drain current density by Al2O3 passivation layer". In: *Japanese Journal of Applied Physics* 51.9R (2012), p. 090112.

[94] M. Kasu et al. "Diamond FET for RF Power Electronics". In: *Japanese Journal of Applied Physics* 56 ().

[95] H. Taniuchi et al. "High-frequency performance of diamond field-effect transistor". In: *IEEE Electron Device Letters* 22.8 (2001), pp. 390–392. DOI: 10.1109/55.936353.

[96] K. Ueda et al. "Diamond FET using high-quality polycrystalline diamond with fT of 45 GHz and fmax of 120 GHz". In: *IEEE Electron Device Letters* 27.7 (2006), pp. 570–572. DOI: 10.1109/LED.2006.876325.

[97] Y. Kitabayashi et al. "Normally-Off C–H Diamond MOSFETs With Partial C–O Channel Achieving 2-kV Breakdown Voltage". In: *IEEE Electron Device Letters* 38.3 (2017), pp. 363–366. DOI: 10.1109/LED.2017.2661340.

[98] N. Oi et al. "Normally-OFF Two-Dimensional Hole Gas Diamond MOSFETs Through Nitrogen-Ion Implantation". In: *IEEE Electron Device Letters* 40.6 (2019), pp. 933–936. DOI: 10.1109/LED.2019.2912211.

[99] J. W. Liu et al. "Control of normally on/off characteristics in hydrogenated diamond metal-insulator-semiconductor field-effect transistors". In: *Journal of Applied Physics* 118.11 (2015), p. 115704. DOI: 10.1063/1.4930294. eprint: https://doi.org/10.1063/1.4930294. URL: https://doi.org/10.1063/1.4930294.

[100] N. Oi et al. "Vertical-type two-dimensional hole gas diamond metal oxide semiconductor field-effect transistors". In: *Scientific Reports* 8 (2018). DOI: 10.1038/s41598-018-28837-5.

[101] C. Masante et al. "175V,> 5.4 MV/cm, 50 mΩ.cm^2 at 250° C Diamond MOSFET and its reverse conduction". In: *2019 31st International Symposium on Power Semiconductor Devices and ICs (ISPSD)*. IEEE. 2019, pp. 151–154.

[102] H. Umezawa, Takeshi Matsumoto, and Shin-Ichi Shikata. "Diamond Metal–Semiconductor Field-Effect Transistor With Breakdown Voltage Over 1.5 kV". In: *IEEE Electron Device Letters* 35.11 (2014), pp. 1112–1114. DOI: 10.1109/LED.2014.2356191.

[103] K. Driche. "Diamond unipolar devices : towards impact ionization coefficients extraction". 2018GREAT115. PhD thesis. 2018. URL: http://www.theses.fr/2018GREAT115/document.

[104] T. Iwasaki et al. "High-Temperature Operation of Diamond Junction Field-Effect Transistors With Lateral p-n Junctions". In: *IEEE Electron Device Letters* 34.9 (2013), pp. 1175–1177. DOI: 10.1109/LED.2013.2271377.

[105] Y. Hoshino et al. "Electrical properties of lateral p–n junction diodes fabricated by selective growth of n+ diamond". In: *physica status solidi (a)* 209.9 (2012), pp. 1761–1764. DOI: https://doi.org/10.1002/pssa.201200053. eprint: https://onlinelibrary.wiley.com/doi/pdf/10.1002/pssa.201200053. URL: https://onlinelibrary.wiley.com/doi/abs/10.1002/pssa.201200053.

[106] Y. Suwa et al. "Normally-Off Diamond Junction Field-Effect Transistors With Submicrometer Channel". In: *IEEE Electron Device Letters* 37.2 (2016), pp. 209–211. DOI: 10.1109/LED.2015.2513074.

[107] T. Matsumoto et al. "Diamond & Related Materials Diamond Schottky- pn diode using lightly nitrogen-doped layer". In: *Diamond & Related Materials* 75 (2017), pp. 152–154. ISSN: 0925-9635. DOI: 10.1016/j.diamond.2017.03.018. URL: http://dx.doi.org/10.1016/j.diamond.2017.03.018.

[108] X. Zhang et al. "Inversion channel MOSFET on heteroepitaxially grown free-standing diamond". In: *Carbon* 175 (2021), pp. 615–619. ISSN: 0008-6223. DOI: https://doi.org/10.1016/j.carbon.2020.11.072. URL: https://www.sciencedirect.com/science/article/pii/S0008622320311519.

[109] W. Schottky and E. Spenke. "Zur quantitativen Durchführung der Raumladungs- und Randschichttheorie der Kristallgleichrichter". In: *Wissenschaftliche Veröffentlichungen aus den Siemens-Werken: Achzehnter Band 1939*. Berlin, Heidelberg: Springer Berlin Heidelberg, 1939, pp. 225–291. ISBN: 978-3-642-99673-3. DOI: 10.1007/978-3-642-99673-3_17. URL: https://doi.org/10.1007/978-3-642-99673-3_17.

[110] W. Shockley. "On the Surface States Associated with a Periodic Potential". In: *Phys. Rev.* 56 (4 Aug. 1939), pp. 317–323. DOI: 10.1103/PhysRev.56.317. URL: https://link.aps.org/doi/10.1103/PhysRev.56.317.

[111] J. Bardeen. "Surface States and Rectification at a Metal Semi-Conductor Contact". In: *Phys. Rev.* 71 (10 May 1947), pp. 717–727. DOI: 10.1103/PhysRev.71.717. URL: https://link.aps.org/doi/10.1103/PhysRev.71.717.

[112] V. Heine. "Theory of Surface States". In: *Phys. Rev.* 138 (6A June 1965), A1689–A1696. DOI: 10.1103/PhysRev.138.A1689. URL: https://link.aps.org/doi/10.1103/PhysRev.138.A1689.

[113] A. M. Cowley and S. M. Sze. "Surface States and Barrier Height of Metal-Semiconductor Systems". In: *Journal of Applied Physics* 36.10 (1965), pp. 3212–3220. DOI: 10.1063/1.1702952. eprint: https://doi.org/10.1063/1.1702952. URL: https://doi.org/10.1063/1.1702952.

[114] M. Schlüter. "Chemical trends in metal-semiconductor barrier heights". In: *Phys. Rev. B* 17 (12 June 1978), pp. 5044–5047. DOI: 10.1103/PhysRevB.17.5044. URL: https://link.aps.org/doi/10.1103/PhysRevB.17.5044.

[115] W. Kohn. "Analytic Properties of Bloch Waves and Wannier Functions". In: *Phys. Rev.* 115 (4 Aug. 1959), pp. 809–821. DOI: 10.1103/PhysRev.115.809. URL: https://link.aps.org/doi/10.1103/PhysRev.115.809.

[116] W. Mönch. "Empirical tight-binding calculation of the branch-point energy of the continuum of interface-induced gap states". In: *Journal of Applied Physics* 80.9 (1996), pp. 5076–5082. DOI: 10.1063/1.363486. eprint: https://doi.org/10.1063/1.363486. URL: https://doi.org/10.1063/1.363486.

[117] J. Tersoff. "Schottky Barrier Heights and the Continuum of Gap States". In: *Phys. Rev. Lett.* 52 (6 Feb. 1984), pp. 465–468. DOI: 10.1103/PhysRevLett.52.465. URL: https://link.aps.org/doi/10.1103/PhysRevLett.52.465.

[118] M. Yoshitake. "Advanced Models for Practical Devices". In: *Work Function and Band Alignment of Electrode Materials: The Art of Interface Potential for Electronic Devices, Solar Cells, and Batteries*. Tokyo: Springer Japan, 2021, pp. 113–126. ISBN: 978-4-431-56898-8. DOI: 10.1007/978-4-431-56898-8_6. URL: https://doi.org/10.1007/978-4-431-56898-8_6.

[119] S. Hara. "The Schottky limit and a charge neutrality level found on metal/6H-SiC interfaces". In: *Surface Science* 494.3 (2001), pp. L805–L810. ISSN: 0039-6028. DOI: https://doi.org/10.1016/S0039-6028(01)01596-5. URL: https://www.sciencedirect.com/science/article/pii/S0039602801015965.

[120] C. R. Crowell and S. M. Sze. "Current transport in metal-semiconductor barriers". In: *Solid State Electronics* 9.11-12 (1966), pp. 1035–1048. ISSN: 00381101. DOI: 10.1016/0038-1101(66)90127-4.

[121] W. Mönch. *Electronic properties of semiconductor interfaces*. Vol. 43. Springer Science & Business Media, 2013.

[122] P.N. Volpe et al. "High hole mobility in boron doped diamond for power device applications". In: *Applied Physics Letters* 94.9 (2009), p. 092102. DOI: 10.1063/1.3086397.

[123] J. Pernot et al. "Hall hole mobility in boron-doped homoepitaxial diamond". In: *Phys. Rev. B* 81 (20 May 2010), p. 205203. DOI: 10.1103/PhysRevB.81.205203. URL: https://link.aps.org/doi/10.1103/PhysRevB.81.205203.

[124] D.K. Schroder. *Material and device semiconductor material*. Vol. 44. 4. 2006, p. 790. ISBN: 9780471739067. DOI: 10.1063/1.2810086. URL: http://www.wiley.com/WileyCDA/WileyTitle/productCd-0471739065.html.

[125] Sheng S. Li. "Metal–Semiconductor Contacts". In: *Semiconductor Physical Electronics*. Ed. by Sheng S. Li. New York, NY: Springer New York, 2006, pp. 284–333. ISBN: 978-0-387-37766-7. DOI: 10.1007/0-387-37766-2_10. URL: https://doi.org/10.1007/0-387-37766-2_10.

[126] L. Zheng, R. P. Joshi, and C. Fazi. "Effects of barrier height fluctuations and electron tunneling on the reverse characteristics of 6H–SiC Schottky contacts". In: *Journal of Applied Physics* 85.7 (1999), pp. 3701–3707. DOI: 10.1063/1.369735. eprint: https://doi.org/10.1063/1.369735. URL: https://doi.org/10.1063/1.369735.

[127] E. L. Murphy and R. H. Good. "Thermionic Emission, Field Emission, and the Transition Region". In: *Phys. Rev.* 102 (6 June 1956), pp. 1464–1473. DOI: 10.1103/PhysRev.102.1464. URL: https://link.aps.org/doi/10.1103/PhysRev.102.1464.

[128] F.A. Padovani and R. Stratton. "Field and thermionic-field emission in Schottky barriers". In: *Solid-State Electronics* 9.7 (1966), pp. 695–707. ISSN: 0038-1101. DOI: https://doi.org/10.1016/0038-1101(66)90097-9. URL: https://www.sciencedirect.com/science/article/pii/0038110166900979.

[129] W. Li et al. "Near-ideal reverse leakage current and practical maximum electric field in -Ga2O3 Schottky barrier diodes". In: *Applied Physics Letters* 116.19 (2020), p. 192101. DOI: 10.1063/5.0007715.

[130] A. Q. Konstantinov et al. "Study of avalanche breakdown and impact ionization in 4H silicon carbide". In: *Journal of electronic materials* 27.4 (1998), pp. 335–341. DOI: 10.1007/s11664-998-0411-x.

[131] T. Tachibana, B. E. Williams, and J. T. Glass. "Correlation of the electrical properties of metal contacts on diamond films with the chemical nature of the metal-diamond interface. II. Titanium contacts: A carbide-forming metal". In: *Phys. Rev. B* 45 (20 May 1992), pp. 11975–11981. DOI: 10.1103/PhysRevB.45.11975. URL: https://link.aps.org/doi/10.1103/PhysRevB.45.11975.

[132] S. Ohmagari et al. "Submicron-scale diamond selective-area growth by hot-filament chemical vapor deposition". In: *Thin Solid Films* 615 (2016), pp. 239–242. ISSN: 00406090. DOI: 10.1016/j.tsf.2016.07.017. URL: http://dx.doi.org/10.1016/j.tsf.2016.07.017.

[133] B. Baliga. *Fundamentals of Power Semiconductor Devices*. Ed. by Springer. 2008. ISBN: 978-0-387-47314-7.

[134] T. T. Mnatsakanov et al. "Carrier mobility model for simulation of SiC-based electronic devices". In: *Semiconductor Science and Technology* 17.9 (Aug. 2002), pp. 974–977. DOI: 10.1088/0268-1242/17/9/313. URL: https://doi.org/10.1088/0268-1242/17/9/313.

[135] P. Muret et al. "Schottky diode architectures on p-type diamond for fast switching, high forward current density and high breakdown field rectifiers". In: *Diamond and Related Materials* 20.3 (2011), pp. 285–289. ISSN: 0925-9635. DOI: https://doi.org/10.1016/j.diamond.2011.01.008. URL: https://www.sciencedirect.com/science/article/pii/S0925963511000112.

[136] H. Umezawa and Shin-ichi Shikata. "Diamond high-temperature power devices". In: *2009 21st International Symposium on Power Semiconductor Devices IC's*. 2009, pp. 259–262. DOI: 10.1109/ISPSD.2009.5158051.

[137] D.J. Twitchen et al. "High-voltage single-crystal diamond diodes". In: *IEEE Transactions on Electron Devices* 51.5 (2004), pp. 826–828. DOI: 10.1109/TED.2004.826867.

[138] Y. Ando et al. "Smooth and high-rate reactive ion etching of diamond". In: *Diamond and Related Materials* 11.3 (2002). 12th European Conference on Diamond, Diamond-Like Materials, Carbon Nanotubes, Nitrides Silicon Carbide, pp. 824–827. ISSN: 0925-9635. DOI: https://doi.org/10.1016/S0925-9635(01)00617-3. URL: https://www.sciencedirect.com/science/article/pii/S0925963501006173.

[139] D.T. Tran et al. "Investigation of mask selectivities and diamond etching using microwave plasma-assisted etching". In: *Diamond and Related Materials* 19.7 (2010). Proceedings of Diamond 2009, The 20th European Conference on Diamond, Diamond-Like Materials, Carbon Nanotubes and Nitrides, Part 2, pp. 778–782. ISSN: 0925-9635. DOI: https://doi.org/10.1016/j.diamond.2010.02.001. URL: https://www.sciencedirect.com/science/article/pii/S0925963510000749.

[140] A. Toros et al. "Reactive ion etching of single crystal diamond by inductively coupled plasma: State of the art and catalog of recipes". In: *Diamond and Related Materials* 108 (2020), p. 107839. ISSN: 0925-9635. DOI: https://doi.org/10.1016/j.diamond.2020.107839. URL: https://www.sciencedirect.com/science/article/pii/S0925963520300406.

[141] F. Lloret et al. "Influence of methane concentration on MPCVD overgrowth of 100-oriented etched diamond substrates". In: *physica status solidi (a)* 213.10 (2016), pp. 2570–2574. DOI: https://doi.org/10.1002/pssa.201600182. eprint: https://onlinelibrary.wiley.com/doi/pdf/10.1002/pssa.201600182. URL: https://onlinelibrary.wiley.com/doi/abs/10.1002/pssa.201600182.

[142] M. P. Alegre et al. "Critical boron-doping levels for generation of dislocations in synthetic diamond". In: *Applied Physics Letters* 105.17 (2014), p. 173103. DOI: 10.1063/1.4900741. eprint: https://doi.org/10.1063/1.4900741. URL: https://doi.org/10.1063/1.4900741.

[143] D. Araujo et al. "Dislocation generation mechanisms in heavily boron-doped diamond epilayers". In: *Applied Physics Letters* 118.5 (2021), p. 052108. DOI: 10.1063/5.0031476. eprint: https://doi.org/10.1063/5.0031476. URL: https://doi.org/10.1063/5.0031476.

[144] S. Ohmagari, T. Teraji, and Y. Koide. *Non-destructive detection of killer defects of diamond Schottky barrier diodes*. 2011.

[145] A. Kobayashi et al. "Suppression of killer defects in diamond vertical-type Schottky barrier diodes". In: 59.SG (Feb. 2020), SGGD10. DOI: 10.7567/1347-4065/ab65b1. URL: https://doi.org/10.7567/1347-4065/ab65b1.

[146] A. Hiraiwa and H. Kawarada. "Blocking characteristics of diamond junctions with a punch-through design". In: *Journal of Applied Physics* 117.12 (2015), p. 124503. DOI: 10.1063/1.4916240. eprint: https://doi.org/10.1063/1.4916240. URL: https://doi.org/10.1063/1.4916240.

[147] B. J. Baliga. "Semiconductors for high-voltage, vertical channel field-effect transistors". In: *Journal of Applied Physics* 53.3 (1982), pp. 1759–1764. ISSN: 00218979. DOI: 10.1063/1.331646.

[148] G. Chicot, D. Eon, and N. Rouger. "Optimal drift region for diamond power devices". In: *Diamond and Related Materials* 69 (2016), pp. 68–73. ISSN: 09259635. DOI: 10.1016/j.diamond.2016.07.006.

[149] H. Umezawa, S. Shikata, and T. Funaki. "Diamond Schottky barrier diode for high-temperature, high-power, and fast switching applications". In: *Japanese Journal of Applied Physics* 53.5 SPEC. ISSUE 1 (2014), pp. 4–8. ISSN: 13474065. DOI: 10.7567/JJAP.53.05FP06.

[150] H. Umezawa, Y. Kato, and S. Shikata. "1Ω On-Resistance Diamond Vertical-Schottky Barrier Diode Operated at 250K". In: *Applied Physics Express* 6 (2013). DOI: /10.7567/APEX.6.011302.

[151] H. Arbess et al. "Original field plate to decrease the maximum electric field peak for high-voltage diamond Schottky diode". In: *IEEE Transactions on Electron Devices* 62.9 (2015), pp. 2945–2951.

[152] M. Brezeanu. "Diamond Schottky barrier diodes". PhD thesis. University of Cambridge, 2008.

[153] J. Cañas et al. "Diamond/-alumina band offset determination by XPS". In: *Applied Surface Science* 535 (2021), p. 146301. ISSN: 0169-4332. DOI: https://doi.org/10.1016/j.apsusc.2020.146301. URL: https://www.sciencedirect.com/science/article/pii/S0169433220310576.

[154] S. Kono et al. "Carbon 1s X-ray photoelectron spectra of realistic samples of hydrogen-terminated and oxygen-terminated CVD diamond (111) and (001)". In: *Diamond and Related Materials* 93 (2019), pp. 105–130. ISSN: 0925-9635. DOI: https://doi.org/10.1016/j.diamond.2019.01.017. URL: https://www.sciencedirect.com/science/article/pii/S0925963518308598.

[155] F.N. Li et al. "Measurement of barrier height of Pd on diamond (100) surface by X-ray photoelectron spectroscopy". In: *Applied Surface Science* 370 (2016), pp. 496–500. ISSN: 0169-4332. DOI: https://doi.org/10.1016/j.apsusc.2016.02.189. URL: https://www.sciencedirect.com/science/article/pii/S0169433216303671.

[156] G. Alba et al. "Comprehensive nanoscopic analysis of tungsten carbide/Oxygenated-diamond contacts for Schottky barrier diodes". In: *Applied Surface Science* 537 (2021), p. 147874. ISSN: 0169-4332. DOI: https://doi.org/10.1016/j.apsusc.2020.147874. URL: https://www.sciencedirect.com/science/article/pii/S0169433220326313.

[157] K. Liu et al. "Investigating the energetic band diagrams of oxygen-terminated CVD grown e6 electronic grade diamond". In: *Carbon* 169 (2020), pp. 440–445. ISSN: 0008-6223. DOI: https://doi.org/10.1016/j.carbon.2020.07.079. URL: https://www.sciencedirect.com/science/article/pii/S000862232030751X.

[158] P. Giannozzi et al. "QUANTUM ESPRESSO: a modular and open-source software project for quantum simulations of materials". In: *Journal of Physics: Condensed Matter* 21.39 (2009), 395502 (19pp). URL: http://www.quantum-espresso.org.

[159] P. Giannozzi et al. "Advanced capabilities for materials modelling with QUANTUM ESPRESSO". In: *Journal of Physics: Condensed Matter* 29.46 (2017), p. 465901. URL: http://stacks.iop.org/0953-8984/29/i=46/a=465901.

[160] P. Giannozzi et al. "Quantum ESPRESSO toward the exascale". In: *The Journal of Chemical Physics* 152.15 (2020), p. 154105. DOI: 10.1063/5.0005082. eprint: https://doi.org/10.1063/5.0005082. URL: https://doi.org/10.1063/5.0005082.

[161] R. Tran et al. "Surface Energies of Elemental Crystals". In: *Scientific Data 3* (2016). DOI: https://doi.org/10.1016/j.jallcom.2012.12.006.

[162] S. Ghodbane, F. Omnès, and C. Agnès. "A cathodoluminescence study of boron doped 111-homoepitaxial diamond films". In: *Diamond and Related Materials* 19.4 (2010), pp. 273–278. ISSN: 0925-9635. DOI: https://doi.org/10.1016/j.diamond.2009.11.003. URL: https://www.sciencedirect.com/science/article/pii/S0925963509003197.

[163] H. Kawarada et al. "Excitonic recombination radiation in undoped and boron-doped chemical-vapor-deposited diamonds". In: *Phys. Rev. B* 47 (7 Feb. 1993), pp. 3633–3637. DOI: 10.1103/PhysRevB.47.3633. URL: https://link.aps.org/doi/10.1103/PhysRevB.47.3633.

[164] F. Omnès et al. "Study of boron doping in MPCVD grown homoepitaxial diamond layers based on cathodoluminescence spectroscopy, secondary ion mass spectroscopy and capacitance-voltage measurements". In: *Diamond and Related Materials* 20.7 (2011), pp. 912–916. ISSN: 09259635. DOI: 10.1016/j.diamond.2011.05.010. URL: http://dx.doi.org/10.1016/j.diamond.2011.05.010.

[165] K. Kanaya and S. Okayama. "Penetration and energy-loss theory of electrons in solid targets". In: *Journal of Physics D: Applied Physics* 5.1 (Jan. 1972), pp. 43–58. DOI: 10.1088/0022-3727/5/1/308. URL: https://doi.org/10.1088/0022-3727/5/1/308.

[166] N. Yamamoto, J. C. H. Spence, and D. Fathy. "Cathodoluminescence and polarization studies from individual dislocations in diamond". In: *Philosophical Magazine B* 49.6 (1984), pp. 609–629. DOI: 10.1080/13642818408227648. eprint: https://doi.org/10.1080/13642818408227648. URL: https://doi.org/10.1080/13642818408227648.

[167] A. Traoré et al. "Zr/oxidized diamond interface for high power Schottky diodes". In: *Applied Physics Letters* 104.5 (2014). ISSN: 00036951. DOI: 10.1063/1.4864060.

[168] H. Umezawa et al. "High temperature application of diamond power device". In: *Diamond and Related Materials* 24 (2012), pp. 201–205. ISSN: 09259635. DOI: 10.1016/j.diamond.2012.01.011.

[169] D. Zhao et al. "Performance Improved Vertical Diamond Schottky Barrier Diode With Fluorination-Termination Structure". In: *IEEE Electron Device Letters* 40.8 (2019), pp. 1229–1232. ISSN: 0741-3106. DOI: 10.1109/led.2019.2923062.

[170] D. Zhao et al. "Reduction in reverse leakage current of diamond vertical Schottky barrier diode using SiNX field plate structure". In: *Results in Physics* 13 (2019), p. 102250. ISSN: 2211-3797. DOI: https://doi.org/10.1016/j.rinp.2019.102250. URL: https://www.sciencedirect.com/science/article/pii/S2211379719304103.

[171] J. Wang et al. "Diamond Schottky barrier diodes with floating metal rings for high breakdown voltage". In: *Materials Science in Semiconductor Processing* 97 (2019), pp. 101–105. ISSN: 1369-8001. DOI: https://doi.org/10.1016/j.mssp.2019.03.004. URL: https://www.sciencedirect.com/science/article/pii/S1369800118321814.

[172] V.D. Blank et al. "Power high-voltage and fast response Schottky barrier diamond diodes". In: *Diamond and Related Materials* 57 (2015). 25th International Conference on Diamond and Carbon Materials – DCM 2014, pp. 32–36. ISSN: 0925-9635. DOI: https://doi.org/10.1016/j.diamond.2015.01.005. URL: https://www.sciencedirect.com/science/article/pii/S0925963515000175.

[173] J. Liu et al. "Effect of Annealing Temperature on Performances of Boron-Doped Diamond Metal–Semiconductor Field-Effect Transistors". In: *IEEE Transactions on Electron Devices* 67.4 (2020), pp. 1680–1685. DOI: 10.1109/TED.2020.2972979.

[174] J. Liu et al. "High Output Current Boron-Doped Diamond Metal-Semiconductor Field-Effect Transistors". In: *IEEE Electron Device Letters* 40.11 (2019), pp. 1748–1751. DOI: 10.1109/LED.2019.2942967.

[175] Williams D. B. and Carter C. B. *Transmission Electron Microscopy*. Springer, 2009. DOI: 10.1007/978-0-387-76501-3.

[176] P. van der Heide. "Spectral Interpretation". In: *X-Ray Photoelectron Spectroscopy*. John Wiley Sons, Ltd, 2011. Chap. 5, pp. 101–140. ISBN: 9781118162897. DOI: https://doi.org/10.1002/9781118162897.ch5. eprint: https://onlinelibrary.wiley.com/doi/pdf/10.1002/9781118162897.ch5. URL: https://onlinelibrary.wiley.com/doi/abs/10.1002/9781118162897.ch5.

[177] S. Sadewasser and T. Glatzel. *Kelvin Probe Force Microscopy*. Springer, 2012. DOI: 10.1007/978-3-642-22566-6.

[178] D. Abou-Ras and T. Kirchartz. "Electron-Beam-Induced Current Measurements of Thin-Film Solar Cells". In: *ACS Applied Energy Materials* 2.9 (2019), pp. 6127–6139. DOI: 10.1021/acsaem.9b01172. eprint: https://doi.org/10.1021/acsaem.9b01172. URL: https://doi.org/10.1021/acsaem.9b01172.

[179] J. Jimenez and J. W. Tomm. "Cathodoluminescence". In: *Spectroscopic Analysis of Optoelectronic Semiconductors*. Cham: Springer International Publishing, 2016, pp. 213–263. ISBN: 978-3-319-42349-4. DOI: 10.1007/978-3-319-42349-4_5. URL: https://doi.org/10.1007/978-3-319-42349-4_5.

[180] R. M. Dreizler and E. K. U. Gross. *Density Functional Theory*. Springer, 1990. DOI: 10.1007/978-3-642-86105-5.

Appendix A

Experimental techniques and simulation tools

A.1 Transmission electron microscopy

A.1.1 Technique description

Transmision electron microscopy (TEM) is a microscopy technique based on an electron beam transmitted through a thin sample to form an image. High energy electrons are used in order to increase the spacial resolution limited by the electron wavelength and the quality of the electron optics with typical subnanometer resolution [175]. The figure A.1 a) shows the basic scheme of the TEM. The specimen is illuminated with a parallel beam acquired thanks to the condenser lenses and aperture. The transmitted electrons are passed through the objective aperture, and a bright field image of the sample is obtained. The signal is magnified and projected on a ccd camera to obtain image of the sample. The contrast between two different areas in TEM depends on the amplitude and phase of the electron wave transmitted through the sample. Heavier regions appear darker in TEM bright field images as heavier atoms scatter electrons more effectively and also diffraction contrasts appears at crystallographic grains or interfaces.

In the figure A.1 b), the basic scheme of the scanning transmission electron microscopy (STEM) is displayed. In STEM, the electron beam is focused on a spot which is then scanned over the sample. The image can be formed by using bright field (BF) or annular dark field (ADF) detectors. Bright field detectors are located in the path of the transmitted electron beam, while dark field images are formed by scattered electrons collected on an annular detector outside of the path of the non-scattered beam. In the latter, the contrast of an atomic column is directly related to the atomic number.

The characteristic beam scanning across the sample makes STEM an ideal microscopy technique to combine with energy dispersive X-ray (EDX) or electron energy loss spectroscopy (EELS) when used in ADF. These signals can be obtained simultaneously, allowing direct correlation of images and spectral information for each point of the sample. EDX provides information on the chemical composition of the sample through the x-rays emitted after the recombination of electrons excited with the beam energy. On the other hand, EELS provides structural and chemical composition information collecting the transmitted

electrons with respect the energy loss they suffer after scattering in the sample. This energy loss is related to electron excitations in the material which are affected by the structure and chemical composition since they directly impact the electronic properties of the material.

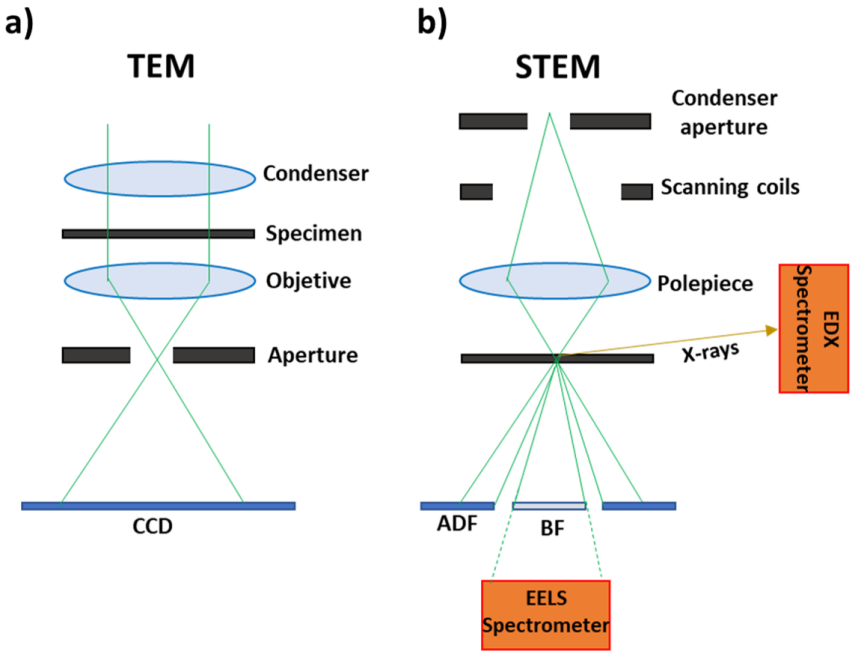

FIGURE A.1: *a) Transmission electron microscopy scheme showing the condenser lens, the beam being transmitted parallel through the specimen and the image formation thanks to the objective lens and aperture in a CCD camera. b) Scanning transmission electron microscopy scheme showing the condenser aperture and polepiece focusing the electron beam on a spot on the specimen. The different images are formed through bright field and annular dark field detectors. Complementary, energy dispersive x-rays and electron energy loss spectroscopy can also be collected to enlarge the chemical and structural composition of the sample.*

A.1.2 TEM in this work

In this work, two different transmission electron microscopes have been used, both belonging to the University of Cadiz. A FEI Titan3 Themis 60-300 that allowed an exquisite analysis with top-of-the-range spectral and spatial resolution by multiple aberrations correction and a monocromator. A Talos F200X (S)TEM that provided fast, precise, quantitative materials characterization. With less resolution but a much higher accessibility and ease of use was fundamental in this work.

The role of TEM in this thesis was to study the metal diamond interfaces. It provided an insight in the structural and chemical composition of the metal contact stacks while also delivering information on the interface of the Schottky metals with diamond. These studies were performed on contacts from the sample LD1 and are included in the section 3.3.

A.2 X-rays photoelectron spectroscopy

A.2.1 Technique description

X-Ray photoelectron spectrometry is a spectroscopic technique that implies the measurement of the photoelectron spectra induced by X-ray beam focused on a sample. It is a technique that allows the quantification of the stoichiometry of materials. It also provides information about the bonding between atoms in a material due to the different screening of the atom potential depending on its bonds [176]. Moreover, it gives physical information about materials, such as the position of the Fermi level or the shape of the valence band and it can be used to measure band settings and Schottky barriers. It is typically characterized by a low spacial resolution in the range of the micrometer. However, the depth resolution of this technique is defined by the mean free path of excited electrons coming out from the material. The typical depth sensitivity is less than 10 nm which makes this technique an excellent candidate for interface and surface characterization studies.

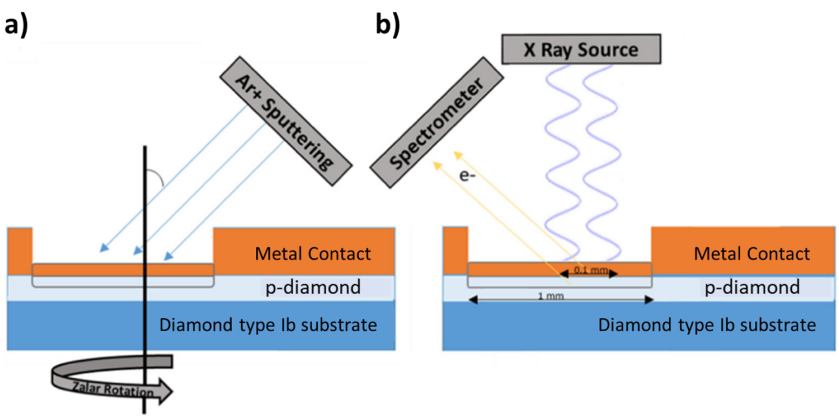

FIGURE A.2: *a) Scheme representing the Ar+ sputtering through the metal contact layer while applying a Zalar compucentric rotation. b) Scheme of the x-rays focused in the well formed by the Ar+ sputtering and the XPS spectrometer collecting the photoemitted electrons to study the depth profile of the contact.*

A.2.2 XPS in this work

In order to study the metal contacts on diamond an XPS depth profile was performed through the metal contacts with low energy (0.5 kV) and oblique angle (57°) Ar+ sputtering, while applying a Zalar compucentric rotation normal to the surface. A scheme of the etching process is represented in figure A.2 a). XPS measurements have been performed alternately (to the sputtering) in the wells as it is represented in figure A.2 b). The alternated XPS measurement and sputtering were stopped when the whole XPS signal was attributed to diamond. The XPS depth profile spectra have been used to determine the contact stoichiometry and Schottky barrier in the sample LD1. These studies are included in the section 3.4.

All the measurements carried out in this work were using a high resolution monochromatic Al K radiation (h = 1486.6 eV) with a PHI 5700 equipment. The spectra were recorded using a 0.1 eV step and a 23.5 eV pass energy. The peak contributions were extracted by combining a Lorentzian and a Gaussian function (Voigt profile). The background was subtracted using Tougaard background model function.

A.3 Kelvin probe force microscopy

A.3.1 Technique description

Kelvin probe force microscopy (KPFM) is a scanning probe microscopy technique that allows measuring the surface potential at the nanoscale [177]. When the tip of the KPFM and a material are brought into contact, a charge redistribution take place until the Fermi energy is constant through the system. As in a plane capacitor, equal and opposite charges will be induced on the surfaces. The potential established between the tip and the material is known as the contact potential difference (CPD) and and is equal to the work function difference between the two materials. This situation is schemed in the figure A.3 a). In KPFM, a potential is applied to the tip until the CPD is cancelled and thus the charges disappear. This situation is schemed in figure A.3 b). The various KPFM techniques developed differ mainly on how the situation where the potential applied equals the CPD is detected. Vibrating the tip over a sample causes the capacitance to vary as the distance changes and this induces charge to flow resulting in an AC current. The potential, at which AC current is at a minimum is found to equal the CPD. The central idea is that the electric force between the tip and the material becomes minimum when the potential and the CPD are equal.

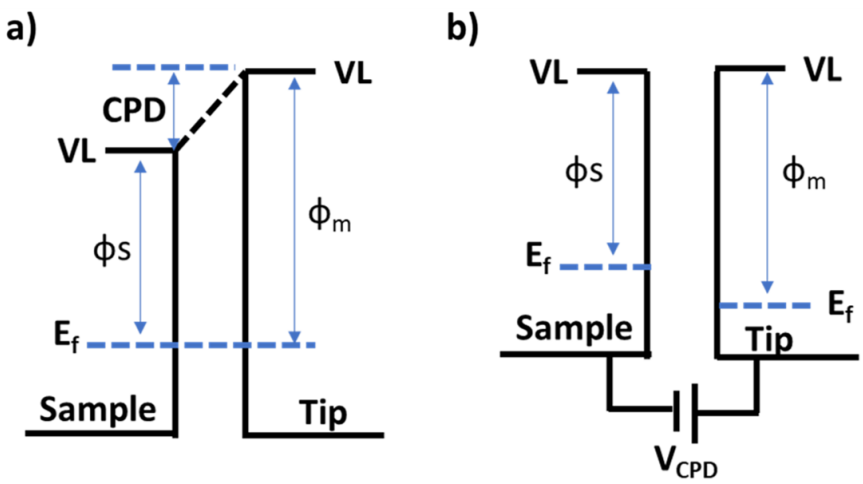

FIGURE A.3: *a) Scheme representing the system KPFM tip-sample at thermal equilibrium. b) Scheme of the system KPFM tip-sample when a potential equal to the contact potential difference is applied.*

A.3.2 Kelvin probe in this work

KPFM was used in this work to investigate the oxygen-terminated diamond surface. By using KPFM, the Fermi level on diamond surface can be measured and thus its depletion layer thickness and band bending estimated. This is extremely important for lateral transistor design since the magnitude of this depletion will impact the electrical characteristics. On the other hand, KPFM has also been used to study the lateral depletion of molybdenum and zirconium contacts. This can be done since the lateral band bending caused by the contacts cause a profile in which the work function is variable, as the energy distance from the Fermi level to the vacuum varies in the lateral depletion. All these studies are included in the section 3.5.

The sample LD1 was studied with a Bruker Dimension Icon atomic force microscope (AFM) with ScanAsyst and equipped with the Nanoscope software (Bruker Nanoscope V). The measurements were performed in air with peak force tapping mode at steps of 20 mm. In peak-force tapping AFM the probe is oscillated at a typical frequency of 2 kHz (far below the resonance of the cantilever) with typical peak-to peak amplitudes in air of 300 nm. The probe is periodically bought into contact with the sample for a short time (0.1 ms) and a periodically oscillating force is exerted onto the sample surface. A silicon tip on nitride lever (ScanAsyst Air model), with a 0.4 N/m spring constant and a nominal tip radius of 2 nm, was used.

A.4 Electric measurements

A.4.1 Electrical measurements in this work

Electrical measurements play a central role in this work. Schottky diodes and transistors electrical characteristics are presented along the chapters 3,4 and 5. The electrical characterizations were performed at the Institut NEEL in a home-made vacuum probe station that is presented in figure A.4. The electrical measurements were performed using a Keithley SMU 2636A and a single channel SMU 2410 for I(V) measurements and a ModuLab XM MTS Solartron analytical system for capacitance - voltage C(V) characteristics. The SMU 2636A in DC measurement mode was used to characterize devices because of its 1 A maximum current capability and a current detection limit of 10^{12} A with a bias range of 200 V. The SMU 2410 was used to investigate the off-state of devices due to its 1100 V of maximum applied bias voltage and 10^{9} A detection limit. Regarding the Solartron, the typical AC signal frequency is ranging from 0.1 Hz to 1 MHz (with a possible DC bias ranging from -8 V to 8 V) and the AC signal voltage amplitude was 50 mV. The probes station uses a binocular microscope and a piezoelectric micro-manipulators for an accurate control of the tips when approaching the metal contact. The temperature of the samples was controlled by a Linkam cooling system (ranging from -196C to 600C) and a resistance thermometers (Pt100) placed on the sample holder.

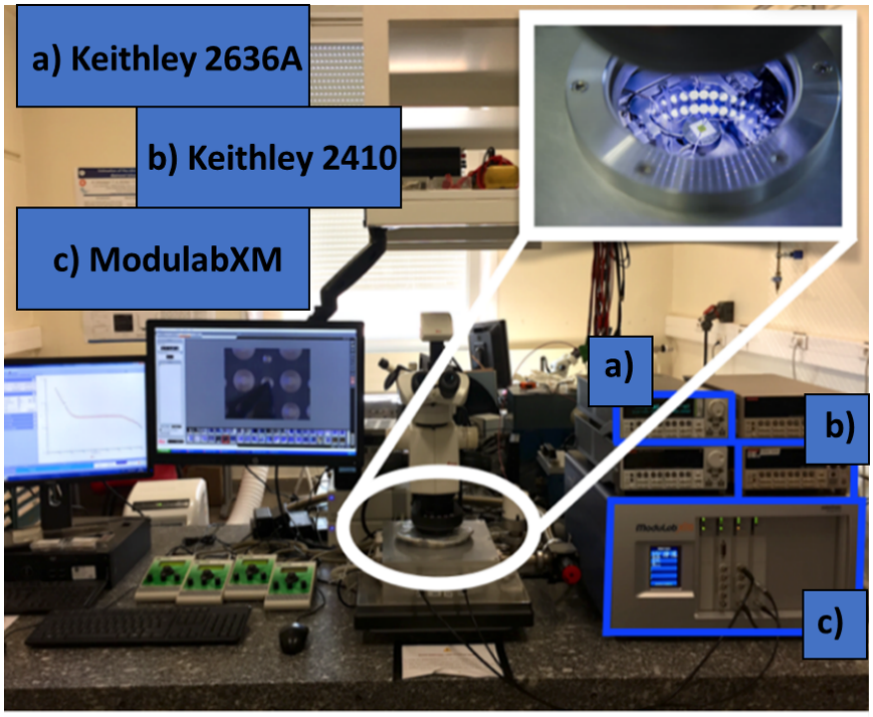

FIGURE A.4: *Home-made vacuum probe station at the Institut NEEL where the electrical measurements were performed using: a) Keithley SMU 2636A, b) SMU 2410 and c) ModuLab XM MTS Solartron.*

A.5 EBIC & Cathodoluminiscence

A.5.1 Techniques descriptions

When an energetic electron beam is focused on a semiconductor sample, it will excite valence bands electrons in to the conduction band creating electron hole pairs (EHP). From these point, two different phenomena that are schemed in the figure A.5 can happen that allow to study the properties of the semiconductor:

1. **EBIC**

   If the semiconductor sample contains an internal electric field, as in a Schottky contact, the EHP will be separated by drift due to the electric field making a current to flow. By using the current level as the imaging signal for each point in which the electron beam is focused, an electron beam induced current (EBIC) image is formed [178]. When EBIC is performed on a semiconductor device, the depletion region will show bright EBIC contrast. EBIC mapping on a contact can be used to identify hot spots from which the leakage can flow through a contact as the higher the current is, the higher the EBIC signal is.

2. **Cathodoluminiscence**

   On the other hand, EHP pairs can also recombine through a radiative process emitting light. If this light is collected and separated into its component wavelengths, a

cathodoluminiscence (CL) spectra of the semiconductor is obtained. CL technique is a non-destructive and a contactless method that is generally used to study defects and dopants in semiconductors [179].

The advantages is that these techniques are typically performed inside a scanning electron microscope with very good resolutions of a few tens nanometers allowing the comparison with the sample morphology. Although for EBIC and CL, the resolution is determined by the pear formed by the interactions of the incoming electrons and the semiconductor of the order of hundreds of nanometers to microns.

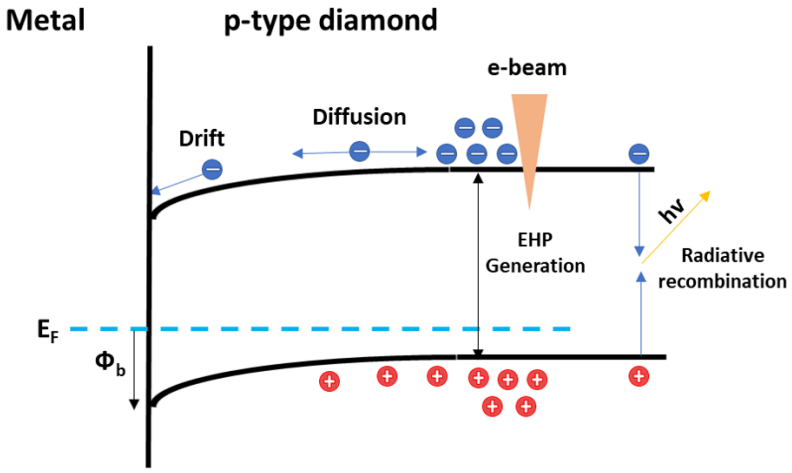

FIGURE A.5: *Scheme of the bands of a Schottky contact on p-type diamond where electon hole pairs (EHP) are generated by an e-beam. Two phenomena are sketched, the diffusion plus drift of the electrons from the EHP that lead to electron beam induced current (EBIC) and the radiative recombination of the EHP which is used in catodoluminiscence (CL) spectroscopy.*

A.5.2 Role in this work

The set-up used for performing EBIC and CL experiments is presented in the figure A.6. The experiments are carried out inside a SEM MEB FEI Quanta200. For the collection of the minority carriers in EBIC a preamplifier and a Keithley 6485 picoammeter is used. For CL, the emitted light are collected thanks to a mirror and analyzed with a spectrometer. The CL experiments were carried out at 5K by using liquid He to cool down.

The role of EBIC in this thesis was to identify hotspots in the Schottky contacts in order to provide an insight on the leakage current detected in these. On the other hand, CL was used to extract the extract the doping level via the excitonic region of the spectra and to study different regions of the samples and its defects through the well-known defects bands spectra.

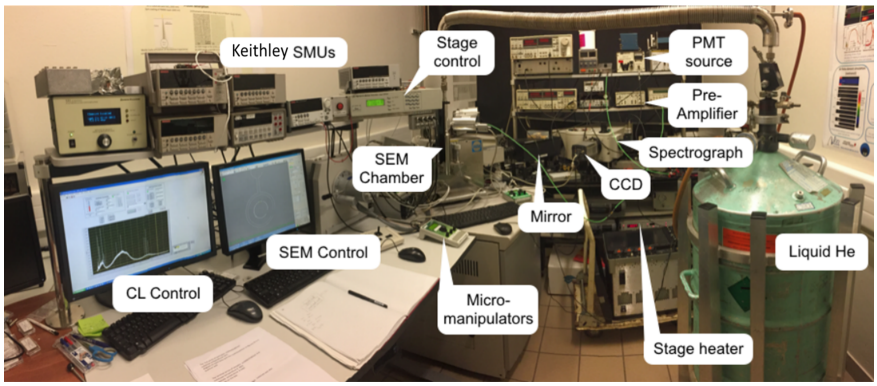

FIGURE A.6: *An image of the used set-up to perform electron beam induced current (EBIC) and cathodoluminiscence (CL) spectroscopy.*

A.6 Density functional theory

A.6.1 Theoretical description

Density-functional theory (DFT) is a quantum mechanical AB-initio method to study the electronic structure of molecules and solids. The fundamental idea under DFT is that, properties of materials are determined by using functionals that depends on the electron density instead of the wavefuction [180].

The many body problem of electrons in a system is described by its quantum mechanical wavefunction (r1, . . . , rN) satisfying the Schrödinger equation (under the Born–Oppenheimer approximation):

$$\hat{H}\Psi = \left[\hat{T} + \hat{V} + \hat{U}\right]\Psi = \left[\sum_{i=1}^{N}\left(-\frac{\hbar^2}{2m_i}\nabla_i^2\right) + \sum_{i=1}^{N} V(\mathbf{r}_i) + \sum_{i<j}^{N} U\left(\mathbf{r}_i, \mathbf{r}_j\right)\right]\Psi = E\Psi, \tag{A.1}$$

where, Ĥ is the Hamiltonian, E is the total energy, $\hat{T}$ is the kinetic energy, $\hat{V}$ is the potential energy from the nuclei, and Û is the electron–electron interaction energy.

DFT provides an alternative to most costly computational approaches to solve the latter equation, as it provides a way to transform the many-body problem onto a single-body problem. In DFT the key variable is the electron density n(r), given by:

$$n(\mathbf{r}) = N\int \mathrm{d}^3\mathbf{r}_1 \cdots \int \mathrm{d}^3\mathbf{r}_N\, \Psi^*(\mathbf{r}, \mathbf{r}_2, \ldots, \mathbf{r}_N)\Psi(\mathbf{r}, \mathbf{r}_2, \ldots, \mathbf{r}_N) \tag{A.2}$$

From this equation, the ground-state density can be calculated from the wavefunction. This equation can also be reversed, i.e., the wavefunction is a unique functional of the ground state density.

Two theorems derived by Hohenberg and Kohn provide the core framework for the DFT approach to the many-body problem. The first theorem demonstrates that the ground-state properties of a many-electron system are determined by the electron density. It reduces the many-body problem of N electrons with 3N spatial coordinates to three spatial coordinates,

through the use the electron density. The second theorem states that the energy defined by the Hamiltonian functional when the charge density is that of the ground state.

The T[n] and U[n] (Kinetic and electron-electron interaction energy functionals) are universal, while V[n] (The potential energy functional from the nuclei) depends on the studied system. Given a system, i.e., having a concrete $\hat{V}$, the functional E[n] must be minimized with respect to n(r):

$$E[n] = T[n] + U[n] + \int V(\mathbf{r})n(\mathbf{r})\,\mathrm{d}^3\mathbf{r} \tag{A.3}$$

A successful minimization of the energy functional will yield the ground-state density.

In the practice, an energy functional without an electron–electron interaction energy term is first considered. The Kohn–Sham equations (a fictitious system of non-interacting electrons that generate the same density as a given system of interacting electrons defined by a local effective (fictitious) external potential V_s(r)) of this auxiliary non-interacting system can be derived:

$$\left[-\frac{\hbar^2}{2m}\nabla^2 + V_\mathrm{s}(\mathbf{r})\right]\varphi_i(\mathbf{r}) = \varepsilon_i\varphi_i(\mathbf{r}) \tag{A.4}$$

which yields the orbitals that reproduce the density n(r) of the original many-body system:

$$n(\mathbf{r}) = \sum_{i=1}^{N} \left|\varphi_i(\mathbf{r})\right|^2 \tag{A.5}$$

And the effective single-particle potential can be written as:

$$V_\mathrm{s}(\mathbf{r}) = V(\mathbf{r}) + \int \frac{n(\mathbf{r}')}{|\mathbf{r}-\mathbf{r}'|}\,\mathrm{d}^3\mathbf{r}' + V_\mathrm{XC}[n(\mathbf{r})] \tag{A.6}$$

where $V(\mathbf{r})$ is the external potential, the second term is the Hartree term describing the electron–electron Coulomb repulsion, and the last term V_{XC} is the exchange–correlation potential. V_{XC} includes all the many-particle interactions. Since the Hartree term and V_{XC} depend on n(r) which depends on V_s, the problem of solving the Kohn–Sham equation is addressed in an iterative way. The iterative resolution typically stats with an initial guess for n(r) and the consequent calculation of the corresponding V_s and solving the Kohn–Sham equations for the charge density. From these one calculates a new density and starts again. This procedure is then repeated until convergence is reached.

The major problem with DFT is that the exact functionals for exchange and correlation are not known. One of the simplest approximations is the local-density approximation (LDA), where the functional depends only on the density where the functional is evaluated. Other pseudo-potentials are obtained inverting the free-atom Schrödinger equation for a given reference electronic configuration and forcing the pseudo-wavefunctions to coincide with the true valence wavefunctions beyond a certain distance as illustrated in A.7.

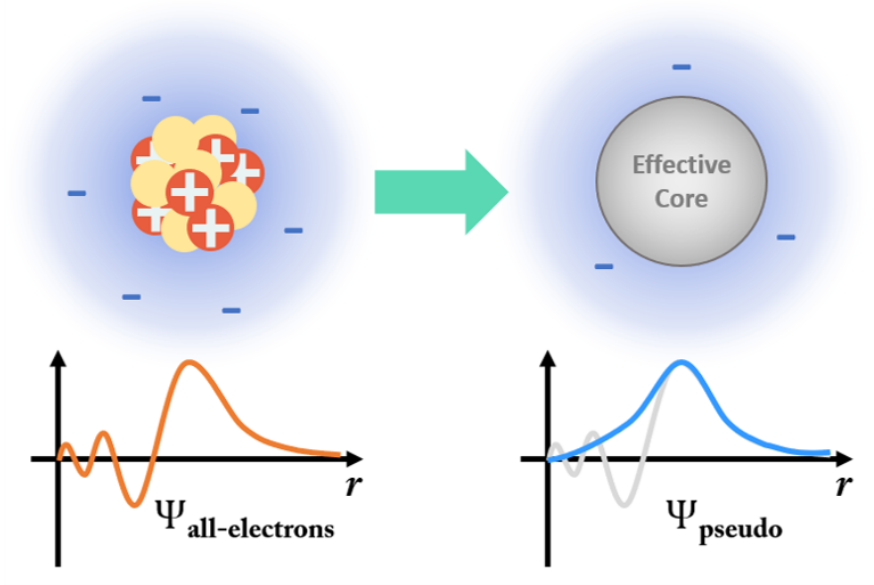

FIGURE A.7: *Illustrative picture on how modern pseudo-potentials are obtained inverting the free-atom Schrödinger equation for a given reference electronic configuration and forcing the pseudo-wavefunctions to coincide with the true valence wavefunctions beyond a certain distance.*

A.6.2 Role in this work

In this work, all the ab-initio calculation have been performed using the free software Quantumespresso 6.5 version. The calculations have been performed in the computational cluster of Centro Informático Científico de Andalucía.

DFT simulations have been performed to study the electronic properties of the oxygen-terminated diamond and its interface with molybdenum. Especial attention was taken in extracting the Schottky barrier of the latter and the band bending potential V_{BB} and electron affinity for the first one. The results accomplished with these simulations can be found in the section 3.6.

Appendix B

Samples summary

Sample	Architecure	Substrate	p drift layer					p+ layer				Schottky
			Doping level	thickness	B/C	C/H	O/H	thickness	B/C	H/C	Type	Stack
LD1	Lateral	Sumitomo (100)	1.6 10^{16} cm^{-3}	900 nm	50ppm	1%	0.25%	No			-	Mo/Zr-Pt-Au
VD1	Vertical	NDT(100)	3.9 10^{16} cm^{-3}	430 nm	60ppm	1%	0.25%	3000 nm	533ppm	4%	Encapsulated	Mo/Zr-Pt-Au
VD2	Vertical	NDT(100)	2-8 10^{15} cm^{-3}	>4.5mic	-	4.2%	-	3000 nm	533ppm	4%	Encapsulated	Mo-Pt-Au
RB	Lateral	Sumitomo (100)	3.5 10^{16} cm^{-3}	450nm	60ppm	1%	0.25%	120 nm	1200ppm	4%	selective	Mo

FIGURE B.1: *Description of the diverse epitaxy conditions and Schottky electrodes used in this thesis samples.*

Appendix C

Thesis summaries

C.1 English Summary

The power electronic market is dominated by silicon devices, which are responsible for most of the energy losses over the whole energy chain. The performance of these devices is limited by the material properties of silicon. The on-state resistance, related to the material resistivity, dissipate heat due to Joule effect during current conduction. The maximum voltage blocked by the devices is related to the maximum electric field sustained by the material. Indeed, these two material properties are connected, resulting in a core trade-off for power electronics: on vs off state performance. Also, switching losses coming from the fact that a device requires time to switch from on to off state (and viceversa) are always present. With the current silicon technology reaching its theoretical limits, the only road to improve the performance is to use new materials with better properties, and thus, better trade-off between on and off states. Wide band gap materials have been under research for the last decades due to their immense potential to block a very high voltage while delivering a very high current. Between them, diamond is the ultimate semiconductor for power electronics due to its outstanding properties. Besides being the hardest material, diamond possesses the best properties among ultra-wide band gap semiconductors including its high electron-hole mobility, high critical electric field and low dielectric constant. Moreover, it surpasses all competitor materials in terms of thermal conductivity with the highest value reported for any material. All these properties make the ideal performance of diamond devices to be above any other material. However, diamond devices are still under development with several technological limitations and bottlenecks that need to be addressed in order to extract diamond's full potential. The main drawback is that both p and n type dopants give rise to relatively deep levels causing partial ionization at room temperature. However, the partial ionization can be easily mitigated for p-type diamond by working at high temperatures (550K) leading to outstanding on-state device performances. Also, substrates are expensive and limited in size, although an encouraging progression have been shown in the last decade. Therefore, the future market of diamond devices seems to be focused to ultra-high power, high frequency and temperature and harsh environment applications.

Concerning diamond field-effect transistors (FET), the majority have been fabricated using 2D hole gas that emerges when an H-terminated diamond surface comes into contact with a range of adsorbates and/or selected metal oxides. However, this unconventional manner of creating a p-type region in a semiconductor suffers from instability and reproducibility problems and low operational mobility issues, although recent progress with the use of metal oxide passivation/gate structures have considerably reduced these problems. Nonetheless, device fabrication strategies that rely upon a conventional doping approach have also been explored. Based on p-type boron doped diamond epilayers, normally-on metal semiconductor FET (MESFET) and metal oxide semiconductors FET have been demonstrated with blocking voltages up to 3 kV. These ensure optimized compatibility for ultimate device integration with existing technology along, with the full realization of the potential for operation in harsh environments. Also, they provide the best performance at elevated temperatures (550K) due to the ionization of boron impurities that can be exploited in power electronics thanks to the self-heating of devices.
On the other hand, diamond Schottky diodes have been fabricated since the 90's and are the most developed component nowadays. Most Schottky contacts are also fabricated based on boron-doped diamond using a pseudo-vertical architecture. Schottky diodes are very promising for its fast-switching capabilities and high voltages. In fact, optimized diamond Schottky diodes can ideally sustain up to 30 KV. Extensive research has led to impressive results reported over the last decade. Different surface treatments and metals (W, WC, Zr, Pt, Mo,etc) have been explored with the purpose of reducing leakage currents and thus obtaining the best possible on vs off trade-off. Diamond Schottky diodes able to sustain up to 10 kV and a record critical electric field of 7.7 MV/cm have been reported. On the other hand, heteroepitaxial Schottky diodes have also been fabricated showing promising results, as diminishing the cost of devices is fundamental for their commercialization. However, technological limitations in etching and epitaxy limits the ultimate performance of diamond Schottky diodes. Also, irreproducibility among samples and fabrication methods is one of the main constraints that has to be faced in the coming years.

This thesis is dedicated to the development of Schottky barrier diodes and Schottky based transistors (MESFET) based on p-type diamond. The optimization of these components is crucial for the diamond future roadmap for power electronics, as a true demonstration of diamond potential still lacks, and it will definitely attract interest from research and companies into it further pushing the development of devices and eventually ending up in their commercialization. In order to get demonstrate diamond potential, various challenging objectives were set regarding Schottky contact based devices: i) The study and optimization of metal-diamond properties from an electronic, physico-chemical and material science point of view in order to extract the best possible performing Schottky contact. ii) The design, fabrication and characterization of an optimized high voltage diamond vertical Schottky diode. iii) The design, fabrication and characterization of a normally-off 1 kV diamond gate-drain Schottky MESFET. The development of such studies and devices is carried on within the institute NÉEL and the University of Cadiz under the frame of two

different projects: The first one, the diamond-HVDC project. Its goal is the fabrication of HV diamond Schottky diodes for its integration inside a commutation cell and test its reliability. The second one is the Green diamond European project. My purpose inside this project was to coordinate and participate on the fabrication and characterize a normally-off 1 kV diamond gate-drain Schottky lateral MESFET. The ultimate goal for these projects is to fabricate ideal performing devices, to demonstrate diamond ultimate capabilities, and their integration into functional power electronic components. The diamond epitaxy, power electronic knowledge and capabilities from the SC2G group in-side NEEL institute in France and the powerful material science analysis techniques and the expertise from the UCA are put together during my PHD to address these challenges.

This works starts by setting the theoretical framework underlying Schottky contact-based devices. Diamond Schottky contacts modelization is presented based on an analytical description of Schottky barriers and the equations governing the forward and reverse conduction mechanisms through the Schottky barrier are introduced and solved numerically. The state of the art diamond resistivity and breakdown models are as well presented and discussed. These physical models are then used for the quantitative comprehension of diamond diodes firstly and diamond lateral MESFET's secondly. On one hand, the different diode structures and their fabrication constraints and technological limitations are introduced. The impact of these constraints is illustrated as well as the optimal performance of diamond diodes. On the other hand, the RBMESFET concept is presented and a 1D model for the on-state current under the gradual channel approximation is developed. Its performance is analyzed relying on the developed physical models.

Once the framework is presented, a dedicated experimental investigation of lateral molybdenum and zirconium Schottky diodes follows. The TEM and XPS extracted compositional profile is correlated to zirconium and molybdenum Schottky contact electrical performance. The ozone passivation treatment, demonstrated to be crucial in reducing leakage currents, is shown to oxidize the molybdenum and zirconium layers. While this did not greatly affect the molybdenum on-state characteristics, the degradation of the zirconium contacts is explained as a result of the high concentration of oxide in the interface. The potential profiles along the contacts edges, extracted from Kelvin probe force microscopy, showed the great passivation capabilities of the oxygen terminated diamond and its possible role in the leakage currents through the edge of the contacts in zirconium. On the other hand, molybdenum built-in voltage is shown to be lower than the oxygen-terminated band bending potential. This plays an important role to avoid leakage currents through the edge of the contacts and support the impressive off-state characteristics extracted. Lastly, a theoretical approach to understand both oxygen-terminated surface and its interface with molybdenum was taken. The theoretical calculation presented qualitative agreement with the experimental KPFM results yielding a Schottky barrier height for molybdenum of ϕ_b=2.45 eV. Also, the bonding pattern between molybdenum and oxygen-terminated diamond was revealed to consist of an ionic-like oxygen-molybdenum bonding.

Concerning vertical diodes, two different Schottky diode samples were fabricated, one

in order to evaluate molybdenum and zirconium Schottky diodes and another one for developing a kV range diode based on the findings. The first sample (VD1) demonstrated the success of the fabrication process used, based on molybdenum, with the crucial importance of the surface passivation treatment for the high blocking voltage capabilities. The superiority of this molybdenum versus zirconium as Schottky contact was demonstrated as the former had higher Schottky barrier, lower ideality factor, better thermal stability and better blocking voltage capabilities. Over half of the contacts presented in the first sample were able to sustain 2.25 MV/cm with at least 4 magnitude orders of rectification. Its application in low doped diamond epilayers could consistently sustain as much as a 60% of low doped diamond breakdown field. The second sample (VD2) implemented the developed fabrication process of molybdenum based Schottky contact into an HV design. It successfully demonstrated >1kV breakdown voltage capabilities with contacts sustaining (a low estimate) electric field of 2.2 MV/cm. This sample drift layer epitaxy produced numerous hillocks and round defects which makes even more noteworthy the contacts performance. The role of these defects was studied and only the hillocks contributed to the leakage currents through the contacts. Although the sample irregularity and high concentration of defects, the irreproducibility in the breakdown voltages was attributed to the electric field crowding on the edge of the contacts and this hypothesis was supported by EBIC measurements. The electric field sustained for contacts in both samples versus the area of the contacts is represented in figure C.1 compared to multiple literature results.

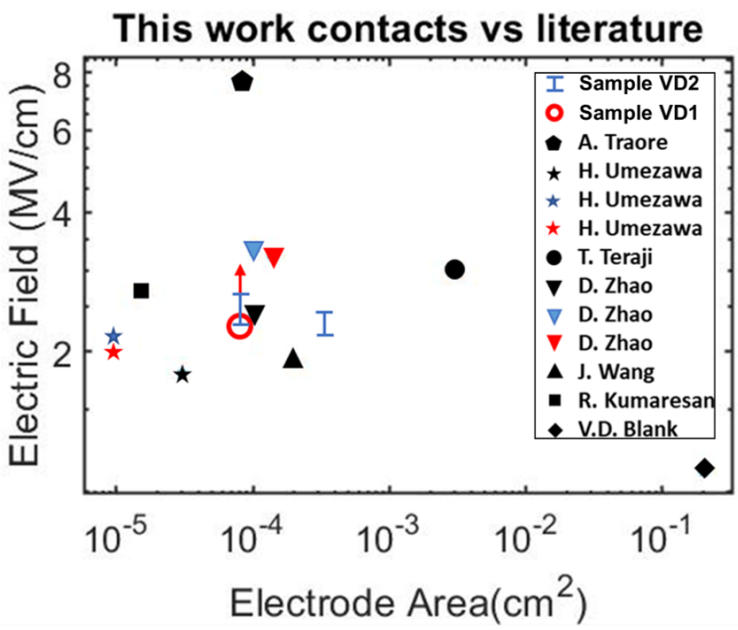

FIGURE C.1: *Sustained electric field versus Schottky electrode area for this work molybdenum contacts compared with numerous bibliographic references [167, 168, 150, 149, 169, 170, 171, 172].*

Therefore, the molybdenum Schottky contacts developed in this work demonstrated

consistently suitable performances for extracting diamond HV potential at high temperature. The leakage current problematic was addressed and by following the fabrication process developed in this thesis, future diamond Schottky diodes will be able to unleash its full potential.

Lastly, a >1kV normally-off lateral reverse-blocking (Schottky Drain) MESFETs based on molybdenum Schottky contacts on O-terminated boron doped diamond have been fabricated. Precise control over epilayer thickness and doping level have been achieved such that full depletion of the channel arises without an applied gate bias with the possibility to open the channel at negative V_{GS}. The devices display undetectable leakage current and a current of 1.5 µA/mm in the on state at RT. Importantly, the transistor´s blocking capabilities were evaluated to be >1kV even at its maximum working temperature of 425K displaying no leakage current and after the HV stress, presenting non-changed reproducible characteristics. Higher temperature characterization (425K) reveals augmented transistor on-state capabilities due to fuller ionization of the boron dopant atoms, with the transistor reaching a current level of 70 $\mu A/mm$ and a transconductance of $147 \mu S mm^{-1}$. The high temperature characteristics of the transistor are shown in figure C.2. However, its working temperature is limited to 425K, below the optimal 500-550K, due to the non-grounded p-n junction between the p-type drift layer and the semi-insulating Ib substrate. Anyways, the high breakdown voltage, the relatively high temperature operation capabilities, normally-off behavior and diamond's inherent radiation hardness as a semiconductor, make these devices an excellent approach towards the goal of achieving diamond transistors for high temperature, high voltage and harsh environment applications.

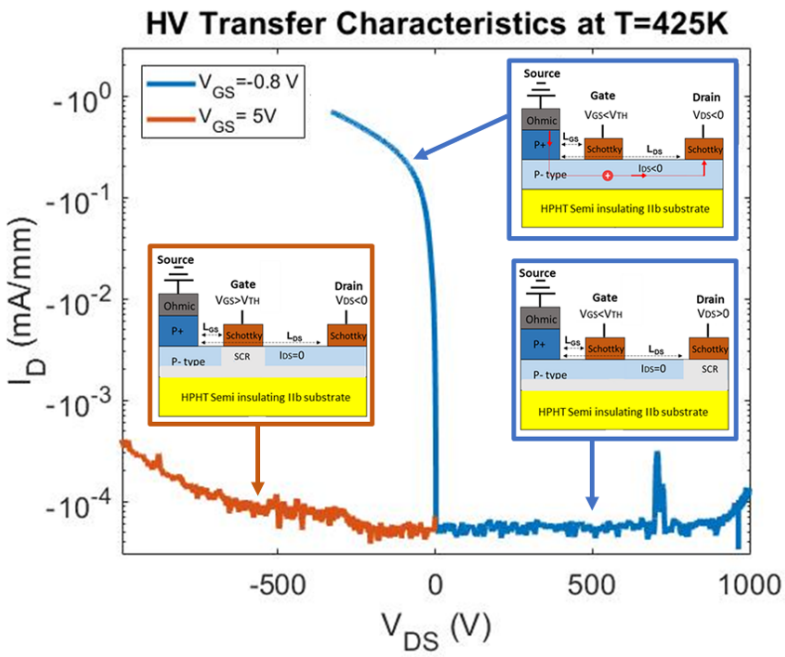

FIGURE C.2: *HV transfer characteristics of the RBMESFET at 425K for the close channel configuration with $V_{GS} = 5V$ in the red curve and for the on-state and Schottky diode configuration in the blue curve with $V_{GS} = -0.8V$.*

As summary, the progress made during this thesis in the optimization of Schottky contacts allowed to push the off-state and reproducibility of vertical diamond Schottky diodes. Future diodes will benefit from the results shown, as the application of the Schottky contacts developed in this thesis together with thicker diamond drift layers could achieve the benchmark of sustaining 10 kV. On the other hand, the demonstration of a >1kV normally-off lateral reverse-blocking (Schottky Drain) MESFETs was the first of its kind. The unusual characteristics of this transistor show the precision acquired in diamond epitaxy technology. A future transition toward vertical transistors using the developed technology will unleash diamond MESFET potential performance.

C.2 Resumé Français

Le marché de l'électronique de puissance est dominé par les dispositifs en silicium, qui sont responsables de la plupart des pertes d'énergie sur l'ensemble de la chaîne énergétique. Les performances de ces dispositifs sont limitées par les propriétés du silicium. La résistance à l'état ON, liée à la résistivité du matériau, dissipe de la chaleur par effet Joule pendant la conduction du courant. La tension maximale bloquée par les dispositifs est liée au champ électrique maximal supporté par le matériau. En effet, ces deux propriétés du matériau sont liées, ce qui entraîne un compromis essentiel pour l'électronique de puissance : les performances à l'état ON et à l'état OFF. En outre, les pertes de commutation dues au fait qu'un dispositif a besoin de temps pour passer de l'état ON à l'état OFF (et vice versa) sont toujours présentes. La technologie actuelle du silicium ayant atteint ses limites théoriques, la seule façon d'améliorer les performances est d'utiliser de nouveaux matériaux dotés de meilleures propriétés, et donc d'un meilleur compromis entre les états ON et OFF. Les matériaux à large bande interdite font l'objet de recherches depuis plusieurs décennies en raison de leur immense potentiel à bloquer une tension très élevée tout en délivrant un courant très élevé. En raison de ses propriétés exceptionnelles, le diamant est le meilleur semiconducteur pour l'électronique de puissance. En plus d'être le matériau le plus dur, le diamant possède les meilleures propriétés parmi les semi-conducteurs à bande interdite ultra large, notamment une mobilité électron-trou élevée, un champ électrique critique élevé et une faible constante diélectrique. En outre, il surpasse tous les matériaux concurrents en termes de conductivité thermique, avec la valeur la plus élevée rapportée pour un matériau quelconque. Toutes ces propriétés font que les performances idéales des dispositifs en diamant sont supérieures à celles de tout autre matériau. Cependant, les dispositifs en diamant sont toujours en cours de développement et présentent plusieurs limitations et goulots d'étranglement technologiques qui doivent être résolus afin d'extraire tout le potentiel du diamant. Le principal inconvénient est que les dopants de type p et n donnent lieu à des niveaux relativement profonds provoquant une ionisation partielle à température ambiante. Cependant, l'ionisation partielle peut être facilement atténuée pour le diamant de type p en travaillant à des températures élevées (550K), ce qui permet d'obtenir des performances exceptionnelles des dispositifs à l'état actif. En outre, les substrats sont

chers et de taille limitée, bien qu'une progression encourageante ait été observée au cours de la dernière décennie. Par conséquent, le marché futur des dispositifs en diamant semble se concentrer sur les applications à ultra-haute puissance, à haute fréquence, à haute température et dans des environnements difficiles. En ce qui concerne les transistors à effet de champ (FET) en diamant, la majorité d'entre eux ont été fabriqués à l'aide d'un gaz de trous 2D qui émerge lorsqu'une surface de diamant à terminaison hydrogène entre en contact avec une série d'adsorbats et/ou d'oxydes métalliques. Cependant, cette manière non conventionnelle de créer une région de type p dans un semi-conducteur souffre de problèmes d'instabilité, de reproductibilité et de faible mobilité opérationnelle, bien que des progrès récents dans l'utilisation de structures de passivation/grille en oxyde métallique aient considérablement réduit ces problèmes. Néanmoins, des stratégies de fabrication de dispositifs reposant sur une approche de dopage conventionnelle ont également été explorées. Sur la base de couches épilées de diamant dopé au bore de type p, des transistors à effet de champ metal-semiconducteur (MESFET) et métal-oxyde-semiconducteur ont été démontrés avec des tensions de blocage allant jusqu'à 3 kV. Ils garantissent une compatibilité optimisée pour une intégration ultime du dispositif dans la technologie existante, avec la pleine réalisation du potentiel de fonctionnement dans des environnements difficiles. En outre, ils offrent les meilleures performances à des températures élevées (550K) grâce à l'ionisation des impuretés de bore qui peuvent être exploitées dans l'électronique de puissance grâce à l'auto-échauffement des dispositifs. D'autre part, les diodes Schottky en diamant ont été fabriquées depuis les années 90 et sont le composant le plus développé actuellement. La plupart des contacts Schottky sont également fabriqués à base de diamant dopé au bore en utilisant une architecture pseudo-verticale. Les diodes Schottky sont très prometteuses pour leurs capacités de commutation rapide et leurs tensions élevées. En fait, les diodes Schottky en diamant optimisées peuvent idéalement supporter jusqu'à 30 KV. Des recherches approfondies ont permis d'obtenir des résultats impressionnants au cours de la dernière décennie. Différents traitements de surface et métaux (W, WC, Zr, Pt, Mo, etc.) ont été explorés dans le but de réduire les courants de fuite et d'obtenir ainsi le meilleur compromis possible entre marche et arrêt. Des diodes Schottky en diamant capables de supporter jusqu'à 10 kV et un champ électrique critique record de 7,7 MV/cm ont été rapportées. D'autre part, des diodes Schottky hétéroépitaxiales ont également été fabriquées, montrant des résultats prometteurs, car la diminution du coût des dispositifs est fondamentale pour leur commercialisation. Cependant, les limites technologiques de la gravure et de l'épitaxie limitent les performances ultimes des diodes Schottky en diamant. De plus, l'irreproductibilité entre les échantillons et les méthodes de fabrication est l'une des principales contraintes auxquelles il faudra faire face dans les années à venir.

Cette thèse est consacrée au développement de diodes Schottky et de transistors MESFET à base de diamant de type p. L'optimisation de ces composants est cruciale pour la future feuille de route du diamant dans le domaine de l'électronique de puissance, car il n'existe toujours pas de véritable démonstration du potentiel du diamant, ce qui attirera certainement l'intérêt de la recherche et des entreprises pour ce matériau, poussant ainsi

le développement des dispositifs et aboutissant finalement à leur commercialisation. Afin de démontrer le potentiel du diamant, plusieurs objectifs ambitieux ont été fixés en ce qui concerne les dispositifs à contact Schottky : i) l'étude et l'optimisation des propriétés métal-diamant d'un point de vue électronique, physico-chimique et de la science des matériaux afin d'obtenir le contact Schottky le plus performant possible ; ii) la conception, la fabrication et la caractérisation d'une diode Schottky verticale en diamant à haute tension optimisée ; iii) la conception, la fabrication et la caractérisation d'un MESFET Schottky à drain de grille en diamant de 1 kV normalement éteint. Le développement de ces études et de ces dispositifs se fait au sein de l'institut NÉEL et de l'Université de Cadix dans le cadre de deux projets différents : Le premier, le projet diamant-HVDC. Son objectif est de fabriquer des diodes Schottky en diamant HV pour les intégrer dans une cellule de commutation et tester leur fiabilité. Le second est le projet européen Greendiamond. Mon objectif au sein de ce projet était de coordonner et de participer à la fabrication et à la caractérisation d'un MESFET latéral Schottky à grille et drain en diamant de 1 kV normalement éteint. L'objectif ultime de ces projets est de fabriquer des dispositifs aux performances idéales, de démontrer les capacités ultimes du diamant et leur intégration dans des composants électroniques de puissance fonctionnels. L'épitaxie du diamant, les connaissances et les capacités en électronique de puissance du groupe SC2G au sein de l'institut NEEL en France et les puissantes techniques d'analyse de la science des matériaux ainsi que l'expertise de l'UCA sont réunies au cours de mon doctorat pour relever ces défis.

Ce travail commence par établir le cadre théorique qui sous-tend les dispositifs à base de contacts Schottky. La modélisation des contacts Schottky en diamant est présentée sur la base d'une description analytique des barrières Schottky et les équations régissant les mécanismes de conduction directe et inverse à travers la barrière Schottky sont introduites et résolues numériquement. L'état de l'art des modèles de résistivité et de claquage du diamant est également présenté et discuté. Ces modèles physiques sont ensuite utilisés pour la compréhension quantitative des diodes en diamant d'une part et des MESFET latéraux en diamant d'autre part. D'une part, les différentes structures de diodes et leurs contraintes de fabrication et limitations technologiques sont introduites. L'impact de ces contraintes est illustré ainsi que la performance optimale des diodes diamant. D'autre part, le concept RBMESFET est présenté et un modèle 1D pour le courant à l'état passant sous l'approximation du canal graduel est développé. Ses performances sont analysées en s'appuyant sur les modèles physiques développés. Une fois le cadre présenté, une étude expérimentale dédiée aux diodes Schottky latérales en molybdène et zirconium suit. Le profil de composition extrait par TEM et XPS est corrélé aux performances électriques des contacts Schottky en zirconium et molybdène. Le traitement de passivation à l'ozone, qui s'est avéré crucial pour réduire les courants de fuite, oxyde les couches de molybdène et de zirconium. Bien que cela n'ait pas beaucoup affecté les caractéristiques de l'état passant du molybdène, la dégradation des contacts en zirconium s'explique par la forte concentration d'oxyde dans l'interface. Les profils de potentiel le long des bords des contacts, extraits de la microscopie de force à sonde Kelvin, ont montré les grandes capacités de passivation du diamant à terminaison oxygène

et son rôle possible dans les courants de fuite à travers le bord des contacts en zirconium. D'autre part, il a été démontré que la tension intégrée du molybdène est inférieure au potentiel de flexion de bande à terminaison oxygène. Cela joue un rôle important pour éviter les courants de fuite à travers le bord des contacts et soutenir les impressionnantes caractéristiques de l'état de repos extraites. Enfin, une approche théorique a été adoptée pour comprendre la surface à terminaison oxygène et son interface avec le molybdène. Le calcul théorique a présenté un accord qualitatif avec les résultats expérimentaux de la KPFM, donnant une hauteur de barrière Schottky pour le molybdène de ϕ_b=2,45 eV. En outre, le modèle de liaison entre le molybdène et le diamant à terminaison oxygène s'est révélé être une liaison de type ionique oxygène-molybdène.

En ce qui concerne les diodes verticales, deux échantillons différents de diodes Schottky ont été fabriqués, l'un afin d'évaluer les diodes Schottky en molybdène et en zirconium et l'autre pour développer une diode de la gamme kV sur la base des résultats obtenus. Le premier échantillon a démontré le succès du procédé de fabrication utilisé, basé sur le molybdène, avec l'importance cruciale du traitement de passivation de surface pour les capacités de haute tension de blocage. La supériorité de ce contact Schottky en molybdène par rapport au zirconium a été démontrée, le premier présentant une barrière Schottky plus élevée, un facteur d'idéalité plus faible, une meilleure stabilité thermique et de meilleures capacités de tension de blocage. Plus de la moitié des contacts présentés dans le premier échantillon ont été capables de supporter 2,25 MV/cm avec au moins 4 ordres de grandeur de rectification. Son application dans des couches de diamant faiblement dopé permettra de maintenir de manière reproductible jusqu'à 60 Le deuxième échantillon a mis en œuvre le processus de fabrication développé du contact Schottky à base de molybdène dans une conception HV. Il a démontré avec succès des capacités de tension de claquage >1kV avec des contacts supportant (selon une estimation basse) un champ électrique de 2,2 MV/cm. L'épitaxie de la couche de dérive de cet échantillon a produit de nombreux défauts ''hillocks" et rond, ce qui rend encore plus remarquable la performance des contacts. Le rôle de ces défauts a été étudié et seuls les ''hillocks" ont contribué aux courants de fuite à travers les contacts. Malgré l'irrégularité de l'échantillon et la forte concentration de défauts, l'irreproductibilité des tensions de claquage a été attribuée à l'encombrement du champ électrique sur le bord des contacts et cette hypothèse a été confirmée par les mesures EBIC. Le champ électrique soutenu pour les contacts dans les deux échantillons par rapport à la surface des contacts est représenté sur la figure C.3 par rapport à plusieurs résultats de la littérature.

Par conséquent, les contacts Schottky en molybdène développés dans ce travail ont démontré des performances constamment appropriées pour extraire le potentiel HV du diamant à haute température. Le problème du courant de fuite a été résolu et en suivant le processus de fabrication développé dans cette thèse, les futures diodes Schottky en diamant seront capables de libérer tout leur potentiel.

Finalement, des MESFETs latéraux à blocage inverse (Drain Schottky) avec >1 kV de tension de blocage basés sur des contacts Schottky en molybdène sur du diamant dopé au bore à terminaison oxygène ont été fabriqués. Un contrôle précis de l'épaisseur de la couche

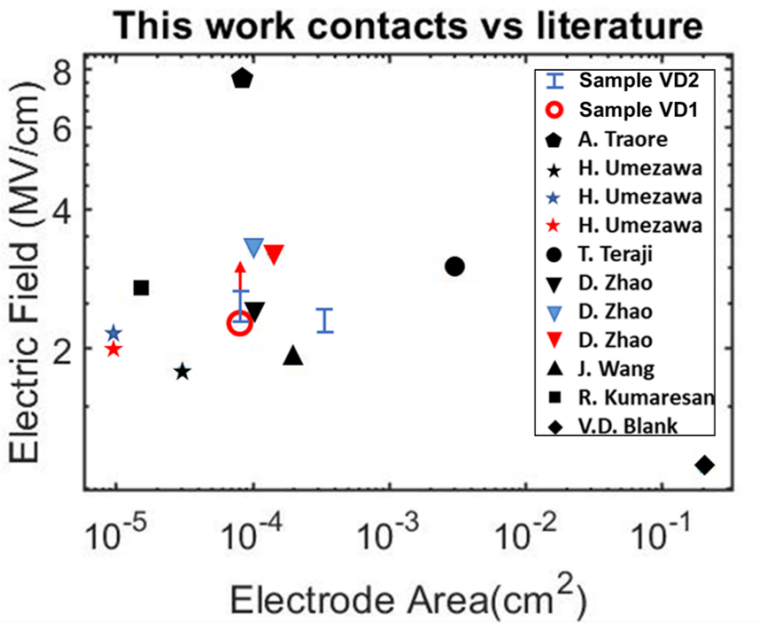

FIGURE C.3: *Champ électrique soutenu versus surface d'électrode Schottky pour les contacts en molybdène de ce travail comparés à de nombreuses références bibliographiques [167, 168, 150, 149, 169, 170, 171, 172].*

de diamant et du niveau de dopage a été réalisé de telle sorte que la déplétion complète du canal se produit sans une polarisation de grille appliquée avec la possibilité d'ouvrir le canal à V_{GS} négatif. Les dispositifs présentent un courant de fuite indétectable et un courant de 1,5 µA/mm à l'état actif à température ambiante. Il est important de noter que les capacités de blocage du transistor ont été évaluées à >1kV, même à sa température de fonctionnement maximale de 425K, sans courant de fuite et après le stress HV, présentant des caractéristiques reproductibles inchangées. La caractérisation à plus haute température (425K) révèle des capacités accrues du transistor à l'état passant en raison d'une ionisation plus complète des atomes de bore dopants, le transistor atteignant un niveau de courant de $70\mu A/mm$ et une transconductance de $147\mu Smm^{-1}$. Les caractéristiques à haute température du transistor sont montrées dans la figure C.4. Cependant, sa température de fonctionnement est limitée à 425K, en dessous de la valeur optimale de 500-550K, en raison de la jonction p-n non mise à la terre entre la couche de dérive de type p et le substrat semi-isolant Ib. Quoi qu'il en soit, la tension de claquage élevée, les capacités de fonctionnement à des températures relativement élevées, le comportement normalement éteint et la résistance inhérente du diamant aux radiations en tant que semi-conducteur, font de ces dispositifs une excellente approche vers l'objectif de réaliser des transistors en diamant pour des applications à haute température, à haute tension et dans des environnements difficiles.

En résumé, les progrès réalisés au cours de cette thèse dans l'optimisation des contacts Schottky ont permis de pousser l'état off et la reproductibilité des diodes Schottky verticales en diamant. Les diodes futures bénéficieront des résultats montrés, car l'application des contacts Schottky développés dans cette thèse avec des couches de dérive en diamant plus épaisses pourrait atteindre la référence de soutenir 10 kV. D'autre part, la démonstration

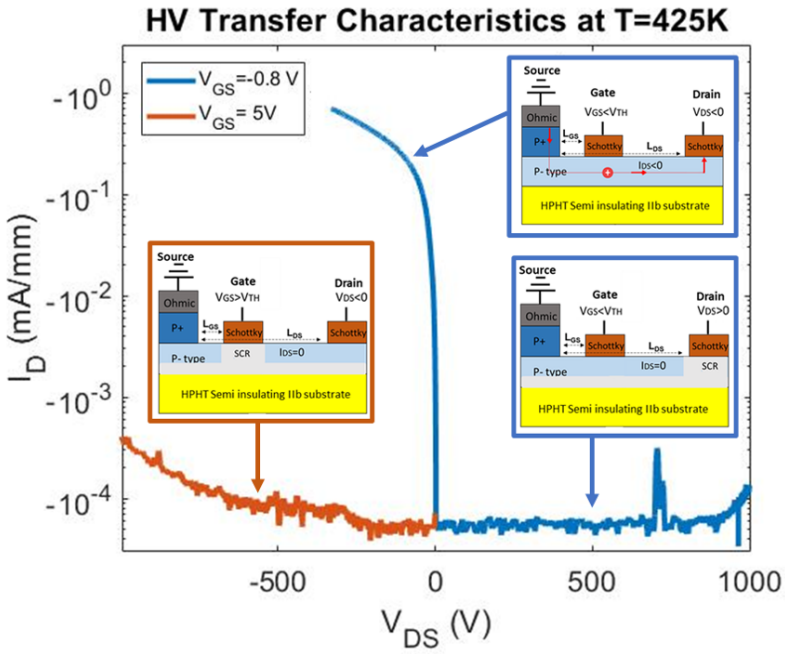

FIGURE C.4: *Caractéristiques de transfert à haute tension du RBMESFET à 425K pour la configuration à canal fermé avec $V_{GS} = 5V$ dans la courbe rouge et pour la configuration à l'état ON et diode Schottky dans la courbe bleue avec $V_{GS} = -0.8V$.*

d'un MESFETs à blocage latéral inverse (Schottky Drain) >1kV normalement éteint est la première de son genre. Les caractéristiques inhabituelles de ce transistor montrent la précision acquise dans la technologie d'épitaxie au diamant. Une future transition vers des transistors verticaux utilisant la technologie développée libérera les performances potentielles des MESFETs en diamant.

C.3 Resumen Español

El mercado de la electrónica de potencia esta dominado por los dispositivos de silicio, que son responsables de la mayor parte de las pérdidas a lo largo de toda red de energía. El rendimiento de los dispositivos esta limitado por las propiedades del silicio. La resistencia del estado encendido de los dispositivos, relacionada con la resistividad del material, disipa energía por efecto Joule durante la condición. El máximo voltaje bloqueado por los dispositivos esta relacionado con el máximo campo eléctrico que puede soportar el material. De hecho, estas dos propiedades están conectadas, como resultado aparece un balance clave para la electrónica de potencia: El rendimiento de los dispositivos en su estado encendido y apagado. Además, existen perdidas debidas al cambio entre encendido y apagado en los dispositivos. Debido a que la tecnología esta llegando a los limites teóricos de rendimiento del silicio, la única vía para mejorar el rendimiento es usar nuevos, materiales con mejores propiedades, y por tanto, mejor balance entre los estados encendido y apagado.

Los materiales de gap ancho llevan estudiándose durante las últimas décadas debido a su enorme potencial para sostener altos voltajes a la vez que pueden conducir altísimas corrientes. Entre ellos, el diamante es el semiconductor definitivo para la electrónica de potencia debido a sus excelentes propiedades. Además de ser el material más duro, el diamante posee las mejores propiedades entre los semiconductores de banda ultra ancha, como su alta movilidad de electrones y huecos, su elevado campo eléctrico crítico y su baja constante dieléctrica. Además, supera a todos los materiales de la competencia en cuanto a conductividad térmica, con el valor más alto registrado para cualquier material. Todas estas propiedades hacen que el rendimiento ideal de los dispositivos de diamante esté por encima de cualquier otro material. Sin embargo, los dispositivos de diamante aún están en fase de desarrollo y presentan varias limitaciones tecnológicas y cuellos de botella que es necesario abordar para extraer todo el potencial del diamante. El principal inconveniente es que tanto los dopantes de tipo p como n dan lugar a niveles relativamente profundos que provocan una ionización parcial a temperatura ambiente. Sin embargo, la ionización parcial se puede mitigar fácilmente en el caso del diamante de tipo p trabajando a altas temperaturas (550K), lo que permite obtener un excelente rendimiento de los dispositivos en estado encendido. Además, los sustratos son caros y de tamaño limitado, aunque en la última década se ha observado un progreso alentador. Por lo tanto, el mercado futuro de los dispositivos de diamante parece centrarse en aplicaciones de potencia ultra elevada, alta frecuencia y temperatura y entornos difíciles. En lo que respecta a los transistores de efecto de campo (FET) de diamante, la mayoría se han fabricado utilizando el gas de huecos 2D que surge cuando una superficie de diamante con terminación de hidrógeno entra en contacto con una serie de moléculas adsorbidas y/o óxidos metálicos. Sin embargo, esta forma poco convencional de crear una región tipo p en un semiconductor adolece de problemas de inestabilidad y reproducibilidad y de baja movilidad operativa, aunque los recientes avances en el uso de estructuras de pasivación/puerta de óxido metálico han reducido considerablemente estos problemas. No obstante, también se han explorado estrategias de fabricación de dispositivos que se basan en un enfoque de dopaje convencional. Basados en capas epitaxiales de diamante dopadas con boro de tipo p, se han demostrado FET de metal-semiconductor (MESFET) y FET de metal-semiconductores-óxido normalmente encendidos con tensiones de bloqueo de hasta 3 kV. Estos garantizan una compatibilidad optimizada para la integración definitiva del dispositivo con la tecnología existente, así como la plena realización del potencial de funcionamiento en entornos difíciles. Además, proporcionan el mejor rendimiento a temperaturas elevadas (550K) debido a la ionización de las impurezas de boro que pueden aprovecharse en la electrónica de potencia gracias al autocalentamiento de los dispositivos. Por otro lado, los diodos Schottky de diamante se fabrican desde los años 90 y son el componente más desarrollado en la actualidad. La mayoría de los contactos Schottky también se fabrican a base de diamante dopado con boro utilizando una arquitectura pseudovertical. Los diodos Schottky son muy prometedores por su capacidad de conmutación rápida y sus altos voltajes. De hecho, los diodos Schottky de diamante optimizados pueden soportar

idealmente hasta 30 KV. La investigación exhaustiva ha dado lugar a resultados impresionantes en la última década. Se han explorado diferentes tratamientos superficiales y metales (W, WC, Zr, Pt, Mo, etc.) con el fin de reducir las corrientes de fuga y obtener así el mejor balance posible entre los estados encendido y apagado. Se han fabricado diodos Schottky de diamante capaces de soportar hasta 10 kV y un campo eléctrico crítico récord de 7,7 MV/cm. Por otra parte, también se han fabricado diodos Schottky heteroepitaxiales con resultados prometedores, ya que la disminución del coste de los dispositivos es fundamental para su comercialización. Sin embargo, las limitaciones tecnológicas en el grabado y el crecimiento epitaxial limitan el rendimiento final de los diodos Schottky de diamante. Además, la irreproducibilidad entre las muestras y los métodos de fabricación es una de las principales limitaciones a las que habrá que hacer frente en los próximos años. Esta tesis está dedicada al desarrollo de diodos de barrera Schottky y transistores basados en Schottky (MESFET) basados en diamante tipo p. La optimización de estos componentes es crucial para la futura hoja de ruta del diamante para la electrónica de potencia, ya que todavía no existe una verdadera demostración del potencial del diamante, y sin duda atraerá el interés de la investigación y de las empresas hacia él, impulsando el desarrollo de los dispositivos y terminando finalmente en su comercialización. Con el fin de demostrar el potencial del diamante, se establecen varios ambiciosos objetivos en relación con los dispositivos basados en el contacto Schottky: i) El estudio y la optimización de las propiedades del metal-diamante desde el punto de vista electrónico, físico-químico y de la ciencia de los materiales, con el fin de extraer el mejor contacto Schottky posible. ii) El diseño, la fabricación y la caracterización de un diodo Schottky vertical de diamante optimizado de alta tensión. iii) El diseño, la fabricación y la caracterización de un MESFET (con puerta y drenador basados en contactos Schottky) de diamante de 1 kV normalmente apagado. El desarrollo de estos estudios y dispositivos se lleva a cabo dentro del instituto NÉEL y la Universidad de Cádiz en el marco de dos proyectos diferentes: El primero, el proyecto diamante-HVDC. Su objetivo es la fabricación de diodos Schottky de diamante de alta tensión para su integración en una célula de conmutación y probar su fiabilidad. El segundo es el proyecto europeo Greendiamond. Mi objetivo dentro de este proyecto era coordinar y participar en la fabricación y caracterización del antes mencionado transistor MESFET de 1 kV normalmente apagado. El objetivo final de estos proyectos es fabricar dispositivos de rendimiento ideal, para demostrar las capacidades finales del diamante y su integración en componentes electrónicos de potencia funcionales. El crecimiento epitaxial del diamante, el conocimiento y las capacidades de la electrónica de potencia del grupo SC2G en el instituto NEEL en Francia y las potentes técnicas de análisis de ciencia de los materiales y la experiencia de la UCA se unen durante mi doctorado para abordar estos retos.

Este trabajo comienza estableciendo el marco teórico subyacente a los dispositivos basados en contactos Schottky. Se presenta la modelización de los contactos Schottky de diamante basándose en una descripción analítica de las barreras Schottky y se introducen y resuelven numéricamente las ecuaciones que gobiernan los mecanismos de conducción directa e inversa a través de la barrera Schottky. También se presenta y discute el estado del

arte de los modelos de resistividad y ruptura del diamante. Estos modelos físicos se utilizan para la comprensión cuantitativa de los diodos de diamante, en primer lugar, y de los MESFET laterales de diamante, en segundo lugar. Por un lado, se presentan las diferentes estructuras de diodos y sus restricciones de fabricación y limitaciones tecnológicas. Se ilustra el impacto de estas limitaciones, así como el rendimiento óptimo de los diodos de diamante. Por otro lado, se presenta el concepto de RBMESFET y se desarrolla un modelo 1D para la corriente de estado activado bajo la aproximación de canal gradual. Se analiza su rendimiento basándose en los modelos físicos desarrollados.

Una vez presentado el marco teórico, se realiza una investigación experimental dedicada a los diodos Schottky laterales de molibdeno y circonio. El perfil composicional extraído por TEM y XPS se correlaciona con el rendimiento eléctrico de los contactos Schottky de circonio y molibdeno. El tratamiento de pasivación con ozono, que se demuestra crucial para reducir las corrientes de fuga, oxida las capas de molibdeno y circonio. Mientras que esto no afectó en gran medida a las características de estado encendido del molibdeno, la degradación de los contactos de circonio se explica como resultado de la alta concentración de óxido en la interfaz. Los perfiles de potencial a lo largo de los bordes de los contactos, extraídos de la microscopía de fuerza con sonda Kelvin, mostraron la gran capacidad de pasivación del diamante con terminación de oxígeno y su posible papel en las corrientes de fuga a través del borde de los contactos de circonio. Por otra parte, se demuestra que el potencial de barrera del molibdeno con el diamante es inferior al potencial de curvatura de bandas de la terminación de oxígeno. Esto juega un papel importante para evitar las corrientes de fuga a través del borde de los contactos y apoyar las impresionantes características de estado apagado extraídas. Por último, se adoptó un enfoque teórico para comprender tanto la superficie terminada en oxígeno como su interfaz con el molibdeno. El cálculo teórico presentó una concordancia cualitativa con los resultados experimentales de KPFM, dando una altura de barrera Schottky para el molibdeno de ϕ_b=2,45 eV. Además, se reveló que el patrón de unión entre el molibdeno y el diamante terminado en oxígeno consiste en un enlace iónico entre el oxígeno y el molibdeno.

En cuanto a los diodos verticales, se fabricaron dos muestras diferentes de diodos Schottky, una para evaluar los diodos Schottky de molibdeno y circonio y otra para desarrollar un diodo de capaz de soportar alto voltaje (en el rango de los kV) basado en los resultados de la primera. La primera muestra (VD1) demostró el éxito del proceso de fabricación utilizado, basado en el molibdeno, con la importancia crucial del tratamiento de pasivación superficial para las capacidades de alta tensión de bloqueo. Se demostró la superioridad de este molibdeno frente al circonio como contacto Schottky, ya que el primero tenía una barrera Schottky más alta, un factor de idealidad más bajo, una mejor estabilidad térmica y una mayor capacidad de tensión de bloqueo. Más de la mitad de los contactos presentados en la primera muestra fueron capaces de sostener 2,25 MV/cm con al menos 4 órdenes de magnitud de rectificación. Su aplicación en capas de diamante de bajo dopaje pudo sostener consistentemente hasta un 60% de campo de ruptura de diamante de bajo dopaje. La segunda muestra

implementó el proceso de fabricación desarrollado del contacto Schottky basado en molibdeno en un diseño de alta tensión. Demostró con éxito capacidades de tensión de ruptura de >1kV con contactos que sostienen (una estimación baja) un campo eléctrico de 2,2 MV/cm. Esta muestra de epitaxia de capa de deriva produjo numerosos defectos "hillocks" y defectos redondos que hacen aún más notable el rendimiento de los contactos. Se estudió el papel de estos defectos y sólo los "hillocks" contribuyeron a las corrientes de fuga a través de los contactos. A pesar de la irregularidad de la muestra y de la alta concentración de defectos, la irreproducibilidad en las tensiones de ruptura se atribuyó al apiñamiento del campo eléctrico en el borde de los contactos y esta hipótesis fue apoyada por las mediciones EBIC. El campo electrico soportado por los diodos fabricados en esta tesis frente al area de los mismos se compara en la figura C.5 frente a multiples resultados de la bibliografía.

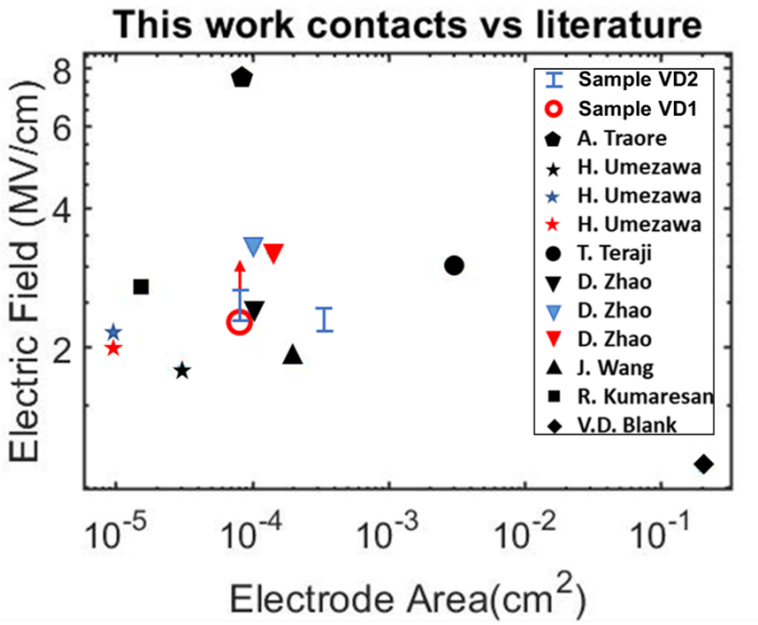

FIGURE C.5: *Campo eléctrico soportado frente al área de los contactos Schottky para los contactos de molibdeno de este trabajo frente a numerosas referencias de la bibliografía [167, 168, 150, 149, 169, 170, 171, 172].*

Por lo tanto, los contactos Schottky de molibdeno desarrollados en este trabajo demostraron unas prestaciones consistentemente adecuadas para extraer el potencial HV del diamante a alta temperatura. Se abordó el problema de la corriente de fuga y, siguiendo el proceso de fabricación desarrollado en esta tesis, los futuros diodos Schottky de diamante podrán liberar todo su potencial.

Por ultimo, se fabricaron MESFETs laterales de bloqueo inverso (drenador basado en un contacto Schottky) de >1kV basados en contactos Schottky de molibdeno sobre diamante dopado con boro. Se ha logrado un control preciso del grosor de la capa de diamante y del nivel de dopaje, de forma que se produce una depleción total del canal sin aplicar una polarización de puerta, con la posibilidad de abrir el canal a V_{GS} negativos. Los dispositivos presentan una corriente de fuga indetectable y una corriente de 1,5 µA/mm en estado encendido a RT. Es importante destacar que la capacidad de bloqueo del transistor se evaluó

en >1kV, incluso a su temperatura máxima de trabajo de 425K, sin mostrar corriente de fuga y después de la tensión HV, presentando características reproducibles sin cambios. La caracterización a mayor temperatura (425K) revela un aumento de las capacidades del transistor en estado encendido debido a una mayor ionización de los átomos dopantes de boro, alcanzando el transistor un nivel de corriente de 70 $\mu A/mm$ y una transconductancia de 147 μSmm^{-1}. La caracterizacion del transistor a alto voltaje y temperatura se presenta en la figura C.6 Sin embargo, su temperatura de trabajo está limitada a 425K, por debajo de la óptima de 500-550K, debido a la unión p-n no conectada a tierra entre la capa de deriva de tipo p y el sustrato semiaislante Ib. En cualquier caso, el alto voltaje de ruptura, la capacidad de funcionamiento a temperaturas relativamente altas, el comportamiento normalmente apagado y la dureza inherente a la radiación del diamante como semiconductor, hacen de estos dispositivos una excelente aproximación al objetivo de conseguir transistores de diamante para aplicaciones de alta temperatura, alto voltaje y entornos hostiles.

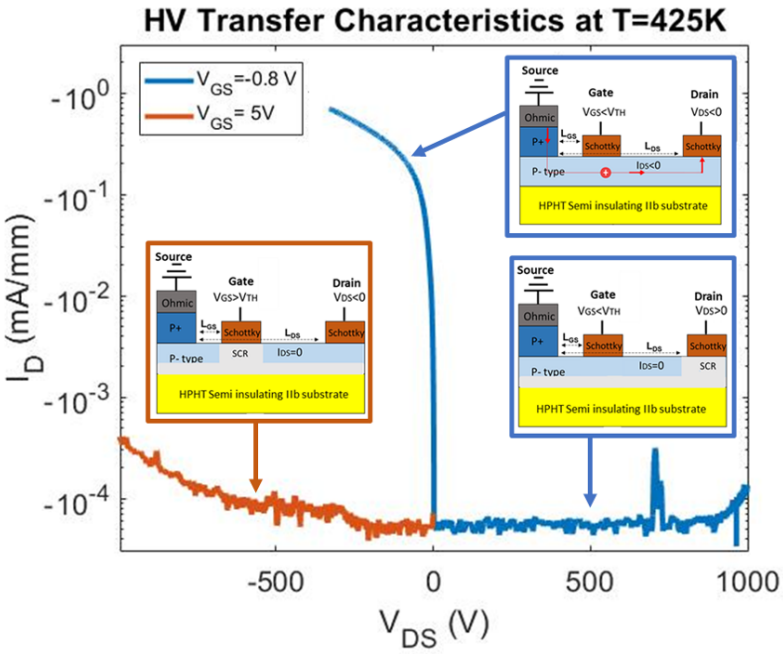

FIGURE C.6: *Características de transferencia de alto voltage del RBMESFET a 425K para la configuración del canal cerrado con $V_{GS} = 5V$ en la curva roja y para el estado encendido y la configuración de diodo Schottky en la curva azul con $V_{GS} = -0.8V$.*

En resumen, los avances realizados durante esta tesis en la optimización de los contactos Schottky permitieron impulsar el estado de apagado y la reproducibilidad de los diodos Schottky verticales de diamante. Los futuros diodos se beneficiarán de los resultados mostrados, ya que la aplicación de los contactos Schottky desarrollados en esta tesis junto con capas de deriva de diamante más gruesas podría alcanzar el punto de referencia de sostener 10 kV. Por otra parte, la demostración de un MESFET lateral de bloqueo inverso de >1 kV normalmente apagado ha sido la primera en la literatura. Las inusuales características de este transistor muestran la precisión adquirida en la tecnología de epitaxia de diamante.

Una futura transición hacia transistores verticales utilizando la tecnología desarrollada dará rienda suelta al rendimiento potencial de los MESFET de diamante.

Appendix D

Publications and Conferences

D.1 Publications

- J. Cañas et al. "Determination of alumina bandgap and dielectric functions of diamond MOS by STEM-VEELS". Applied Surface Science (2018). doi: 10.1016/j.apsusc.2018.06.163.
- M. Gutiérrez, F. Lloret, T.T. Pham, J. Cañas, D.F. Reyes, D. Eon, J. Pernot, D. Araújo. Control of the Alumina Microstructure to Reduce Gate Leaks in Diamond MOSFETs. Nanomaterials (2018) doi: 10.3390/nano8080584.
- G. Alba, D. Eon, M.P. Villar, R. Alcántara, G. Chicot, J. Cañas, J. Letellier, J. Pernot, D. Araujo. H-Terminated Diamond Surface Band Bending Characterization by Angle-Resolved XPS. Surfaces. (2020) doi:10.3390/surfaces3010007.
- J. Cañas et al. "Diamond/gamma-alumina band offset determination by XPS". Applied Surface Science (2021), 10.1016/j.apsusc.2020.146301.
- J. Cañas et al., "Normally-off Diamond Reverse Blocking MESFET," in IEEE Transactions on Electron Devices (2021), doi: 10.1109/TED.2021.3117237.

D.2 Conferences

D.2.1 Oral presentations

- 2018 J.Cañas , J.C. Piñero, F. Lloret, G. Alba, M. Gutierrez , T. Pham, J. Pernot, D. Araújo, Hasselt, Determination of alumina bandgap and dielectric functions in diamond MOSFET by STEM-VEELS. SBBD, Hasselt, Belgium.
- 2019 M. Gutiérrez, J. Cañas, F. Lloret, D. Leinen, D. Eon, J. Pernot, D. Araujo. Crystallographic Effects on the Alumina/Diamond Band Setting in Diamond MOSFETs. E-MRS Warsaw.
- 2019 M. Gutiérrez, A. Coronilla, J. Cañas, J. Navas, F. Lloret, T. Pham, D. Eon, J. Pernot, D. Araujo. Optimization of diamond/alumina interfaces for diamond-based MOSFETs by TEM and DFT calculations. 29th International Conference on Diamond and Carbon Materials, Dubrotnik.

- 2019 J. Cañas, G. Alba, D. Leinen, F. Lloret, M. Gutierrez, D. Araujo. X-Ray Photoelectron Spectroscopy of Diamond/-alumina interface, French Japanese workshop on diamond power devices, Aussois.
- 2019 D. Araujo, J. Cañas, M. Gutiérrez, F. Lloret, D. Fernandez de los Reyes. New transmission electron microscopy issues for the diamond-based power electronics materials characterisation. French Japanese workshop on diamond power devices, Aussois.
- 2019 G. Alba, R. Alcántara, M.P. Villar, J. Cañas, D. Eon, J. Lettellier, G. Chicot, D. Araujo, J. Pernot. Diamond surface band bending estimation by ARXPS. MRS Fall meeting Boston.
- 2019 J. Cañas, B. Soto, M. Gutiérrez, P. Villar, D. Fernandez, F. Lloret, D. Eon, J. Pernot, D. Leinen and D. Araujo. Diamond/oxide interface issues to optimize MOSFET gate band setting. Workshop on Compound Semiconductor Devices and Integrated Circuits 2019, Cabourg.
- 2019 J. Cañas, G. Alba, M. Gutiérrez, E. Gheeraert and D. Araujo. Thin amorphous alumina films on (100) oriented O-terminated diamond studied by XPS and HRTEM (oral). 30th International Conference on Diamond and Carbon Materials, Seville.
- 2019 J. Canas, O. Loto, M. Gutierrez, D. Eon, E. Gheeraert. Silicon dioxide MOS capacitors on (100) p- diamond (oral). Grenoble-Barcelona twin conference : From quantum systems to new materials and smart electrical energy, Grenoble.
- 2020 J. Cañas, O. Loto, C. Masante, M. Gutierrez, D. Eon, E. Gheeraert. Detailed analysis of ALD grown SiO2 MOS capacitors on (100) p-type. SBBD, Hasselt, Belgium.
- 2021 J. Cañas, A. Pakpour-Tabrizi, E. Gheeraert, R. Jackman. Normally-OFF Diamond Reverse Blocking MESFET. MRS Spring Meeting, Seattle. (Best Oral Award).

D.2.2 Poster presentations

- 2018 M.Gutierrez, A. Coronilla, J.Navas, J.Cañas, D.Araujo. Crystallinity of alumina-diamond interface in MOSFET devices. Interfaces in Energy Materials, Trinity college, Cambridge.
- 2018 S. Forster, J. Canas, F. Lloret,, M. Gutierrez, D. Araujo, K. Kalna, and D. Chaussende. Experimental Extraction of the Bandgap for Al4SiC4, UK Semiconductor conference 2018.
- 2019 G. Alba, R. Alcántara, M. P. Villar, J. Letellier, J. Cañas, G. Chicot, D. Eon, D. Araujo. H2 plasma effect on (100)-oriented HPHT diamond surface by AFM and ARXPS. SBBD, Hasselt, Belgium.

- 2019 J. Cañas, J. Pernot, G. Alba, E. Gheeraert, M. Gutierrez, D. Araujo. Low temperature ALD synthesis of crystalline alumina thin films on (100) oriented diamond. SBBD, Hasselt, Belgium.
- 2019 D. Leinen, J. Cañas, M.P. Villar, D. Araujo, D. Eon, J. Pernot. XPS depth profiling with low energy Ar ions for band offset determination. (Poster).
- 2020 B. Soto, J. Cañas, E. Mossang, M. Gutiérrez, M.P. Villar, D. Araujo, and J. Pernot. Metal/ZrO2/O-terminated p-type diamond MOSCAP: From the electrical analysis to the microstructure. SBBD, Hasselt, Belgium.
- 2020 J. Cañas, A. Pakpour-Tabrizi, E. Gheeraert, R. Jackman Normally-Off Reverse Blocking MESFET. Second Worshop on Diamond Electronics. Michigan state university. US.

Appendix E

Abstracts

Schottky contact based diamond power devices: tuning the interfacial properties to demonstrate diamond unleashed performance

The current silicon technology is reaching its theoretical limits and the only road to improve the performance is to use new materials with better properties. Among all possible candidates, diamond is the ultimate semiconductor for power electronics due to its outstanding properties. Besides being the hardest material, diamond possesses the best properties among ultra-wide band gap semiconductors including its high electron-hole mobility, high critical electric field and low dielectric constant. Moreover, it surpasses all competitor materials in terms of thermal conductivity with the highest value reported for any material. All these properties make the ideal performance of diamond devices to be above any other material. However, diamond devices are still under development with several technological limitations and bottlenecks that need to be addressed in order to extract diamond's full potential. This thesis is dedicated to the development of Schottky barrier diodes and Schottky based transistors (MESFET) based on p-type diamond. The optimization of these components is crucial for the diamond future roadmap for power electronics, as a true demonstration of diamond potential still lacks, and it will definitely attract interest from research and companies further pushing the development of devices and eventually ending up in their commercialization. In order to get demonstrate diamond potential, various challenging objectives were accomplished regarding Schottky contact based devices during this thesis: i) The optimization of metal-diamond junction properties from an electronic, physico-chemical and material science point of view in order to extract the best possible performing Schottky contact. Molybdenum was selected as the best option due to its high Schottky barrier, low ideality factor, great blocking capabilities and good thermal stability. The oxygen termination of diamond interface with molybdenum and its role as a passivation surface were demonstrated to be crucial for the blocking voltage capabilities of the contacts. ii) The design, fabrication and characterization of a vertical Schottky contact based on molybdenum sustaining >2 MV/cm and 1.1 kV. These promising results will allow the fabrication of 10 kV Schottky diodes with reproducibility with the use of thicker diamond layers in the future. iii) The design, fabrication and characterization of a normally-off 1 kV blocking voltage diamond gate-drain Schottky lateral MESFET. The fabricated transistor is

the first normally-off MESFET reported in literature and its future implementation into a vertical architecture will allow to boost the performance up to 100 times.

Dispositifs de puissance en diamant à contact Schottky : réglage des propriétés interfaciales pour démontrer les performances illimitées du diamant.

La technologie actuelle du silicium atteint ses limites théoriques et la seule façon d'améliorer les performances est d'utiliser de nouveaux matériaux dotés de meilleures propriétés. Parmi tous les candidats possibles, le diamant est le semi-conducteur ultime pour l'électronique de puissance en raison de ses propriétés exceptionnelles. En plus d'être le matériau le plus dur, le diamant possède les meilleures propriétés parmi les semi-conducteurs à bande interdite ultra large, notamment une mobilité électron-trou élevée, un champ électrique critique élevé et une faible constante diélectrique. En outre, il surpasse tous les matériaux concurrents en termes de conductivité thermique, avec la valeur la plus élevée rapportée pour un matériau quelconque. Toutes ces propriétés font que les performances idéales des dispositifs en diamant sont supérieures à celles de tout autre matériau. Cependant, les dispositifs en diamant sont toujours en cours de développement et présentent plusieurs limitations et goulots d'étranglement technologiques qui doivent être résolus afin d'extraire tout le potentiel du diamant. Cette thèse est dédiée au développement de diodes à barrière Schottky et de transistors à base de Schottky (MESFET) basés sur le diamant de type p. L'optimisation de ces composants est cruciale pour le développement de la technologie du diamant. L'optimisation de ces composants est cruciale pour la future feuille de route du diamant dans le domaine de l'électronique de puissance, car une véritable démonstration du potentiel du diamant fait encore défaut, et elle attirera certainement l'intérêt de la recherche et des entreprises, ce qui poussera le développement des dispositifs et aboutira finalement à leur commercialisation. Afin de démontrer le potentiel du diamant, plusieurs objectifs ambitieux ont été atteints concernant les dispositifs à contact Schottky au cours de cette thèse : i) L'optimisation des propriétés de la jonction métal-diamant d'un point de vue électronique, physico-chimique et de la science des matériaux afin d'obtenir le contact Schottky le plus performant possible. Le molybdène a été sélectionné comme la meilleure option en raison de sa barrière Schottky élevée, son faible facteur d'idéalité, ses grandes capacités de blocage et sa bonne stabilité thermique. La terminaison en oxygène de l'interface du diamant avec le molybdène et son rôle en tant que surface de passivation se sont avérés cruciaux pour les capacités de tension de blocage des contacts. ii) La conception, la fabrication et la caractérisation d'un contact Schottky vertical à base de molybdène supportant >2 MV/cm et 1,1 kV. Ces résultats prometteurs permettront la fabrication de diodes Schottky de 10 kV avec reproductibilité grâce à l'utilisation de couches de diamant plus épaisses à l'avenir. iii) La conception, la fabrication et la caractérisation d'un MESFET latéral avec grille et drain Schottky en diamant à tension de blocage de 1 kV. Le transistor fabriqué est le premier MESFET normalement OFF rapporté dans la littérature et sa future implémentation dans une architecture verticale permettra d'augmenter les performances jusqu'à 100 fois.